

FINAL REPORT

Particulate Matter Emissions Factors for Dust from Unique Military Activities

SERDP Project SI-1399

June 2010

Dr. J. A. Gillies
Dr. V. Etyemezian
Dr. H. Kuhns
Dr. H. Moosmüller
Dr. J. Engelbrecht
Dr. J. King
Mr. S. Uppapalli,
Mr. G. Nikolich,
Mr. J. D. McAlpine,
Mr. D. Zhu,
Dr. M. Skiba,
Dr. D.A. Gillette
Desert Research Institute

Dr. Will Shaw
Pacific Northwest National Laboratory

Dr. Ram Hashmonay
Environ



Strategic Environmental Research and
Development Program

Report Documentation Page

Form Approved
OMB No. 0704-0188

Public reporting burden for the collection of information is estimated to average 1 hour per response, including the time for reviewing instructions, searching existing data sources, gathering and maintaining the data needed, and completing and reviewing the collection of information. Send comments regarding this burden estimate or any other aspect of this collection of information, including suggestions for reducing this burden, to Washington Headquarters Services, Directorate for Information Operations and Reports, 1215 Jefferson Davis Highway, Suite 1204, Arlington VA 22202-4302. Respondents should be aware that notwithstanding any other provision of law, no person shall be subject to a penalty for failing to comply with a collection of information if it does not display a currently valid OMB control number.

1. REPORT DATE JUN 2010		2. REPORT TYPE		3. DATES COVERED 00-00-2010 to 00-00-2010	
4. TITLE AND SUBTITLE Particulate Matter Emissions Factors for Dust from Unique Military Activities				5a. CONTRACT NUMBER	
				5b. GRANT NUMBER	
				5c. PROGRAM ELEMENT NUMBER	
6. AUTHOR(S)				5d. PROJECT NUMBER	
				5e. TASK NUMBER	
				5f. WORK UNIT NUMBER	
7. PERFORMING ORGANIZATION NAME(S) AND ADDRESS(ES) Desert Research Institute, 2215 Raggio Parkway, Reno, NV, 89512				8. PERFORMING ORGANIZATION REPORT NUMBER	
9. SPONSORING/MONITORING AGENCY NAME(S) AND ADDRESS(ES)				10. SPONSOR/MONITOR'S ACRONYM(S)	
				11. SPONSOR/MONITOR'S REPORT NUMBER(S)	
12. DISTRIBUTION/AVAILABILITY STATEMENT Approved for public release; distribution unlimited					
13. SUPPLEMENTARY NOTES					
14. ABSTRACT SERDP project SI-1399 carried out an empirically-based study using in situ measurements to characterize and quantify dust emissions from unique Department of Defense sources operating during testing and training maneuvers on U.S. military installations. This project focused on developing an understanding of the dust emission process and strength of these emissions for artillery backblast on improved gun-sites (surface treated with dust palliatives), tracked and wheeled vehicles travelling on unpaved surfaces, and rotary-winged aircraft travelling close to desert surfaces. Based on the measured dust emissions from these sources the greatest amount of emissions is from tracked and wheeled vehicles due to their high emission rates and frequency of use. Dust emissions from both artillery backblast and rotary-winged aircraft are representative of only minor contributing sources in the overall attribution of airborne particulates to DoD sources. In partnership with SI-1400 a hybrid measurement system for estimating fugitive emissions of dust was also tested, which combined elements of optical remote sensing and in situ measurements. This testing showed that such a system will allow for the development and eventual deployment of other open path extinction measurements tools such as LIDAR or digital cameras, which can be used to develop fugitive PM emission factors. The dust emission relationships and defined emission factors developed as part of this project were incorporated into the DUSTRAN model that can be used to forecast and hind-cast dust emissions based on testing and training scenarios involving these source types with knowledge of the meteorology.					
15. SUBJECT TERMS					
16. SECURITY CLASSIFICATION OF:			17. LIMITATION OF ABSTRACT Same as Report (SAR)	18. NUMBER OF PAGES 166	19a. NAME OF RESPONSIBLE PERSON
a. REPORT unclassified	b. ABSTRACT unclassified	c. THIS PAGE unclassified			

This report was prepared under contract to the Department of Defense Strategic Environmental Research and Development Program (SERDP). The publication of this report does not indicate endorsement by the Department of Defense, nor should the contents be construed as reflecting the official policy or position of the Department of Defense. Reference herein to any specific commercial product, process, or service by trade name, trademark, manufacturer, or otherwise, does not necessarily constitute or imply its endorsement, recommendation, or favoring by the Department of Defense.

TABLE OF CONTENTS

1.	ABSTRACT	1
2.	PROJECT OBJECTIVES	2
3.	BACKGROUND	3
3.1.	ARTILLERY BACKBLAST	4
3.2.	DUST EMISSIONS BY OFF-ROAD VEHICLE TRAVEL	4
3.3.	DUST EMISSIONS BY BY ROTARY-WINGED AIRCRAFT	5
4.	MATERIALS AND METHODS	8
4.1	DUST FLUX AND EMISSION FACTOR DETERMINATION, GENERAL PRINCIPLES ...	8
4.2	METHODS: DUST EMISSIONS FROM ARTILLERY BACKBLAST	13
4.3	METHODS: DUST EMISSIONS FROM OFF-ROAD MILITARY VEHICLE ACTIVITY	15
4.4	METHODS: DUST EMISSIONS FROM ROTARY-WINGED AIRCRAFT	18
4.5	MINERALOGY AND CHEMISTRY OF AIRBORNE DUST COLLECTED DURING FIELD MEASUREMENT CAMPAIGNS	22
4.5.1	Methods: Particle Characterization	22
4.6	METHODS: HYBRID REMOTE SENSING AND IN-SITU MEASUREMENT SYSTEM TO MEASURE FUGITIVE DUST FLUX	23
4.6.1	Hybrid System Operating Principles	23
5.	RESULTS AND DISCUSSION	25
5.1	ARTILLERY BACKBLAST	25
5.2	DUST EMISSIONS FROM OFF-ROAD MILITARY VEHICLE ACTIVITY	28
5.2.1	PI-SWERL Measurements of Emission Potential, YTC & Ft. Carson	33
5.3	DUST EMISSIONS FROM ROTARY-WINGED AIRCRAFT	35
5.3.1	PI-SWERL Emission Potential Measurements, YPG	45
5.4	ROTARY-WINGED AIRCRAFT GROUND EFFECT CHARACTERIZATION	45
5.5	ASSESSMENT OF THE APPLICABILITY OF A COMPUTATIONAL FLUID DYNAMIC (CFD) METHOD TO SIMULATE A ROTORCRAFT DUST EMISSION SOURCE	46

5.6	PARTICLE PHYSICAL AND MINERALOGICAL CHARACTERISTICS	48
5.6.1	Preliminary Investigation	48
	5.6.1.1 <i>Polarizing Microscopy</i>	48
	5.6.1.2 <i>X-ray Diffraction (XRD)</i>	48
	5.6.1.3 <i>Secondary Electron Images</i>	48
	5.6.1.4 <i>Computer Controlled Scanning Electron Microscopy (CCSEM)</i>	52
	5.6.1.5 <i>Chemical Analysis of Filters</i>	53
	5.6.1.6 <i>Normative Mineral Calculations</i>	54
5.6.2	Particle Characterization at Field Sites	55
	5.6.2.1 <i>Yuma Proving Ground, Arizona (2005)</i>	55
	5.6.2.2 <i>Yakima Training Center, Washington (2006)</i>	56
	5.6.2.3 <i>Yuma Proving Ground (2007)</i>	58
	5.6.2.4 <i>Ft. Carson, Colorado (2008)</i>	60
5.6.3	Particle-Size Distributions of PM at the Field Sites	60
5.7	HYBRID REMOTE SENSING AND IN-SITU MEASUREMENT SYSTEM TO MEASURE FUGITIVE DUST FLUX	64
5.8	DUSTRAN	70
6	CONCLUSIONS	72
6.1	ARTILLERY BACKBLAST	72
6.2	OFF-ROAD VEHICLE DUST EMISSIONS	72
6.3	ROTARY-WINGED AIRCRAFT EMISSIONS	73
6.4	PARTICLE CHARACTERIZATION	74
6.5	HYBRID METHOD	74
6.6	DUSTRAN	75
6.7	SI-1399 EMISSION MEASUREMENTS AND US EPA, AP-42 COMPILATION OF EMISSION FACTORS	75
7.	LITERATURE CITED	78

APPENDICES Mineralogy & Chemistry of Dust Emissions

A	SEM, Secondary Electron Images and Spectra, YPG Site 1.....	A-1
B	SEM, Secondary Electron Images and Spectra, YPG Site 2.....	B-1
C	SEM, Secondary Electron Images & Spectra, Yakima 2006, Dirt Road, Site 1	C-1
D	SEM, Secondary Electron Images & Spectra, YPG 2007, Desert Pavement, Site 1	D-1
E	SEM, Secondary Electron Images & Spectra, YPG 2007, Disturbed Desert, Site 2	E-1
F	SEM, Secondary Electron Images & Spectra, Ft. Carson, 2008, Site 1	F-1
G	SEM, Secondary Electron Images & Spectra, Ft. Carson, 2008, Site 2	G-1
H	Chemical Results of 20 PM₁₀ and PM_{2.5} Filter Samples.....	H-1
I	Particle Size Distribution Data	I-1

LIST of TABLES

Table 1. Instrumentation used by SI-1399 and SI-1400 to Quantify PM Flux Rates.....9

Table 2. Modular Artillery Charge System (MACS) combinations used to generate emissions using a 155 mm Model M198 or M109 howitzer.....14

Table 3. Minimum, maximum, mean and standard deviations of the measured PM₁₀ and PM_{2.5} artillery backblast emission fluxes.....26

Table 4. Flux calculation data recovery statistics from the Yakima and Ft. Carson vehicle dust flux experiments.....29

Table 5. Summary of surface material silt content, emission factors, and cumulative PI-SWERL emissions for four test locations.....33

Table 6. Dust emission test conditions and measurement parameters for the rotary-winged aircraft flights.....36

Table 7. Report on of the reliability of the acquired dust emission data, rotary-winged aircraft tests.....37

Table 8. Summary of mineralogical compositions of samples collected during the four sampling campaigns.....49

Table 9. CCSEM/EDS mineral abundance summaries of PM₁₀ samples on Nuclepore filters.....52

LIST of FIGURES

1. Schematic diagrams of rotor wake flow regimes and images of the aircraft for these ground effect states taken at the Yuma Proving Ground.....7

2. Instrument configuration to measure dust emissions from artillery backblast13

3. Instrument configuration and layout to measure dust emissions from military vehicles, Ft. Carson.....16

4. Images of wheeled and tracked off-road military vehicles used in this study17

5. Instrument configuration to measure dust emissions from rotary-winged aircraft, YPG20

6. Instrument placement used to define dust emissions relationships rotary-winged aircraft, YPG.....21

7. Schematic of the hybrid method instrument configuration.....24

8. Mean PM₁₀ and PM_{2.5} emission fluxes from a 155 mm howitzer plotted as a function of charge zone.....27

9. Comparison of Gravimetric PM₁₀ Emission Factors versus vehicle speed from Ft. Bliss, Ft. Carson, and Yakima.30

10.	Comparison of tracked vehicle PM ₁₀ emission factors versus vehicle momentum for three different vehicles	32
11.	Comparison of tracked and wheeled vehicle DustTrak emission factors versus vehicle momentum operating at the same locations	32
12.	Image of M1A1 (Abrams) traveling at 40 km hr ⁻¹ on unpaved road at the YPG ..	33
13.	Emissions of PM ₁₀ as a function of forward travel speed for Sites 1 and 2, YPG speed.....	39
14.	Emissions of PM ₁₀ as a function of advance ratio for Sites 1 and 2, YPG.....	40
15.	Normalized emissions of PM ₁₀ and PM _{2.5} as a function of mean forward travel speed.....	41
16.	The relationship between normalized mean peak pressure and mean forward travel speed	41
17.	The relationship between normalized mean peak pressure and distance from the centerline of the aircraft flight line	42
18.	Normalized dust concentration as a function of normalized disk loading.....	44
19.	Comparison of emissions of PM ₁₀ as a function of vehicle speed for the rotary-winged aircraft and light and heavy wheeled military vehicles.....	44
20.	CCSEM/EDS summary plots of PM ₁₀ samples on Nuclepore filters	53
21.	Summary plots of PM ₁₀ and PM _{2.5} filter chemical results	54
22.	Summary plots of PM ₁₀ and PM _{2.5} filter results, normative mineral abundances ..	56
23.	SEM secondary electron images and EDS spectra of particles collected on Nuclepore filters, e.g., from YPG	57
24.	SEM secondary electron images and EDS spectra of particles collected on Nuclepore filters, YTC test road.....	59
25.	SEM secondary electron images and EDS spectra of particles collected on Nuclepore filters, YPG desert pavement	61
26.	SEM secondary electron images and EDS spectra of particles collected on Nuclepore filters, Ft. Carson test road	62
27.	CCSEM measured particle number distributions per size bin from PM ₁₀ Nuclepore filters.....	63
28.	CCSEM measured particle mass distributions per size bin from PM ₁₀ Nuclepore filters.....	64
29.	OP-LT calibration measurements made at YPG.....	65
30.	Plot of the OP-LT and DM PM ₁₀ calibration measurements	66
31.	Plot of the OP-LT and DM PM ₁₀ calibration measurements at Ft. Carson	67
32.	Comparison of PIMC determined with the new method to the PIMC determined from the grid of DT monitors.....	68

33.	Comparison of PIMC determined with the new method to the PIMC determined from the grid of DT monitors for 20 events at Ft. Carson	70
-----	---	----

LIST OF ACRONYMS

AA	Atomic Absorption
AC	Automated Colorimetry
AGL	Above Ground Level
ASL	Atmospheric Surface Layer
BEI	Backscattered Electron Imagery
CCSEM	Computer Controlled Scanning Electron Microscopy
CFD	Computation Fluid Dynamic
DM	Dust Monitor
DoD	Department of Defense
DT	DustTrak
DRI	Desert Research Institute
EDS	Energy Dispersive Spectra
EDXRF	Energy Dispersive X-ray Fluorescence Spectrometry
ERDC-CERL	Engineer Research and Development Center – Construction Engineering Research Laboratory
HEMTT	Heavy Expanded Mobility Tactical Truck
HMMVW	High Mobility Multipurpose Wheeled Vehicle
IC	Ion Chromotography
IMPROVE	Interagency Monitoring of Protected Visual Environments
LMTV	Light Medium Tactical Vehicles
MACS	Modular Artillery Charge System
NMPSS	Normalized mean peak shear stress
NPSS	Normalized peak shear stress
MPL	Micro-Pulse Lidar
NRB	Normalized Relative Backscatter
OP-FTIR	Open Path Fourier Transform Infrared (FTIR)
OP-LT	Open Path Transmissometer
ORS	Optical Remote Sensing
PAE	Path-Averaged Extinction

PIE	Path-Integrated Extinction
PIMC ₁₀	Plane-Integrated PM ₁₀ Mass Concentration
PI-SWERL	Portable In-Situ Wind EROsion Laboratory
PM	Particulate Matter
PNNL	Pacific Northwest National Laboratory
RPM	Revolutions per Minute
SEM	Scanning Electron Microscopy
SERDP	Strategic Environmental Research and Development Program
SON	Statement of Need
TEOM	Tapered Element Oscillating Microbalance
TOR	Thermo Optical Reflectance
US EPA	United States Environmental Protection Agency
USACE	United States Army Corps of Engineers
WD	Wind direction
WS	Wind speed
XRD	X-Ray Diffraction
YPG	Yuma Proving Ground
YTC	Yakima Training Center

Keywords: dust emissions, emission factors, particulate matter (PM), fugitive dust, testing and training activities

ACKNOWLEDGEMENTS

The SI-1399 research team would like to acknowledge the SERDP, Sustainable Infrastructure program for their sponsorship. The team would also like to thank the following installations for their logistical and financial support: US Army Yuma Proving Ground, Yuma AZ, and specifically the Natural Events Test Office, Yakima Training Center, Yakima WA, and Ft. Carson, CO. We would also like to acknowledge the support of SERDP project SI-1400, the success of our joint field campaigns and the fruitful discussions during the execution of this research.

1. ABSTRACT

SERDP project SI-1399 carried out an empirically-based study using in situ measurements to characterize and quantify dust emissions from unique Department of Defense sources operating during testing and training maneuvers on U.S. military installations. This project focused on developing an understanding of the dust emission process and strength of these emissions for artillery backblast on improved gun-sites (surface treated with dust palliatives), tracked and wheeled vehicles travelling on unpaved surfaces, and rotary-winged aircraft travelling close to desert surfaces. Based on the measured dust emissions from these sources the greatest amount of emissions is from tracked and wheeled vehicles due to their high emission rates and frequency of use. Dust emissions from both artillery backblast and rotary-winged aircraft are representative of only minor contributing sources in the overall attribution of airborne particulates to DoD sources.

In partnership with SI-1400 a hybrid measurement system for estimating fugitive emissions of dust was also tested, which combined elements of optical remote sensing and in situ measurements. This testing showed that such a system will allow for the development and eventual deployment of other open path extinction measurements tools such as LIDAR or digital cameras, which can be used to develop fugitive PM emission factors.

The dust emission relationships and defined emission factors developed as part of this project were incorporated into the DUSTRAN model that can be used to forecast and hind-cast dust emissions based on testing and training scenarios involving these source types with knowledge of the meteorology.

2. OBJECTIVES

The research presented in this report represent the culmination of a series of experiments designed to address the SERDP Statement of Need CPSON-04-04 “Particulate Matter Emission Factors for Dust from Unique Military Activities”, which requested that work be undertaken to identify, characterize, and monitor airborne emissions of PM resulting from Department of Defense (DoD) testing/training activities related to unique military activities. The Statement of Need (SON) also requested that PM₁₀ and PM_{2.5} emissions be characterized specifically for tracked vehicles, rotor and propeller wash, and backblasts from range firing positions. This SON also emphasized that developed emission factors should be generated for each of these activities and situations and be made adaptable through modeling to localized conditions.

In response to this request the Desert Research Institute (DRI) team and its partner Pacific Northwest National Laboratory (PNNL), developed and executed a research program that involved field-based empirical measurements to quantify particulate emissions from several unique DoD testing and training activities including artillery backblast, tracked vehicle travel on unpaved surfaces, and dust emissions created by rotary-winged aircraft traveling close to the Earth’s surface. In addition to measurements to quantify the flux of mineral dust emissions from these source types the experiments were also designed to characterize the relationships between the magnitude of the emissions, the operational parameters of the source (e.g., travel speed in the case of vehicles), their physical characteristics (e.g., weight), and the characteristics of the surface from which the dust was emitted. In addition, physical, and chemical properties of the emitted PM were measured and catalogued in a database that is available for assessing source attribution and visibility impairment. This project also further developed a GIS-based dust dispersion model (DUSTRAN) and incorporated the new dust emission factors to enhance its applicability for DoD applications.

In consultation with SERDP it was decided that due to the infrequent nature of fixed-wing aircraft in testing and training scenarios within the continental U.S. that this emission source would not be investigated as part of this project.

The specific objectives of this research program were: 1) carry out field measurement campaigns to quantify dust emissions and develop emission factors for tracked military vehicles, rotary-winged aircraft, and artillery pieces for various unpaved surfaces, while extending our understanding of the important vehicle, activity, and surface characteristics that influence the magnitude of the observed emissions, 2) carry out measurement campaigns using the DRI flux tower system to develop emission factors of artillery backblast, tracked vehicles, and rotary-winged aircraft, 3) link the measured emission factors with indices of surface dust emission potential using a new portable wind tunnel and an on-vehicle measurement system thereby creating a cost effective mechanism to extend the use of the emission factors into different environments, 4) continue to develop a database from field and laboratory measurements that characterizes the chemical, physical, and optical properties of the dust emissions that are important for assessing source contribution estimates and impacts on regional visibility degradation, 5) further develop a Geographic Information System-based dust dispersion modeling system that integrates the newly-developed emission factors into its user interface, and 6) to disseminate the information, methods, and modeling products generated from this

research to the military and civilian user community to improve their abilities to gather information, make decisions based on that information, and develop cost-effective solutions that will enhance military preparedness.

The execution of this project also involved close collaboration with SERDP Project SI-1400 “Development of Emission Factors for Dust Generated by Unique Military Activities” with Dr. Byung Kim, USACE ERDC-CERL as the Principal Investigator. The objectives of SI-1400 were complimentary to SI-1399 and included: 1) to measure PM to determine emission factors from DoD’s non-facility PM generation sources, (2) develop and modify instrumentation/methods/systems for PM emission factor measurement, and (3) develop model components that better describe the generation of DoD’s fugitive PM. SI-1400 used principally remote sensing technology to characterize, and monitor airborne PM_{2.5} and PM₁₀ emissions from tracked vehicle maneuvers, rotary-wing aircraft moving near the ground surface, and back blast emissions from artillery and mortar pieces. As part of our collaboration SI-1399 developed their seventh objective, i.e., carry out in situ measurements of dust emissions for comparison with the more experimental remote sensing measurements of SI-1400, allowing for comparison of this method with an established method and to corroborate the developed emission factors.

As these two projects progressed the opportunity arose from the collaborative effort to test the effectiveness of a hybrid measurement system, which combined a single remote sensing measurement of light extinction using a transmissometer with point measurements of dust concentration. The objective of this work was to evaluate the performance of this hybrid measurement approach to capture data with sufficient accuracy to estimate emission factors that were equivalent (and within acceptable levels of uncertainty) to those derived from the more extensive measurements that used the full complement of in situ and/or remote sensing data. Data were collected at the field study sites in Yuma, AZ and Ft. Carson, CO, to allow us to evaluate the performance potential of the hybrid measurement technique.

3. BACKGROUND

Particulate Matter (PM) emission is a critical problem for the Department of Defense (DoD). PM emitted during DoD testing and training activities threatens the safety and respiratory health of military personnel and can impact the health of urban populations encroaching on military installations. Moreover, new regulations protecting visibility at Class I national parks, forests, and wilderness areas mandate reductions in PM emissions and its chemical precursors over the next 60 years. Since many military installations are located near Class I areas, these regulations have the potential to affect training activities in coming years. Military activities have unique dust emission sources not encountered in the civilian environment, which have not been accurately characterized and quantified. Without source specific emissions factors of known precision and accuracy, the uncertainties on these estimates are high.

Contributions of particulate matter to the atmosphere by source types unique to the military are not addressed in conventional air emissions information resources such as the U.S. EPA’s (1996) “AP-42, Compilation of Air Pollutant Emission Factors, Vol. 1: Stationary Point and Area Sources.” Nor is there much information available in the literature that relates operating parameters to dust generation by these source types when

they interact with a surface that is susceptible to dust emission. This section provides information on the state of knowledge of dust emission processes related to the source types studied as part of this project.

3.1 Artillery Backblast

At the initiation of this project the only known data on emissions created by the firing of artillery was for the combustion-related emissions (gases and PM) that are produced by the detonation and subsequent combustion of the propellant. Emission factors for a variety of ordnance are available in the US EPA AP-42, Fifth Edition, Volume I, Chapter 15: Ordnance Detonation (available on-line at: <http://www.epa.gov/ttn/chief/ap42/ch15/index.html>). For projectile cartridges that approach the size of those used in our dust emission testing, emissions are expressed on a mass of emission per mass of net explosive weight. The firing of, for example, a 120 mm high explosive anti-tank cartridge releases 0.04 kg of PM₁₀ per (net) kg of propellant. Prior to the work of this project, data on the dust raised at the point-of-firing of large artillery pieces has not been available.

3.2 Dust Emissions by Wheeled and Tracked Vehicles

Sources of PM dust associated with DoD testing and training activities such as wheeled vehicle travel have equivalent or similar source types within the civilian environment. For example, Gillies et al. (2005) and Moosmüller et al. (2004) have characterized the mass emissions of PM₁₀ (PM with aerodynamic diameter ≤10 μm) and incremental visibility impairment for wheeled military and civilian vehicles traveling on an unpaved road. They observed that vehicle mass and speed were the most important vehicle characteristics affecting the magnitude of the emission factors. Vehicles traveling on unpaved roads emit particles as tires or tracks entrain particles. Studies have found that dust emission rates from unpaved surfaces depend on the fine particle content of the road (Cowherd et al., 1990; MRI, 2001), soil moisture content, vehicle speed (Nicholson et al., 1989; Etyemezian et al., 2003a, b), and vehicle weight (US EPA, 1996, 2003; MRI, 2001). For unpaved roads where there is an effectively infinite reservoir of material to be suspended into the air (Gillies et al., 2005a, b). Gillies et al. (2005a, b) found unpaved PM₁₀ emissions are linearly correlated with both vehicle speed and mass.

For the movement of heavy vehicles on haul roads, which bear some resemblance to large military vehicles, the U.S. EPA (2003) emission factor (EF) neglects the effect of vehicle speed. The equation used for vehicles traveling at industrial sites has the form:

$$EF \text{ (g PM}_{10}\text{/vkt)} = 83 s^{0.9} M^{0.45} \quad (1)$$

where s is the silt fraction of the surface material (with respect to the sum of sand, clay, and silt) and M is the vehicle mass in metric tons (Mg). A second emission factor equation for unpaved public roads is also presented in AP-42 that includes a dependence on the square root of vehicle speed and soil moisture, but no dependence on vehicle mass. These emission factors were derived from experiments conducted in the 1970s and 1980s. Given the relative size of the unpaved road dust source, these factors should be revised to incorporate the combined effect of speed and mass (i.e., momentum) from more recent studies.

Limited research has been conducted to analyze the PM emissions from tracked vehicle operation. Dornbusch et al. (1988) assembled dust emission measurements from tracked vehicle tests and derived a power law equation linking dust emissions to vehicle weight, tread area, speed, and silt loading. The source of these data was unavailable in their published report but they relied on integrated filter samples for the emission factor calculations. Filter sampling greatly limits the utility of such datasets since substantial resources are required to extract trends related to vehicle operating parameters.

Goossens and Buck (2009) conducted controlled off road recreational vehicle emission studies on unpaved road surfaces in Southern Nevada. They found that dust emission strength was linked to soil type with emissions increasing from sandy areas and drainages, to mixed terrain, with the highest emissions from silty areas.

3.3 Dust Emissions by Rotary-Winged Aircraft

Dust is created by rotary-winged aircraft when they are in ground-effect, i.e., when the rotor downwash interacts with the surface, and during take-off and landing. The military has taken an interest in dust emissions by this source due to the condition they can create known as a “brown out”, which is caused by the aircraft’s rotor blades entraining sufficient amounts of dust sized material to lower visibility to levels that affect safe operation of the aircraft. Only recently has research been directed to measure “brown out” conditions. Cowherd (2007) reported that measured dust concentrations in plumes raised by five different rotary-winged and a tilt-rotor aircraft performing a hover-taxi maneuver scaled with the helicopter mass divided by area swept by the rotor (i.e., $A \text{ (m}^2\text{)} = \pi R^2$, where R = length of rotor blade, and termed the disk loading) for a disturbed desert surface at the YPG. He also observed that as aircraft size increased, the particle size of entrained dust converged, but the sand-sized particles entrained by the rotor-wash increased indicating that the stronger downwash and outflow for larger aircraft is more effective in entraining larger particles into the dust cloud. The results of this project examined the concentration levels and particle size distributions of aircraft-created plumes, but they were not used to establish relationships between vehicle operating parameters and the strength of emissions, nor did they link dust concentration measurements with local and regional air quality impacts.

As this dust source has not been reported on in the peer-reviewed literature some background drawn from relevant published information that describes rotary-winged aircraft flight principals is provided. A rotary-winged aircraft controls its forward travel speed by changing the pitch of the rotor, which creates an uneven distribution of the lift force, with more downward thrust at the rear and less downward thrust at the front, which causes the main rotor mass to tilt forward. The revolutions per unit time for the blades are relatively invariant once take-off has occurred. During near surface flight operations the ground effect flow pattern created by the aircraft can be classified into different flow regimes: jet-wake, recirculation, ground-vortex, and trailing sweep (Curtiss et al., 1984, 1986; Ganesh and Komerath, 2004a, 2004b, 2006). The flow regime that develops is dependent upon the advance ratio of the helicopter and height of the rotor above the ground. Advance ratio, μ^* , is defined as follows:

$$\mu^* = \frac{V}{\Omega R} \quad (2)$$

where V is forward speed of the helicopter multiplied by the cosine of the ambient wind direction (m s^{-1}) with respect to travel direction, Ω is the rotor angular velocity (m s^{-1} , constant for a given aircraft), and R is the rotor radius (m). For details relating to flow regime physics the reader is referred to Curtiss et al. (1984) and Brown et al. (2004). The strength of dust emissions could be affected by the type of flow regime created by the aircraft as they have different flow features that interact with the surface.

Under all flow regimes, a feature of the ground-effect wake is asymmetry of the vortex on different sides of the helicopter. The ground vortex on the advancing side of the rotor (i.e., blade moving in the forward travel direction) is stronger and more established while weaker and more unstable on the retreating side of the rotor due to the rotor blade trimming (Brown et al., 2004).

The flow regime conditions can be described as follows:

Jet-wake: this regime occurs with low free stream wind speeds opposing the induced ground jet of the wake, so no vortex forms within the wake. The flow is like an impinging jet, impacting the surface below the rotor and fanning out radially.

Recirculation: this regime is characterized by a semi-permanent large vortex in front of the helicopter. This flow regime is also characterized by a distinct ground jet that expands beyond the length of the rotor to a separation point. At this point the jet turns vertically and wraps back around towards the rotor due to forcing by the free-stream wind.

Ground vortex: this flow regime is characterized by a contracted horseshoe-shaped vortex positioned under the rotor. The ground vortex flow regime is typically characterized by a more stable flow structure than the recirculation regime.

Trailing sweep: in this flow regime the wake tends to flatten and take the characteristics of a fixed wing wake, with two counter-rotating “wingtip” vortices extending downwind of the rotor edges. The bottom edge of the vortices can be in contact with the surface and hence low enough to potentially induce dust entrainment.

Schematic representations and images of the aircraft in these ground effects are illustrated in Fig. 1.

As rotor angular velocity and radius are important factors in the development of flow regime character, it needs to be noted that the data collected as part of this study are representative of the helicopter being tested (or one of similar rotor characteristics). Rotor size and angular velocity will scale principally with the weight of the aircraft and also be complicated, for purposes of comparison among different types of helicopters, by the configuration of rotors (i.e., tail rotor or tandem rotor designs).

As the emissions of dust from rotary-winged aircraft were identified as a potentially important source category for PM originating from military testing or training activities. The ability to estimate contributions from this source was, prior to the research of SI-1399, severely hampered by a lack of data and a limited understanding of the interaction of rotary-winged aircraft-created wakes with surfaces that have the potential to emit dust.

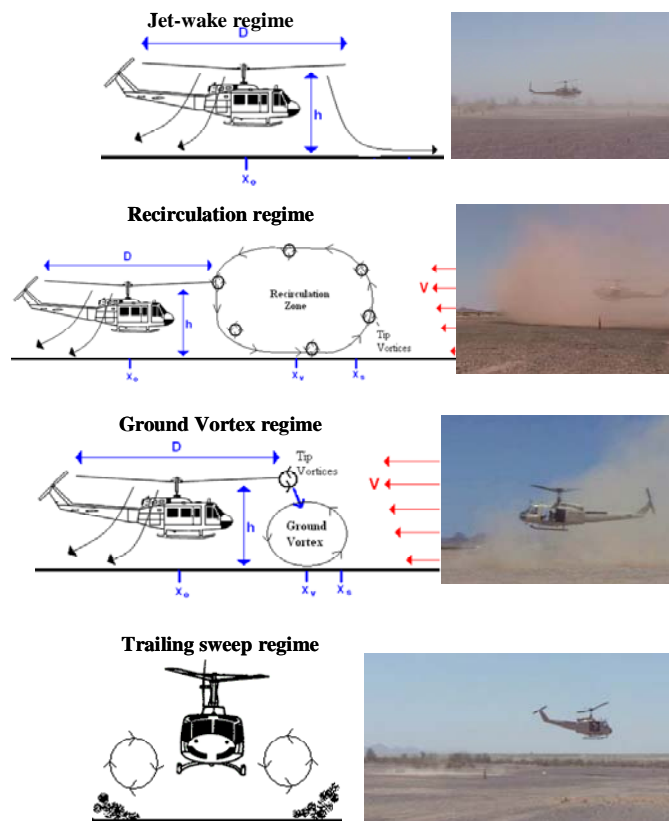


Figure 1. Schematic diagrams of rotor wake flow regimes and images of the aircraft for these ground effect states taken at the Yuma Proving Ground. Arrows beside images show direction the ambient winds are approaching from with respect to the aircraft (after McAlpine, 2009).

4. MATERIALS AND METHODS

To meet objectives one through five as well as objective seven, DRI conducted a systematic, empirically-based research program that combined environmental monitoring and controlled field experimentation to quantify and characterize dust emissions from unique DoD training and operational activities. Field measurement campaigns for characterizing emissions and developing emission factors for artillery backblast and rotary-winged aircraft were undertaken at the Yuma Proving Ground (YPG), Yuma, AZ. Measurements of dust emissions from tracked vehicles were carried out at the Yakima Training Center, (YTC) Yakima, WA, and Ft. Carson, CO.

4.1 DUST FLUX AND EMISSION FACTOR DETERMINATION, GENERAL PRINCIPLES

DRI utilized its flux tower measurement system and a back-ground/downwind measurement method to quantify the emissions of PM generated by the different unique source types. Samples of the emitted particulates were collected on filters for laboratory analyses to characterize the chemical properties of the emissions, and bulk surface samples were collected to characterize the chemistry and mineralogy of the sediments from which the dust was liberated.

The suite of instruments used by SI-1399 and SI-1400 including the variables they measure, their principles of operation and potential measurement biases is shown in Table 1.

Both SI-1399 and SI-1400 base the estimation of PM mass flux and emission factors on measuring the mass of emitted particles that pass through a defined flux plane through a unit of time and a unit of activity related to the emission source. In addition, both methods use the same measurement variables to calculate emission flux (i.e., mass concentration, wind speed, wind direction). The main difference between the approaches is the measurement methods used to obtain mass concentration and to define the area of the plume as it passes through the vertical plane where the measurements occur.

In the SI-1400 approach, emission factors are determined by integrating all 2-D mass concentration profiles with respect to length, height, and time during a plume event, along with wind velocities and directions measured by anemometers and wind vanes. This is similar to the approach of SI-1399, but the flux planes are defined differently. SI-1400 attempts to scale the flux plane to the shape of the plume, while SI-1399 constructs a rectangular flux plane of fixed dimensions based on the placement of the flux towers and instruments within that rectangle. It is expected that the relative values of emissions measured by both approaches should scale proportionally as both measure the same emitted plumes. All other things being equivalent (i.e., measurements of wind speed, PM concentration, etc.) the difference in the measured flux should be accounted for by the difference in the area of plume capture. It is expected that the optical remote sensing (ORS) method should capture a greater portion of the dust plume as the micro-pulse lidar (MPL) scans through the entire height of the plume as it passes by the flux plane. This is balanced against the number of scans that can be made as a plume passes by the plane scanned by the MPL. The longer it takes the MPL to complete a scan the greater the possibility that more of the plume will be missed. This will also be influenced by the ambient wind speed that is transporting the plume through the flux plane. The faster the wind, the fewer the number of effective scans there would be.

Table 1. Instrumentation Used by SI-1399 and SI-1400 to Quantify PM Flux Rates.

Instrument	Variable Measured	Principle of Operation	Potential Measurement Biases (by converting signal to $\mu\text{g m}^{-3}$)	Additional Measurement Issues Related to PM Source Type or Activity
TSI DustTrak	PM ₁₀ and PM _{2.5} (1 Hz)	Forward scattering of infrared light	Calibration specific to particle size distribution and complex refractive index	
TEOM	PM ₁₀ and PM _{2.5} (10 minute average)	Tapered element oscillating microbalance	Volatilization of volatile species causes mass loss	Volatile species are generally not an issue for mineral dust
Med-Vol	PM ₁₀ and PM _{2.5} (Time integrated average)	Gravimetry		
Open path (OP) Fourier Transform Infrared (FTIR)	Light extinction (absorption + scattering) as a function of wavelength	The returned light signal is received by a single telescope and directed to a detector. The light is absorbed and scattered by the molecules and particles in the beam path as the light propagates to the retro-reflecting mirror and again after the light is reflected back and propagates back to the analyzer. Extinction is measured at 7 wavelengths.	The mass concentration retrieval was calibrated using concurrent measurements by DustTrak (DT) aerosol monitors (Model 8520, TSI, Inc., Minnesota, USA) measuring PM ₁₀ and PM _{2.5} that were traced back to particulate mass filter calibrations	Retrieval of particle size assumes particles are spheres and applies Mie theory. Also assumes a static refractive index for the particles

Instrument	Variable Measured	Principle of Operation	Potential Measurement Biases (by converting signal to $\mu\text{g m}^{-3}$)	Additional Measurement Issues Related to PM Source Type or Activity
Micro-pulse lidar	Optical backscattering	<p>A short pulse of laser light is transmitted from the telescope. As the pulse travels along, part of it is scattered by molecules, water droplets, and PM.</p> <p>The greater the number of scatterers, the greater the part scattered. A small portion of the scattered light is scattered back, collected by the telescope, and detected. The system uses a 1.0 W laser operating at $0.523 \mu\text{m}$ wavelength with a pulse repetition rate of 2500 Hz.</p>	Assumes an extinction-to-concentration conversion factor (K^*) that is constant for a plume event. Also assumes a particle density of 2.8 g cm^{-3} and refractive index of $1.55+0i$ for K^* .	
Open path laser transmissometer (OP-LT)	Path integrated light extinction	The open path laser transmissometer (OP-LT) operates in the visible spectrum with the path-averaged extinction coefficient derived from the return beam power after travel to and from the retro-reflector	The OP-LT is calibrated by performing a linear regression fit of the path-averaged extinction coefficient to the average value of the PM_{10} measurements by the DMs, distributed along the cross-plume OP-LT beam path.	

The tower method of SI-1399 has limited area of coverage that is defined by the height and width of the tower placements. The greater the vertical extent of the dust plume the less of it will be accurately characterized by the SI-1399 method. SI-1399 attempts to limit the errors associated with plume height by optimizing the placement of the towers with respect to the emission source to minimize the chance that a plume will extend to a height greater than the highest monitor.

As both teams performed measurements of the emitted dust plumes, for the most part simultaneously, differences that could be related to local meteorological conditions and the operating parameters of the test sources were minimized and are not considered a critical factor in affecting how the two approaches derived emission factors.

SI-1399 used a traditional approach using tower-mounted instruments to measure the concentration of PM over what is assumed to be representative portions of the emitted dust plume from which local extrapolations are made to estimate the concentration characteristics of the entire plume. The concentration data are paired with wind speed data to estimate the one second flux of particles through the defined flux plane. Based on a measure of activity of the source an emission factor is calculated (refer to Gillies et al., 2005, 2007, 2010; Kuhns et al., 2010). To relate the PM measured by the TSI DustTraks (DT) used by SI-1399 to a gravimetric equivalent concentration, laboratory-derived relationships between PM measured with the DT and filter-based (i.e., gravimetric) methods were developed. Site specific calibration relationships were developed using dust from all areas where testing was undertaken.

SI-1400 used a suite of remote sensing instruments (Table 1) to obtain path-integrated measurements of light backscatter and light extinction from which they derived particle size distributions using the methods of Varma et al. (2008) that were then used to estimate mass flux through the defined flux plane. For the SI-1400 approach the MPL signals are first corrected to normalized relative backscatter (NRB) signals according to the method described by Campbell et al. (2002) NRB signals are then converted to extinction values using a discretized form of an analytical solution to the lidar equation by Fernald et al. (1972). This analytical solution requires a calibrated lidar system (or knowledge of a boundary value) and knowledge of the lidar ratio, which can be obtained by measuring or estimating the extinction integrated over the lidar path (Fernald et al., 1972). The resulting 1-D extinction profiles from a complete MPL scan cycle are combined into a 2-D extinction profile by interpolating these data along all scan paths in a scan cycle. Time for a scan cycle is typically 10 to 14 seconds, so multiple scans are needed to capture longer-lasting plume events. This methods assumes an extinction-to-concentration conversion factor (K^*) that is constant for a plume event. This approach also assumes a particle density of 2.8 g cm^{-3} and refractive index of $1.55+0i$ for K^* . These values are typical for desert dust particles and assume no light absorption by the particles (i.e., the imaginary part of the complex refractive index is zero, which is generally a good assumption for desert dust in the absence of iron oxides, especially hematite (Fe_2O_3)).

In the SI-1400 method, particle size distribution is determined by collocated OP-FTIR and OP-LT measurements that occur parallel to the MPL scan plane. They use seven wavelengths in their OP-FTIR spectrum to obtain light extinction values at each

wavelength that are due to scattering alone. They use interpolation to generate a set of data points that are used to compute the extinction efficiency (kernel) matrix (Q_{eij}). The resulting interpolated extinction values define the baseline offset (when dust is encountered by light) that excludes the extinction caused by H₂O vapor and CO₂ and avoids other gaseous and PM absorption features. Bins of particle numbers are estimated for particle diameters ranging from 0.25 to 20 μm . The bins that correspond to PM₁₀ (i.e., <10 μm) are used to estimate PM₁₀ concentrations. To arrive at the concentration of PM₁₀ they assume an initial complex refractive index of (1.6, 0), which is representative of airborne dust from deserts (Grams et al. 1974) for a range of non-absorbing wavelengths. However, the final calibration relies on an accurate and concurrent measurement of PM_{2.5} and PM₁₀, which for this project has been obtained through the use of the DT.

This calibration to the DustTrak is the critical link between the projects for estimating emissions. SI-1399 proceeds directly from PM measurements made by the array of DustTraks in a defined flux plane, and converts these measurements to gravimetric equivalent measurements based on the laboratory-derived relationship for DustTrak versus gravimetric mass concentration. SI-1400 has to make several intermediate calculations (inversion process) prior to the adjustment of their measured signal to DustTrak equivalent measurement and finally to gravimetric equivalent mass concentration. Each additional step has the potential to introduce more error into the final derived values for gravimetric equivalent PM₁₀ or PM_{2.5}.

In comparing the flux values obtained using both systems at YTC the average absolute difference between the two methods was 42%, while the average difference was only 2%. There did not appear to be a systematic negative or positive bias between the two methods. A T-test showed that the mean difference between the results from the ORS system and flux tower method is not significantly >0 or <0, at the confidence level of 95%. This suggests that there is no systematic difference between the results from these two methods at a confidence level of 95%.

The combined measurement efforts of SI-1399 and SI-1400 offered the opportunity to evaluate a hybrid remote-sensing and in situ measurement system, which could potentially combine the strengths of both systems, while minimizing their weaknesses. Remote sensing offers the advantage of increasing the scale of the measurements to capture more of the dust plume as opposed to the point measurements of the in situ methods. Point measurements however offer the opportunity to quantify mass concentration measurements without the disadvantage of complicated signal inversion techniques, which use multiple assumptions to derive an estimate of mass or particle concentrations.

This research generated location-specific emission factors and also investigated relationships between emission strengths and vehicle and surface characteristics that allow for their use at other installations. A new instrument system, the Portable In-Situ Wind Erosion Laboratory (PI-SWERL), developed at DRI to provide data on emission potential was also used for this project. This small portable wind tunnel is used to develop an index that characterizes a surface's propensity to emit dust. By relating this index of emission potential for the test sites with measured emission factors derived from

the environmental monitoring, it was hoped that emission potentials at different sites for different sources could be inferred using the cost effective PI-SWERL method. This methodology shows promise and is, in our opinion, worthy of further development to refine its use as a transfer standard.

4.2 METHODS: DUST EMISSIONS FROM ARTILLERY BACKBLAST

Emissions of dust raised by artillery backblast were quantified at the YPG using a flux measurement technique similar to that described in previous work by Gillies et al. (2005). Three towers – one “master” and two “satellite” - were set up downwind of the artillery firing position and aligned perpendicular to the expected wind direction (Fig. 2). The distance from the firing position was limited by safety considerations and varied between 40 and 60 m depending on the site. The trailer-mounted, 9 m-high “master” tower was instrumented with paired DTs configured to measure PM_{10} and $PM_{2.5}$ at five heights spaced logarithmically above the ground surface. A wind vane was mounted at the top of the tower and a cup anemometer was approximately collocated with each pair of DT samplers. The two 15 m-high telescoping “satellite” towers were mounted on pick-up trucks and

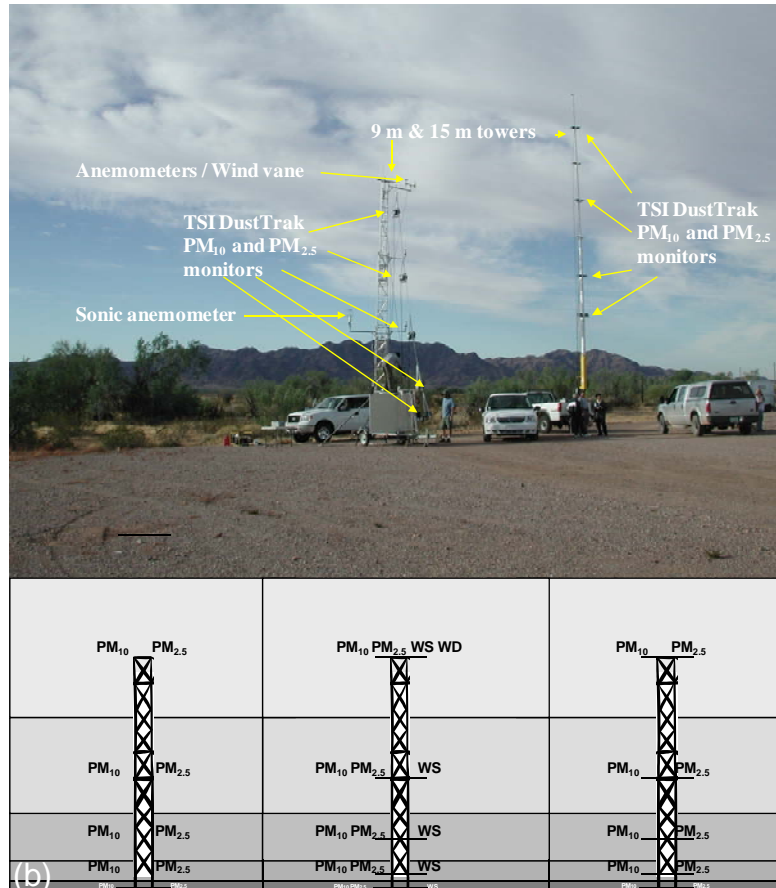


Figure 2. (a) Photograph of two of the instrumented towers for measuring emission flux, and (b) schematic diagram of the flux planes for the three-tower array. WS and WD are the code for wind speed and wind direction and indicate the measurement position of these environmental parameters.

equipped with paired PM₁₀/PM_{2.5} DTs at five heights that were dictated by available attachment positions.

PM emissions from artillery backblast were monitored during regular testing programs being operated under the control of YPG engineers. Over the testing period 70 plumes were measured at three different locations at the YPG. Data presented represent firings from a 155 mm artillery piece (Model M198 or M109 Howitzer). The emissions were created from the firing of the 155 mm shells that can vary in three ways; 1) projectile model, 2) propelling charge model, and 3) charge zone. Charge zone is the most important of these characteristics as it represents the amount of propellant. The first two characteristics describe design elements of the artillery shell and charge. The combinations of the Modular Artillery Charge System (MACS) represented by the above listed criteria measured at the YPG are listed in Table 2. For all measurements, the moisture content of the improved surfaces, expressed as a percent difference between the weight of samples before and after oven drying was <0.5%.

PM₁₀ and PM_{2.5} emissions were calculated for each downwind tower by integrating the flux of particles through a vertical surface downwind of the firing position that was represented by fifteen rectangles. It was assumed that the concentrations measured by each PM₁₀/PM_{2.5} DT pair were representative of a rectangle with height that spanned from halfway to the DT pair located lower to the ground up to halfway to the DT pair located higher from the ground. DT PM measurements were later converted to equivalent gravimetric mass following a laboratory comparison using a resuspension technique (refer to Gillies et al., 2005).

Table 2. Modular Artillery Charge System (MACS) combinations used to generate emissions using a 155 mm Model M198 or M109 howitzer.

Projectile Model	Propelling Charge Model	Charge Zone	Number of Firing Events Measured
M107	M231	1	9
M107	M3A1	2	15
M5491A	M203A1	5	26
M795	M203A1	5	20

The time series of the PM₁₀ and PM_{2.5} concentrations were examined for each DT at each location and peak start and stop times were identified for every firing event. An emission factor (EF) for each event was calculated using the equation:

$$EF = \alpha \left[\cos(\theta) \sum_{FT=1}^3 \sum_{i=1}^5 \sum_{t=0}^T u_{t,i,FT} \cdot C_{t,i,FT} \cdot A_{i,FT} \cdot (1 \text{ sec}) \right] \quad (3)$$

where FT represents the tower number, *i* refers to the rectangle represented by the DT height, *t* is the time (sec) after the peak starts, *T* is the total peak duration (sec), *u* is the wind speed (m s⁻¹), *C* is the measured concentration (g m⁻³), *A* is the area (m²) of the rectangle corresponding to position *i*, θ is the angle of the 1-sec average wind direction relative to the flux plane, and α is a constant that is discussed below. For all emission factor calculations only the concentration data associated with wind approach angles (θ) of $\leq 45^\circ$ with respect to the tower line were used.

4.3 METHODS: DUST EMISSIONS FROM OFF-ROAD MILITARY VEHICLE ACTIVITY

The same flux tower system used to measure emissions from artillery backblast (Gillies et al., 2007) was used to measure emissions of dust for tracked and wheeled vehicles at YTC and Ft. Carson with some adjustments for the physical and logistical constraints imposed by the different test areas (Fig. 3).

The instrumentation used to measure the dust emissions in situ consisted of three of the DRI Flux Towers. The master tower has five paired PM₁₀ and PM_{2.5} samplers collocated with cup anemometers. A typical set up was for the master tower to be positioned half way between the starting and ending driving points of the unimproved tank trail or unpaved road surface. The satellite towers each hold paired PM₁₀ and PM_{2.5} samplers to measure the vertical concentration gradient of particulates at locations approximately 40 m either side of the master tower. Satellite towers were positioned also based on the environmental conditions of the day, particularly wind direction. Typically, one tower was placed 30 to 50 m down the road on the same side as the master tower with the other placed on the opposite side of the road in line with the master tower. This was done for two reasons. It would 1) allow for the continued measurement of emissions should the wind reverse directions, and 2) it allowed for measurement of background dust concentrations upwind of the road. DT PM measurements were later converted to equivalent gravimetric mass following a laboratory comparison using a resuspension technique (refer to Gillies et al., 2005; Kuhns et al., 2010).

The vertical concentration data are combined with the wind speed and wind direction data to calculate an emission flux (EF) of grams of PM₁₀ or PM_{2.5} per vehicle kilometer traveled. The emission flux is calculated using the same method as Gillies et al. (2005a) to calculate emissions of dust created by wheeled vehicles traveling on an unpaved road. The equation used to define the Emission Factor (EF) is:

$$EF = \sum_{\text{start time of peak}}^{\text{end time of peak}} \left\{ \cos(\theta) \sum_{i=1}^5 u_i C_i \Delta z_i \Delta t_i \right\} \quad (4)$$

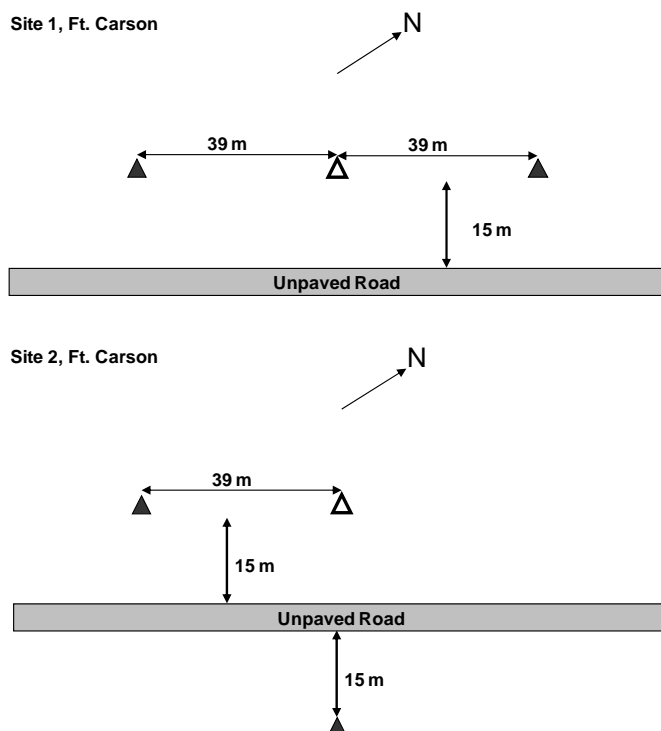


Figure 3. Tower positions at the two Ft. Carson test sites. The open triangle represents the master tower and the two solid triangles the satellite towers. Prevailing winds were expected to be perpendicular to the road. Distances are to approximate scale. The measurement set up at the Yakima Training Center was similar to that of Site 1 Ft. Carson, but the between-tower distances were 32 m on the east side and 45 m on the west side.

where θ is the angle of the mean 1 second wind direction relative to the flux plane, i is monitor position (1 through 5) on the tower, u_i is the 1 second average wind speed (m s^{-1}) over the height interval represented by the i^{th} monitor, C_i is 1 second PM concentration (g m^{-3}) as measured by the i^{th} monitor, Δz (m) is the vertical interval represented by the i^{th} monitor, and Δt (s) is the duration that the plume impacts the tower. On the outer most summation, the term peak refers to the peak in particle concentrations associated with a single vehicle pass when all data are presented as a graphical time series. For all emission factor calculations only the concentration data associated with wind approach angles of $\leq 45^\circ$ with respect to the tower line were used. Winds speeds and directions measured on the master tower were assumed to be representative of the speeds at the other towers.

Ten types of military off road vehicles were measured at three locations between 2002 and 2008. Images of each vehicle type are shown in Fig. 4. The test wheeled vehicles range in mass from 2400 kg for the HMMWW light truck to 20000 kg for the HEMTT cargo truck. Tracked vehicles tested ranged from 10000 kg for the M113 armored personnel carrier to 60000 kg for the M1A1 tank. At each site, test sections were on straight roads or tracks with no visible turns.



Figure 4. Images of the tested tracked and wheeled military vehicles.

The DRI PI-SWERL (Etyemezian et al. 2007; Sweeney et al. 2008; Kavouras et al., 2009) was used to measure emission potential of the unpaved roads before and after vehicle testing at the Fort Carson and YTC locations.

The PI-SWERL is a cylindrical chamber ($D = 30$ cm, $H = 20$ cm) that has an open end that is placed over the soil surface to be tested. Ventilation of the PI-SWERL chamber is accomplished by a DC blower (AMETEK, Mini-Jammer) and monitored by a mass flow meter (TSI, Model 42350101). Filtered air that is introduced by the blower, mixes with the air in the chamber and the flow is exhausted through a port (diameter = 5.0 cm) at the top of the chamber. Dust suspension within the chamber is induced by a rotating, flat annular ring (inner diameter = 0.16 m, outer diameter = 0.25 m). Once the measurement cycle is initiated, one-second concentrations of PM_{10} are measured by a DT.

The PM_{10} concentration (C , $\mu\text{g m}^{-3}$) at the outlet of the instrument is recorded at 1 Hz while a blower vents clean air through the PI-SWERL at a constant rate (F , $\text{m}^3 \text{s}^{-1}$) and the emission flux ($\mu\text{g m}^{-2} \text{s}^{-1}$) or amount of PM_{10} produced per area per second is calculated as:

$$E_{i,\text{cum}} = \frac{\sum_{\text{begin},i}^{\text{end},i} C \times F}{t_{\text{end},i} - t_{\text{begin},i}} / A_{\text{eff}} \quad (5)$$

Where the summation occurs over every one second measurement during level i , beginning at $t_{\text{begin},i}$ and ending at $t_{\text{end},i}$, with t as integer seconds. The measured dust concentration and flow rate are converted to an emission flux by the effective area of the PI-SWERL annular ring, A_{eff} , which is 0.026 m^2 . The PI-SWERL tests measure the potential fugitive PM_{10} dust emissions from the surface at different equivalent wind speeds up to a wind speed of roughly 30 m s^{-1} at 2 m AGL.

The PI-SWERL was operated on the unpaved test road at the Yakima training Center on 8/24/06, midway through the testing period. Thus, PI-SWERL measurements at YTC correspond to thoroughly disturbed roadway conditions. Five replicate measurements were completed across the width of the unpaved road. The measurement cycle comprised a series of step increases in the rate of rotation of the PI-SWERL annular blade as described in Etyemezian et al. (2007). Each RPM step was held for 90 seconds. The test cycle consisted of: 1) a 120 s clean air flush, 2) a step increase to 600 RPM, 3) a step increase to 900 RPM, 4) a step increase to 1200 RPM, 5) a step increase to 1800 RPM, 6) a step increase to 2400 RPM, and 7) turn off motor and clean air flush for 90 s.

4.4 METHODS: DUST EMISSIONS FROM ROTARY-WINGED AIRCRAFT

To measure dust emissions from a rotary-winged aircraft (UH-1 Huey/Bell 212) at YPG the flux tower system was re-configured to meet the logistical challenges of the terrain, the expected strength of the dust emissions, and to meet safety requirements of the flight crew (Fig. 5).

The emissions of dust generated by the low-level flight of the aircraft were measured downwind of the flight path at distances between 100 m and 145 m using a three-tower measurement system similar to that used by Gillies et al. (1999, 2005, 2007) and Kuhns et al. (2010) to measure dust emissions from wheeled and tracked military vehicles and

artillery backblast. Meteorological variables were also collected including wind speed profiles, point measurements of three-dimensional wind vectors, wind direction, and surface shear stress. In addition to the dust flux measurements, surface dust emission potential measurements were made using the PI-SWERL described by Etyemezian et al. (2007), Sweeney et al. (2008), and Kavouras et al. (2009). These measurements provide a means to compare how the surface conditions affect the strength of the dust emissions.

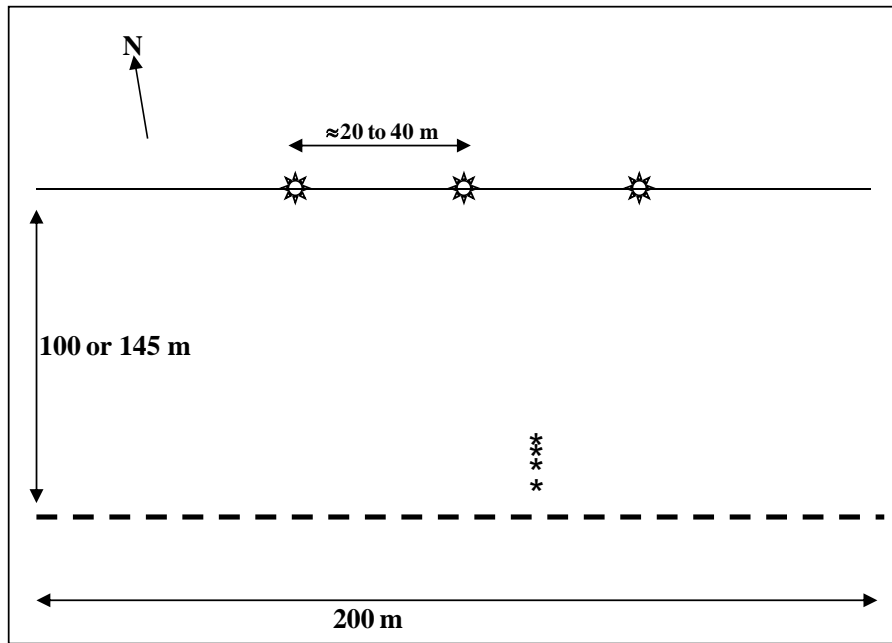
To measure the dust emissions and ambient wind conditions the three towers were set up perpendicular to a section of desert surface delineated with traffic cones. Each section was ≈ 200 m long and ≈ 50 m wide. An image of the tower monitoring system and a schematic of the instrument positions are shown in Fig. 5. The center tower was instrumented with ten real-time dust monitors (i.e., DTs): five configured to measure PM_{10} and five configured to measure $PM_{2.5}$. On the center tower, the dust monitors were spaced logarithmically in the vertical direction at heights AGL of 1.67 m, 2.64 m, 3.98 m, 6.47 m, and 9.12 m. The DustTrak is a portable, battery-operated, laser-photometer that uses light scattering technology to determine mass concentration in real-time and has been used in other field studies measuring dust emissions (e.g., Gillies and Berkofsky, 2000; Gillies et al., 2005, 2007) and particulate emissions from mobile sources (e.g., Moosmüller et al., 2001a, 2001b).

Wind speed was measured using cup anemometers (RM Young Wind Sentry) at the same height above the ground as the dust measurements. Wind direction was measured at 9.12 m AGL with a wind vane (RM Young Wind Sentry). Three-dimensional wind vectors associated with the rotor-wash were measured with a sonic anemometer at 1.5 m AGL at one position on the flight path, approximately 7.3 m from the centerline where the outer edge of the rotor-blade was expected to pass as the helicopter made its low-level pass down the flight corridor.

The two towers on either side of the center tower held PM_{10} dust monitors (also TSI Model 8520 DustTraks) at 2.74 m, 5.1 m, 6.9 m, and 14.2 m and $PM_{2.5}$ dust monitors at 2.74 m and 5.1 m AGL. These towers were collinear with the center tower and placed on opposite sides of the center tower at distances of 29 m and 20 m at Site 1, and 34 m and 41 m at Site 2. The background levels of PM_{10} and $PM_{2.5}$ at each measurement level and position were estimated from 15 one second concentration measurements prior to the arrival of the aircraft at the test site. These 15 second average concentration values were subsequently subtracted from each one second measurement during the time the dust plume impacted the monitors.

The mass of particulate matter produced by the part of the dust plume that passed the instrument array can be calculated as:

$$\text{Total Mass of particulate (kg)} = \sum_1^{14} C \times u \times T \times A \times \text{cosine WD} \quad (6)$$



- ☼ Tower Positions
- * Irwin Sensor Positions
- Flight Path

Figure 5. Schematic diagram of the test area and instrumentation layout set up to measure dust emissions generated by the helicopter. The three visible towers comprise the DRI flux tower system. Additional instrumentation consisting of optical remote sensing instruments is also shown.

where: C = background subtracted particulate matter concentration (kg m^{-3})

u = wind speed (m s^{-1})

T = duration of plume impact (s)

A = area of plane (m^2 , represented by an individual dust monitor)

WD = wind direction (degrees)

The summation represents the 14 defined planes in the instrument array (Fig.6).

This calculation makes the following assumptions (Fig. 6): 1) the point concentration measurement of PM_{10} (or $\text{PM}_{2.5}$ for the center tower) is constant throughout an area

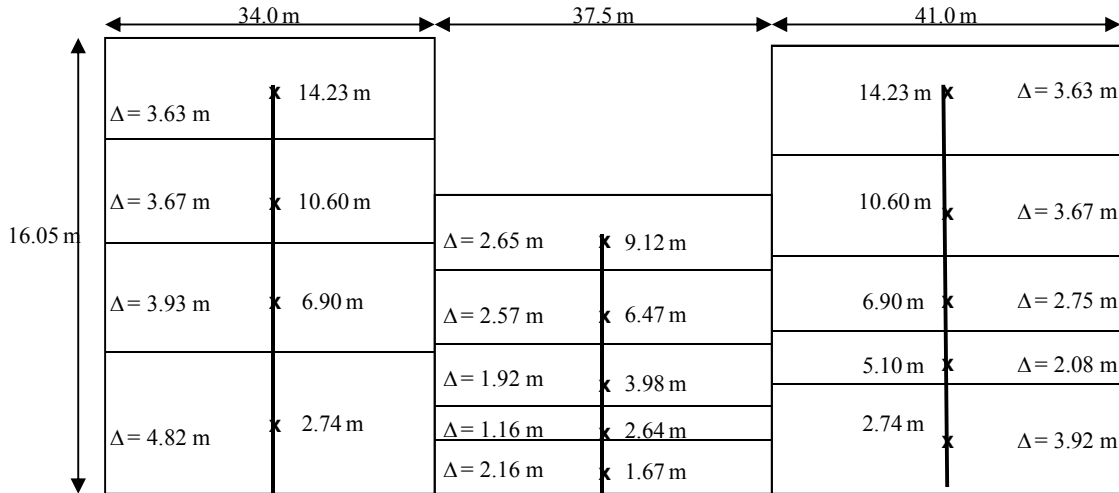


Figure 6. Schematic diagram of the instrument placements and 14 defined flux planes used to calculate the emission flux of PM_{10} and $PM_{2.5}$ created by the aircraft.

defined by the length dimensions equal to one-half the horizontal distance between the two closest towers and extending that same distance outward from the two end towers and a height of one-half the distance between two dust monitors in the vertical on the same tower; 2) the vertical extent of the area defined for the highest sensors is assumed to extend in the vertical the same distance as one-half the distance to the next lowest sensor; 3) the wind speed is assumed to be constant in a horizontal plane defined for each anemometer that extends in the vertical to a point that is one-half the distance between two anemometers in the vertical on the central tower that extends horizontally to the entire defined length of the instrument array; and 4) winds approaching the instrument array at an angle ≥ 45 degrees from the perpendicular invalidate the measurements associated with a flight pass.

To link the light scattering measurements made with the DT with gravimetrically-derived concentration measurements, a comparison was made between DT measurements and filter-based methods using a resuspension technique (Chow et al., 1994) in the laboratory. The details of this procedure are given in Kuhns et al. (2010). All reported PM concentrations and fluxes have been converted to gravimetric equivalent measurements based on the laboratory-established relationship.

In addition, four Irwin sensors (Irwin, 1981) were emplaced in the ground along an ≈ 19 m-long transect normal to the flight path, beginning at a location 10 m from the center of the flight line. The four Irwin sensors were separated in decreasing distance from the edge of where the rotor-wash was expected to become directed laterally (i.e., 10 m, 15 m, 17.5 m, and 18.75 m) and sweep across the surface creating a horizontal shear stress. Irwin sensors have been previously used to measure surface shear stress generated by atmospheric boundary-layer winds (Gillies et al., 2006, 2007). The purpose of these measurements is to relate helicopter operating conditions with the surface winds they generate and the associated dust emission strength.

To create the dust emissions the helicopter pilot was requested to make low level passes travelling in the direction along the defined flight-path corridor opposite to the prevailing

wind. The target forward travel speed range was 15 km hr⁻¹ (4 m s⁻¹) to 60 km hr⁻¹ (17 m s⁻¹). For each pass the target speed was increased incrementally from the minimum to maximum and then decreased incrementally from maximum to minimum. Actual forward travel speeds were resolved using video imagery recorded for each flight pass. The dust plume was allowed to completely pass by the instruments before the next flight pass was requested.

As a means to compare the emission potential of different surface types that could be impacted by low-level helicopter passes, in the absence of tower-based measurements of dust flux, the PI-SWERL instrument (Etyemezian et al., 2007; Sweeney et al., 2008; Kavouras et al., 2009) was used to collect data on particulate matter emission potential driven by aerodynamic shear stress imparted to the surface. The PI-SWERL is being used increasingly as a primary tool to evaluate windblown dust emissions from natural and artificial soil surfaces and relating dust emission strength to, for example, soil parameters and salt content (Etyemezian et al., 2006; Kavouras et al. 2009; Goossens and Buck, 2009; King et al., submitted). Unlike large (10 m or longer) field wind tunnels, the PI-SWERL does not meet many of the scaling criteria that are theoretically required for realistic simulations of aeolian sediment transport processes. However, recent research, and comparison of measured emission fluxes with those derived from large portable field wind tunnel testing indicate that the PI-SWERL does provide a reliable measure of windblown dust emission potential (Sweeney et al., 2008).

PI-SWERL tests were conducted at each site before and after the helicopter passes. At each site multiple PI-SWERL tests were conducted on a parallel transect directly below where the helicopter flew. At site 1, 11 tests were conducted with eight before the helicopter passes and three tests after the passes were completed. Seventeen PI-SWERL tests were conducted at site 2. The potential emissions of PM₁₀ were calculated using the same method as for the tracked and wheeled vehicle measurements (i.e., Eq. 6).

4.5 MINERALOGY AND CHEMISTRY OF AIRBORNE DUST COLLECTED DURING FIELD MEASUREMENT CAMPAIGNS

Filter samples, both PM₁₀ and PM_{2.5} on Teflon[®] membrane and quartz fiber substrates for chemical analysis, and on Nuclepore[®] for scanning electron microscopic based individual particle analysis, were collected in the course of the four field campaigns, one each year from 2005 to 2008.

In addition, grab samples of surface dust were collected from each of the localities, two from gunnery sites at YPG in 2005, two from dirt roads at YTC in 2006, two from undisturbed and disturbed desert pavements at Yuma in 2007, and two from dirt roads at Ft. Carson in 2008. Sample splits of the grab samples were screened through a <38 μm nylon sieve for re-suspension and collection on filter substrates, for chemical, and mineralogical analysis.

4.5.1 Methods: Particle Characterization

The particulate matter filter, and <38 μm sieved bulk samples, were analyzed both chemically and mineralogically to provide better understanding of their physical properties, and with the aim of linking these properties to the strength of dust emissions from these different soils. The mineralogy of the sieved bulk and PM₁₀ filter samples

was compiled from the X-ray diffraction (XRD) results, optical microscopy, individual particle Scanning Electron Microscopy (SEM) and Computer Controlled Scanning Electron Microscopy (CCSEM), reactivity with dilute hydrochloric acid, and visual inspection.

4.6 METHODS: HYBRID REMOTE SENSING AND IN-SITU MEASUREMENT SYSTEM TO MEASURE FUGITIVE DUST FLUX

A new test method for measuring fugitive dust emissions was deployed and its performance evaluated by SI-1399 & SI-1400 at the YPG during the rotary-winged aircraft testing and at Ft. Carson during the tracked vehicle testing. The measurement system includes one open path laser transmissometer (OP-LT) operating in the visible wavelength, (at least) two time-resolved dust monitor (DM) instruments, and (at least) two wind speed instruments. Each DM was capable of measuring PM₁₀ and PM_{2.5} concentrations and may consist of a co-located pair of separate monitors for PM₁₀ and PM_{2.5} concentrations (DM₁₀ and DM_{2.5}, respectively). Figure 7 shows a schematic of the setup configuration with three DM instruments mounted on the tower at different elevations. The hybrid system optical remote sensing instrument (i.e., a path integrated transmissometer) was calibrated to DTs collocated along the beam line. These were subsequently converted to gravimetric-equivalent concentrations based on the SI-1399-derived relationship between DT and gravimetric determinations of mass concentration of PM₁₀.

The OP-LT beam path distance from the sensor to the retro-reflector can vary according to the expected plume width and possible trajectories. Typically, the path distance will be on the order of several hundred meters. The simplest configuration would use one tower located at the expected plume center-line. The two (or three) DM pairs and the two wind monitors would be distributed evenly at different heights, the lowest at the same height as the OP-LT beam.

4.6.1 Hybrid System Operating Principles

The concept behind this emission measurement method is to use the OP-LT to determine the entire cross-plume, plume-averaged mass concentration of PM₁₀ dust at ground level, $\overline{C_y^{PM_{10}}}$, and use the vertically distributed PM₁₀ DM instruments to determine the vertical distribution of the dust mass concentration. These two parameters can be used to determine the plane-integrated PM₁₀ mass concentration (PIMC₁₀), which is the mass concentration integrated over the vertical downwind measurement plane:

$$PIMC_{10} = \iint C^{PM_{10}}(y,z) dy dz \quad (7)$$

In order to determine $\overline{C_y^{PM_{10}}}$ from the OP-LT measurements, the OP-LT must be calibrated against the DM₁₀ instruments.

The PIMC₁₀ is calculated by the following expression:

$$PIMC_{10} \cong \frac{\overline{C_y^{PM_{10}}}}{\overline{C_{z_0}^{DM_{10}}}} \overline{C_{z_0}^{DM_{10}}} A \quad (8)$$

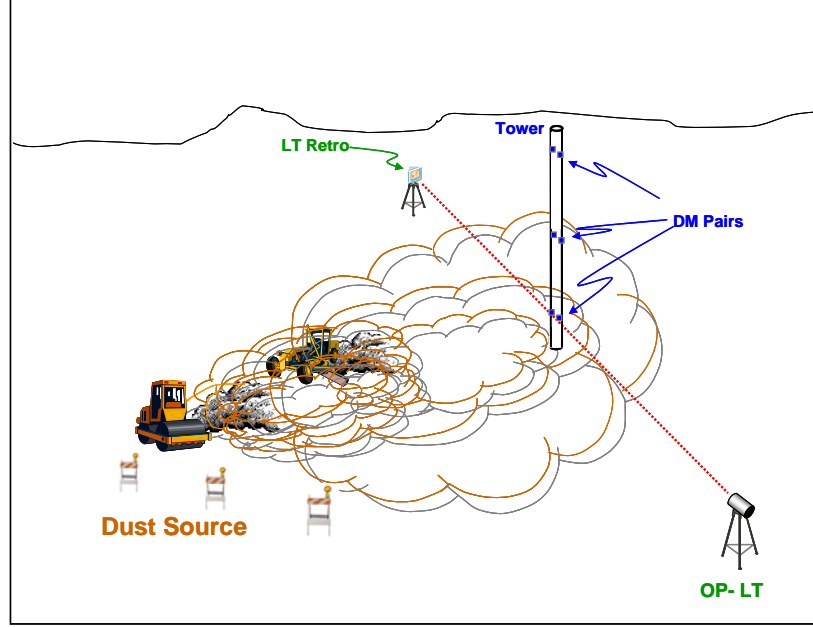


Figure 7. Schematic of the hybrid method instrument configuration. The DM pairs consist of one PM_{10} and one $PM_{2.5}$ monitor.

where $C_{z_0}^{DM_{10}}$ is the measurement of DM_{10} at the same height as the OP-LT beam. $C_z^{DM_{10}}$ is the average of all of the measurements by the vertically distributed DM_{10} monitors on the tower, and A is the area of the plane defined by the product of the OP-LT path distance, L , and the height of the top DM on the tower, H . The values for $PIMC_{10}$ are in units of $g\ m^{-1}$. The ratio $C_y^{PM_{10}} : C_{z_0}^{DM_{10}}$ is a correction factor for the horizontal capture of the plume by the single tower. This factor depends on the position and width of the plume. If the ratio has a value of 1, the plume is distributed uniformly over the OP-LT beam path. The correction factor ratio would be <1 when a narrow plume is centered on the tower and the PM_{10} concentrations measured at the tower location overestimate the plane average concentration. This ratio would be >1 when a narrow plume misses the tower and the PM_{10} concentrations measured at the tower location underestimate the plane average concentration.

The PM_{10} flux, $\phi_{PM_{10}}^A$, through the measurement area is given by:

$$\phi_{PM_{10}}^A = PIMC_{10} \overline{U_x} \quad (9)$$

where $\overline{U_x}$ is the normal wind component averaged over the two or three vertically distributed anemometers. If the entire plume is encompassed by the measurement area, $\phi_{PM_{10}}^A$ is equal to the total mass emission rate for PM_{10} released from the target fugitive source. The flux of $PM_{2.5}$ would be calculated similarly by substituting the measurements from the $DM_{2.5}$ instruments and using the same wind speed data.

5 RESULTS AND DISCUSSION

5.1 ARTILLERY BACKBLAST

The range of estimated emission flux values and the mean and standard deviation of emission flux for each zone charge are listed in Table 3. These emission flux data show a high degree of variability, as evidenced by the high standard deviation of the mean values. The emissions do not show dependence with wind direction. However, the variability likely results, in part, from a combination of low wind speeds that occur for certain tests combined with the variability of the wind direction as the wind transports the particles to the flux plane. Typically the dust plumes impacted all three towers, which suggest minimum widths of 50 meters. The emissions of PM_{10} and $PM_{2.5}$ scale linearly with zone (i.e., propellant amount) (Fig. 8).

Based on observations of backblast emissions made at YPG a conceptual model of the emission process is presented. The emission mechanism is hypothesized to be the force that is transferred to the soil surface by the detonation of the propellant. As the backblast force impacts the earth surface at the gun position, the earth responds by compressing and then rebounding. The rebound ejects the dust vertically into the atmosphere where it is subsequently transported by the wind. The greater the force created by the artillery blast, the greater is the potential to raise dust as demonstrated by the relationship between emission flux and charge zone.

Several characteristics of the surface are expected to limit the emissions. The most important surface characteristics are hypothesized to be the availability of dust-sized particles and the amount of cohesion in the earth material the artillery piece is sitting upon. Cohesion will be affected by the textural qualities of the soil material, climate-driven pedogenic processes, and moisture content. Dust emissions from backblast will maximize at an optimum balance between supply of PM and strength of the substrate material on which the artillery is fired.

Measurements were made for emissions created by backblast from firing artillery on improved gun positions at the YPG in October 2005. For a 155 mm howitzer firing a range of propellant charges or zones, amounts of emitted PM_{10} ranged from approximately 19 g- PM_{10} per firing event for a zone 1 charge to 92 g- PM_{10} per firing event for a zone 5. The corresponding rates for $PM_{2.5}$ were approximately 9 g- $PM_{2.5}$ and 49 g- $PM_{2.5}$ per firing. The average measured emission rates for PM_{10} and $PM_{2.5}$ appear to scale linearly as a function of the zone charge value (Gillies et al., 2007). Although the testing carried out used a 155 mm howitzer, it is likely that the scaling in emissions as a function of zone charge will be consistent between artillery pieces firing different caliber shells but with equivalent zone charge amounts. It is the force transmitted through the shockwave from the detonation to the soil surface that releases the dust from the surface, so the amount of charge should be the primary control on emission strength for a given surface.

Table 3. Minimum, maximum, mean and standard deviations of the measured PM₁₀ and PM_{2.5} artillery backblast emission fluxes.

Test Date	Zone Charge	PM ₁₀ Emission			Std. Dev. PM ₁₀ Emission
		Min. PM ₁₀ Emission Flux (g per firing event)	Max. PM ₁₀ Emission Flux (g per firing event)	Mean PM ₁₀ Emission Flux (g per firing event)	Flux (g per firing event)
10/20/2006	1	2.5	44.3	19.0	16.5
10/27/2006	2	22.2	103.0	48.2	19.7
10/24/2006	5	1.3	211.8	80.5	84.1
10/27/2006	5	8.0	178.5	97.7	54.9

Test Date	Zone Charge	PM _{2.5} Emission			Std. Dev. PM _{2.5} Emission
		Min. PM _{2.5} Emission Flux (g per firing event)	Max. PM _{2.5} Emission Flux (g per firing event)	Mean PM _{2.5} Emission Flux (g per firing event)	Flux (g per firing event)
10/20/2006	1	1.2	22.4	8.5	6.5
10/27/2006	2	2.6	68.9	28.6	19.8
10/24/2006	5	0.1	134.7	45.2	50.2
10/27/2006	5	1.3	103.3	54.0	30.1

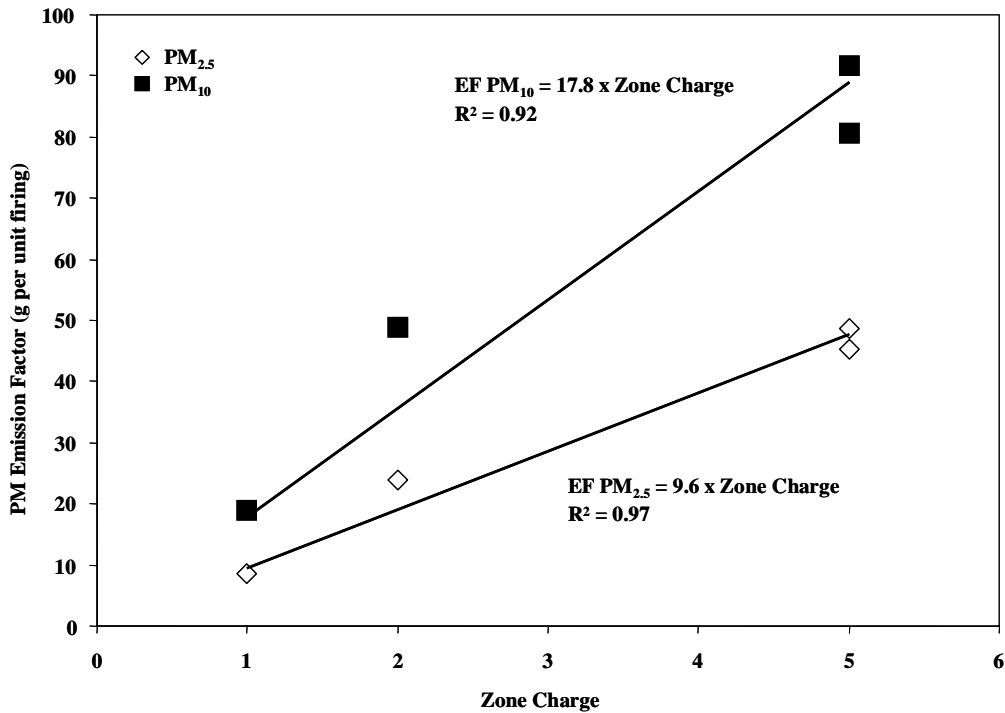


Figure 8. Mean PM₁₀ and PM_{2.5} emission fluxes from a 155 mm howitzer plotted as a function of charge zone. Black solid squares represent the PM₁₀ emission flux and white open squares represent the PM_{2.5} emission flux.

Based on available DoD data of the number of rounds of artillery shells fired for 2004, an estimate of the annual contributions of dust emission from the 15 most frequently fired howitzers and vehicles with artillery capabilities can be developed. The annual PM emissions for artillery backblast are based on the assumptions that all firings use a charge zone 5 and all artillery pieces are equivalent to the 155 mm piece tested at YPG. This is likely an overestimate because zone 5 is the maximum charge used in training and testing and some activities may utilize lower zones and because a significant fraction (~33%) of the artillery corresponds to guns with calibers less than 155 mm. Based on the total number of rounds fired in 2004 the maximum emission contributions for PM₁₀ and PM_{2.5} based on the scenario described above is 52.2 metric tons (57.4 US short tons) and 28.5 metric tons (31.4 US short tons), respectively.

The estimated contributions of PM₁₀ and PM_{2.5} from the measured artillery backblast emission rates would be at levels that are orders of magnitude lower than any of the recognized source categories defined as fugitive emissions. From the perspective of control measures, reducing PM emissions from artillery backblast activities would not be a cost effective measure for DoD installations to consider for lessening the PM burden in areas adjacent to installations where this activity occurs. More effective reductions in this burden are likely to result from mitigative measures designed to reduce contributions of PM created by vehicular activity.

5.2 DUST EMISSIONS FROM OFF-ROAD MILITARY VEHICLE ACTIVITY

The research carried out to characterize dust emissions from off-road vehicle activity also draws upon the already published work of Gillies et al. (2005) that describes off-road wheeled vehicle emission factors collected at Ft. Bliss, TX with new data sets including tracked vehicle PM₁₀ emission factors from YTC and Ft. Carson, CO. In addition, discussion is presented based on the results from PI-SWERL testing to evaluate its utility to predict unpaved road dust emissions without the deployment of flux tower systems. As it is important to characterize the quality of the data collected to provide information on its representativeness and its potential use to develop emission factors with defined uncertainties this aspect of the data are described first.

Data quality for the tracked vehicle measurements is described in terms of instrument acquisition faults, height of dust plumes with respect to tower heights, wind direction, and detectable limits. Table 4 reports the criteria used to validate emission factors measurements.

Instrument Acquisition: On 2006/08/29, data acquisition faults associated with instrument power failures invalidated two vehicle passes from the Tower 1 PM₁₀ data set and three vehicle passes from Tower 2 PM₁₀ data set.

Plume Height: Usually under low wind conditions, the top DT on a tower would report PM concentrations above 1 mg m⁻³ as the plume height exceeded the tower height. Under these conditions, the flux measurement was invalidated since it was impossible to define the vertical extent of the plume. On the top PM₁₀ DT on Tower 1, seven vehicle passes were invalidated. On Tower 2, nine vehicle passes were invalidated.

Wind Direction: Vehicle pass fluxes were calculated only when the wind vectors were within 45 degrees of perpendicular to the road direction. Out of 131 vehicle passes, six were invalidated due to wind direction being outside of the ±45 degree sector.

Detectable Limits: Unlike in previous studies (e.g., Gillies et al., 2005), plume concentrations at the test site frequently exceeded the 150 mg m⁻³ maximum detection limit of the dust sensors. Above these concentrations, the dust sensor has a nonlinear response that is difficult to relate to filter based measurements with confidence. Vehicle passes where one sensor on the tower exceeded 150 mg m⁻³ for 1 second were invalidated. This factor invalidated the largest number of vehicle passes: 118 for PM₁₀ on Tower 1, 73 for PM_{2.5} on Tower 1, and 92 for PM₁₀ on Tower 2.

After applying the criteria listed above, the data recovery percentages were 8% for PM₁₀ on Tower 1, 41% for PM_{2.5} on Tower 1, and 26% for PM₁₀ on Tower 2. Interpreting only the valid emission factor results from this study would negatively bias the summary since the largest emission factors are preferentially invalidated. In order to glean as much useful information from the study as possible, a flux calculation quality scheme was devised:

Class A: Highest Quality Flux Calculations: These data passed all of the criteria listed above.

Class B: PM₁₀ Flux Calculations based on collocated PM_{2.5} measurements: Since PM_{2.5} is a subset of PM₁₀, the maximum concentration of PM_{2.5} for each vehicle pass has the

Table 4. Flux calculation data recovery statistics from the Yakima and Ft. Carson vehicle dust flux experiments.

	YTC 2006			Ft. Carson S1				Ft. Carson S2			
	T1 PM ₁₀	T1 PM _{2.5}	T2 PM ₁₀	T1 PM _{2.5}	T1 PM ₁₀	T2 PM ₁₀	T3 PM ₁₀	T1 PM _{2.5}	T1 PM ₁₀	T2 PM ₁₀	T3 PM ₁₀
Total Vehicle Passes	131	131	131	80	80	80	80	70	70	70	70
Data Acquisition Fault	2	0	3	0	0	18	0	0	0	0	0
WD >45 degrees	6	6	6	7	7	7	7			4	4
Avg. pf Top DT > 1 mg m ⁻³	7	0	9	11	11	11	11	70	70	22	22
Max. of any DT >150 mg m ⁻³	118	73	92	0	0	0	0	0	0	0	0
Number invalid due to WD or top DT >150 mg m ⁻³	12	6	14	18	18	18	18	70	70	26	26
Emission Factor Data Recovery											
Class A: No Faults	8%	41%	27%	78%	78%	55%	78%	0%	0%	0%	0%
Class B: PM ₁₀ inferred from collocated PM _{2.5}	31%										
Class C: PM ₁₀ inferred from DT mounted above	52%	54%	63%								
Total	91%	95%	89%	78%	78%	55%	78%	0%	0%	0%	0%

potential to be valid when the maximum PM₁₀ is greater than 150 mg m⁻³. Averaged values of PM₁₀/PM_{2.5} for each vehicle pass when all values are less than 150 mg m⁻³ were calculated for each position on Tower 1. These values were multiplied by the pass average PM_{2.5} concentration for each pass to calculate PM₁₀ concentrations when the maximum value of the collocated PM₁₀ concentration exceeded 150 mg m⁻³. The resulting value of PM₁₀ (inferred from collocated PM_{2.5}) was then used to calculate the PM₁₀ flux past the tower. Class B has higher uncertainty than Class A, since the relationship between PM₁₀ and PM_{2.5} can change. This uncertainty should be small since the source of the road dust does not change over time.

Class C: PM₁₀ Flux Calculated from next highest dust sensor on Tower: For many vehicle passes on Tower 1, even the maximum PM_{2.5} concentration was greater than 150 mg/m³. For these cases, we used data from the DT at the next highest level on the tower to infer the concentration at the lower level. Using the set of vehicle passes where none of the maximum PM_{2.5} concentrations exceed 150 mg m⁻³, average ratios of neighboring PM_{2.5} dust sensors were calculated (i.e., lower concentration/upper concentration). For vehicle passes where the maximum PM_{2.5} concentrations exceed 150 mg m⁻³, the valid PM_{2.5} concentrations from the sensor above were multiplied by the ratio. In turn, the calculated average PM_{2.5} concentration was multiplied by the ratio described for Class B to infer the pass averaged PM₁₀ concentration. When more than one PM_{2.5} sensor exceeded the maximum value criterion, PM₁₀ concentrations were estimated by sequentially propagating the concentrations of the lowest valid PM_{2.5} measurement down the tower. This method compounds the error introduced in the Class B calculation and is prone to additional error associated with variations in the average plume profile passing the tower. Consequently, Class C flux calculations are assumed to have higher uncertainty than Class B.

For Tower 2, only dust sensors with PM₁₀ inlets were deployed. Class C fluxes were calculated using the ratio of the PM₁₀ concentrations with values from the PM₁₀ sensor mounted above the over-ranged sensor. Table 4 shows the number of vehicle passes that fall within each data quality class. All data from Classes A, B, and C are presented in the results section.

The variation of PM₁₀ emission factor (EF) magnitude based on tracked vehicle speed and location is shown in Fig. 9. Each point represents the average emission factor of multiple passes measured by one or more towers at each site. The error bars in the figure are the standard error (i.e., standard deviation divided by the square root of the number of replicate samples) of the mean that describes how well the mean is known based on repeated measurements. The average EF coefficient of variation (i.e., standard deviation/mean) for a site/vehicle/speed group was 0.7 emphasizing the need to collect replicate measurements (average n = 10) to better define the underlying trends with speed or weight. The upper two panels (Fig. 9) show the relationship between vehicle speed and emission factors measured at Ft. Bliss and Ft. Carson. The horizontal lines on the upper left panel show the AP-42 wheeled vehicle emission factors based on silt content and vehicle weight. The AP-42 model results are in the same range as the measured data however the omission of speed in the model can result in biases up to a factor of three in predicted PM₁₀ emissions.

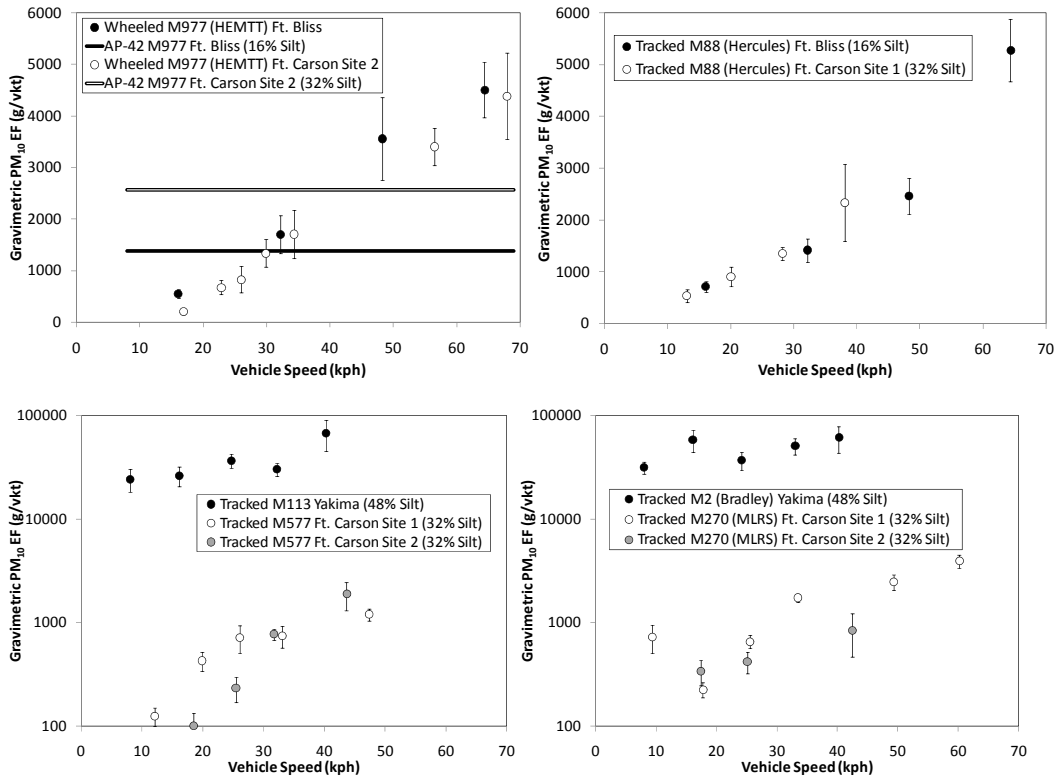


Figure 9. Comparison of Gravimetric PM₁₀ Emission Factors versus vehicle speed from Ft. Bliss, Ft. Carson, and Yakima.

For the same vehicles, emission factors and their increasing trend with vehicle speed are nearly equivalent (<30% difference) between the two sites. In contrast, the lower two panels show a comparison of similar weight tracked vehicle emission factors between Ft. Carson and YTC. These panels are shown with a logarithmic y-axis to show that emission factors at YTC are approximately two orders of magnitude higher than at Ft. Carson due to the highly emissive soils at the YTC. All sites show a strong correlation between gravimetric PM₁₀ emission factors and vehicle speed for the same vehicle. The trend is less visible on the lower panels due to the logarithmic axis.

In agreement with Gillies et al. (2005) wheeled vehicle results, tracked vehicle PM emissions from both YTC and Ft. Carson are correlated with vehicle momentum (i.e., velocity times mass). The relationship between tracked vehicle momentum and gravimetric PM₁₀ emission factor for three different vehicles is shown in Fig. 10. The central grouping of the data supports the parameterization of emissions factors being proportional to vehicle momentum.

The relationship between tracked and wheeled emission factors versus emissions from both the Ft. Bliss and Ft. Carson sites are shown in Fig. 11. At both locations, wheeled vehicles emit ≈ 2 times more PM₁₀ than tracked vehicles for the same momentum. One hypothesis is that this effect may be due to the fact that the tracked vehicle spreads its weight over two treads whereas a wheeled vehicle has four or more wheels. Wheeled vehicles emit dust in front of or behind the point where the tire is in contact with the surface. An image of a tracked vehicle on an unpaved road (Fig. 12) shows that dust emissions occur both at the front and rear of the tank as the tread is first contacting and then separating from the ground. Each element (tread or tire) emits dust when it first makes contact with the ground and when it detaches from the ground. A wheeled vehicle has at least twice as many contact points that serve as sources for dust emissions, which may help to explain the observed relationships (Fig. 11).

All emission factors from all four sites (Ft. Bliss, YTC, and Ft. Carson 1 and 2) were grouped based on location and tread type (i.e., wheel or track). The average ratios of emission factor to momentum were calculated for each group and are presented in Table 5 along with the standard deviation and number of tower flux measurements used to calculate the average. The tracked vehicle emission factor to momentum ratios are generally consistent at Ft. Bliss and both Ft. Carson sites ranging from 0.004 to 0.006 (g-PM vkt⁻¹)/(kg m s⁻¹), but are a factor of 60 less than the values observed in Yakima at 0.38 (g-PM vkt⁻¹)/(kg m s⁻¹). These results show that the location and the soil type of the area in question are critical factors that must be considered to accurately estimate tracked and wheeled unpaved road emissions.

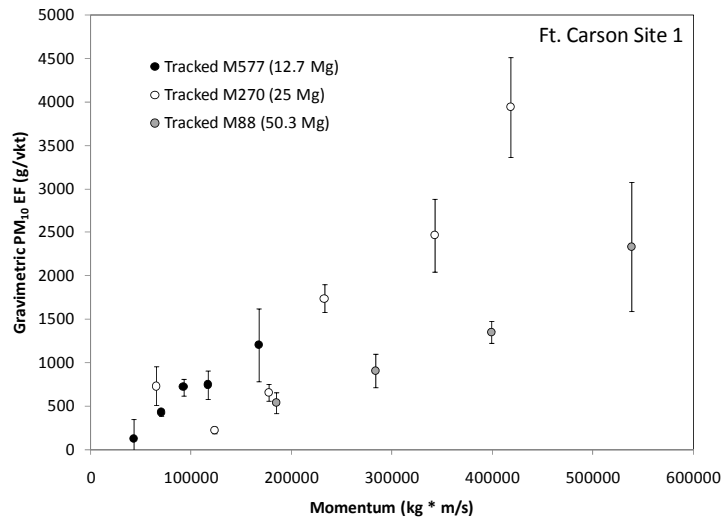


Figure 10. Comparison of tracked vehicle PM₁₀ emission factors versus vehicle momentum for three different vehicles.

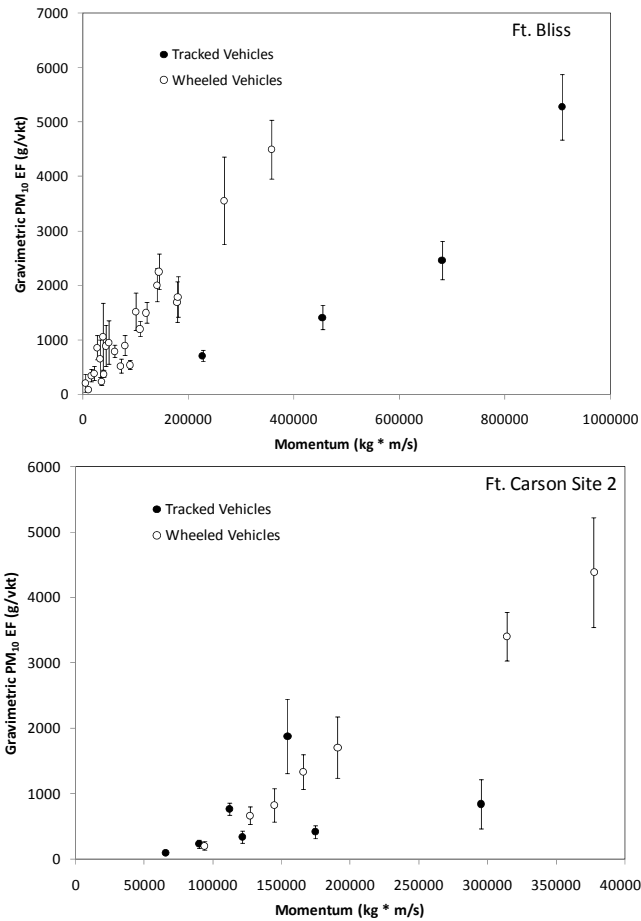


Figure 11. Comparison of tracked and wheeled vehicle DustTrak emission factors versus vehicle momentum operating at the same locations.



Figure 12. Image of M1A1 (Abrams) traveling at 40 km hr⁻¹ on unpaved road at the YPG. Tower 1 is seen in the background along with PM₁₀ and PM_{2.5} filter samplers. The vehicle is moving to the left of the image and the turret is pointing backwards.

Table 5. Summary of surface material silt content, emission factors, and cumulative PI-SWERL emissions for four test locations. Uncertainties are standard deviations of the emission factors. The number in parenthesis represents the number of replicate samples in the average. PI-SWERL measurements have different emission factor units and, like the silt content, are shown to provide a relative comparison.

Sample Location	Silt Content of Surface Material (SSURGO, 2009)	Tracked Gravimetric PM ₁₀ EF/Momentum [g PM/vkt]/[kg * m/s]		Wheeled Gravimetric PM ₁₀ EF/Momentum [g PM/vkt]/[kg * m/s]		PI-SWERL Cumulative Gravimetric Emissions (mg/m ² s) at u* = 0.2 m/s	
Ft. Bliss	16%	0.004 ± 0.001	(54)	0.016 ± 0.008	(207)		N/A
Yakima	48%	0.38 ± 0.28	(246)		N/A	1.7 ± 0.8	(4)
Ft. Carson (site 1)	32%	0.006 ± 0.003	(157)		N/A	0.4 ± 0.2	(2)
Ft. Carson (site 2)	32%	0.004 ± 0.004	(34)	0.008 ± 0.003	(52)	0.2 ± 0.1	(2)

5.2.1 PI-SWERL Measurements of Emission Potential, YTC & Ft. Carson

The DRI PI-SWERL (Etyemezian et al. 2007; Sweeney et al. 2008; Kavouras et al., 2009) was used to measure emission potential of the unpaved roads before and after vehicle testing at the Ft. Carson and Yakima Training Center locations. The PI-SWERL tests measure the potential fugitive PM₁₀ dust emissions (mg m² s⁻¹) from the surface at different equivalent wind speeds. The tests are conducted at pre-set equivalent shear velocities (u*, m s⁻¹) that can span the range 0.1 to 1.2 m s⁻¹, corresponding to a wind over 90 km hr⁻¹ at 2 m above the ground.

The PI-SWERL was operated on the unpaved test road at the YTC on 8/24/06, midway through the testing period. Thus PI-SWERL measurements at YTC correspond to thoroughly disturbed roadway conditions. Five replicate measurements were completed across the width of the unpaved road. The measurement cycle comprised a series of step increases in the rate of rotation of the PI-SWERL annular blade as described in Etyemezian et al. (2007). Each revolution per minute (RPM) step was held for 90 seconds. The test cycle consisted of: 1) a 120 s clean air flush, 2) a step increase to 600 RPM, 3) a step increase to 900 RPM, 4) a step increase to 1200 RPM, 5) a step increase to 1800 RPM, 6) a step increase to 2400 RPM, and 7) turn off motor and clean air flush for 90 s.

The PI-SWERL was operated at the two unpaved roads in Ft. Carson, CO. At the first unpaved road (Site 1), the PI-SWERL was operated before any tracked vehicles traversed the road (9/16/08), after the heaviest tracked vehicle traversed the road for emissions measurements (9/16/08), and after all three tracked vehicles had traversed the roads (9/17/08). At the second unpaved road site, the PI-SWERL was operated before any tracked vehicles traversed the road (9/18/08) and after all three tracked vehicles and a HEMMT traversed the road for emission testing (9/19/08). At each of these measurement intervals a minimum of six replicate measurements was completed.

For all measurements a hybrid ramp/step measurement cycle was used consisting of: 1) a 60 s clean air flush, 2) a sharp acceleration to 500 RPM, 3) a 60 s linear ramp to 2000 RPM, 4) maintain 2000 RPM for 60 s, 5) a 60 s ramp to 3000 RPM, 6) maintain 3000 RPM for 90 s, 7) a 60 s ramp to 4000 RPM, 8) maintain 4000 RPM for 90 s, and 9) turn off motor and clean air flush for 60 s.

PI-SWERL was deployed at YTC and Ft. Carson in hopes that the measurement would serve as a surrogate to infer the variation of emission factor with site characteristics. The PI-SWERL measures the potential for a surface to emit PM based on simulating wind erosion processes (Etyemezian et al. 2007). The mechanism of saltation induced particle entrainment is quite different from the interaction of a vehicle tire or track with a road surface. Depending on the surface type, the tire or tread may penetrate through or deform the road surface and suspend material from deeper layers than are available to wind erosion.

PI-SWERL measurements were collected on the same roads measured with the flux tower and are compared with the road dust emission factors in Table 4. PI-SWERL measures the concentration of particles suspended from a surface while increasing the shear stress ($\tau \text{ N m}^{-2} = \rho_a u_*^2$, where ρ_a is air density, kg m^{-3}) applied to the surface. A modified test cycle was required for testing the Yakima soils due to the high dust emissivity. The test cycles at both YTC and Ft. Carson overlapped between $u_* = 0.17 \text{ m s}^{-1}$ and 0.23 m s^{-1} . For comparison purposes, all PI-SWERL PM_{10} emissions were interpolated to $u_* = 0.2 \text{ m s}^{-1}$. A comparison of cumulative PI-SWERL emissions from Yakima and Ft. Carson is shown in Table 4. PI-SWERL emissions are ≈ 6 times larger at YTC than at Ft. Carson for the same shear velocity, much less than the change in emission factors that occurred for vehicles with similar momentum. A larger data set is needed to evaluate if these two measurement methods scale similarly, which if proved could provide a means to evaluate emission potential from unpaved roads created by vehicle travel.

5.3 DUST EMISSIONS FROM ROTARY-WINGED AIRCRAFT

The results of this experiment are detailed in Gillies et al. (2010), which defines emission factors for a specific rotary-winged aircraft (UH-1H Huey) flying at low altitude over two desert surfaces, one much more emissive than the other. This work also examines the scaling relationship between aircraft operating conditions and dust emission strength. McAlpine (2009) and McAlpine et al. (submitted) describe in detail the ground effect conditions created by this rotary-winged aircraft as measured at the full-scale, which has not, to the best of our knowledge, been previously published. McAlpine (2009) corroborates wind tunnel modeling efforts of ground effect phenomena and will be extremely useful for research that is seeking to understand and potentially mitigate dangerous brown out conditions caused by low-level rotary winged aircraft flight. McAlpine et al. (submitted) evaluates the ability of Computation Fluid Dynamic (CFD) modeling to be used as a means to develop a model that can be used to evaluate the contributions of dust to ambient air caused by rotorcraft flight.

To provide data on the potential magnitude of dust emissions caused by this military source, a field measurement campaign was undertaken from 21-25 May, 2007, at the YPG. Emissions of dust created by a low-flying rotary-winged aircraft were measured for helicopter passes over two different surfaces, which represented a desert pavement with minimal disturbance and an area within the YPG that is used for drop zone testing (parachute-aided landings of military matériel and personnel) and can be considered a disturbed desert surface. Both test locations were flat with large upwind fetches relative to the defined flight path line.

The flight maneuvers made by the helicopter at each of the two test sites are summarized as follows: 1) Site 1, 36 passes spanning the target forward travel speed range and four landing and take-offs; 2) Site 2, 37 passes covering the target forward travel speed range. Based on analysis of the video imaging of each flight pass the average height of the rotor-blade AGL was 7.1 m (± 0.5 m). The type of flow regimes associated with the flight passes were calculated based on advance ratio estimates. The most commonly occurring flow regime was ground vortex (39% occurrence), followed by re-circulating (30% occurrence) and trailing sweep (21%), no jet wakes were observed. The remaining 16% were categorized as transitional (13%) or un-defined (3%) (Table 6).

An accounting of the reliability of the acquired dust emission data for subsequent analysis is provided in Table 7. Reliability for these data is defined in terms of data acquisition faults, angle of wind approach to the instrument array, particulate matter concentrations in exceedance of the instrument limits (i.e., $\geq 1.5 \times 10^5 \mu\text{g m}^{-3}$), and for minor extrapolation of dust concentration when less than 90% or between 70% to 80% of the instruments were operating (individual instrument failure sometimes occurred during testing, which could not be rectified in the time between passes). Reasons for a failure to observe emissions were attributed to variable winds that caused the plume to miss the instrument array, or because winds dropped to near-zero speed creating a plume that dispersed mostly due to thermal instabilities, which is not amenable to a standard horizontal flux calculation.

Table 6. Dust emission test conditions and measurement parameters for the rotary-winged aircraft flights at Sites 1 and 2, YPG. Upper table entries are for PM10 and the lower entries for PM2.5.

Site	Target Forward Travel Speed (km hr ⁻¹)	Average Forward Travel Speed (km hr ⁻¹)	Standard Deviation of Forward Travel Speed (km hr ⁻¹)	Average Advance Ratio	Standard Deviation of Advance Ratio	Average Per Tower Total Emissions ¹ (kg of PM ₁₀ per flight pass)	Standard Deviation of Total Emissions ¹ (kg of PM ₁₀ per flight pass)	Average Per Tower Unit Emissions per m width (g of PM ₁₀ m ⁻¹)	Number of Flight Passes
1	15	19.4	1.4	0.012	0.006	0.266	0.336	0.019	14
1	30	30.3	11.1	0.029	0.029	0.070	0.117	0.005	13
1	60	58.3	6.8	0.066	0.012	0.065	0.059	0.005	15
2	15	19.1	1.4	0.025	0.007	15.717	10.541	0.301	27
2	25	26.6	1.2	0.035	0.004	6.202	6.062	0.119	24
2	35	35.6	2.2	0.045	0.006	3.955	3.794	0.076	25
2	45	44.9	3.6	0.055	0.008	0.683	0.792	0.013	28
2	60	58.5	0.7	0.061	0.002	0.071	0.071	0.001	3

¹Based on total flux for each of the three towers

Site	Target Forward Travel Speed (km hr ⁻¹)	Average Forward Travel Speed (km hr ⁻¹)	Standard Deviation of Forward Travel Speed (km hr ⁻¹)	Average Advance Ratio	Standard Deviation of Advance Ratio	Average Per Tower Total Emissions ¹ (kg of PM _{2.5} per flight pass)	Standard Deviation of Total Emissions ¹ (kg of PM _{2.5} per flight pass)	Average Per Tower Unit Emissions per m width (g of PM _{2.5} m ⁻¹)	Number of Flight Passes
1	15	19.4	1.4	0.012	0.006	N/A			
1	30	30.3	11.1	0.029	0.029	N/A			
1	60	58.3	6.8	0.066	0.012	N/A			
2	15	19.1	1.4	0.025	0.007	1.641	1.590	0.031	27
2	25	26.6	1.2	0.035	0.004	0.497	0.451	0.010	24
2	35	35.6	2.2	0.045	0.006	0.404	0.393	0.008	25
2	45	44.9	3.6	0.055	0.008	0.049	0.062	0.001	28
2	60	58.5	0.7	0.061	0.002	N/A			

Table 7. Report on of the reliability of the acquired dust emission data, rotary-winged aircraft tests.

Date of Test	5/21/2007	5/25/2007
Total Flight Passes	36	37
Error Types:		
1) Data Acquisition Faults	0	0
2) Wind Approach Angle >45 degrees	5 (14%)	1 (3%)
3) Maximum of any DustTrak >150,000 $\mu\text{g m}^{-3}$	0	0
4) Number of invalid plume events due to both wind direction or maximum PM concentration at highest positioned DustTrak >150,000 $\mu\text{g m}^{-3}$	0	0
5) PM ₁₀ inferred from minor extrapolation with 90 to 100% of meteorological instruments recording	30 (83%)	36 (97%)
6) 70-80% of DustTracks recording plume, 100% meteorological instruments working	1 (3%)	
Average of top DustTrak >100,000 $\mu\text{g m}^{-3}$ (caution only, no error reported)	Tower 1, 0 events Tower 2, 1 event Tower 3, 1 events	Tower 1, 17 events Tower 2, 19 events Tower 3, 9 events

The duration that the helicopter-generated plumes impacted the towers ranged from 7 s to 107 s at Site 1, and 13 s to 180 s at Site 2. These times depended primarily on wind speed and wind direction in the ambient boundary-layer wind flow.

Peak concentrations of PM_{2.5} measured (with the DustTrak sensors) at the towers associated with the dust plumes ranged from 1,285 $\mu\text{g m}^{-3}$ to 9,925 $\mu\text{g m}^{-3}$ at Site 1. Peak concentrations of PM₁₀ at Site 1 ranged from 6,046 $\mu\text{g m}^{-3}$ to 38,860 $\mu\text{g m}^{-3}$. Background ambient concentrations between helicopter passes ranged between 24 $\mu\text{g m}^{-3}$ and 108 $\mu\text{g m}^{-3}$ for PM_{2.5} and between 55 $\mu\text{g m}^{-3}$ and 499 $\mu\text{g m}^{-3}$ for PM₁₀.

At Site 2, peak concentrations of PM_{2.5} measured at the towers associated with the dust plumes ranged from 924 $\mu\text{g m}^{-3}$ to 5,874 $\mu\text{g m}^{-3}$. Peak concentrations of PM₁₀ at Site 2 ranged from 33,147 $\mu\text{g m}^{-3}$ to 53,170 $\mu\text{g m}^{-3}$. Background ambient concentrations between helicopter passes ranged between 19 $\mu\text{g m}^{-3}$ and 139 $\mu\text{g m}^{-3}$ PM_{2.5} and between 40 $\mu\text{g m}^{-3}$ and 205 $\mu\text{g m}^{-3}$ for PM₁₀. These background concentration measurements represent average 15 second concentrations (measured at 1 Hz) prior to the arrival of dust plumes.

The one second dust concentration data measured during the passage of the dust plumes at each of the three towers at multiple heights can be combined with the wind speed and direction data to provide an estimate of how much dust passed through the tower-defined flux plane for each dust plume raised by the helicopter traveling down the flight line (i.e., Eq. 5). It should be noted that the actual amounts of dust will be greater than reported here as the defined flux plane does not capture the entire vertical scale of the plumes. The calculation of how many kilograms of dust are passing by the defined flux plane as a function of target and average forward travel speed of the helicopter (determined from individual flight pass video images) are provided in Table 6. The average emissions per meter width (g m^{-1}) of the defined flux plane for both particle sizes are also provided. These latter estimates could form the basis of an emission factor for this type of rotary-

winged aircraft flying close to an emissive surface similar to those that are representative of this study.

Clearly, Site 2, the disturbed desert soil generates much higher PM_{10} dust emissions for the same helicopter traveling above the ground at the same height and over a similar range of speeds. For the same forward travel speeds of $\approx 15 \text{ km hr}^{-1}$ and $\approx 30 \text{ km hr}^{-1}$ the emissions increase at Site 2 by approximately 60 and 72 times, respectively. This indicates that disturbance of the soil can have a dramatic impact on the strength of the dust emissions as these two sites are essentially the same surface separated by less than 1,000 m from each other, but Site 2 has been mechanically disturbed at some time in the past to facilitate its use as a drop-zone. This disturbance has removed the desert pavement and mixed the upper soil horizons. The emissions of $PM_{2.5}$ (Table 5) are approximately 9% ($\pm 2\%$) of the PM_{10} , which is likely dependent, in part, on soil textural and aggregate size properties that change depending on geographic location. It should be noted that the $PM_{2.5}$ emissions are based on fewer measured point concentrations and use the average $PM_{2.5}:PM_{10}$ mass concentration ratio to extrapolate concentrations of $PM_{2.5}$ where sensors for this particle size range are missing in the array. This occurs only on the two towers on either side of the center tower. Due to instrument difficulties, adequate data were not available for $PM_{2.5}$ emission calculations at Site 1.

The effect of forward travel speed and advance ratio of the aircraft on dust emissions is also evident in the data presented in Table 6. The mean total mass of PM_{10} passing through the array (Eq. 5) is plotted as a function of forward travel speed for Sites 1 and 2 in Fig. 13 and advance ratio in Fig. 14 (error bars represent standard deviations of the mean values). These two figures show that the mass of PM_{10} emitted from the surface decreases exponentially with increasing forward travel speed and advance ratio. In the larger data set for Site 2, forward travel speed seems to be more correlated with emissions than advance ratio, suggesting for these tests forward travel speed is a better predictor for estimating dust emissions.

Normalizing the emissions to the slowest forward travel speed for both sites and including the available $PM_{2.5}$ data (also normalized to the slowest forward travel speed) it can be seen from Fig. 15 that the emissions of either size class of particulate matter, from both sites, scale similarly with forward travel speed of the aircraft.

That the emission of dust is related to the forward travel speed of the aircraft suggests that the force driving the emissions is related to the shear stress created by the rotor downwash, similar to wind-generated dust emissions (Shao, 2000). The Irwin sensor data provide a means to examine the near surface shear stress generated by the outflow of air from the rotor-blade.

The effect of forward travel speed on surface shear stress is shown in Fig. 16 in which the normalized mean peak shear stress at each Irwin sensor location is plotted against mean forward travel speed. The peak shear stress at each measurement position was normalized by dividing by the mean peak shear stress for the 15 km hr^{-1} speed. This relationship (Fig. 16) reveals that the shear stress changes proportionally the same amount at each measurement location for an incremental change in forward travel speed. At each of the Irwin sensor locations there is an $\approx 0.12\%$ decrease in mean peak shear stress for every 10 km hr^{-1} increase in forward travel speed.

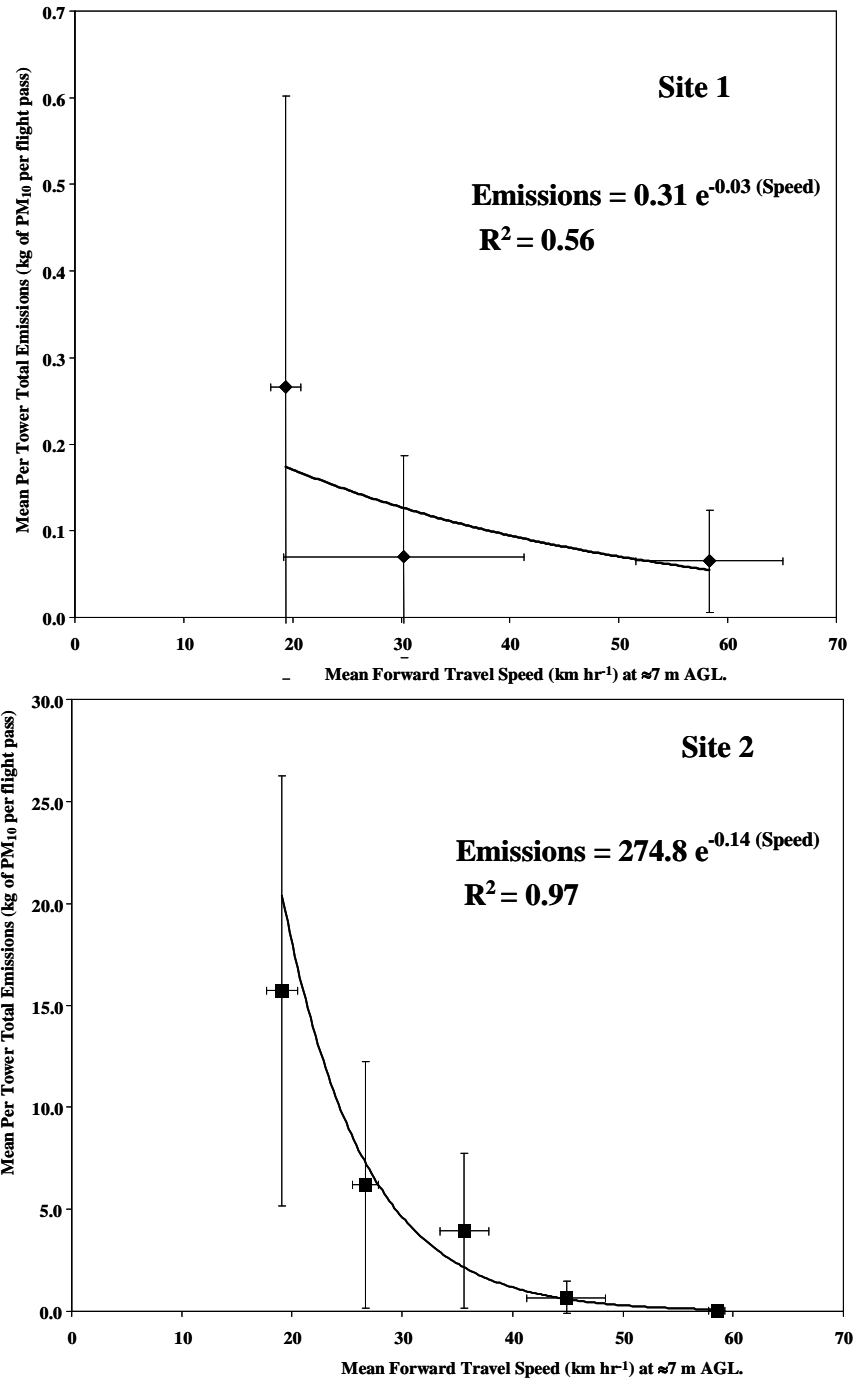


Figure 13. Emissions of PM₁₀ as a function of forward travel speed for Sites 1 and 2, YPG.

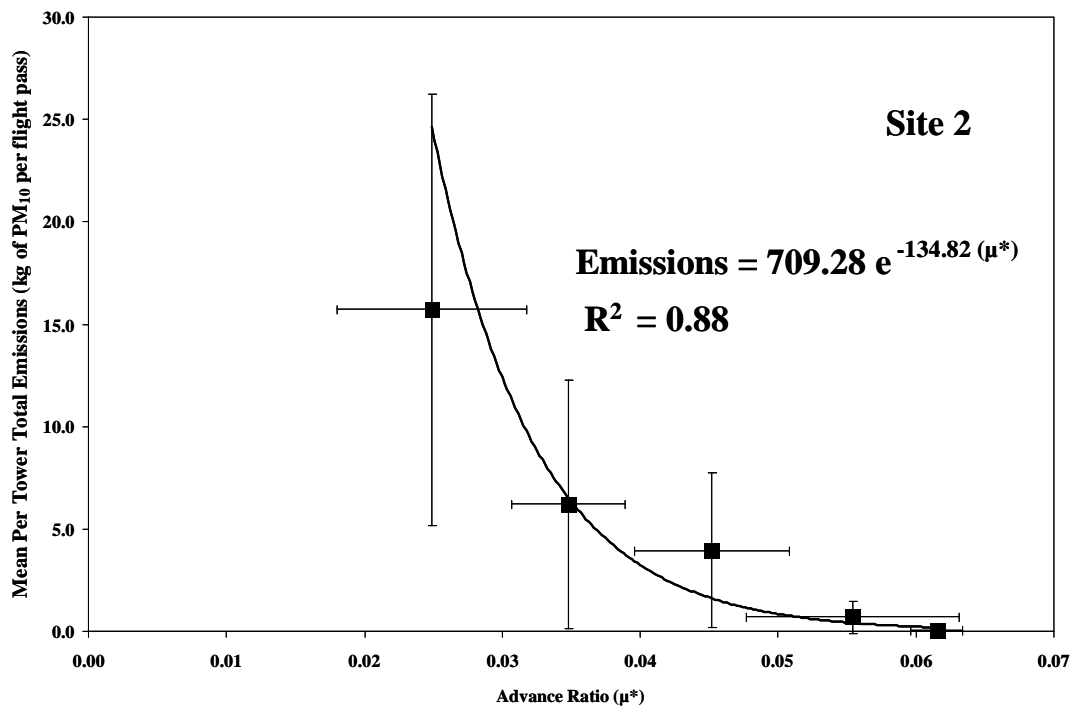
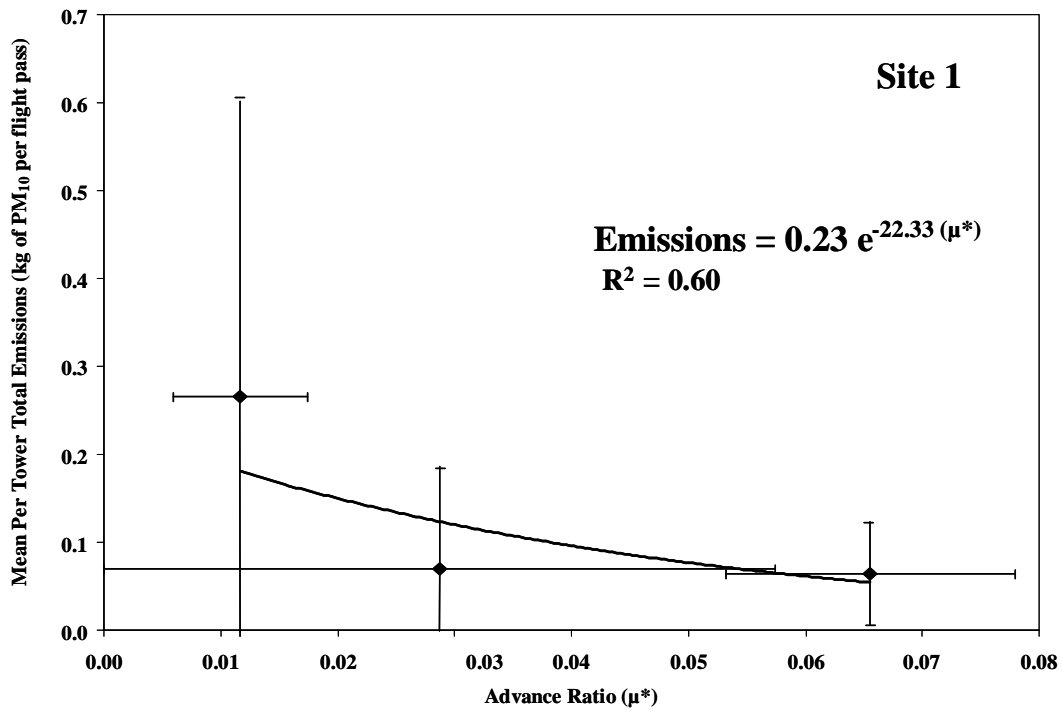


Figure 14. Emissions of PM_{10} as a function of advance ratio for Sites 1 and 2, YPG.

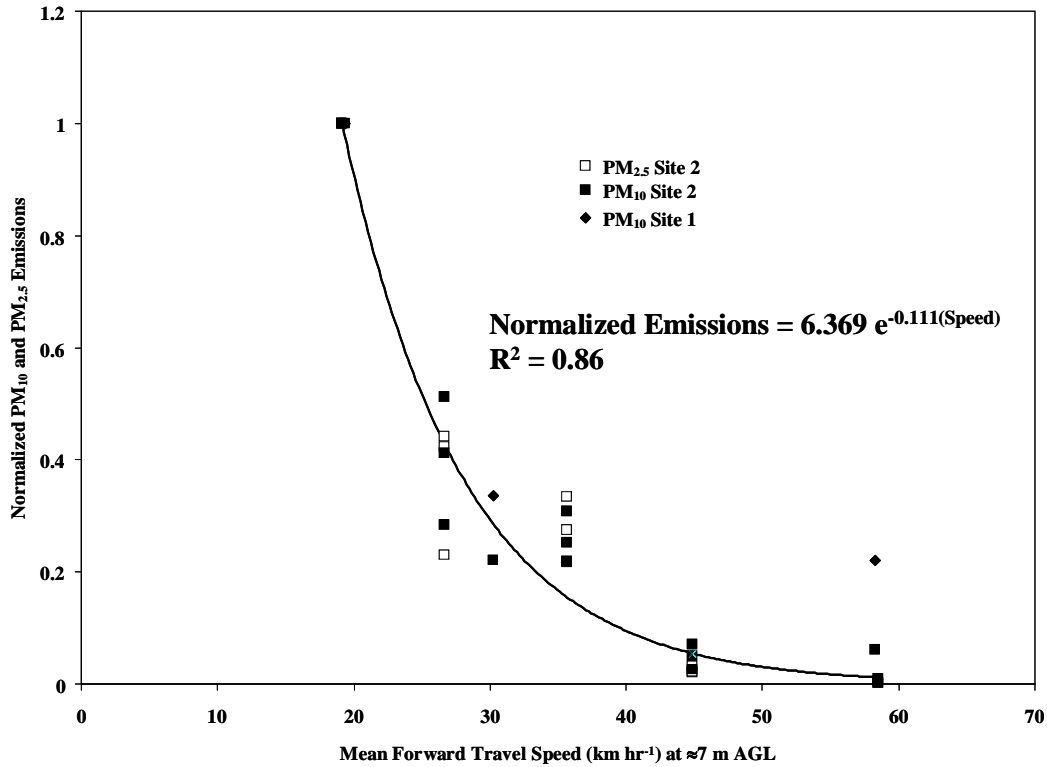


Figure 15. Normalized emissions of PM₁₀ and PM_{2.5} as a function of mean forward travel speed for Sites 1 and 2, YPG.

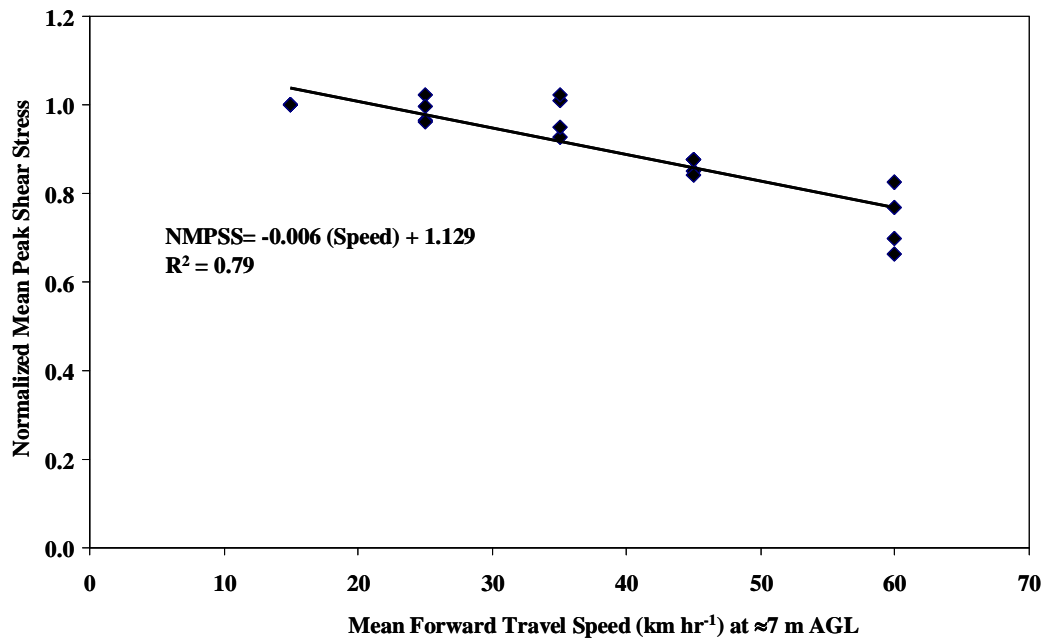


Figure 16. The relationship between normalized mean peak pressure and mean forward travel speed for Sites 1 and 2 combined showing that peak shear stress decreases at the same increment at each measurement location over the ≈19 m measurement length as aircraft speed increases.

The Irwin sensor data can also be used to evaluate how the shear stress distribution changes as a function of distance from the flight line. The decrease in mean peak shear stress as a function of distance from the flight line and for all average test speeds is shown for Sites 1 and 2 in Fig 17. In Fig. 17 these data are normalized by dividing the measured mean peak shear stress at each instrument position by that measured at the first Irwin sensor (i.e., 10 m from the flight line center), which collapses the data for each travel speed and each site.

At Site 1 the emissions from three landings and four take-offs in close proximity to each other were measured. The average emission value for a take-off is approximately 0.5 kg of PM₁₀ and for a landing approximately 1 kg, which likely reflects the time associated with each maneuver as a takeoff occurs more quickly than a landing.

As Fig. 15 shows there is a clear reduction in PM emissions as aircraft speed increases. A two-part mechanism can be proposed that explains this relationship. First, as the helicopter's forward speed increases its residence time over any location on the surface diminishes, so the time the downward rotor-generated flow is acting upon that surface also decreases. This reduces the duration that the shear stress is applied at any one point on the flight path so the duration during which emissions of dust could occur also decreases.

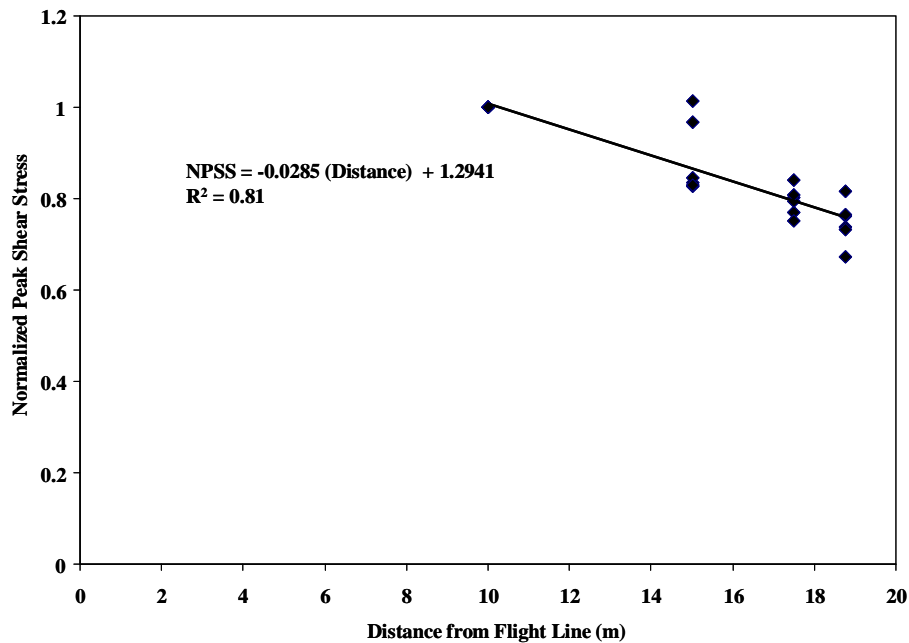


Figure 17. The relationship between normalized mean peak pressure and distance from the centerline of the aircraft flight line (i.e., centerline is 0 m) for Sites 1 and 2 combined showing that peak shear stress decreases linearly with increasing distance over the ≈ 19 m measurement length independent of aircraft speed.

Second, as mentioned previously, changes in forward travel speed are controlled only by the rotor-blade positional characteristics while the rate of revolution of the helicopter rotor is essentially held constant. As the helicopter increases its forward speed, the rotor blades change their pitch over the 360° rotation. This change in pitch alters the strength and distribution of the shear stresses created by the downward directed air flow from the rotor, which will also affect the dust emission process. This is clearly seen in the Irwin sensor data (i.e., Fig. 16), which show that mean peak shear stress decreases with increasing forward travel speed. The relative change in the shear stress at locations perpendicular to the flight-line (outside of the area defined by the rotor diameter) scale predictably with travel speed.

Another potentially critical component affecting dust emissions may be the flow regime that is created under the aircraft, which will be dictated to a large degree by the ambient wind speed and the rotor blade pitch (forward travel speed). The more ambient wind conditions force the advance ratio towards a trailing sweep or ground vortex regime, the lower peak shear stresses at the surface are likely to be. The data collected do not allow for an evaluation of the potential influence of flow regime on dust emissions.

Based on these observations, for similarly configured aircraft (i.e., one main rotor and one tail rotor), several physical characteristics of the aircraft are likely to have a direct bearing on the strength of the dust emissions. These are the weight of the aircraft, the length of the rotor blades, and possibly the number of rotor blades. Weight is critical because it defines how much force is needed to keep the aircraft aloft. The length of the rotor-blades and their number will also be important as they affect the force per unit area felt on the ground surface. With the present data set it is not possible to evaluate how different rotor-blade and weight configurations may affect dust emissions.

Cowherd (2007) however, presents data for dust concentrations measured in plumes generated by five different rotary-winged aircraft (UH-1, CH-46, HH-60, CH-53, and MH-53) at two different positions downwind (17.5 m and 35 m from the rotor edge) of low level flight passes and at two different heights (0.5 m and 1.4 m), which can be used to demonstrate the effect of aircraft weight and rotor-blade length on dust emissions. Normalizing Cowherd's (2007) data (refer to Table 11 in Cowherd, 2007) by dividing each disk loading value by the lowest value (for the UH-1) and normalizing each concentration by dividing by the lowest measured value collapse these data and produces the relationship shown in Fig. 18. This relationship (Fig. 18) shows normalized concentration increases as a power function of normalized disk loading, which suggests that the dust flux should also increase as a power function of disk loading.

A comparison of emissions of PM₁₀ from the rotary-winged test aircraft and the military wheeled vehicles tested by Gillies et al. (2005) (i.e., HUMMWV, LMTV, 5-ton, and HEMMT) for the speed range of 15 km hr⁻¹ to 60 km hr⁻¹ is shown in Fig. 19. As this figure shows, the emissions of PM₁₀ dust from low-flying rotary-winged aircraft only approach the levels associated with wheeled vehicles when they travel slowly over surfaces that have similar emission potentials to the test sites at YPG.

Emissions of PM₁₀ dust calculated from available emission factor relationships for wheeled military vehicles (Gillies et al., 2005) would exceed those generated by this type of helicopter, for essentially all normal operating speeds for both types of vehicles, for

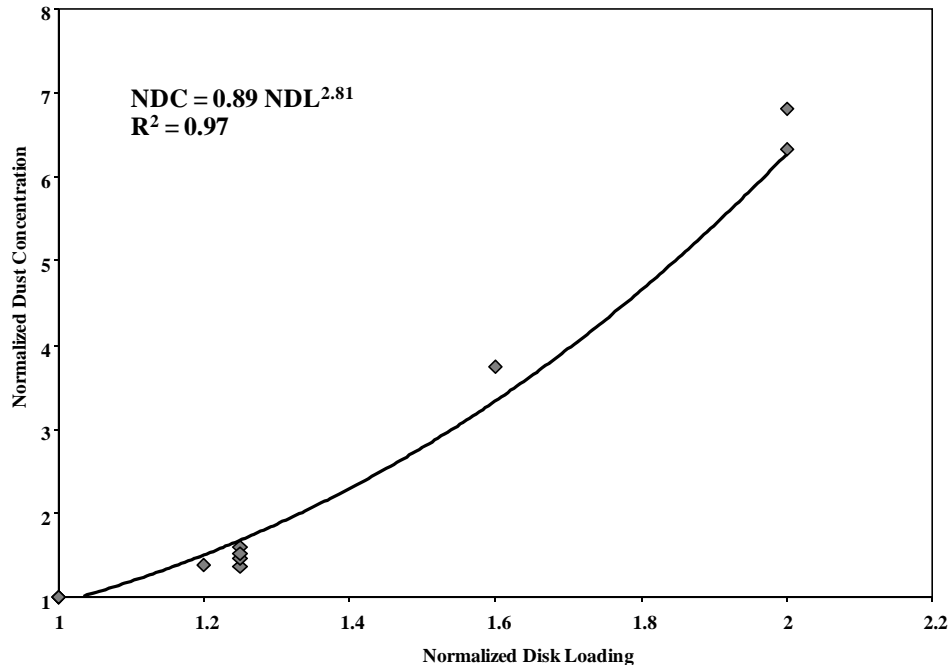


Figure 18. Normalized dust concentration as a function of normalized disk loading showing how aircraft weight and the area swept by the rotor-blades affect the strength of the dust concentrations in the plume (after Cowherd, 2007).

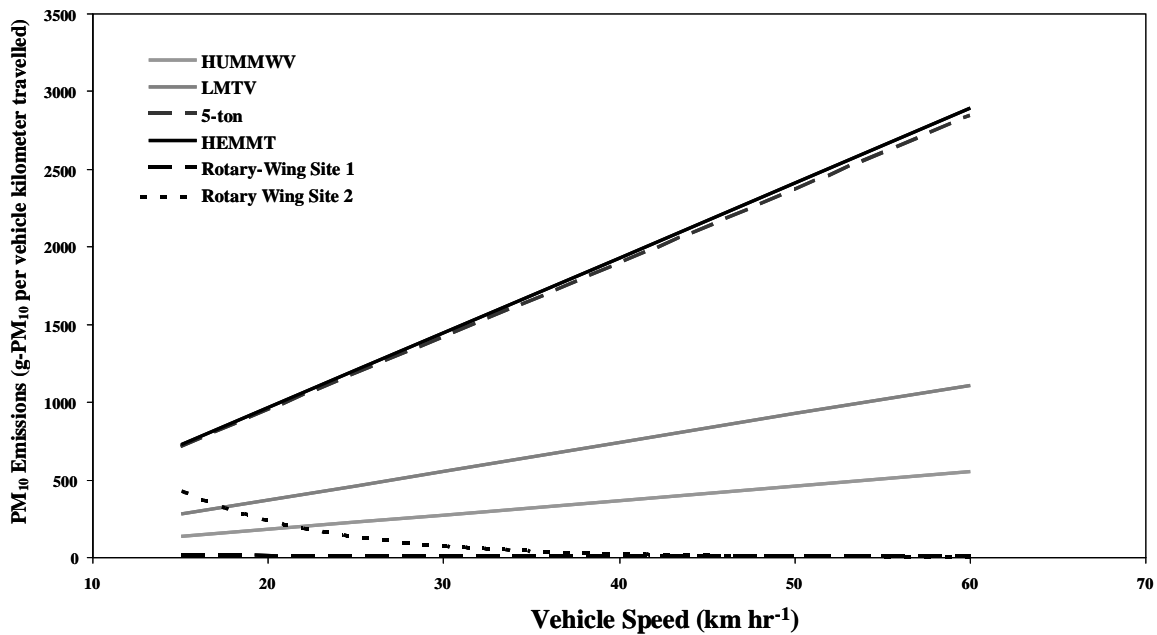


Figure 19. Comparison of emissions of PM₁₀ as a function of vehicle speed for the rotary-winged aircraft and light and heavy wheeled military vehicles. Wheeled vehicle emission factors are from Gillies et al. (2005).

Site 1. For Site 2, the aircraft-generated PM₁₀ emissions would exceed those of the lowest weight wheeled vehicle for travel speeds less than ≈ 23 km hr⁻¹. For the two heaviest wheeled vehicles (HEMMT and 5-ton) the rotary winged aircraft will emit more PM₁₀ per kilometer of travel when both vehicle speeds are less than ≈ 12 km hr⁻¹.

5.3.1 Results: PI-SWERL Emission Potential Measurements, YPG

At Site 1, the transect of PI-SWERL measurements produced shear stresses ranging from 0.06 N m⁻² to 0.77 N m⁻² with the highest shear stress generating PM₁₀ dust emissions that exceeded the limit (150 mg m⁻³) of the dust monitor incorporated into the instrument. The variability between tests is considerable with the standard deviation of the tests (pre- and post-helicopter passes) exceeding the geometric mean of the tests at each shear stress interval. The range of PM₁₀ emissions can be expressed by the geometric mean of all of the tests combined for shear stresses of 0.06 N m⁻², 0.18 N m⁻², 0.36 N m⁻², 0.55 N m⁻², and 0.77 N m⁻², which were 0.011 mg m⁻² s⁻¹, 0.060 mg m⁻² s⁻¹, 0.346 mg m⁻² s⁻¹, 2.168 mg m⁻² s⁻¹, 4.069 mg m⁻² s⁻¹, respectively. The difference before and after the helicopter passes in dust emissions was not statistically significant, but the emissions were higher on average for the same shear stress for the PI-SWERL tests post-helicopter passes (e.g., for a shear stress of 0.77 N m⁻² the PM₁₀ emissions were 2.86 mg m⁻² s⁻¹ and 6.87 mg m⁻² s⁻¹ for the pre and post-helicopter passes, respectively).

The range of PM₁₀ emissions estimated using PI-SWERL for Site 2 expressed by the geometric mean of all of the tests combined for shear stresses of 0.06 N m⁻², 0.18 N m⁻², 0.36 N m⁻², and 0.55 N m⁻² were 0.062 mg m⁻² s⁻¹, 0.167 mg m⁻² s⁻¹, 3.244 mg m⁻² s⁻¹, and 21.635 mg m⁻² s⁻¹, respectively. The variability in emissions amongst the tests at this site is relatively large resulting in a large standard deviation of the measured emission flux. On average, however, the emissions from the Site 2 were an order of magnitude larger than at Site 1 for the same shear stresses. The surfaces at the second site were very emissive and exhibited PM₁₀ emissions beyond those measured at typical natural southwest desert surfaces measured with the PI-SWERL (Sweeney et al., 2008).

5.4 ROTARY-WINGED AIRCRAFT GROUND EFFECT CHARACTERIZATION

When a rotary-winged aircraft operates near to the ground at low airspeeds the wake of the aircraft interacts with the surface forming particular flow features and the aircraft is said to be operating in “ground-effect.” The ground-effect wake often contains strong jets and recirculation zones that affect the operation of the rotorcraft by interaction of the wake with the rotor. Operation in ground-effect over a surface with loose material may lead to dangerous “brown-out” conditions where dust- and sand-sized particles on the surface are entrained into the wake, obscuring the pilot’s vision. There has been a renewed concern with the brown-out phenomenon in recent years as military activities in arid regions have increased.

The opportunity to carry out a full scale study on ground-effect phenomenon was realized as part of this SERDP project to characterize the dust entrainment source strength potential of rotorcraft operating at slow speeds near the desert surface (Gillies et al., 2010). The study was conducted in May 2007 at the U.S. Army Yuma Proving Grounds (YPG) in Yuma, Arizona. During the execution of that research, complimentary measurements were taken to provide data to characterize features of the ground-effect wake. Digital video of the helicopter maneuvers was captured, as well as velocity

measurements within the wake using a sonic anemometer. Surface shear stress (Irwin, 1980) also measured the shearing force of the wake at the surface responsible for entraining dust.

Measurements from a full scale study of a rotary-winged aircraft operating in ground effect over desert terrain provided a unique opportunity to compare wake flow characteristics to those observed in scaled wind tunnel studies. Digital video data and sonic anemometer wake velocity data collected for over 60 flight maneuvers provided an adequate dataset to analyze the characteristics of the ground-effect wake over the applicable range of advance ratios, including brown-out conditions caused by entrainment of dust-sized materials by the aircraft wake. The findings presented here appear to verify and extend the results reported in the literature over the past few decades derived from scaled wind-tunnel studies over a μ^* range of 0.02 to 2.4. The main conclusions of this study (McApline, 2009) (for a mean flight height $h/D=0.51$ with standard deviation of 0.05) are:

1. The recirculation wake flow regime occurred in the μ^* range of 0.2-0.6, agreeing with other studies reported in the literature.
2. A transitional flow regime could be classified in the μ^* range of 0.6-0.8 as fluctuation between the recirculation and ground vortex regimes was observed.
3. The central transition point between the recirculation and ground vortex regimes was a μ^* of 0.7, which agrees closely with the results reported in the literature.
4. The ground vortex regime was observed over the μ^* range of 0.7-1.4, which expands on the range reported in the literature.
5. The trailing sweep regime occurs over the μ^* range of 1.4 – 2.0 and no dust entrainment is observed above a μ^* of 2.0.
6. A linear relationship between forward separation point of the ground jet and the normalized advance ratio was observed.
7. Vortex centroid heights compare well to those reported in the literature for $\mu^* > 0.6$ but compare unfavorably for $\mu^* < 0.6$.
8. A simple method to estimate ground vortex vorticity was applied and it was found that ground vortex vorticity increases linearly with increasing μ^* . These findings could be used to compare vortex strengths to those reported in the literature.

5.5 ASSESSMENT OF THE APPLICABILITY OF A COMPUTATIONAL FLUID DYNAMIC (CFD) METHOD TO SIMULATE A ROTORCRAFT DUST EMISSION SOURCE

When the rotorcraft wake interacts with the surface it is said to be within “ground-effect.” Significant entrainment of debris or dust in ground-effect flight can result in “brown-out” conditions where visibility in the local area of the rotorcraft is severely reduced. Modeling methods to simulate the ground effect wake and brown-out have advanced to the point that the wake can be simulated accurately in real time (Keller et al., 2006). These advances have made it possible to perform pilot-in-loop simulations of brown-out conditions for training as well as study wake influences on aerodynamics closely. However, for air quality applications it may not be necessary to use such a detailed simulation of the wake.

For air quality modeling it would in fact be advantageous to avoid using a complex real-time model to describe the amount of dust being entrained. Occurrences of regional impact would likely involve multiple point sources, each requiring their own emission characterization. Simple methods, such as application of a particulate-matter area source, would not be sufficient because the rotor wake represents a significant perturbation in the atmospheric surface layer (ASL) whose forcings not only determine the amount of dust entrained but the vertical distribution of dust upon its exit from the wake into the unperturbed ASL.

The purpose of this component of the research was to ascertain the ability of a steady-state CFD simulation using a state-of-the-art actuator disk rotor parameterization to simulate the structure of a rotor wake in ground-effect operation. Use of a steady state wind field in describing rotor wakes would be advantageous for use in a regional air quality model where the dust entrainment from aircraft could result in air quality degradation. It has been noted that the actuator disk method is unable to accurately predict the rotor wake structure due to the excessive dissipation of vorticity in the wake (Brown, 2000). This study examined the ability of the CFD-Virtual Blade Model to simulate basic wake structure by comparing the results of CFD simulations to measurements from the full-scale study of rotorcraft in ground-effect (McApline et al, submitted).

For this study the commercial CFD software FLUENT[®] was used (FLUENT, 2006). The model solves the Reynolds Averaged Navier-Stokes (RANS) equations using second-order closure over a grid of discrete volumes with proper boundary conditions applied. We employed the Realizable K- ϵ second-order turbulence closure model for the CFD simulations (Shih et al., 1995). This closure scheme is a modified version of the K- ϵ model that contains a method of calculating turbulent viscosity based on a modifiable constant C_{μ} , dependent on the strain rate of the flow. With this approach, flow regions with high curvature can be better modeled, as determined from validation studies (FLUENT, 2006).

Two features were identified as being critical for proper simulation of dust distribution in the ASL upon entrainment and transport by the rotor wake: proper simulation of the vertical dust profile and proper simulation of shear stress magnitude and position. The simulations were shown to under-predict the vorticity of the forward recirculation zone and ground vortex. This results in wider vortices and lower wind speed values of the upward velocity component in the front lobe of the vortices. The discrepancies between measured and modeled are great enough to suggest that the vertical distribution of dust would be spurious in a simulation using this method. No conclusion can be made considering the distribution and amplitude of shear stress because of the limited measurements made during the experiment. However, it is estimated that it is affected to some degree by the displacement of velocity due to the ground vortex differences, since shear stress is dependent on the velocity of air immediately above the surface.

Lower degree of error with lower airspeeds of the rotorcraft can lead one to assume that the method would be more appropriate at these airspeeds, which would be advantageous since under low forward travel speeds dust emissions approach their maximum (Gillies et al., 2010). Application of the wake results in an air quality model may be appropriate for airspeeds resulting in jet-wake or recirculation wake flow regimes depending on the

acceptable degree of error. Based on these findings, it can be concluded that the method should not be used for higher airspeeds when the wake forms a ground-vortex flow regime.

5.6 PARTICLE PHYSICAL AND MINERALOGICAL CHARACTERISTICS

5.6.1 Preliminary Investigation

Visual inspection of the sieved samples provided evidence of the presence of oxides, such as the red hematite [Fe₂O₃] seen in the four YPG sieved grab samples. Each sample was also tested for carbonate by treating with dilute hydrochloric acid. High calcite [CaCO₃] concentrations in the YPG samples resulted in them being very effervescent, while the YTC and Ft. Carson samples were much less so, evidence of minor amounts of calcite, or dolomite.

5.6.1.1 Polarizing Microscopy

The <38 μm particle size fractions were investigated under a Nikon petrographic microscope, applying the immersion liquid method (Kerr, 1959). The advantage of this method is that major and minor minerals in the dust mixture could be identified, also providing an estimate of their relative abundances. Minerals that were readily identified in the six samples including quartz [SiO₂], plagioclase [NaAlSi₃O₈ – CaAl₂Si₂O₈] and microcline [KAlSi₃O₈] feldspars, biotite mica [K(Fe,Mg)₃AlSi₃O₁₀(OH)₂], and minor mineral components, including chlorite [(Mg,Fe⁺⁺)₅Al(Si₃Al)O₁₀(OH)₈], rutile [TiO₂], zircon [ZrSiO₄], and amphibole [(Ca,Na)₂₋₃(Mg,Fe,Al)₅[(Si,Al)₈O₂₂](OH)₂]. Because of their sub-microscopic particle sizes, calcite, dolomite [CaMg(CO₃)₂], clay minerals and hematite could not be readily identified by this method.

5.6.1.2 X-ray Diffraction (XRD)

X-ray diffraction (XRD) provided an assessment of minerals present in the samples at concentrations greater than ≈2%, the latter being the approximate detection limit for minerals in dust by this technique (Table 8). Both the bulk sieved samples and the PM₁₀ Teflon[®] filter samples of airborne dust collected in the field were qualitatively analyzed by XRD, confirming the presence of quartz, plagioclase, potassium feldspar, and biotite mica, also identified by petrographic microscopy. In addition the mineral species calcite, dolomite, kaolinite [Al₂Si₂O₅(OH)₄], gypsum [CaSO₄.2H₂O], muscovite [KAl₂Si₃AlO₁₀(OH,F)₂], chlorite, pyrolusite [MnO₂] and bismuth [Bi] were identified. The XRD intensities from the PM₁₀ and PM_{2.5} filter samples were quantified, applying the peak intensity ratio method (Chung, 1974), with quartz in the samples acting as an internal standard.

5.6.1.3 Secondary Electron Images

Appendices A to G contain high resolution secondary electron images and energy dispersive spectra (EDS) of mineral grains from each of the sampling sites. These show a variety of crystal forms, including those of quartz, feldspar, biotite, and calcite, as well as aggregates and coatings of clay minerals. Although detailed clay mineral analysis was not performed on these samples, several are evidence for K-Mg-Al-Si particles being a

Table 8. Summary of mineralogical compositions of samples collected during the four sampling campaigns, with estimates of mineral compositions from PM₁₀ filters. Methods by which the minerals had been identified include optical microscopy (o), XRD (x), scanning electron microscopy (s) and chemistry (c).

Sample	Site	Abundance	Minerals (method)	XRD Est. % in PM ₁₀	Diagnostics
1	Yuma 2005, Site 1 #001	Major	Quartz (o, x, s)	22	Conchoidal fracture
			Calcite (x, s, c)	35	Strong effervescence in HCl
			Dolomite (x)	7	
			Plagioclase feldspar (o, x, s)	18	Polysynthetic twinning
			Biotite mica (o)		Brown pleochroic flakes
		Minor	Bismuth (x, s, c)	17	
			Hematite (o)		Red coloration of soil
			Chlorite (o)		
			Gypsum (x)		
			Opaque minerals (o, s)		Bi, Pb, Cu, Ti
			Evaporites (K ₂ SO ₄) (s)		Surface coatings on individual particles
			Potassium feldspar (x)		
			Clay minerals (x, s)		
Gypsum (s)					
2	Yuma 2005, Site 2 #003	Major	Quartz (o, x, s)	32	Conchoidal fracture
			Calcite (x, s, c)	18	Strong effervescence in HCl
			Dolomite (x)	6	
			Plagioclase feldspar (o, x)	36	Polysynthetic twinning
			Potassium feldspar (o, x, s)	8	Polysynthetic twinning
		Minor	Biotite mica (o, x)		Brown pleochroic
			Hematite (o)		Red coloration of soil
			Rutile (o, s)		Needles in biotite
			Opaque minerals (o, s)		Pb, Cu, Ti
			Muscovite (x)		
			Evaporites (K ₂ SO ₄) (s)		Surface coatings on individual particles
			Clay minerals (x, s)		Surface coatings on individual particles
			Gypsum (s)		

Sample	Site	Abundance	Minerals (method)	XRD Est. % in PM ₁₀	Diagnostics
3.	Yakima 2006, Site 2 #010	Major	Quartz (o, x, s)	27	Conchoidal fracture
			Calcite (x, c)	4	Moderate effervescence in HCl
			Plagioclase feldspar (o, x)	51	Polysynthetic twinning
			Biotite mica (o, x, s)	19	Brown pleochroic flakes
		Minor	Amphibole (o)		Green pleochroic prisms
			Pyroxene (o)		
			Muscovite (o, x)		
		Chlorite (o, x)			
		Clay minerals (x, s)		Surface coatings on individual particles	
4	Yuma 2007, Site 1 #025	Major	Quartz (o, x, s)	37	Conchoidal fracture
			Calcite (x, s, c)	11	Strongly effervescent in HCl
			Plagioclase feldspar (o, x)	24	Polysynthetic twinning
			Biotite mica (o, x, s)	16	Brown pleochroic
		Minor	Hematite (o)		Red coloration of soil
			Muscovite (x)		
			Potassium feldspar (x)		
			Chlorite (x)		
			Dolomite (x)		
			Clay minerals (x, s)		Surface coatings on individual particles
		Gypsum (s)			
5	Yuma 2007, Site 2 #029	Major	Quartz (o, x, s)	26	Conchoidal fracture
			Calcite (x, c)	20	Strongly effervescent in HCl
			Plagioclase feldspar (o, x)	12	Polysynthetic twinning
			Potassium feldspar (o, x)	9	
		Minor	Biotite mica (o, x, s)	9	Brown pleochroic
			Hematite (o)		Red coloration of soil
			Muscovite (x)		
			Dolomite (x)		
		Clay minerals (s)		Surface coatings on individual particles	

Sample	Site	Abundance	Minerals (method)	XRD Est. % in PM ₁₀	Diagnostics
6	Ft Carson 2008, Site 1 #035	Major	Quartz (o, x, s)	44	Conchoidal fracture
			Calcite (x, c)	3	Slightly effervescent in HCl
			Dolomite (x)	2	
			Plagioclase feldspar (o, x)	23	Polysynthetic twinning
			Potassium feldspar (o, x, s)	8	Polysynthetic twinning
			Biotite mica (o, x, s)	13	
		Minor	Rutile (o)		Needles
			Muscovite (x)		
			Clay minerals (x, s)		Surface coatings on individual particles
			Gypsum (s)		

clay phase. We interpret rods and fibers occasionally observed, as palygorskite and the platelets as montmorillonite-illite mixed layers montmorillonite or kaolinite.

5.6.1.4 Computer Controlled Scanning Electron Microscopy (CCSEM)

CCSEM was performed on individual aerosol particles collected in the field on Nuclepore® membrane filters (Martello, 2001). CCSEM is a combination of Backscattered Electron Imagery (BEI) and Energy Dispersive Spectroscopy (EDS), which automatically analyzes in a cost-effective fashion a large number (1,000) of individual particles, for particle size, shape, and chemical composition. The particles are grouped in “bins” by chemical composition and particle size. From these chemical measurements, mineralogy of individual particles can be inferred, for example Si particles being quartz and Ca particles being calcite. The concentrations are expressed as percentages of the number of particles in each size bin, and as mass percentages after allowing for particle size and assessing mineral phase densities from the particle chemistry. From each of the sites, one PM₁₀ Nuclepore® filter was analyzed by CCSEM. Summaries of the CCSEM/EDS results from eight sampling sites are given in Table 9 and Fig. 20.

The CCSEM results show a high percentage of clay minerals in all samples, when compared to their XRD and optical results. This is interpreted as quartz and other silicate minerals, as well as dolomite, and calcite particles to a limited degree being coated by clay minerals such as montmorillonite-illite mixed layers, montmorillonite, kaolinite, and palygorskite. The CCSEM provides measurements of surface coatings, but the coatings result in an underestimation of the chemical composition of the complete particle by this technique. This is ascribed to the attenuation of the SEM electron beam, and SEM/EDS results are therefore biased towards the surface coatings, not providing accurate results of the substrate mineral compositions.

Table 9. CCSEM/EDS mineral abundance summaries of PM₁₀ samples on Nuclepore filters. Chemical compositions are re-calculated to mineral abundances, from minerals identified by X-ray diffraction (XRD).

	Y47N001	Y47N003	Y47N007	Y47N010	Y47N025	Y47N029	Y47N035	Y47N041
	Yuma PG	Yuma PG	Yakima TC	Yakima TC	Yuma PG	Yuma PG	Ft Carson	Ft Carson
Mineral	2005	2005	2006	2006	2007	2007	2008	2008
Quartz	2.1	4.7	5.3	5.4	6.3	4.6	9	7.5
Feldspar	1.9	4.1	0.5	0.3	5.7	7.3		1
Clay	31.3	45.8	92.8	92.7	78.2	82.7	83.5	86.7
Carbonate	1.3	7.70	0.1	0.0	5.4	4.4	1.2	2.8
Gypsum	0.9	0.4			2	0	2.6	0
Carbon	0.1	0.3	0.1	0.1	0.3	0.2	1.5	0.1
Evaporite	2.5	15.4	0		0.2	0.1	0	0.1
Hematite		0.3	0.1	1.2	0.2	0.1	0.6	1.2
Bi-bearing	8.8							
Cu-bearing	28.3	2.1						
Pb-bearing	0.0	6.9				0		
Ti-bearing	20.7	8.3	0.1	0	0	0.2	0.1	
Misc	2.2	3.9	1	0.2	1.5	0.4	1.4	0.6
	100	100	100	100	100	100	100	100

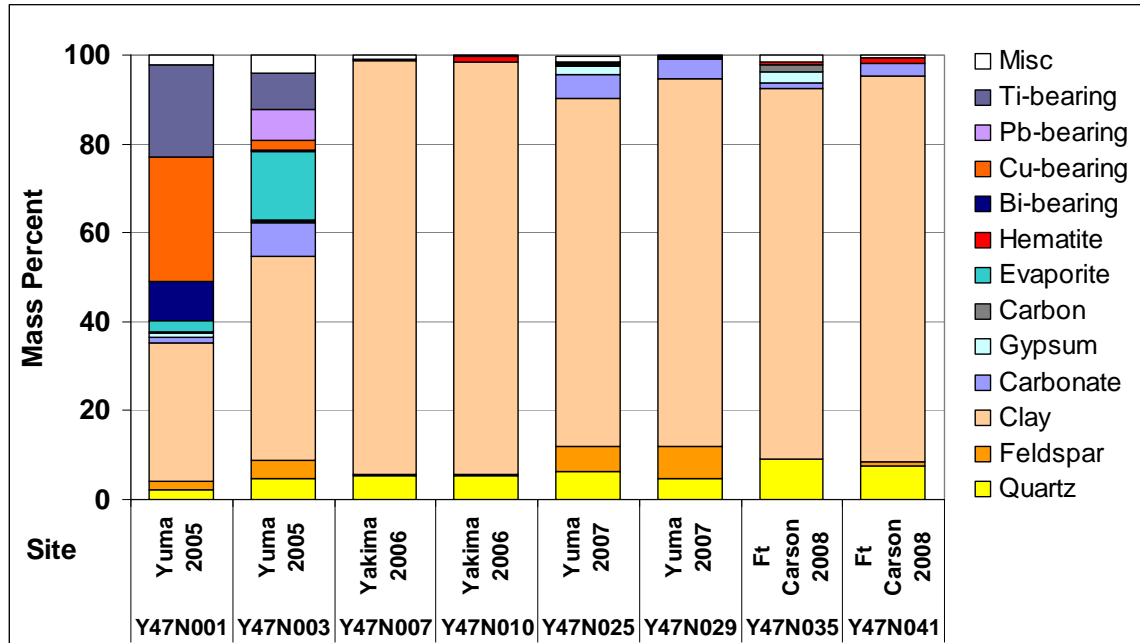


Figure 20. CCSEM/EDS summary plots of PM₁₀ samples on Nuclepore filters. Chemical compositions are re-calculated to mineral compositions, from minerals identified by X-ray diffraction (XRD).

5.6.1.5 Chemical Analysis of Filters

The Teflon® membrane filters were conditioned and weighed prior to and after sampling to measure the mass of particulate matter sampled.

In the course of this study, 20 Teflon® filters, excluding field and laboratory blanks were analyzed by Energy Dispersive X-ray Fluorescence Spectrometry (EDXRF) (Watson et al., 1999) for 32 chemical elements including sodium (Na), magnesium (Mg), aluminum (Al), silicon (Si), phosphorus (P), sulfur (S), chlorine (Cl), potassium (K), calcium (Ca), titanium (Ti), vanadium (V), chromium (Cr), manganese (Mn), iron (Fe), cobalt (Co), nickel (Ni), copper (Cu), zinc (Zn), arsenic (As), selenium (Se), bromine (Br), rubidium (Rb), strontium (Sr), yttrium (Y), zirconium (Zr), cadmium (Cd), tin (Sn), antimony (Sb), barium (Ba), lead (Pb), bismuth (Bi), and uranium (U).

Water extractions were performed on one half of each of the 20 quartz fiber filters. Aliquots of the extractions were analyzed by three methods, (i) by Atomic Absorption (AA) for water soluble cations, sodium (Na⁺), potassium (K⁺), calcium (Ca²⁺), and magnesium (Mg²⁺), (ii) by Ion Chromatography (IC) (Chow, 1999) for water soluble anions, sulfate (SO₄²⁻), nitrate (NO₃⁻), and chloride (Cl⁻), and (iii) by Automated Colorimetry (AC) for the ammonium (NH₄⁺) concentrations.

Punches from the remaining half of each of the 20 quartz fiber filters were analyzed by Thermal Optical Reflectance (TOR) (Chow, 1993) for four organic carbon (OC) and three elemental carbon (EC) fractions, following the Inter-Agency Monitoring of Protected Visual Environments (IMPROVE) protocol (Chow et al., 2001). Separate

punches were acidified by dilute hydrochloric acid, to dissolve carbonate (CO_3^-), and the resultant CO_2 measured as carbonate carbon by the same method. Because of the high carbonate content of most of these soil samples, and the inadequacy of the TOR method to distinguish between or accurately quantify carbonate and organic carbon, carbon results are not further discussed in this report.

The chemical results, calculated as percentages of the measured mass on the Teflon® filters, are presented in Appendix H, with summary plots in Fig. 21.

5.6.1.6 Normative Mineral Calculations

In order to compare the chemical results with the mineralogy characterized by optical microscopy and XRD, “normative” mineral compositions were calculated from the chemical results (Johannsen, 1931). This process involves recalculating the chemical results as mineral compositions, as previously identified by optical microscopy and XRD.

The sequence in which the minerals were calculated, and their compositions, are ammonium nitrate [NH_4NO_3], followed by the six evaporites: potassium chloride [KCl], sodium chloride [NaCl], magnesium chloride [MgCl_2], magnesium sulfate [MgSO_4], potassium sulfate [K_2SO_4], and sodium bisulfate [NaHSO_4], gypsum [$\text{CaSO}_4 \cdot 2\text{H}_2\text{O}$], the feldspars orthoclase [KAlSi_3O_8], albite [$\text{NaAlSi}_3\text{O}_8$], anorthite [$\text{CaAl}_2\text{Si}_2\text{O}_8$], dolomite [$\text{CaMg}(\text{CO}_3)_2$], ferro-actinolite (amphibole) [$\text{Ca}_2\text{Fe}_5\text{Si}_8\text{O}_{22}(\text{OH})_2$], calcite [CaCO_3], biotite [$\text{KFe}_3\text{AlSi}_3\text{O}_{10}(\text{OH})_2$], chlorite [$\text{Fe}_4\text{Al}_2(\text{Al}_2\text{Si}_2\text{O}_{10})(\text{OH})_8$], kaolinite

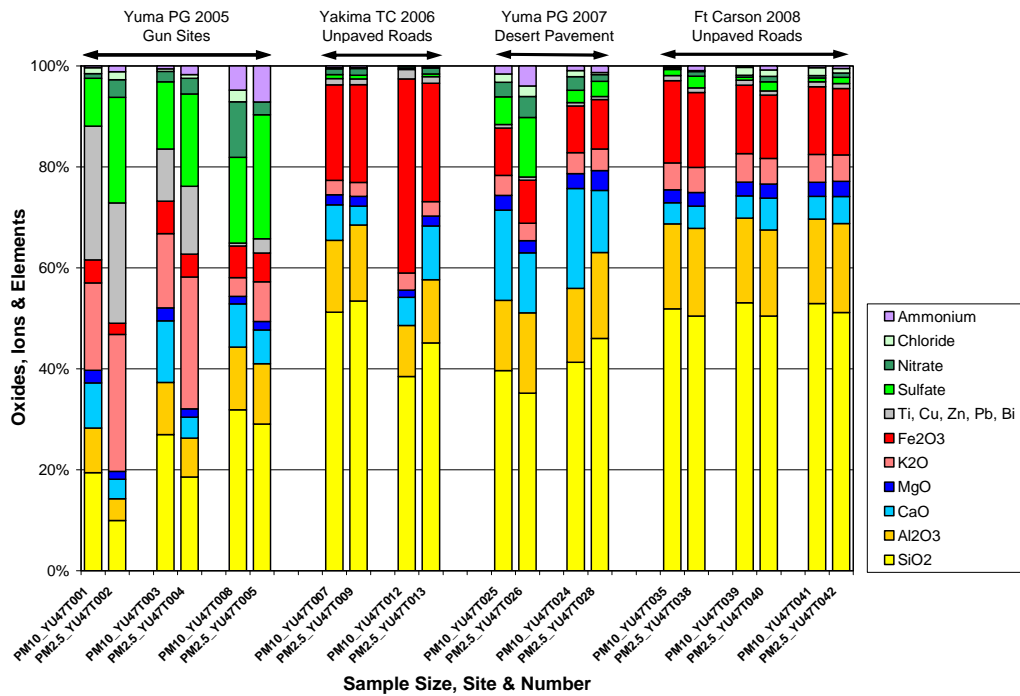


Figure 21. Summary plots of PM₁₀ and PM_{2.5} filter chemical results. The major elements expressed as oxides.

[Al₄(Si₄O₁₀)(OH)₈], quartz [SiO₂], hematite [Fe₂O₃], pyrolusite [MnO₂], rutile [TiO₂], and the metals bismuth [Bi], copper [Cu], lead [Pb], and zinc [Zn].

In this fashion normative mineral compositions (Fig. 22) are substituted for the raw chemical results (Fig. 21), providing a mineralogical inter-comparison of the sample sets from the four sampling campaigns.

5.6.2 Particle Characterization at Field Sites

5.6.2.1 Yuma Proving Ground (YPG), Arizona (2005)

Ambient and grab samples were collected at three gunsites during artillery deployment (Gillies et al., 2007). To suppress the dust and subsequently limit dust emissions from the gun backblast, the gun-pads had been treated with brine containing dissolved potassium sulfate [K₂SO₄] and other evaporites. This is evident from encrustations on most aerosol particles collected during this sampling campaign (Appendices B and C). The major mineral components as measured by XRD, CCSEM, SEM, and observed optically (Table 9, Samples 1, 2) at the gun-sites include quartz [SiO₂], calcite [CaCO₃], and plagioclase feldspar [NaAlSi₃O₈ – CaAl₂Si₂O₈], with lesser amounts of orthoclase feldspar [KAlSi₃O₈], biotite [K(Fe,Mg)₃AlSi₃O₁₀(OH)₂], dolomite [CaMg(CO₃)₂], and gypsum [CaSO₄.2H₂O]. Some particles, if not encrusted by potassium sulfate (Figs. 20 and 23), have microscopically thin surface coatings of clay minerals and hematite, similar to desert varnish on chemically weathered rock surfaces (Potter and Rossman, 1977). The compositions (Si-Al-Mg-Fe-K) of the particle coatings as measured by CCSEM/EDS and SEM/EDS point to the clay mineral in most instances being montmorillonite-illite mixed layers, with kaolinite in a few cases. A summary plot (Fig. 20, first two stacked bars), and Table 9 of the CCSEM results shows the high concentration of metals as well as the surface coatings of potassium sulfate and clay minerals on individual particles.

Of note at the three gun-sites is the abundance of metallic particles that are likely from military activities. These vary in composition, from bismuth [Bi]-copper [Cu]-titanium [Ti]-lead [Pb] in varying proportions at gun-site 1, to particles without the bismuth at the other two gun-sites. In a few instance the metal particles also contained zinc [Zn]. It is evident that these minute globules of mixed metals are from percussion caps, propellants, missiles, or other components of artillery ordnance.

The chemical results for both PM₁₀ and PM_{2.5} size fractions, from the Teflon[®] and quartz fiber filters, for the three gun-sites are tabulated in Appendix H along with their normative mineral compositions. As can be expected, filter results from all three sites show high concentrations of water soluble sulfate [SO₄⁻] and potassium [K⁺], from the dust suppressant (brine) sprayed on the gun-pads. Both the sulfate and potassium are highest for gun-site 1, with 5.0% sulfate and 6.8% water soluble potassium for the PM₁₀, and 14.0% sulfate and 15.5% water soluble potassium for the PM_{2.5} fraction.

Both gun-sites 1 and 2 filter samples have high concentrations of copper, varying from 3.1% to 6.7% by mass. The bismuth found only at gun-site 1, varied between 4.7% in PM₁₀ to 8.3% in PM_{2.5}, implying that this metal is concentrated in the finer fraction, possibly formed by the condensation of metal vapors during artillery operations.

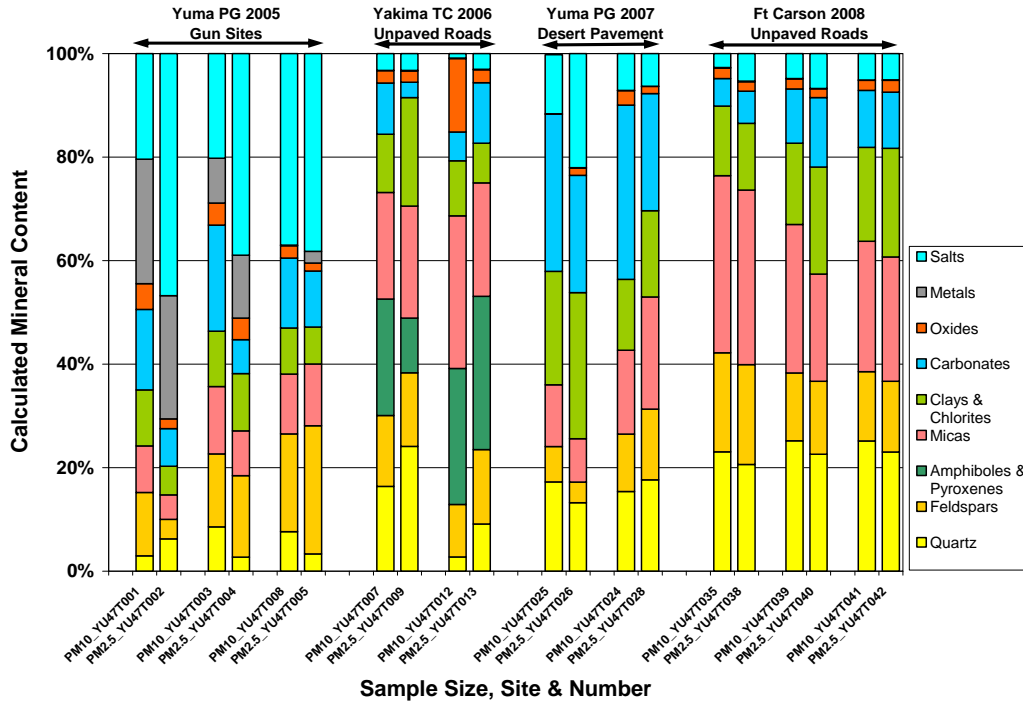
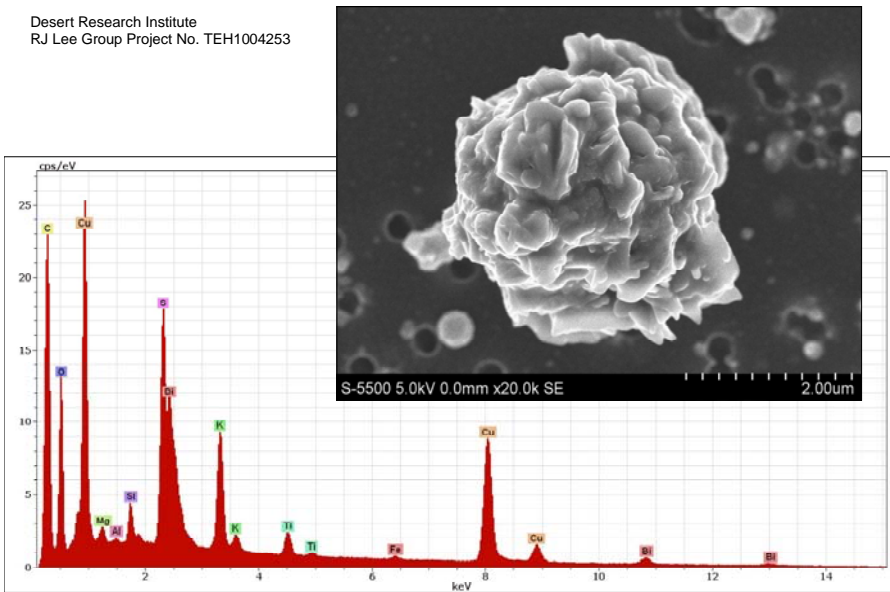


Figure 22. Summary plots of PM₁₀ and PM_{2.5} filter results. Normative mineral abundances calculated from chemical results, and minerals identified by X-ray diffraction (XRD).

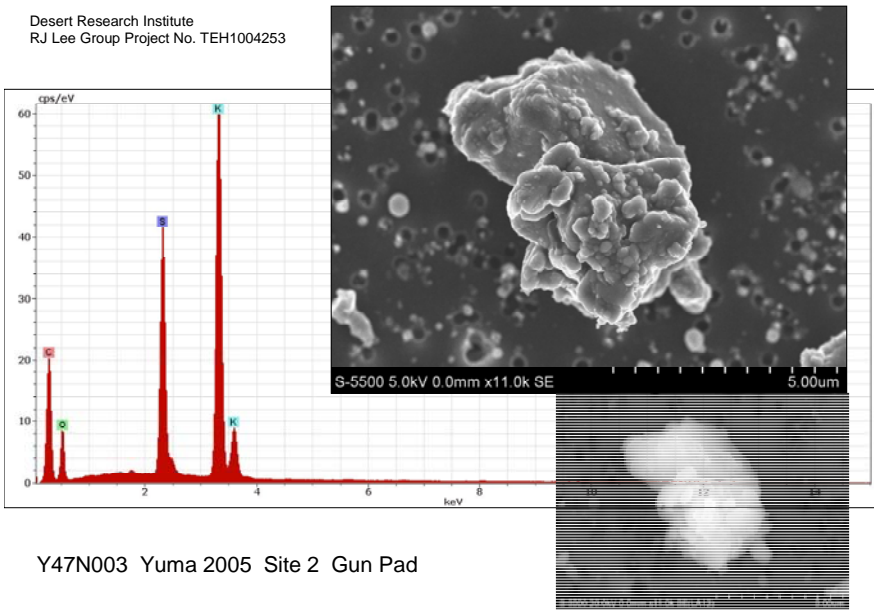
In order to compare the samples from each of the three sites, a normative mineral content (Fig. 22) (Johannsen, 1931) for each sample set was calculated from its chemistry, identified mineralogy (XRD, optical) and observed electron optical properties. In comparison to the samples from the other three campaigns, the dusts from the gun-sites are low in the mineral quartz, but high in evaporites (K₂SO₄ and other soluble salts), and metals (Bi, Cu, Pb, Ti).

5.6.2.2 Yakima Training Center, Washington (2006)

Sediments from the test area are underlain by the Columbia River Basalts, and contain mafic minerals typical of this volcanic domain. The abundance of primary mafic minerals also points to partial chemical weathering, and an immature soil development. Phases identified by XRD and/or optically in the colluvial hillside deposit include plagioclase feldspar, quartz, and biotite, together with smaller amounts of green pyroxene [Ca(Mg,Fe)Si₂O₆], green pleochroic amphibole [Ca₂Fe₅Si₈O₂₂(OH)₂], green chlorite, muscovite, and clay minerals (Table 9, Sample 3). Quantitative XRD of the filter samples show plagioclase to be more than 50% of the mineral mass on the PM₁₀ filter, together with major amounts of quartz (27%) and mica (19%).



(a)
Sample Y47N001,
Yuma 2005
Gunpad Site 1
Copper-bismuth
particle with surface
coating of potassium
sulfate.



(b)
Sample Y47N003,
Yuma 2005
Gun pad, Site 2
Thick coating of
potassium sulfate on
unknown (silicate?)
mineral.
Backscattered
electron image (BEI)
shown on bottom
right.

Figure 23. SEM secondary electron images and EDS spectra of particles collected on Nuclepore filters. Samples from YPG gun pad sites collected in 2005. The pore sizes in the Nuclepore membrane filters are approximately 0.4 μm.

As for some of the YTC sites, all silicate particles have microscopically thin surface coatings of clay minerals (Figs. 20 & 24, Table 9, Appendices D, E). The compositions (Si-Al-Mg-Fe-K) of the particle coatings as measured by CCSEM/EDS and SEM/EDS point to the clay being montmorillonite, montmorillonite-illite mixed layers, or kaolinite. Sub-micron size spheres of carbon, possibly vehicle combustion products were also found in these samples. A summary plot (Fig. 20, third and fourth stacked bars), and Table 9 of the CCSEM results show that nearly all particles in these samples have clay mineral coatings.

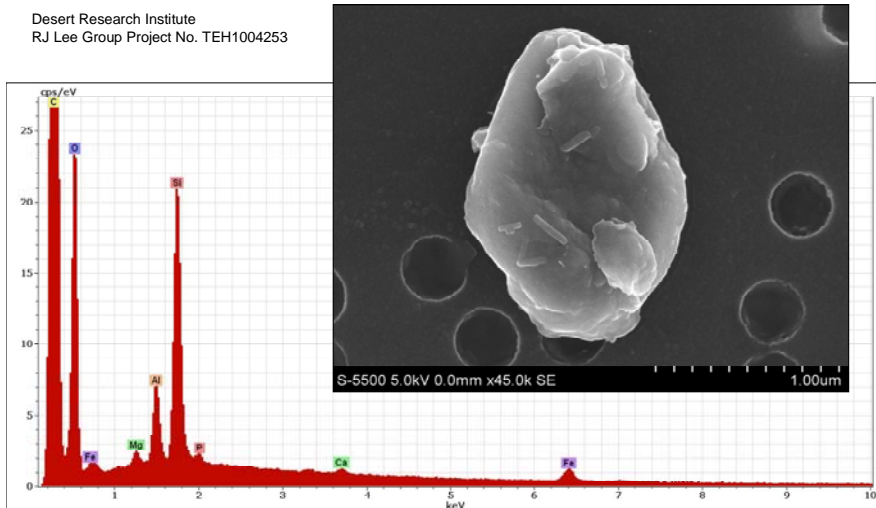
The samples differ from those of YPG, by having less than 0.1% calcite (Table 8) and not enough hematite on the particle surface coatings to provide a red coloration. The khaki coloration of the YTC dust is ascribed to the green amphibole and pyroxene, as well as minor amounts of chlorite.

The chemical results, for both PM₁₀ and PM_{2.5} size fractions, from the Teflon[®] and quartz fiber filters for the YTC dirt road sites are tabulated in Appendix J (c, d), and the normative mineral compositions are tabulated in Appendix H (f). Summary plots (Fig. 22) show variable high concentrations of Si (2.7-17.0%), and Fe (4.0-9.23%) for the YTC sample sets. Normative minerals (Fig. 22, Appendix H (f)), include amphibole, biotite, plagioclase, and lesser amounts of carbonates, and clay minerals as particle coatings.

5.6.2.3 Yuma Proving Ground (2007)

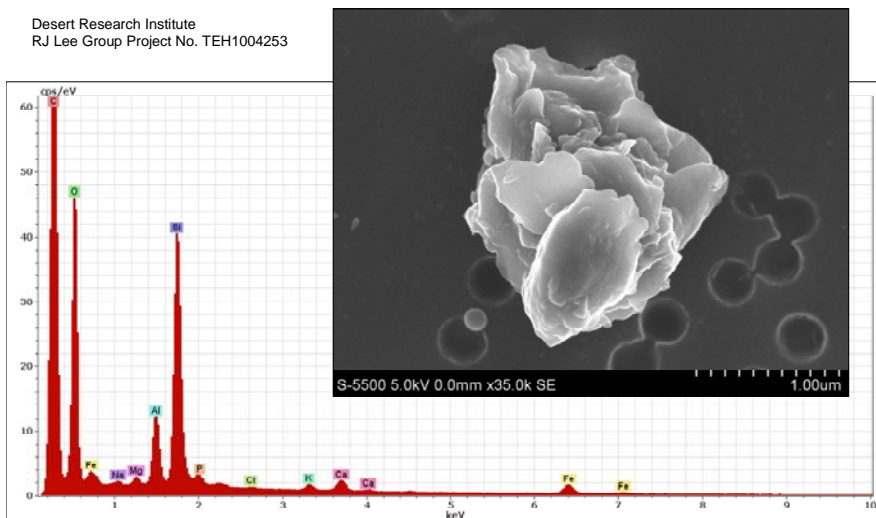
These red colored desert pavement samples are mineralogically similar to those collected at the gun-sites in 2005, but without the potassium sulfate from the soil treatment, and without the metal particles from the artillery activities. They are similarly very effervescent in dilute hydrochloric acid, pointing to high concentrations of calcite. Quantitative XRD (Table 9, Samples 4, 5) confirms major amounts of quartz (26-37%), calcite (11-20%), plagioclase feldspar (12-24%) and biotite mica (9-16%), with minor amounts of potassium feldspar, muscovite, chlorite, dolomite, gypsum, clay minerals and hematite, the latter two, often as surface coatings on the silicate mineral grains (Figs. 25 & 20 stacked bars five and six, Table 9). From the SEM images and EDS (Appendices D, and E), the clay minerals have been identified as montmorillonite-illite mixed layers, with occasional needles of the palygorskite. These samples also contain carbon particles, some with bowl-shaped fingers, probably of biogenic origin (see Appendices D and E).

The chemical results, for both PM₁₀ and PM_{2.5} size fractions, from the Teflon[®] and quartz fiber filters, for the two YPG desert pavement sites are tabulated in Appendix K (c), with summary plots in Fig. 25. The filter samples have high concentrations of Si (9.4-13.5%), Ca (4.2-7.1%), Fe (3.4-4.3%) and Al (4.0-5.6%). A normative mineral content for each sample set was calculated (Fig. 22, Appendix H (f)) to include carbonates (mostly calcite), clay minerals, biotite and quartz.



(a)
Sample Y47N007,
Yakima 2006
Dirt road, Site 1
Flake of possibly
biotite, with coating
of clay minerals,
possibly
montmorillonite, and
needles of the clay
mineral palygorski

Y47N007 Yakima 2006 Site 1 Dirt Road



(b)
Sample Y47N010,
Yakima 2006
Dirt road, Site 1
Flakes of clay
minerals, possibly
montmorillonite

Y47N010 Yakima 2006 Site 1 Dirt Road

Figure 24. SEM secondary electron images and EDS spectra of particles collected on Nuclepore filters. Samples from YTC dirt roads collected in 2006. The pore sizes in the Nuclepore membrane filters are approximately 0.4 μm .

5.6.2.4 Ft. Carson, Colorado (2008)

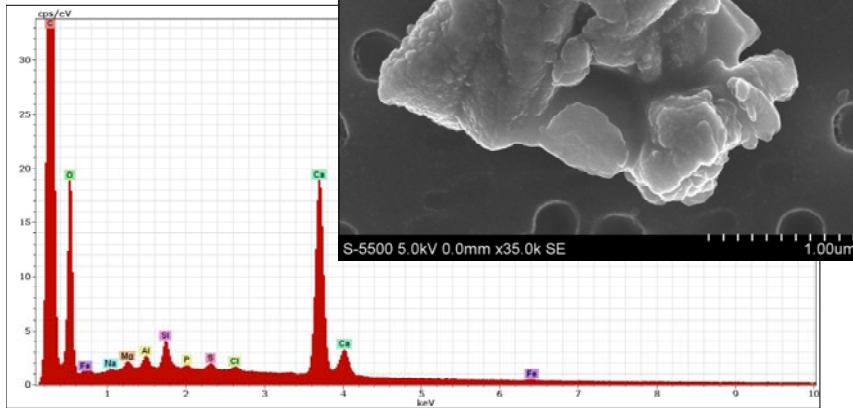
The khaki colored dust samples from unpaved roads show slight effervescence with dilute hydrochloric acid, pointing to a low concentration of calcite and perhaps some dolomite, also confirmed by XRD (Table 9, Sample 6). The samples contain major amounts of quartz (44%) as well as plagioclase and potassium feldspars, together comprising more than 30% of the aerosol, and biotite. Minor minerals include dolomite, rutile, muscovite, gypsum, and clay minerals (montmorillonite-illite mixed layer) as surface coatings (Figs. 20 & 26, Appendices F, G). Elemental carbon chains identified by SEM/EDS (Appendix F(h, k), and G(b)) are evidence of combustion processes, possibly from diesel powered vehicle emissions.

The six Ft. Carson samples are chemically (Appendix H(d)) and mineralogically (Appendix I(g, h)) similar to each other, with major components of Si (10.9-12.3%), Al (4.1-4.7%), and Fe (4.2-5.4%). The major normative minerals in the sample sets from Ft. Carson are quartz, biotite, plagioclase and orthoclase feldspars, and dolomite.

5.6.3 Particle-Size Distributions of PM at the Field Sites

Particle-size distributions were obtained from the CCSEM data files (Appendix I). The measurements were performed on particulate matter on Nuclepore[®] filters collected after a PM₁₀ size-selective inlet, preventing the accurate measurement of particles greater than 10 µm in aerodynamic diameter. Appendix I shows the results in each chemical and size bin. The classification is shown both by the number of particles, and by a calculated mass of each species per bin. Figure 27 shows that the largest number of particles falls in the <2 µm size fraction, while by mass the largest proportions lie in the 2.0 to 5.0 µm size range (Fig. 28). Most soil forming silicate and oxide minerals fall in the latter identified size range (Appendix I). In most instances the distributions are approximately uni-modal, except for the two Yuma 2005 samples (Y47N001/N003) where the number distributions (Fig. 27) are strongly positively skewed towards the 0.2 to 0.5 µm size bin. For these two samples the mass distributions are bimodal, with one mode falling in the 2.0 to 5.0 µm and the second in the 10 to 15 µm size range. Differences in the YPG 2005 samples from the other three sampling campaigns are principally the large numbers of metallic [Bi, Pb, Cu] particles (Appendix I(a, b)) in the less than 1.0 µm size bin. These metals and the associated carbon [C] are likely from the artillery barrel emissions (Gillies et al., 2007). The minerals falling in the 10 to 15 µm size range are largely coarse quartz (Si-rich) and clays (Al-Si), as well as titanium mineral clusters (rutile) (Appendix A) associated with the gun backblast sites.

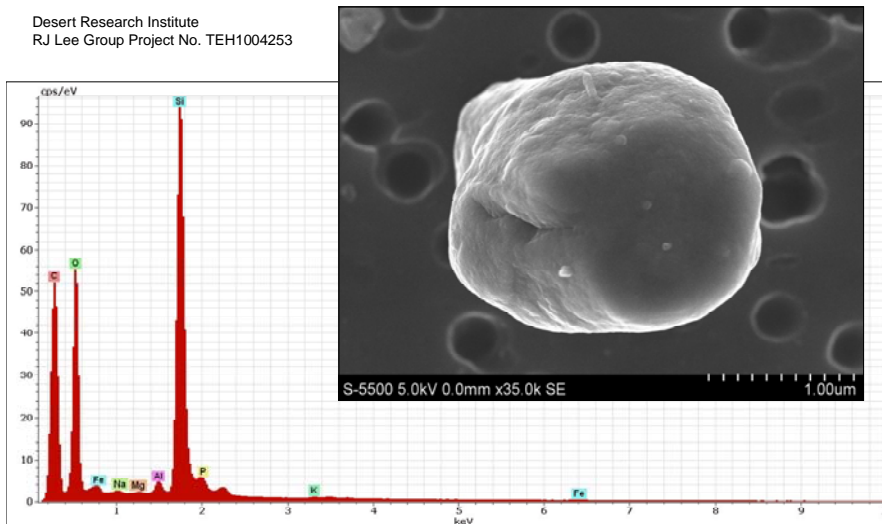
Desert Research Institute
RJ Lee Group Project No. TEH1004253



Y47N025 Yuma 2007 Site 1 Desert Pavement

(a)
Sample Y47N025,
Yuma 2007
Desert Pavement,
Site 1
Rhombohedral crystal
crystal of calcite with
dissolution cavities
and surface re-
crystallizations

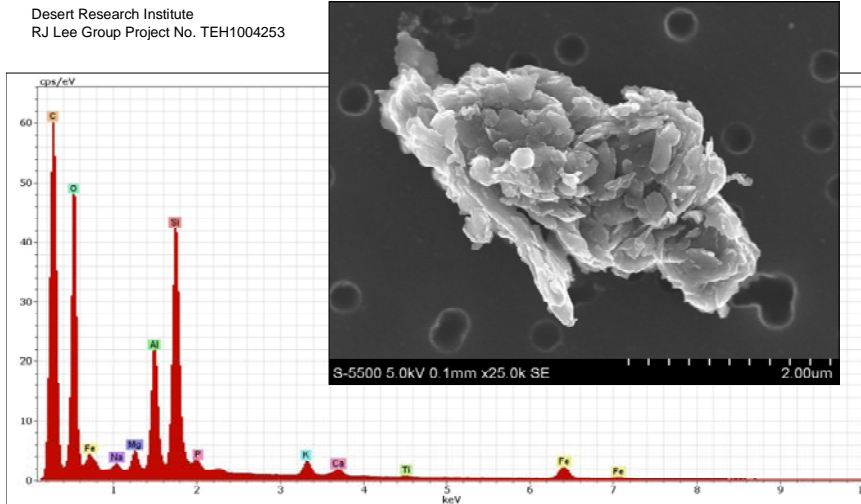
Desert Research Institute
RJ Lee Group Project No. TEH1004253



Y47N025 Yuma 2007 Site 1 Desert Pavement

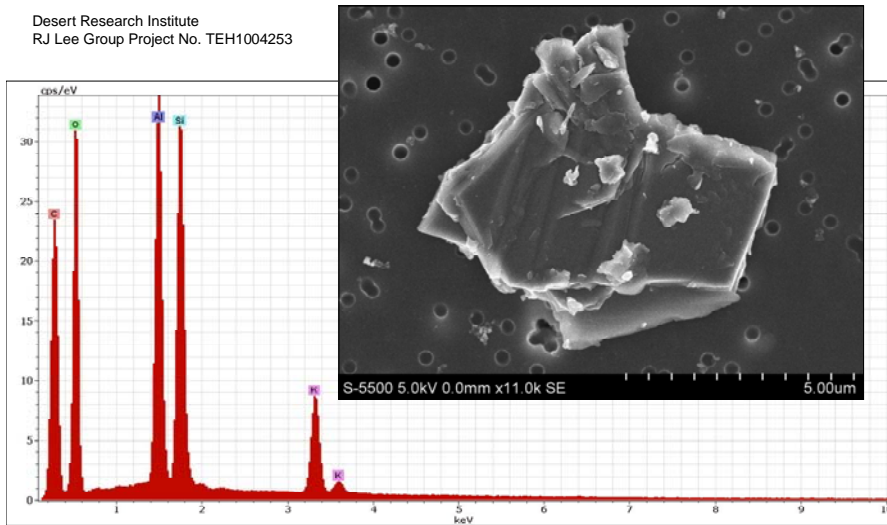
(b)
Sample Y47N025,
Yuma 2007
Desert Pavement,
Site 1
Rounded particle of
quartz with minor
amount of clay
mineral

Figure 25. SEM secondary electron images and EDS spectra of particles collected on Nuclepore filters. Samples from YPG desert pavement collected in 2007. The pore sizes in the Nuclepore membrane filters are approximately 0.4 μm .



(a)
Sample Y47N035, Ft
Carson 2008
Dirt road, Site 1
Platelets of the clay,
possibly
montmorillonite-illite

Y47N035 Ft Carson 2008 Site 1 Dirt Road



(b)
Sample Y47N041- Ft
Carson 2008
Dirt road, Site 2
Potassium feldspar
crystal, showing
twinning lamellae,
and few clay
particles attache

Y47N041 Ft Carson 2008 Site 2 Dirt Road

Figure 26. SEM secondary electron images and EDS spectra of particles collected on Nuclepore filters. Samples from Ft. Carson dirt roads collected in 2007. The pore sizes in the Nuclepore membrane filters are approximately 0.4 μm .

Surface coatings on the quartz and other silicate particles, often of montmorillonite-illite mixed layers were found to be abundant in all samples. In the case of the YPG 2005 and 2007 samples, the red coloration of the dust is ascribed to iron oxides (hematite or goethite) mixed into the clay mineral coatings, providing a sub-microscopic desert varnish (Potter and Rossman, 1977). SEM analysis of carbonate mineral (i.e., calcite and dolomite) particles found no or very little clay coatings, evidence that clay does not easily adhere to carbonate. In the case of the YPG 2005 samples, the particles are coated by evaporites, largely potassium sulfate, from brine sprayed onto gun-pads as a dust suppressant.

The Yakima samples (Y47N007/N010) differ from those from the other sites, in that they contain a high fraction of un-weathered minerals of igneous origin, including plagioclase, amphibole, and pyroxene, and very little secondary carbonate (calcite, dolomite). As measured by CCSEM, these samples have the largest particle fractions (93%) coated by clay (Table 9, Appendices C, I(c, d)).

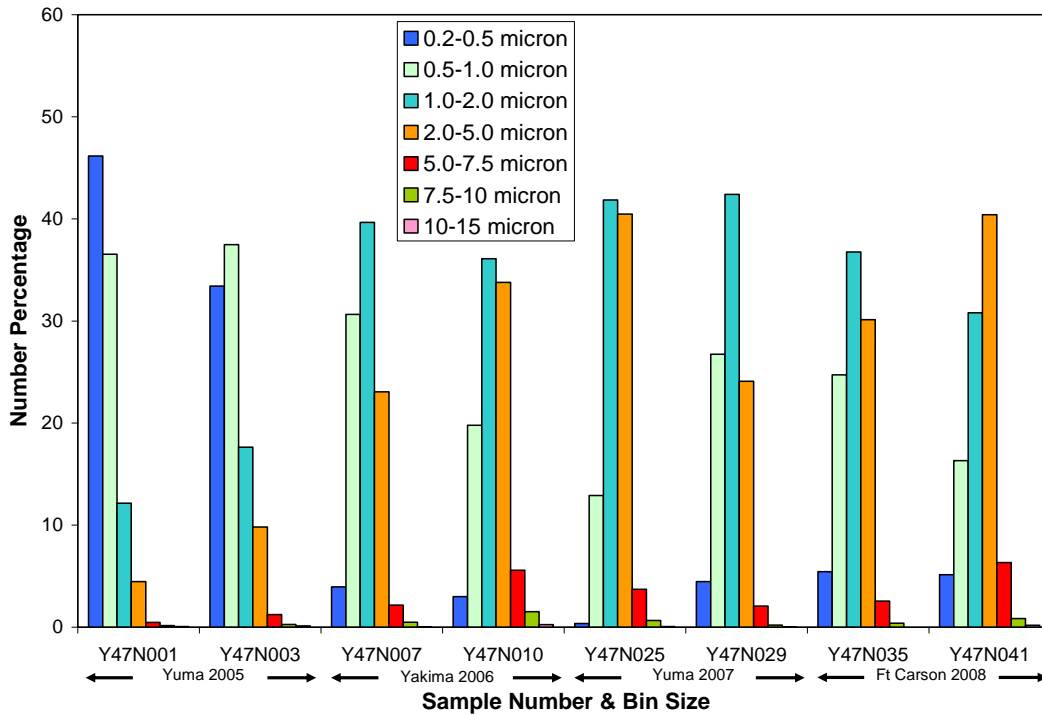


Figure 27. CCSEM measured particle number distributions per size bin from PM₁₀ Nuclepore filters.

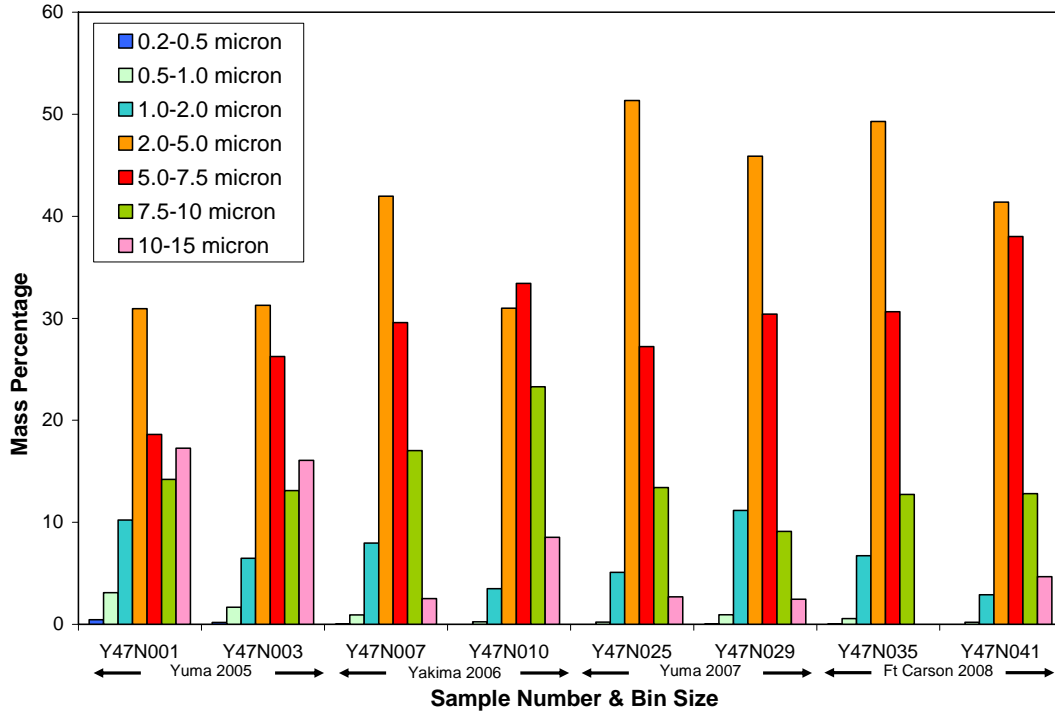


Figure 28. CCSEM measured particle mass distributions per size bin from PM₁₀ Nuclepore filters.

5.7 HYBRID REMOTE SENSING AND IN-SITU MEASUREMENT SYSTEM TO MEASURE FUGITIVE DUST FLUX

The hybrid measurement system for fugitive emission characterization was initially tested during the rotary-winged aircraft measurement field campaign at YPG, in May 2007. Subsequently the validity of the new dust monitoring method was demonstrated with data collected as part of the tracked vehicle measurement campaign at Ft. Carson in October 2008. These campaigns provided us with an abundance of OP-LT and DM measurement data to test and validate the new method. The measurements were event-based with each dust plume originating from the aircraft or tracked vehicle as it passed the instrument array. The PM and extinction data were recorded as the dust plume passed through the measurement plane.

The OP-LT measures the path-integrated extinction (PIE) given by:

$$\text{PIE}^{\text{LT}} = \int_0^L \varepsilon(y) dy \quad (10)$$

where $\varepsilon(y)$ is the extinction value at a location y along the beam path; L is the beam-path distance from the OP-LT sensor to the retro-reflector. For fixed particle composition and size distribution, the path-averaged extinction, PAE: PIE^{LT}/L , is proportional to the path-averaged dust concentration.

The OP-LT is calibrated by performing a linear regression fit of the path-averaged extinction to the average value of the PM₁₀ measurements by the DM instruments,

distributed along the cross-plume OP-LT beam path $C_y^{\overline{DM_{10}}}$, to compute the calibration factor, $F^{\overline{DM_{10}}}$

$$C_y^{\overline{DM_{10}}} = F^{\overline{DM_{10}}} PAE^{LT} \quad (11)$$

At YPG 1840, 1 s dust plume measurements were collected for 32 plume events. For YPG measurements the 1 s PM_{10} concentration data (calibrated to gravimetric filter-based measurements) from the lowest DMs (situated along the OP-LT beam path) were spatially averaged ($C_y^{\overline{DM_{10}}}$) and synchronized against the path-averaged extinction. The Pearson correlation was calculated for each event and six events out the total 32 had a Pearson correlation >0.9 (Fig. 29). The other 26 events had Pearson correlation values between 0.6 and 0.9, which indicates a less homogeneous plume along the LT path length. Figure 30 shows the calibration data from all events (32 events, 1840 points) as well as just the six events with the highest correlation between the three DMs averaged PM_{10} concentration and the OP-LT path-averaged extinction (Fig. 29).

The slope coefficient of this linear plot for the full data set, which is the calibration factor, F^{DT-LT} , is 551 mg m^{-2} and the R^2 , the square of the Pearson correlation coefficient, has a value of 0.69. As one may expect, reducing the data set to the six high-correlation events results in much less scatter in the linear plot (Fig. 30b). The linear plot of just the six highest-correlated events resulted in the improved R^2 value of 0.83 and a calibration factor of 592 g m^{-2} . The six highly correlated events represent the case when the plume is most evenly distributed along the OP-LT beam path and conditions are

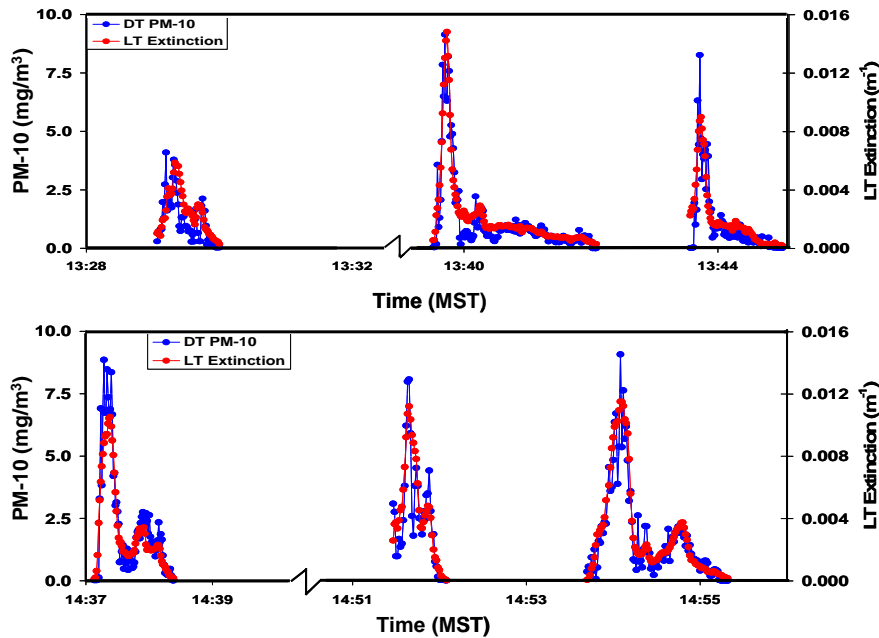


Figure 29. OP-LT calibration measurements made at YPG - The six dust events with high dust correlations ($R>0.9$).

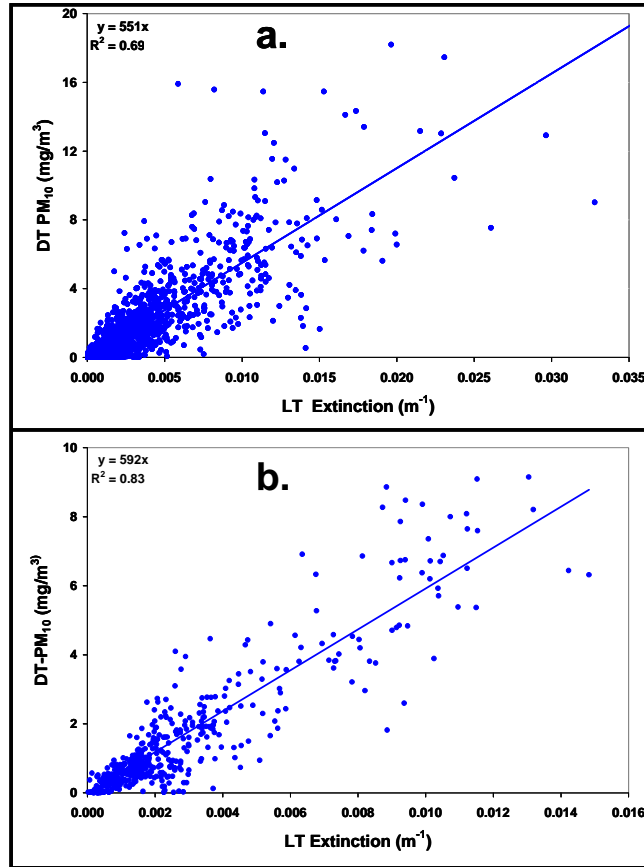


Figure 30. Plot of the OP-LT and DM PM₁₀ calibration measurements. a) The full 1840-point data set, and b) the six high-correlation events (508-point) data set.

favorable for such a calibration procedure. It is not necessary to use any preset number of DM monitors along the OP-LT beam path as long as there are a large number of data sets with Pearson correlation coefficients >0.9 , and an overall $R^2 >0.8$ in the linear regression calibration curve.

At Ft. Carson the second by second correlation between the OP-LT extinction and average (3 bottom DT PM₁₀ monitors) PM₁₀ concentrations for each event was quite poor ($R < 0.5$). This may be due to the type of fugitive dust source (track vehicle). Therefore, the calibration curve was generated event by event for 20 events on September 16th 2008. Figure 31 shows a very strong correlation and a calibration factor almost identical to that of the Yuma tests. This calibration factor (593 mg m^{-2}) was used for the dust PIMC calculations for the hybrid method.

The fifteen DM₁₀s form a 3×5 grid of point measurements that defines the measurement area, A, as a 105 m wide by 10 m high plane. The plane integrated PM₁₀ mass concentration ($\text{PIMC}_{10}^{\text{Grid}}$) is calculated as the product of the mean value of the 15 DM₁₀s for the three towers and the area A:

$$\text{PIMC}_{10} \cong \overline{\text{DM}_{10}^{\text{Grid}}} A \quad (12)$$

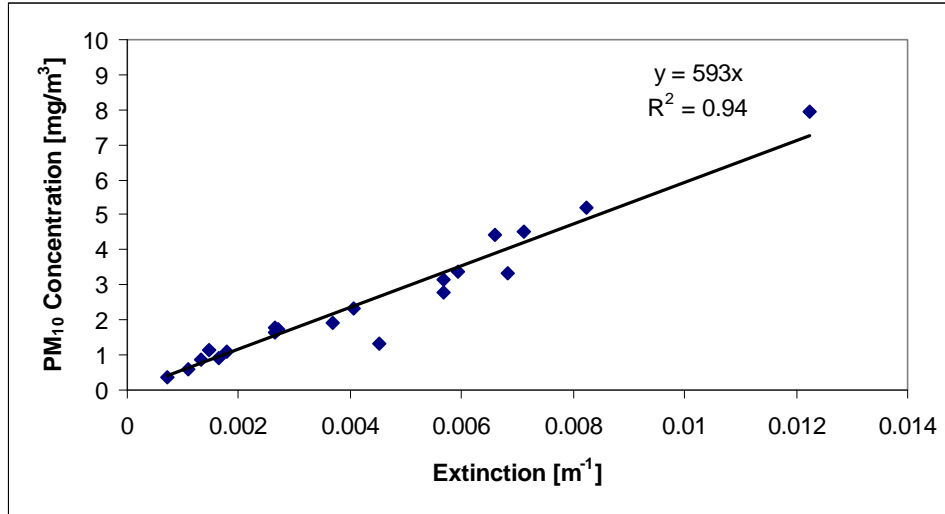


Figure 31. Plot of the OP-LT and DM PM₁₀ calibration measurements at Ft. Carson by event.

The configuration used at YPG has the elements required for applying the hybrid method if towers one and three are ignored. The calculation of $PIMC_{10}^{Grid}$ can be compared to the PIMC₁₀ hybrid method (i.e., Eq. 7) by performing a linear regression for all 32 rotary-winged plume events. We tested the effect of reducing the number of DM pairs on the PIMC₁₀ emission estimate, the results of which are shown in Fig. 32 for three cases: five, three, and two DM₁₀s. These results indicate that the new method (OP-LT and DM hybrid) to calculate PIMC₁₀ (equivalent to flux for the same wind conditions) values is comparable (slope close to one with $R^2 > 0.85$) to the calculation of $PIMC_{10}^{Grid}$. Also, it is shown that the use of five DM instruments on the tower for the hybrid method is not required, as similar results can be obtained by using only two or three DM instruments, which simplifies the instrumentation set up and logistics of deployment, making this method an attractive alternative to the more costly emission profiling method.

At Ft. Carson the variability in the DT data, for the tracked vehicles, was much larger than the rotary-wing data, and there was no one event that the Pearson correlation was larger than 0.5 between the LT and DT data (see 6 events in Fig. 29 for the rotary wing source tests). Therefore it is expected that the agreement between the Grid and the Hybrid method will be worse and the regression R^2 will be also quite poor. However, the results are quite comparable as can be seen in Fig. 33. It is observed that the agreement is better with four and three DT monitors on the middle tower but the correlation is the best for two DT monitors on the middle tower.

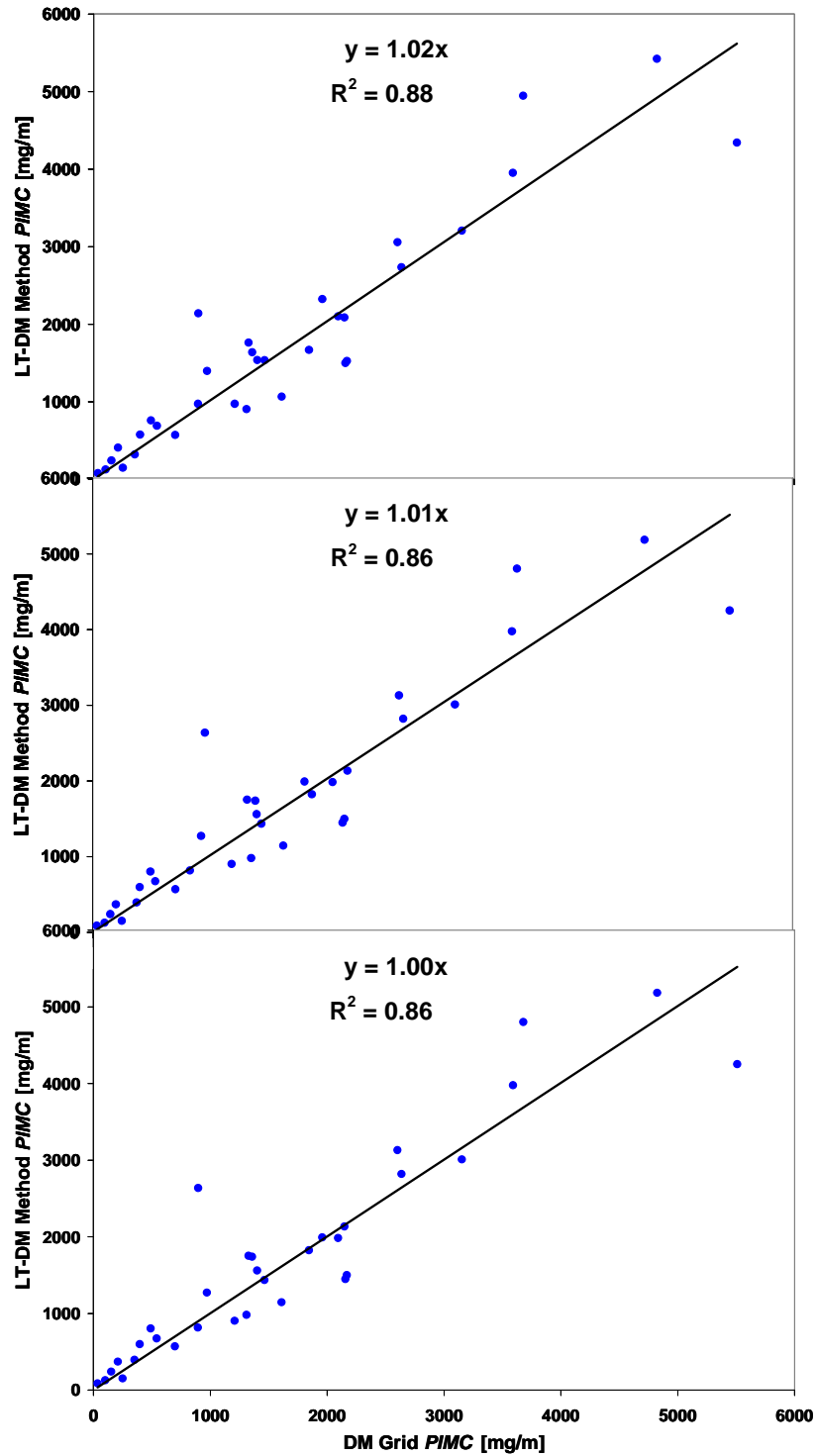


Figure 32. Comparison of PIMC determined with the new method to the PIMC determined from the grid of DT monitors. Top: five DT monitors in new method, middle: three DT monitors in new method, bottom: two DT pairs in new method.

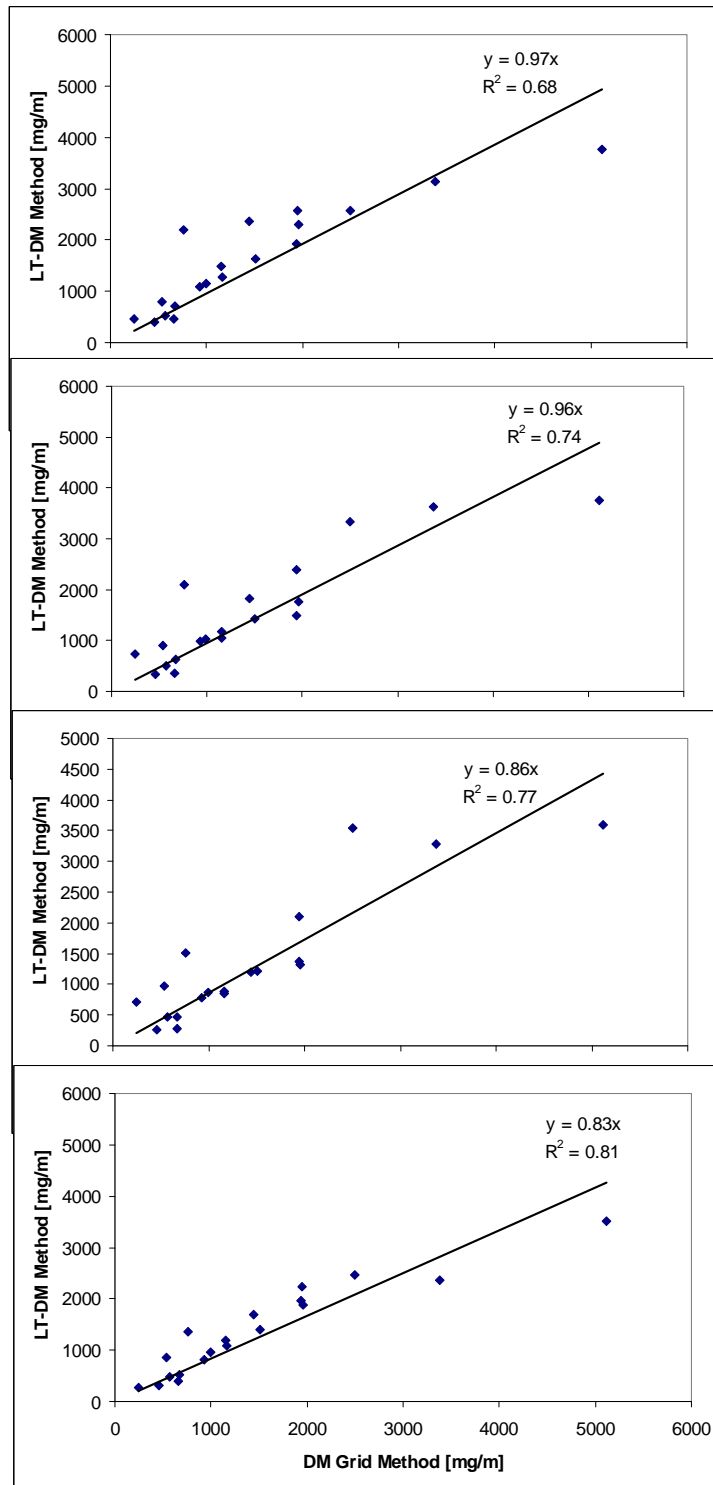


Figure 33. Comparison of PIMC determined with the new method to the PIMC determined from the grid of DT monitors for 20 events at Ft. Carson. Top: four DT monitors in new method, second and third from top: three DT monitors in new method (1, 2, 4 and 1, 3, 4), bottom: two DT pairs in new method.

5.8 RESULTS: DUSTRAN

PNNL activities involving the atmospheric dispersion modeling system DUSTRAN for the SERDP Unique Dust Emissions Project SI-1399 focused on improvement of the already substantial user-friendliness of DUSTRAN in addition to accommodating artillery backblast and tank activities as dust sources. Highlights include the following:

- Initial development on DUSTRAN to add a new tab under the point source input window to include the dust emission factors from artillery backblast. Based upon the input form used for wheeled vehicles, this new tab will allow users the ability to enter input data for artillery activities including times fired, zone charge, and bore size. Initial modifications have also taken place on the vehicle tab to include the ability to select tracked vehicles such as the M1A1 Abrams as well as the current wheeled vehicles. New data displayed as input in the window will include information concerning the tracks of the vehicles such as track width and pad length and pad width.
- Two modules to provide automated checks and conditioning of input meteorological data required for DUSTRAN simulations were developed, tested, and integrated into the DUSTRAN system. The CALMET meteorological model of DUSTRAN requires certain surface and upper air information in a specific input format, the surf.dat and up.dat files, respectively. DUSTRAN automatically generates these CALMET-required files from either user-specified meteorological information or from National Weather Service data captured using the MetArchiver tool, a DUSTRAN utility developed in 2006. Now two new FORTRAN-based executables, “SURFCheck” and “UPCheck,” perform a series of range checks against the meteorological data as well as ensuring that all of the required upper-air and surface observations are present. These checks are particularly important when real-time meteorological data are being used. The two new modules serve to make DUSTRAN even more user-friendly by preventing the sudden termination of DUSTRAN simulations due to missing or erroneous meteorological data.
- The DUSTRAN modeling system and interface were modified to allow a user the ability to specify many point-source locations via a file (XML text) rather than just specifying by graphical means through DUSTRAN maps. The source file is read and automatically adds the sources to an ongoing simulation as well as creating a default “unit” release for each of the source locations. With the unit release specified for each source, DUSTRAN can be immediately run displaying the plume footprint of potential emissions from these points. This modification improves the user-friendliness of the DUSTRAN system by automating a potentially time-consuming user-input task. Graphical output was also modified to allow the display of simulation results from the different sources in varying colors, permitting easy identification of which sources are most directly impacting a particular receptor region.
- The MetArchiver tool, a utility developed in 2006 to automate the tasks of locating and preparing either historical or real-time meteorological data for DUSTRAN simulations, underwent several modifications and improvements. The tool was originally developed to obtain upper-air and surface meteorological data from the

National Oceanic and Atmospheric Administration's websites and store these data in a local database. This year the MetArchiver application and database were modified to allow the downloading and processing of data from localized meteorological networks, greatly increasing the number of potential sources for real-time meteorological information. The database file used by the MetArchiver application was expanded to include more station-specific information as well as more types of meteorological data. The expanded database file includes time zone, station elevation, anemometer height, and standard deviation of wind speed and direction. Additionally, a "station characteristics" file now can be used to import information on upper air and surface stations into the MetArchiver tool. This file contains a list of stations and their characteristics, such station identification, latitude, longitude, elevation, and anemometer height, and, as a comma separated text file, is extremely easy for a user to generate. Lastly, the MetArchiver tool was modified to allow the import and export of the upper-air and surface station name files (UNF and SNF) used by the DUSTRAN modeling system. With this modification, the system now automatically creates the meteorological station files required by DUSTRAN for a new simulation site as well as automatically updating the MetArchiver station fields for existing site station files. All of these changes together serve to improve and expand the user-friendliness of both the MetArchiver utility and the overall DUSTRAN system.

- It was discovered that wind vectors displayed at meteorological station locations were not being scaled in the same manner as the wind vector fields created by the CALMET model. Although this situation did not affect winds used in dispersion routines and thus did not affect predicted concentrations, scaling was modified so that all displayed wind vectors are scaled in a consistent manner throughout the modeling domain.

Although not funded directly under SI-1399, four additional activities related to the scientific and public dissemination of DUSTRAN deserve mention. First, a manuscript entitled "An evaluation of the wind erosion module in DUSTRAN" by W.J. Shaw, K.J. Allwine, B.G. Fritz, F.C. Rutz, J.P. Rishel and E.G. Chapman was accepted for publication in the scientific journal *Atmospheric Environment*. The article focuses on the scientific underpinnings of the wind erosion source term in DUSTRAN and comparison of DUSTRAN-derived PM₁₀ concentrations with observations (Shaw et al., 2007). Second, the DUSTRAN modeling system was the subject of an invited oral presentation at the 2007 Annual Meeting of the Emergency Management Issues - Special Interest Group (EMI-SIG). The presentation focused on a description of DUSTRAN and its potential for use as an emergency response tool (Rishel and Allwine, 2007). Third, the final technical report on the development of DUSTRAN was submitted to SERDP and published as a PNNL report (Allwine et al., 2007). Fourth, because of wide-spread interest in DUSTRAN, development was initiated on a website describing the DUSTRAN and SPRAYTRAN modeling systems and providing links to open literature publications.

6 CONCLUSIONS AND IMPLCATIONS FOR FUTURE RESEARCH/IMPLEMENTATION

6.1 CONCLUSIONS: ARTILLERY BACKBLAST

Dust emissions of PM₁₀ and PM_{2.5} from this unique DOD source type appear to be very low based on our measurements, and it would not seem to be cost effective to pursue emission controls beyond what is already being done at improved firing positions. The quality of the controls such as surface treatments to stabilize the surface should be maintained to insure low emission rates.

As we were not able to measure backblast emissions created by firing on un-improved surfaces (i.e., surfaces with no amendments or alteration), the effect on the magnitude of the emissions from this type of surface remains uncertain. The split between the numbers of tests carried out on improved versus un-improved artillery firing positions at DoD installations is poorly resolved. At the YPG it appears most testing occurs on improved sites typical of the ones tested, but at another installation, the YTC, where artillery are fired for training purposes, all the firing positions are un-improved (Mr. T. Felix, personal communication, 2005). If we assume somewhat conservatively, however, that the emissions of fugitive dust PM (combustion component would not change) was two orders of magnitude higher than at improved sites, the contribution to annual US emissions would still only represent 0.05% of the total fugitive PM₁₀ contributions and 0.16% of the total fugitive PM_{2.5}.

Based on quantified effects of disturbance on wind erosion (Gillies et al., 2005b), it would not be unreasonable, in our opinion, to consider that emissions caused by backblast could be increased by one order of magnitude when estimating emissions on un-improved sites. Wind tunnel testing of disturbed versus undisturbed sites consistently shows that emissions increase by one order of magnitude as a result of the disturbance (Gillies et al., 2005b; Macpherson et al., 2008).

6.2 CONCLUSIONS: OFF-ROAD VEHICLE EMISSIONS

Unpaved road PM₁₀ emissions factors are systematically dependent on vehicle propulsion type (i.e., wheel or track), momentum, and the textural qualities of the surface as well as the depth of the disturbed surface layer. Texture of the unpaved road surface (i.e., % sand, silt and clay) affects the amount of available dust-sized particles and the depth of the disturbed layer affects how much material can be forced to the sides of the tracks during compression and lifted from the surface as the track turns upward at the rear of the vehicle.

The emissions relationships (momentum versus dust emission) developed as part of this project can provide the basis for developing emission inventory estimates of PM₁₀ and PM_{2.5} from DoD testing and training activities for the military bases where the measurements were collected. In light of these results, the AP-42 unpaved road emission factors may be biased high or low by a factor of three if both speed and mass are not simultaneously factored into the calculation.

Results could be extended with caution to other locations with similar soil textures, but broad applicability of the momentum versus emission relationships will require that an

effective scalar be established to account for the emission properties of the surface from which the dust is emitted.

PI-SWERL is an effective and easy method to use for inferring potential for dust emissions caused by wind erosion processes. The physical mechanism of entraining dust by a tire or track appears to be sufficiently different from wind entrainment that PI-SWERL may have limited value as a surrogate to predict road dust emission potential. At the two sites tested, flux tower-derived emission factors were a factor of ≈ 60 higher at Yakima than at Ft. Carson, whereas PI-SWERL cumulative PM_{10} emissions were larger by only a factor of ≈ 6 . Other measurement systems that use a tire to physically disturb the soil such as Testing Re-entrained Aerosol Kinetic Emissions from Roads (TRAKER) (Etyemezian et al., 2003 and Kuhns et al., 2001) may provide a more accurate means of comparing emissions potential between locations.

The TRAKER measurement platform (Kuhns et al., 2005; Etyemezian et al., 2006) offers the potential to serve as transfer standard for evaluating dust emission potential from unpaved surfaces. The TRAKER is a wheeled vehicle that creates dust emissions similar to the vehicles tested as part of this project. It measures the emissions of PM_{10} directly behind the front wheels and captures the speed and direction of a vehicle using a Global Positioning System, thus providing a real time measurement of vehicle momentum, dust flux, and position. As Gillies et al. (2005) and Kuhns et al. (2010) have demonstrated momentum is a critical variable affecting dust emissions by vehicles travelling on unpaved surfaces. TRAKER could potentially be used as a transfer standard for dust emissions for other vehicle types and provide time and space resolved maps of dust emission potential for surfaces that are used by wheeled and tracked vehicles.

6.3 CONCLUSIONS: ROTARY-WINGED AIRCRAFT EMISSIONS

This work provides data on the strength of dust emissions created by low-level rotary winged aircraft flight, which to the best of our knowledge have not been reported elsewhere in the peer-reviewed literature. For rotary-winged aircraft flying under the conditions prescribed by the testing, emission rates of PM_{10} for each meter of forward travel were observed to scale primarily as a function of forward travel speed, decreasing exponentially as travel speed increases. Based on surface shear stress measurements, for each increase in speed there is a decrease in the peak shear stress in a zone extending from ≈ 19 m beyond the edge of the main rotor that decays as a function of distance from near the rotor edge. This decay in shear stress as a function of distance is likely exponential, but this was not observed due to the relatively short (≈ 19 m) measurement distance. Speed affects dust emissions in two ways: 1) as speed increases, peak shear stress was observed to decline proportionally, and 2) as the helicopter's forward speed increases its residence time over any location on the surface diminishes, so the time the downward rotor-generated flow is acting upon that surface also decreases. Altitude of the aircraft will also affect emissions, but this affect was not quantified in this study.

Based on the measured emission rates for the test aircraft, it is fairly certain that dust emissions from rotary-winged aircraft do not constitute a significant source of PM_{10} and $PM_{2.5}$ originating from testing and training on U.S. military installations. Given that wheeled and tracked vehicles produce more emissions per unit distance traveled than rotary-winged aircraft for speeds that exceed 15 km hr^{-1} , it is suggested here that

controlling or mitigating emissions from wheeled and tracked vehicles offers a greater opportunity to reduce dust loading associated with testing and training than activities using rotary-winged aircraft.

The PI-SWERL emissions measurements showed that Site 2 was potentially more emissive than Site 1, which was reflected in the tower-based measurements of the aircraft-generated emissions. Both measurements were approximately an order of magnitude different between the Sites. It will require a larger data set to evaluate if these two measurement methods scale similarly, which if proved would allow PI-SWERL to be used as an economical means for evaluating emission potential for rotary-winged aircraft.

6.4 CONCLUSIONS: PARTICLE CHARACTERIZATION

The physical and optical properties of mineral dusts are not just related to their chemical compositions alone. Except for the gun-pad samples where potassium sulfate was added to the soil to resist release of the dust, and metal emissions from artillery activities, several chemical similarities exist amongst samples from the four campaigns.

Not only mineral content of the dusts, but also their interrelationships contribute largely to their optical and other physical properties. In the case of the investigated sample sets, secondary carbonate minerals (e.g., calcite and dolomite) formed from weathering processes, together with evaporites (including artificially added potassium sulfate) serve to cement the silicate and other particles in the soils, so lowering the potential for dust emissions. This will be more evident when the soil surface is disturbed by vehicular traffic, or exposed to wind erosion processes.

A sub-microscopic veneer (desert varnish) of clay minerals, with or without iron oxides generally coats the silicates, making the different mineral particles indistinguishable by SEM or CCSEM. This also has an effect on the optical properties of mineral dusts.

6.5 CONCLUSIONS: HYBRID METHOD

SI-1399 and SI-1400 jointly evaluated the performance characteristics of a hybrid in situ and ORS system to determine whether it could be used as a measurement system for quantifying fugitive dust emissions, which offers advantages of flexibility and reduced instrumentation requirements while delivering reliable results. The performance of the hybrid system was determined through a comparison of results for emission flux measurements with the full in situ flux tower system, which uses multiple (three) towers and 30 individual dust monitoring instruments. The results indicate that the hybrid system can provide equivalent measurements as compared with the flux tower system.

Acceptance of the new test method would offer an accurate, cost-effective method to acquire dust emission measurement data for the development of fugitive dust emission factors. The hybrid method also brings closure to an issue that has hindered the development of other ORS techniques used to define fugitive dust emission flux, which is the relationship between open path extinction (or opacity) and mass concentration for specific dust plumes has previously been highly uncertain. This new method provides a calibration relationship between ORS and in situ PM measurements and will allow for the development and eventual deployment of other open path extinction measurements tools such as LIDAR or digital cameras, which can be used to develop fugitive PM emission factors.

6.6 DUSTRAN

The state of the DUSTRAN modeling system and interface at the conclusion of this project provides users the ability to specify many point-source locations with increased ease of operation. In the current release version with the unit release specified for each source, DUSTRAN can be immediately run displaying the plume footprint of potential emissions from these points. This modification improves the user-friendliness of the DUSTRAN system by automating a potentially time-consuming user-input task. The emissions module contains the relationships for the unique DoD sources that were defined as part of this research. The next generation of DUSTRAN will, for ease of use by DoD users, require several important changes including moving the operating system from a dedicated GIS-source code to an open source code to provide more flexibility to the user and will remove the need for continually upgrading of the commercial software that DUSTRAN was first developed for, thus lowering its operating costs.

6.7 SI-1399 EMISSION MEASUREMENTS AND US EPA, AP-42 COMPILATION OF EMISSION FACTORS

Measurements obtained during this project of PM emissions from unique military activities represent a valuable contribution to the emission estimation literature. In some cases, such as artillery backblast and rotary-winged aircraft, they represent the only measurements of their kind, while in other cases, such as tracked vehicle travel on unpaved roads, they quantify emissions under ranges of conditions that are more representative of military settings and activities than emissions reported from other studies. These include the ranges of vehicle weights and track types, the speeds of travel, and the soil surfaces that are prevalent on military bases. Therefore, beyond publication in the peer-reviewed literature, ideally, emissions data from this project would be available to air quality practitioners as part of a larger structured database. The publication of these results in the peer-reviewed literature (e.g., Gillies et al., 2005, 2007, 2010; Kuhns et al., 2010) provides a clear indication that the major objectives of this study were achieved.

The EPA Office of Air Quality Planning and Standards, Sector Policy and Programs Division, Measurement Policy Group (OAQPS/SPPD/MPG) directs a national program for improving emissions quantification, including standardizing and streamlining emissions data collection and reporting. Although personnel from the OAQPS/SPPD/MPG were involved in an advisory role throughout the execution stages of this SERDP project, recent communications with the office have focused on how best to disseminate emissions measured by the project to the user community through an EPA approved pathway.

In general, there are two levels of archiving/documenting the work completed as part of this project. For cases where emissions may need to be estimated on a repeated basis using a number of different parameters, a method for estimating emissions could be published in the EPA AP-42 guidance document. For cases where it is either not possible or not useful to pursue publication of an approved method, the emission data may be published in an EPA database with appropriate documentation of the methods used. In this latter case, the methods themselves may not be approved (i.e., not included in AP-

42), but the specific measurement results may be used under circumstances where they represent the best available information.

In consultation with OAQPS/SPPD/MPG, work has begun on documenting the emissions measurement completed as part of this study. The process can be divided roughly into three steps. First, reports and publications that describe similar emissions measurements must be gathered. This set of records comprises the “test reports” for the emissions category of interest. Second, a “background” document must be drafted. This document contains information about the relevance of the emissions source as well as a review of each of the test reports for applicability and data quality. If applicable, the background document may also recommend a method for estimating emissions based on some measured or assumed parameters. For example, in the case of road dust PM emissions (Chapter 13.2 of AP-42), the background document discusses why and how roadway silt loading can be used as a surrogate for PM emissions. The background document then goes through a series of revisions based on comments by EPA staff as well as those from the public. Third, if appropriate, the findings of the background document, including a possible method for estimating emissions from a certain activity are summarized in a Chapter that is included in the AP-42 guidance document.

There are four types of PM fugitive dust emissions measurements for which some level of formal approval is being sought. They are: emissions from artillery backblast, emissions from rotary-winged aircraft take-off, landing, and low-level flight, emissions from wheeled vehicle travel on unpaved roads, and emissions from tracked vehicle travel on unpaved roads. In consultation with EPA, we have begun the process with the rotary-winged aircraft emissions in anticipation that it will be relatively uncomplicated because of the dearth of similar data. Upon becoming familiar with the process using the rotary-winged aircraft measurements, we will initiate the process for artillery backblast, followed by tracked vehicle emissions, and finally wheeled vehicle emissions. For the latter two, one possibility would be to work with OAQPS/SPPD/MPG to incorporate the findings of this project into future revisions of the relevant AP-42 Chapter. At the time of writing of this report, a background document for PM emission from rotary-winged aircraft take-off, landing, and low-level flight is in draft.

Approval as an EPA AP-42 emission factor requires that we develop and submit background reports with detailed summaries of the test data used for developing the emission factors. Following this, an under EPA guidance an AP-42 Chapter or a subsection is added to an existing chapter. For emissions of fugitive dust attributable to artillery backblast EPA OAQPS suggests that it be incorporated into an existing chapter on artillery backblast developed for the combustion-created aerosols. Building on our experience in developing an AP-42 Chapter for Rotary-Winged aircraft fugitive dust emissions, our plan is to then begin to develop a fugitive dust artillery backblast emission factor section for inclusion into AP-42.

The successful completion of this project also produced valuable information on the comparability of in situ and remote sensing measurements to quantify fugitive dust emissions. This project also made advances in our understanding of the physics of the dust emission processes for sources that have not been previously quantified. This insight is not only important to the DoD, which now has access to the developed emission factor relationships to improve upon their emission inventories, but also has the potential

to assist with other problems faced by the DoD regarding operations of their vehicles and aircraft under conditions impacted by dust.

7. LITERATURE CITED

- Al-Awadhi, J.M., 2005. Dust fallout characteristics in Kuwait: a case study. *Kuwait Journal of Science and Engineering*, 32 (2): 135-151.
- Al-Juboury, A.I., 2006. Authigenic palygorskite in the Middle Miocene rocks of Iraq: environmental and geochemical indicators. *Geophysical Research Abstracts*, 8: 01584.
- Brown, R. and Whitehouse, G., 2004. Modelling rotor wakes in ground effect. *Journal of the American Helicopter Society*, 49 (3): 238-249.
- Çagatay, M.N., 1990. Palygorskite in the Eocene rocks of the Dammam Dome, Saudi Arabia. *Clays and Clay Minerals*, 38 (3): 299-307.
- Campbell, J.R., Hlavka, D.L., Welton, E.J., Flynn, C.J., Turner, D.D., Spinhirne, J.D., Scott III, V.S., and Hwang, I.H., 2002. Full-time, eye-safe cloud and aerosol Lidar observation at Atmospheric Radiation Measurement program sites: Instruments and data Processing. *Journal of Atmospheric and Oceanic Technology*, 19 (4): 431-442.
- Chow, J.C. and Watson, J.G., 1999. *Ion Chromatography in elemental analysis of airborne particles*. Gordon and Breach Science, Amsterdam.
- Chow, J.C., Watson, J.G., Crow, D., Lowenthal, D.H., and Merrifield, T., 2001. Comparison of IMPROVE and NIOSH carbon measurements. *Aerosol Science and Technology*, 34 (1): 23-34.
- Chow, J.C., Watson, J.G., Houck, J.E., Pritchett, L.C., Rogers, C.F., Frazier, C.A., Egami, R.T., and Ball, B.M., 1994. A laboratory resuspension chamber to measure fugitive dust size distributions and chemical compositions. *Atmospheric Environment*, 28 (21): 3463-3481.
- Chow, J. C., Watson, J.G., Pritchett, L.C., Pierson, W.R., and Purcell, R.G., 1993. The DRI Thermal/Optical Reflectance carbon analysis system: Description, evaluation and applications in U.S. air quality studies. *Atmospheric Environment* 27A, 1185-1201.
- Chow, J.C. and Watson, J.G., 1999. *Ion Chromatography in elemental analysis of airborne particles*. *Elemental Analysis of Airborne Particles*, vol. 1. Gordon and Breach Science, Amsterdam, 97-137 pp.
- Chung, F.H., 1974. Quantitative interpretation of X-ray diffraction patterns of mixtures. I. Matrix-flushing method for quantitative multicomponent analysis. *Journal of Applied Crystallography*, 7: 519-525.
- Cowherd, C., 2007. Sandblaster 2 Support of See-Through Technologies for Particulate Brownout. Task 5 Final Technical Report, MRI Project No. 110565, 42 p.
- Cowherd, C., Englehart, P., Muleski, G.E., Kinsey, J.S., and Rosbury, K.D., 1990. *Control of Fugitive and Hazardous Dusts*. Noyes Data Corp., Park Ridge, NJ.
- Curtiss, H., Erdman, W., and Sun M., 1987. Ground effect aerodynamics. *Vertica*, 11 (1/2): 29-42.

- Curtiss, H.C., Sun, M. Putman, W.F., and Hanker, E.J., 1984. Rotor aerodynamics in ground effect at low advance ratios. *J. of the American Helicopter Society*, 29 (1): 48-55.
- Dornbusch, W., Strange, J., and Rooke, A., 1988. Prediction of Dust Propensity for Military Operations in Desert Areas. Final. SCIENCE AND TECHNOLOGY CORP HAMPTON, VA, November. <http://oai.dtic.mil/oai/oai?verb=getRecord&metadataPrefix=html&identifier=ADA202899>.
- Engelbrecht, J.P., McDonald, E.V., Gillies, J.A., Jayanty, R.K.M., Casuccio, G., and Gertler, A.W., 2009. Characterizing mineral dusts and other aerosols from the Middle East – Part 1: Ambient sampling. *Inhalation Toxicology*, 21 (4): 297-326.
- Etyemezian, V., Kuhns, H. and Nikolich, G., 2006. Precision and repeatability of the TRAKER vehicle-based paved road dust emission measurement. *Atmospheric Environment* 40: 2953-2958.
- Etyemezian, V., Kuhns, H., Gillies, J., Chow, J., Hendrickson, K., McGown, M., and Pitchford, M., 2003a. Vehicle-based road dust emission measurement (III): effect of speed, traffic volume, location, and season on PM₁₀ road dust emissions in the Treasure Valley, ID. *Atmospheric Environment*, 37 (32): 4583-4593.
- Etyemezian, V., Kuhns, H., Gillies, J., Green, M., Pitchford, M., and Watson, J., 2003b. Vehicle based road dust emissions measurements (I): methods and calibration. *Atmospheric Environment*, 37: 4559–4571.
- Etyemezian, V., Nikolich, G., Ahonen, S., Pitchford, M., Sweeney, M., Purcell, R., Gillies, J., and Kuhns, H., 2007. The Portable In Situ Wind Erosion Laboratory (PI-SWERL): A new method to measure PM₁₀ windblown dust properties and potential for emissions. *Atmospheric Environment*, 41 (18): 3789-3796.
- Fernald, F.G., Herman, B.M., and John, A.R., 1972. Determination of aerosol height distributions by Lidar. *Journal of Applied Meteorology*, 11 (3): 482-489.
- FLUENT, Inc., 2006. *Fluent User's Guide*, Version 6.3, FLUENT Inc., Lebanon, NH.
- Ganesh, B. and Komerath, N., 2006. Study of ground vortex structure of rotorcraft in ground effect at low advance ratios. *Proc of the 24th Applied Aerodynamics Conf.*, 5-8 Jun. 2006, San Francisco, CA, AIAA-2006-3475.
- Ganesh, B. and Komerath, N., 2004a. Unsteady aerodynamics of rotorcraft in ground effect. *Proc. of the 34th AIAA Fluid Dynamics Conf.*, 28 Jun. – 1 Jul. 2004, Portland, Oregon AIAA-2004-2431
- Ganesh, B., and Komerath, N., 2004b. Unsteady aerodynamics of rotorcraft in ground effect. *Proc. of the 22nd Applied Aerodynamics Conf.*, 16-19 Aug. 2004, Providence, Rhode Island, AIAA-2004-5287.

- Gillies, J.A., Arnott, P., Etyemezian, V., Gillette, D.A., Kuhns, H., McDonald, E., Moosmüller, H., Nickling, W. G., Schwemmer, G., and Wilkerson, T., 2005b. Characterizing and Quantifying Local and Regional Particulate Matter Emissions from Department of Defense Installations: Final Report. Prepared for Strategic Environmental Research and Development (SERDP), Arlington, VA, 22203-1821, March 2005.
- Gillies, J.A. and Berkofsky, L.B., 2004. Eolian suspension above the saltation layer, the concentration profile. *Journal of Sedimentary Research*, 74: 176-183.
- Gillies, J.A., Etyemezian, V., Kuhns, H., Nikolic, D., and Gillette, D.A., 2005a. Effect of vehicle characteristics on unpaved road dust emissions. *Atmospheric Environment*, 39: 2341–2347.
- Gillies, J.A., Etyemezian, V., Kuhns, H., McAlpine, J.D., Uppapalli, S., Nikolich, G., and Engelbrecht, J., 2010. Dust emissions created by low-level rotary-winged aircraft flight over desert surfaces. *Atmospheric Environment*, 44 (8): 1043-1053.
- Gillies, J.A., Kuhns, H.D., Engelbrecht, J.P., Uppapalli, S., Etyemezian, V., and Nikolich, G., 2007. Particulate emissions from U.S. Department of Defense artillery backblast testing. *Journal of the Air & Waste Management Association*, 57: 551-560.
- Gillies, J.A., Nickling, W.G., and King, J., 2006. Aeolian sediment transport through large patches of roughness in the atmospheric inertial sublayer. *Journal of Geophysical Research - Earth Surface*, 111: doi:10.1029/2005JF000434.
- Gillies, J.A., Nickling, W.G., and King, J., 2007. Shear stress partitioning in large patches of roughness in the atmospheric inertial sublayer. *Boundary-Layer Meteorology*, 122: 367-396.
- Gillies, J.A., Watson, J.G., Rogers, C.F., DuBois, D., and Chow, J.C., 1999. Long-term efficiencies of dust suppressants to reduce PM10 emissions from unpaved roads. *Journal of the Air & Waste Management Association*, 49: 3-16.
- Goossens, D. and B. Buck, 2009. Dust emission by off road driving: Experiments on 17 arid soil types, Nevada, USA. *Geomorphology*, 107 (3-4): 118-138.
- Goossens, D. and Buck, B., 2009. Dust dynamics in off-road vehicle trails: Measurements on 16 arid soil types, Nevada, USA. *Journal of Environmental Management*, 90 (11): 3458-3469.
- Grams, G.W., Blifford, Jr., I.H., Gillette, D.A., and Russell, P.B., 1974. Complex refractive index of airborne soil particles. *J. Appl. Meteor.*, 13: 459-471
- Hashmonay R.A., Kagann, R.H., Rood, M.J., Kim, B.J., Kemme, M.R., and Gillies, J., 2009. An advanced test method for measuring fugitive dust emissions using a hybrid system of optical remote sensing and point monitor techniques. *Atmospheric and Biological Environmental Monitoring*, Springer B.V., doi: 10.10007/978-1-4020-9674-7_6.

- Hussein, T., Johansson, C., Karlsson, H., and Hansson H.-C., 2008. Factors affecting non-tailpipe aerosol particle emissions from paved roads: On-road measurements in Stockholm, Sweden. *Atmospheric Environment*, 42 (4): 688-702.
- Irwin, H.P., 1980. A simple omnidirectional sensor for wind tunnel studies of pedestrian level winds. *Journal of Wind Engineering and Industrial Aerodynamics*, 7 (3): 219-239.
- Johannsen, A., 1931. *A Descriptive Petrography of the Igneous Rocks*. University of Chicago Press, Chicago, 267 pp.
- Kahlaf, F.I., Al-Kadi, A. and Al-Saleh, S., 1985. Mineralogical composition and potential sources of dust fallout deposits in Kuwait. *Sedimentary Geology*, 42: 225-278.
- Kavouras, I.G., Etyemezian, V., Nikolich, G., Young, M., Gillies, J., and Shafer, D., 2009. A new technique for characterizing the efficacy of fugitive dust suppressants. *Journal of the Air and Waste Management Association*, 59 (5): 603-612.
- Kerr, P.F., 1959. *Optical Mineralogy*. McGraw-Hill Book Company, Inc., 442 p.
- King, J., Etyemezian, V., Sweeney, M., Buck, B., Nikolich, G., submitted. Dust emission variability at the Salton Sea, California, USA, submitted. *Geomorphology*.
- Kuhns, H., Etyemezian, V., Gillies, J.A., Ahonen, S., Durham, C., and Nikolic, D., 2005. Spatial variability of unpaved road dust emissions factors near El Paso, Texas. *Journal of the Air and Waste Management Association*, 55: 3-12.
- Kuhns, H., Etyemezian, V., Landwehr, D., MacDougall, C., Pitchford, M., and Green, M., 2001. Testing Re-entrained Aerosol Kinetic Emissions from Roads (TRAKER): A New Approach to Infer Silt Loading on Roadways. *Atmospheric Environment* 35: 2815-2825.
- Kuhns, H., Gillies, J.A., Etyemezian, V., Nikolich, G., King, J., Zhu, D., Uppapalli, S., Engelbrecht, J., and Kohl, S., 2010. Particulate matter emissions from wheeled and tracked vehicles operating on unpaved roads. *Aerosol Science and Technology*, 44: 193-202.
- Macpherson, T., Nickling, W.G., Gillies, J.A., and Etyemezian, V., 2008. Dust emissions from undisturbed and disturbed supply limited desert surfaces. *Journal of Geophysical Research, Earth Surface* 113, F02S04: doi:10.1029/2007JF000800.
- Martello, D.V., Anderson, R.R., White, C.M., Casuccio, G.S., and Schlaegle, S.F., 2001. Quantitative scanning electron microscopy methods to characterize ambient air PM_{2.5}. *ACS Fuel Chemistry Division Preprints*, 46 (2): 606-608.
- McAlpine, J.D., 2009. Lagrangian stochastic dispersion modeling in the atmospheric surface layer with an embedded strong flow perturbation. Unpublished M.Sc. Thesis, Department of Physics, University of Nevada Reno, 186 p.
- McAlpine, J.D., Koracin, D., Boyle, D., Gillies, J.A., and McDonald, E., 2009. Assessment of the applicability of a CFD method to simulate a rotorcraft dust emission source. *Environmental Fluid Mechanics* (submitted).

- Moosmüller, H., Arnott, W.P., Rogers, C.F., Bowen, J.L., Gillies, J.A., Pierson, W.R., Collins, J.F., Durbin, T.D., and Norbeck, J.M., 2001a. Time resolved characterization of diesel particulate emissions: 1. Instruments for particle mass measurements. *Environmental Science & Technology*, 35: 781-787.
- Moosmüller, H., Arnott, W.P., Rogers, C.F., Bowen, J.L., Gillies, J.A., Pierson, W.R., Collins, J.F., Durbin, T.D., and Norbeck, J.M., 2001b. Time resolved characterization of diesel particulate emissions: 2. Instruments for elemental and organic carbon measurements. *Environmental Science & Technology*, 35: 1935-1942.
- Moosmüller, H., Varma, R., Arnott, W.P., Kuhns, H.D., Etyemezian, V., and Gillies, J.A., 2005. Scattering cross section emission factors for visibility and radiative transfer applications: military vehicles traveling on unpaved roads. *Journal of the Air and Waste Management Association*, 55: 1743-1750.
- MRI (Midwest Research Institute), 2001. Revisions to AP-42 Section 13.2.2 “Unpaved Roads”. Technical Memorandum Prepared for the US EPA, Research Triangle Park, NC, Midwest Research Institute, Kansas City, MO.
- Nicholson, K.W., Branson, J.R., Geiss, P., and Cannel, R.J., 1989. The effects of vehicle activity on particle resuspension. *Journal of Aerosol Science*, 20: 1425–1428.
- Potter, R.M. and Rossman, G.R., 1977. Desert varnish: The importance of clay minerals. *Science*, 24: 1446-1448.
- Shao, Y., 2000. *Physics and Modelling of Wind Erosion*. Kluwer Academic Publishers, Dordrecht, 393 pp.
- Shaw, W.J., Allwine, K.J., Fritz, B.G., Rutz, F.C., Rishel, J.P., and Chapman, E.G., 2007. An evaluation of the Wind Erosion Module in DUSTRAN. *Atmospheric Environment*, doi: 10.1016/j.atmosenv.2007.11.022.
- Shih, T.H., Liou, W.W., Shabbir, A., Yang, Z., and Zhu, J., 1995. A new $k-\epsilon$ eddy viscosity model for high Reynolds number turbulent flows. *Computers and Fluids*, 24 (3): 227-238.
- SSURGO, 2009. Soil Survey Geographic Database, Natural Resources Conservation Service. <http://soils.usda.gov/survey/geography/ssurgo/>.
- Shaw, W.J., Allwine, K.J., Fritz, B.G., Rutz, F.C., Rishel, J.P. and Chapman, E.G., 2007. An evaluation of the Wind Erosion Module in DUSTRAN. *Atmospheric Environment*, doi:10.1016/j.atmosenv.2007.11.022.
- Sweeney, M., Etyemezian, V., Macpherson, T., Nickling, W., Gillies, J., Nikolich, G., and McDonald, E., 2007. Comparison of PI-SWERL with dust emission measurements from a straight-line field wind tunnel. *Journal of Geophysical Research, Earth Surface*, 113, F01012 doi: 10.1029/2007JF000830.
- US EPA, 1996. *Compilation of Air Pollutant Emission Factors, Vol.1, Stationary Point and Area Sources*. US EPA Office of Air and Radiation, Office of Air Quality Planning and Standards, RTP, NC.

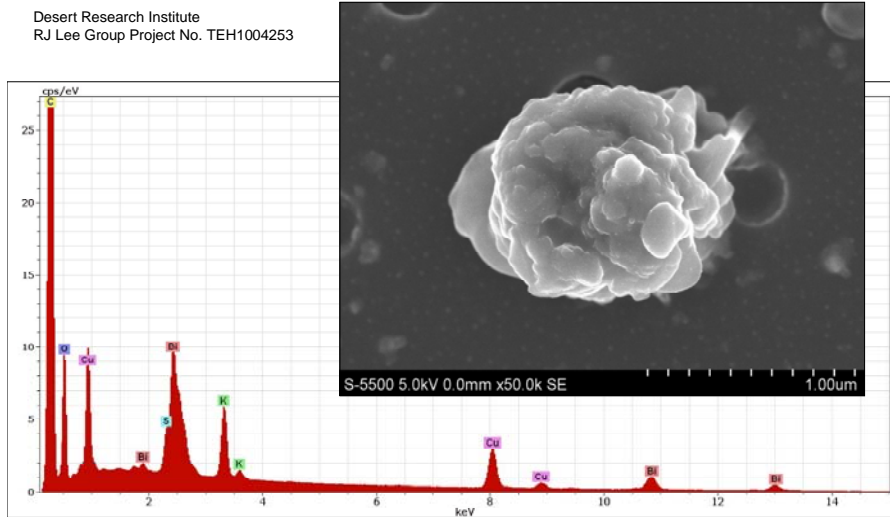
- US EPA, 2003. AP-42, fifth ed., vol.1, Miscellaneous Sources, US Environmental Protection Agency, Research Triangle Park, NC; (Chapter 13) (<http://www.epa.gov/ttn/chief/ap42/ch13/final/c13s0202.pdf>).
- US EPA, 2009. AP-42 Compilation of Air Pollutant Emission Factors, <http://www.epa.gov/ttn/chief/ap42/>
- Varma, R.M., Hashmonay, R.A., Du, K., Rood, M.J., Kim, B.J., and Kemme, M.R.A., 2007. Novel method to quantify fugitive dust emissions using optical remote sensing. In *Advanced Environmental Monitoring*, Kim, Y.J. and Platt, U. eds., Springer, Netherlands, 143-154.
- Veranth J., Pardyjak, E.R., and Seshadri, G., 2003. Vehicle-generated fugitive dust transport: analytic models and field study. *Atmospheric Environment*, 37 (16): 2295-2303.
- Watson, J.G., Chow, J.C., and Frazier, C.A., 1999. X-ray fluorescence analysis of ambient air samples. In *Air Sampling Instruments for Evaluation of Atmospheric Contaminants*, B. S. Cohen, and S. V. Herring, Eds., pp. 51-57, Cincinnati, OH.

SERDP Unique Dust Study – Mineralogy & Chemistry

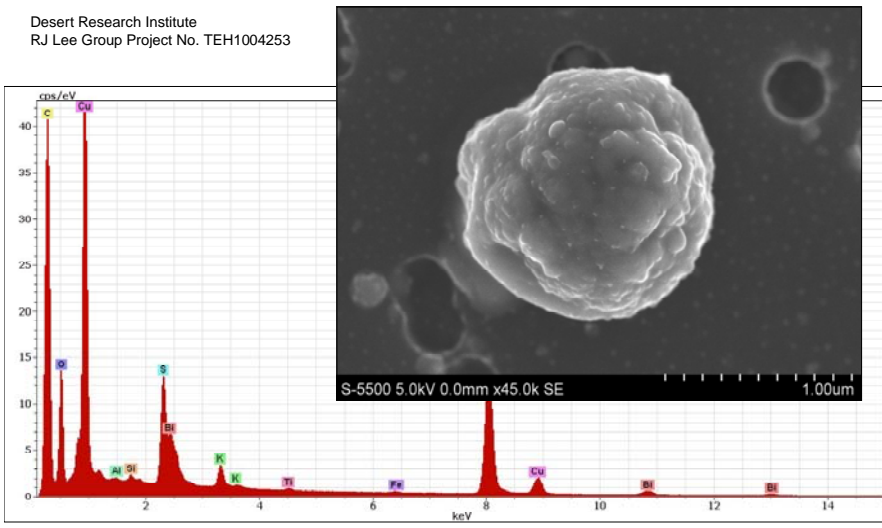
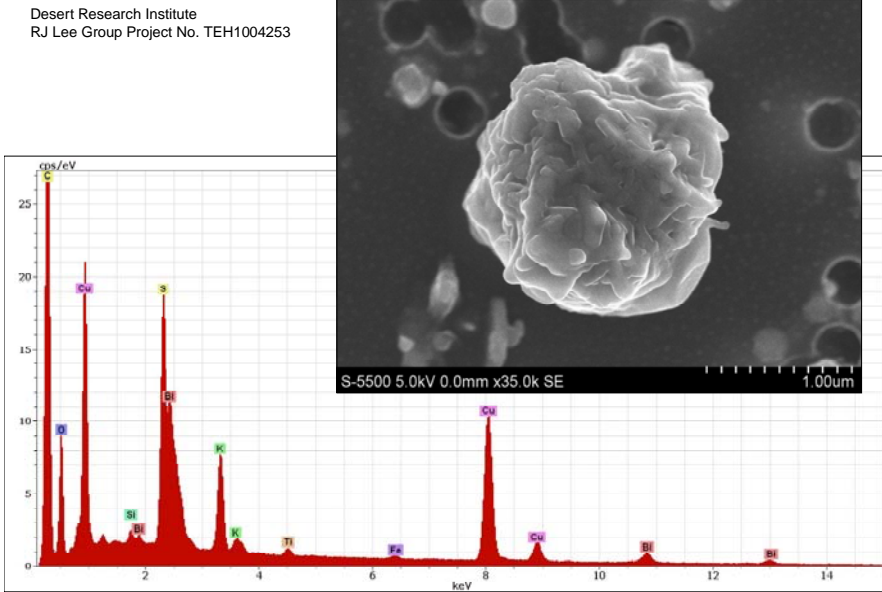
Sampling and Analysis
Appendices A-I

Appendix A – SEM, Secondary Electron Images & Spectra, YPG2005, Gunpad Site
1

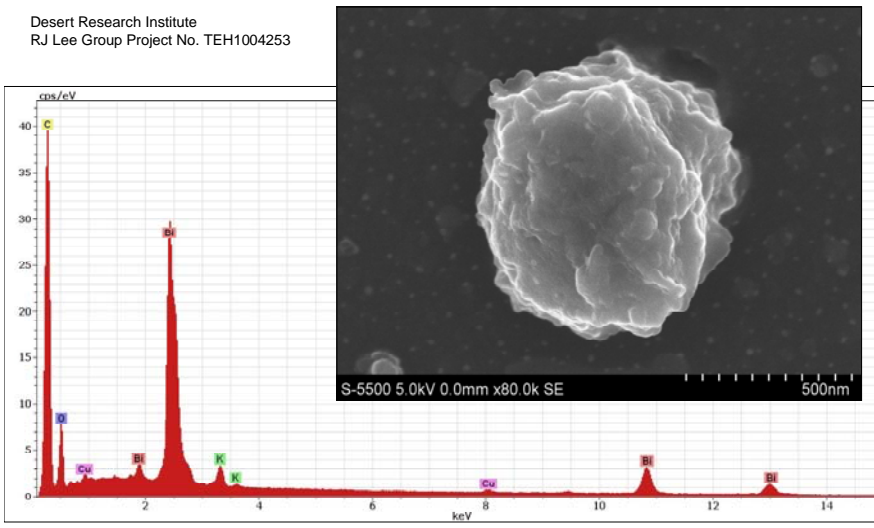
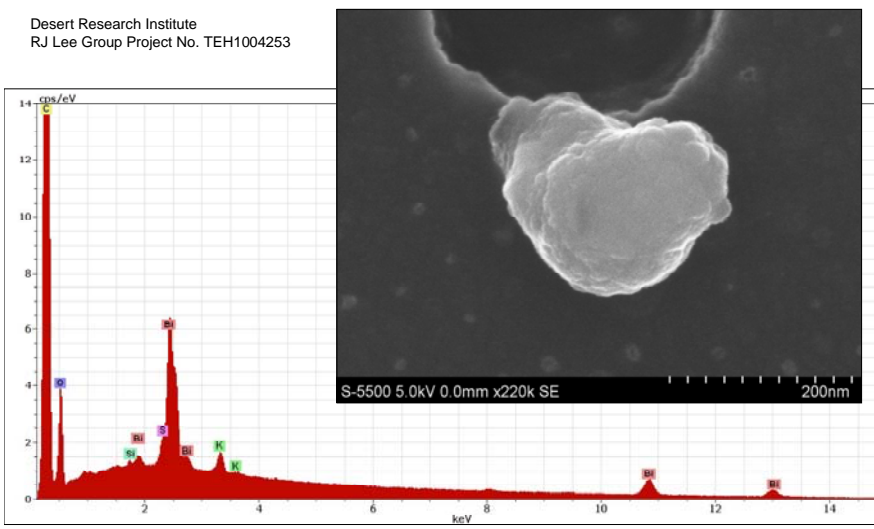
<p>RJG <i>RJ LeeGroup, Inc.</i> Analysis. Consulting. Development.</p> <p>Y47N001 Yuma 2005 Site 1 Gun Pad</p>  <p>S-5500 5.0kV 0.0mm x1.30k SE 40.0um</p> 	<p>SEM Images & Spectra Yuma 2005 Filter # Y47N001 Gunpad, Site 1 Small dots on Nuclepore membrane filter approximately 0.4 μm in diameter App. A (a to q)</p>
---	---

<p>Desert Research Institute RJ Lee Group Project No. TEH1004253</p>  <p>Y47N001 Yuma 2005 Site 1 Gun Pad</p>	<p>App. A(a) Y47N001, Yuma 2005 Gunpad Site 1 Particle of bismuth and copper, with coating of potassium sulfate</p>
--	--

Appendix A – SEM, Secondary Electron Images & Spectra, YPG2005, Gunpad Site
1

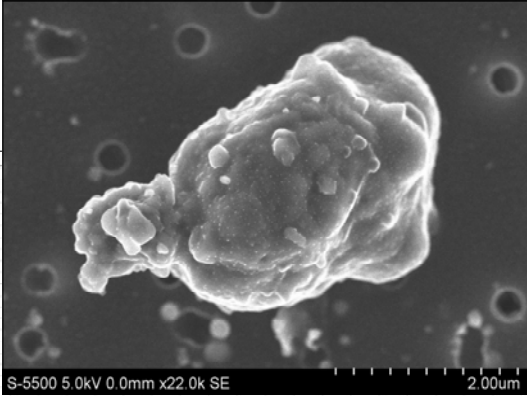
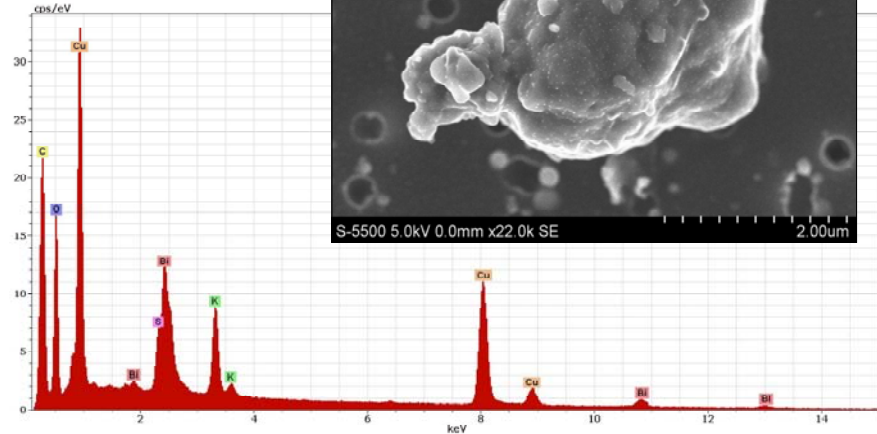
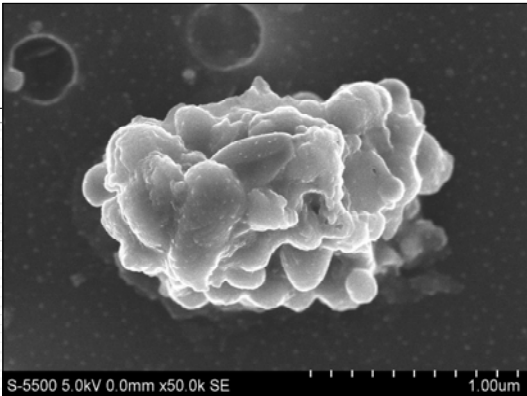
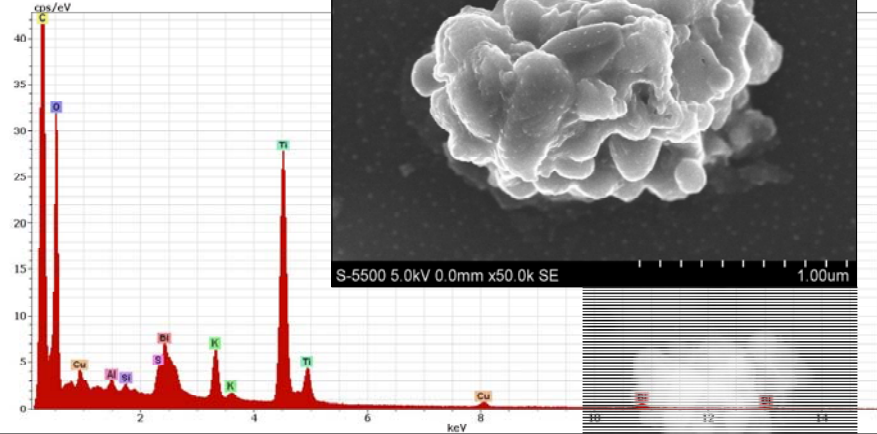
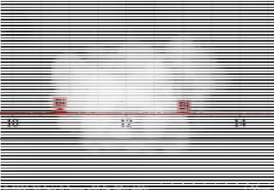
<p>Desert Research Institute RJ Lee Group Project No. TEH1004253</p>  <p>The SEM image shows a spherical, textured copper particle. The EDS spectrum displays peaks for Carbon (C), Oxygen (O), Copper (Cu), Aluminum (Al), Silicon (Si), Bismuth (Bi), Potassium (K), Titanium (Ti), Iron (Fe), and Bismuth (Bi) at higher energy levels. The x-axis is labeled 'keV' and ranges from 0 to 14. The y-axis is labeled 'cps/eV' and ranges from 0 to 40.</p> <p>Y47N001 Yuma 2005 Site 1 Gun Pad</p>	<p>App. A(b) Y47N001, Yuma 2005 Gunpad, Site 1 Copper particle with small amounts of bismuth and coating of potassium sulfate</p>
<p>Desert Research Institute RJ Lee Group Project No. TEH1004253</p>  <p>The SEM image shows a spherical, textured copper particle. The EDS spectrum displays peaks for Carbon (C), Oxygen (O), Copper (Cu), Silicon (Si), Bismuth (Bi), Potassium (K), Titanium (Ti), Iron (Fe), and Bismuth (Bi) at higher energy levels. The x-axis is labeled 'keV' and ranges from 0 to 14. The y-axis is labeled 'cps/eV' and ranges from 0 to 25.</p>	<p>App. A(c) Y47N001, Yuma 2005 Gunpad, Site 1 Copper particle with bismuth and coating of potassium sulfate</p>

Appendix A – SEM, Secondary Electron Images & Spectra, YPG2005, Gunpad Site
1

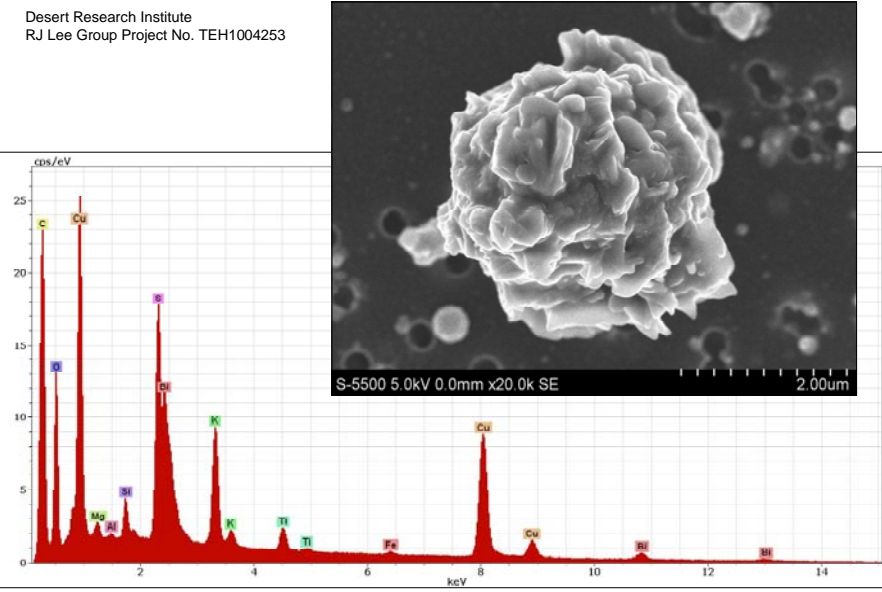
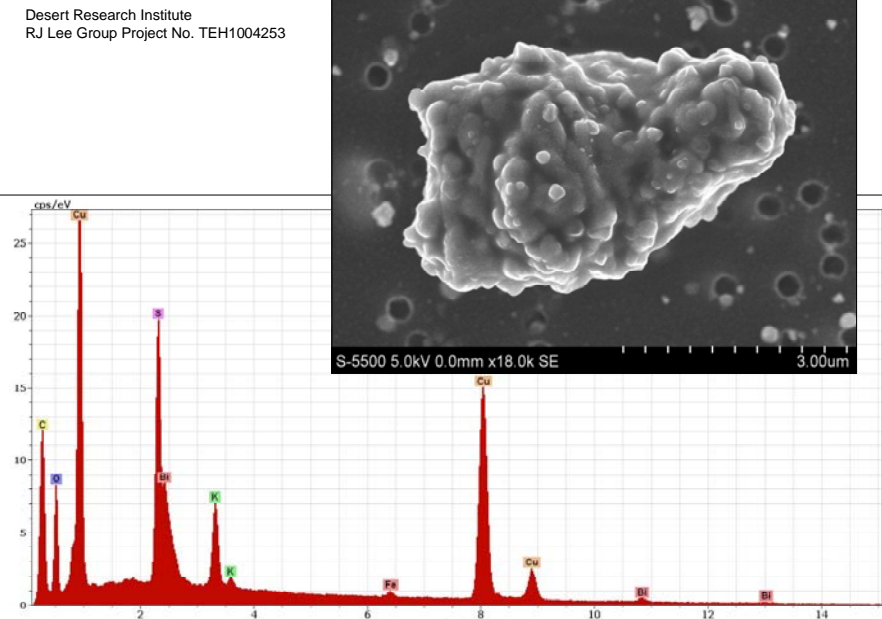
<p>Desert Research Institute RJ Lee Group Project No. TEH1004253</p>  <p>Y47N001 Yuma 2005 Site 1 Gun Pad</p>	<p>App. A(d) Y47N001, Yuma 2005 Gunpad Site 1 Bismuth particle with traces of copper and coating of potassium sulfate</p>
<p>Desert Research Institute RJ Lee Group Project No. TEH1004253</p>  <p>Y47N001 Yuma 2005 Site 1 Gun Pad</p>	<p>App. A(e) Y47N001, Yuma 2005 Gunpad Site 1 Sub-micron size bismuth particle with surface coating of small amounts of potassium sulfate</p>

Appendix A – SEM, Secondary Electron Images & Spectra, YPG2005, Gunpad Site

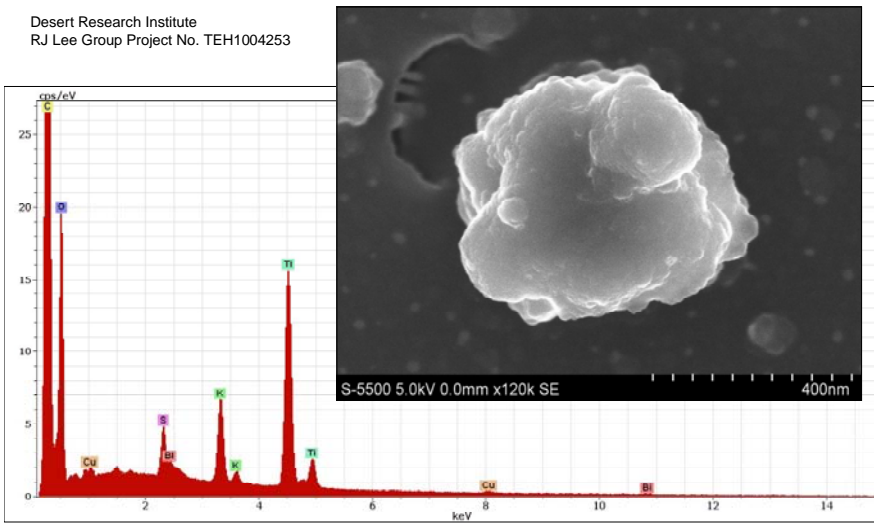
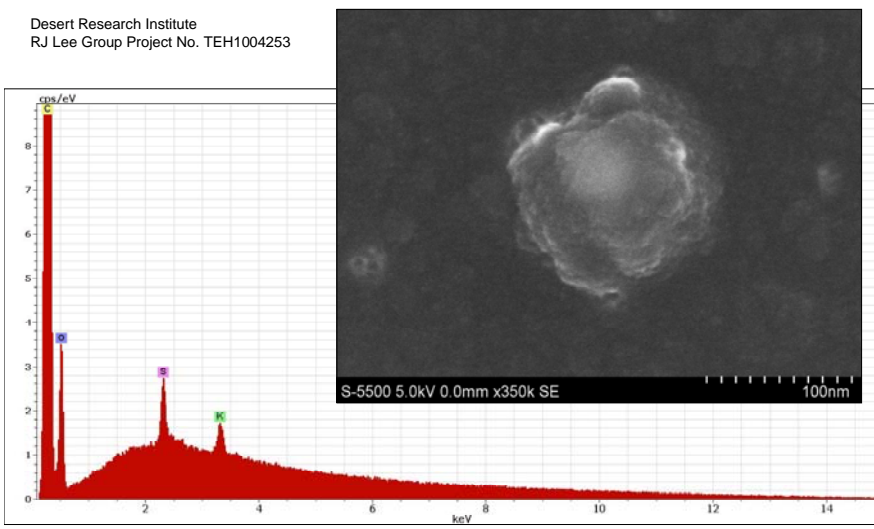
1

<p>Desert Research Institute RJ Lee Group Project No. TEH1004253</p>  	<p>App. A(f) Y47N001, Yuma 2005 Gunpad Site 1 Copper-bismuth particle with surface coating of small amount of potassium sulfate</p>
<p>Desert Research Institute RJ Lee Group Project No. TEH1004253</p>   <p>Y47N001 Yuma 2005 Site 1 Gun Pad</p> 	<p>App. A(g) Y47N001, Yuma 2005 Gunpad Site 1 Cluster of titanium particles with small amount of bismuth, with surface coating of potassium sulfate</p> <p>Backscattered Electron Image (BEI) of same particle</p>

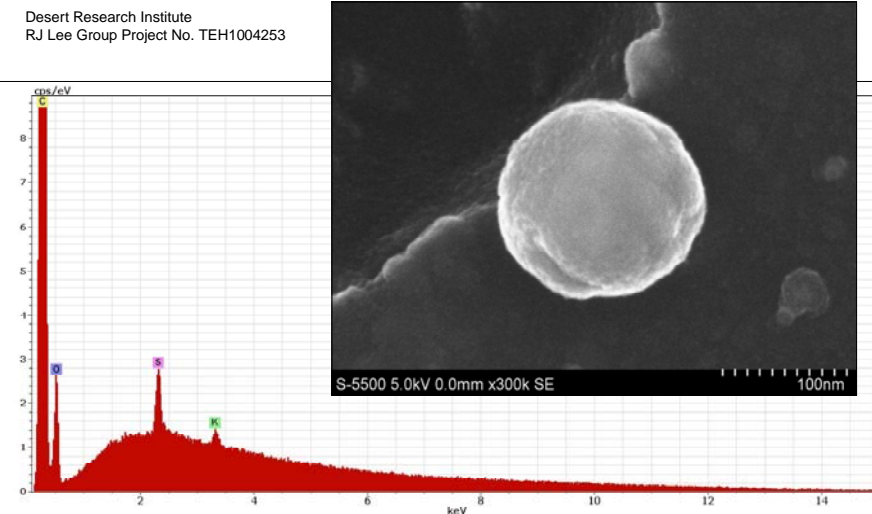
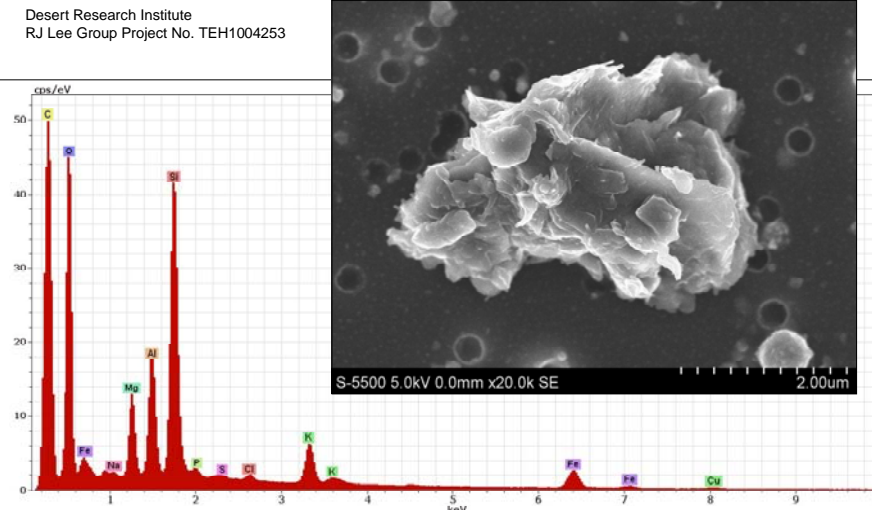
Appendix A – SEM, Secondary Electron Images & Spectra, YPG2005, Gunpad Site 1

<p>Desert Research Institute RJ Lee Group Project No. TEH1004253</p>  <p>S-5500 5.0kV 0.0mm x20.0k SE 2.00um</p>	<p>App. A(h) Y47N001, Yuma 2005 Gunpad Site 1 Copper-bismuth particle with surface coating of potassium sulfate.</p>
<p>Desert Research Institute RJ Lee Group Project No. TEH1004253</p>  <p>S-5500 5.0kV 0.0mm x18.0k SE 3.00um</p>	<p>App. A(i) Y47N001, Yuma 2005 Gunpad, Site 1 Copper-bismuth particle with surface coating of potassium sulfate</p>

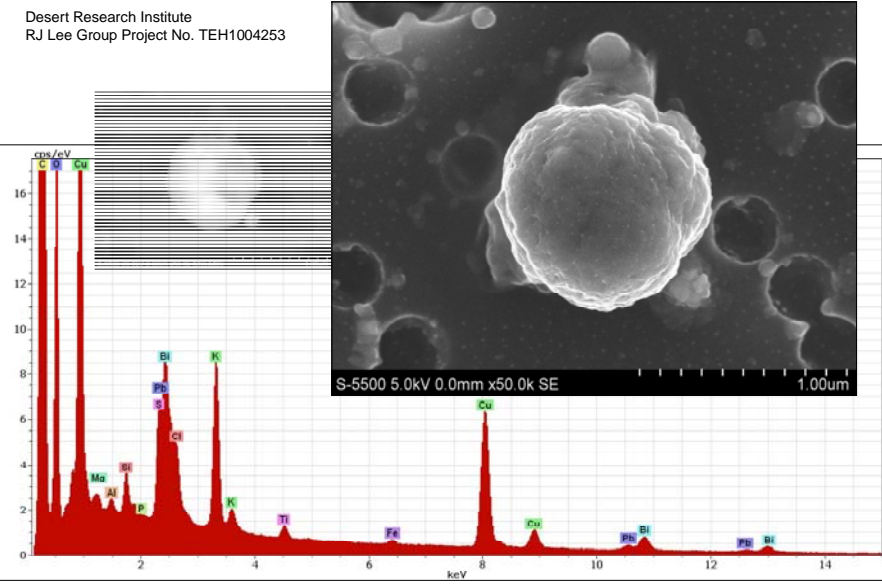
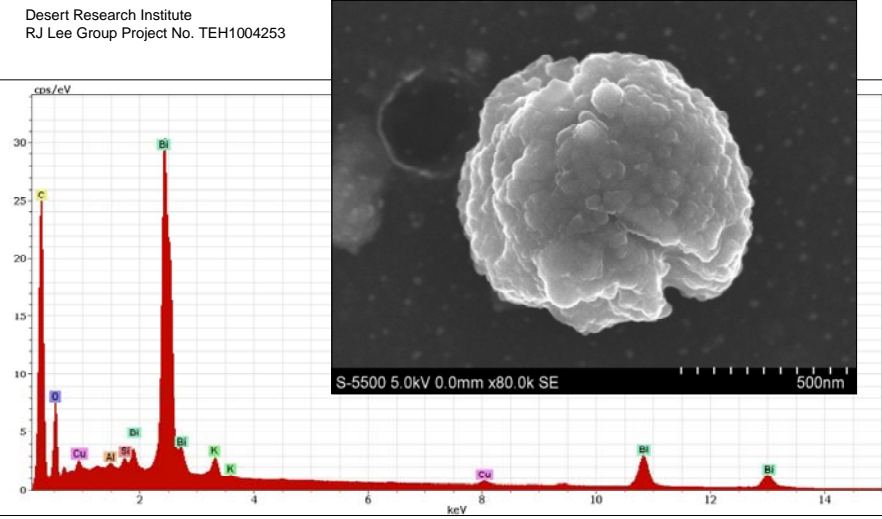
Appendix A – SEM, Secondary Electron Images & Spectra, YPG2005, Gunpad Site 1

<p>Desert Research Institute RJ Lee Group Project No. TEH1004253</p>  <p>Y47N001 Yuma 2005 Site 1 Gun Pad</p>	<p>App. A(j) Y47N001, Yuma 2005 Gunpad, Site 1 Titanium particle, possibly the mineral rutile, with surface coating of potassium sulfate</p>
<p>Desert Research Institute RJ Lee Group Project No. TEH1004253</p>  <p>Y47N001 Yuma 2005 Site 1 Gun Pad</p>	<p>App. A(k) Y47N001, Yuma 2005 Gunpad, Site 1 Sub-micron particle of carbon partly coated with potassium sulfate</p>

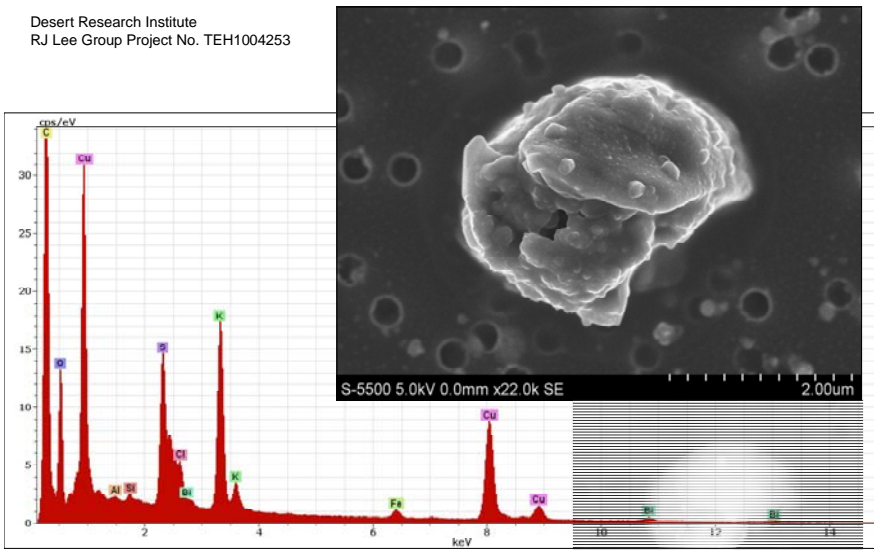
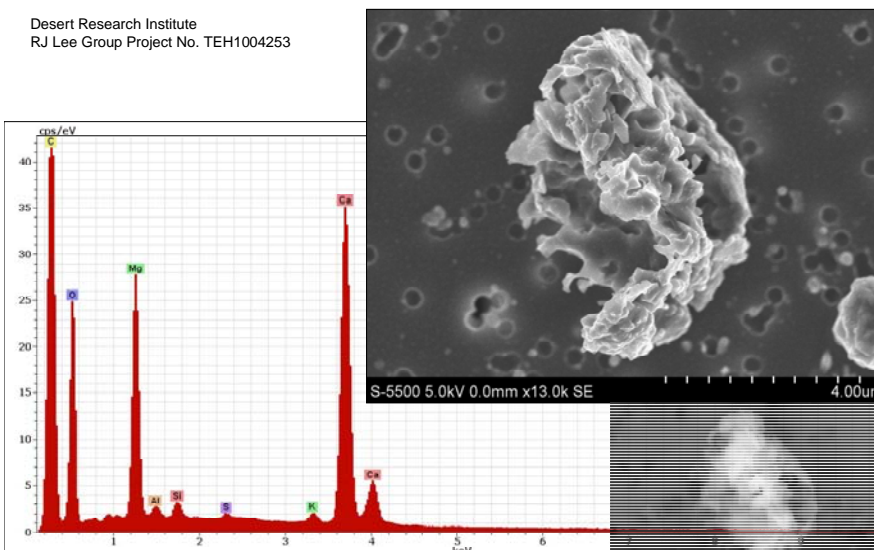
Appendix A – SEM, Secondary Electron Images & Spectra, YPG2005, Gunpad Site 1

<p>Desert Research Institute RJ Lee Group Project No. TEH1004253</p>  <p>S-5500 5.0kV 0.0mm x300k SE 100nm</p>	<p>App. A(l) Y47N001, Yuma 2005 Gunpad, Site 1 Sub-micron carbon particle with coating of potassium sulfate</p>
<p>Y47N001 Yuma 2005 Site 1 Gun Pad</p>	
<p>Desert Research Institute RJ Lee Group Project No. TEH1004253</p>  <p>S-5500 5.0kV 0.0mm x20.0k SE 2.00um</p>	<p>App. A(m) Y47N001, Yuma 2005 Gunpad, Site 1 Small flakes of clay minerals, possibly montmorillonite-illite</p>
<p>Y47N001 Yuma 2005 Site 1 Gun Pad</p>	

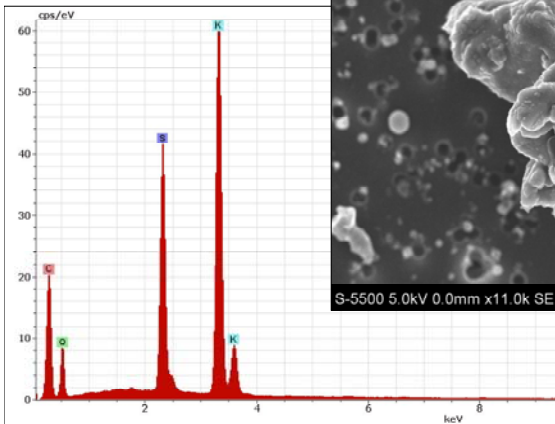
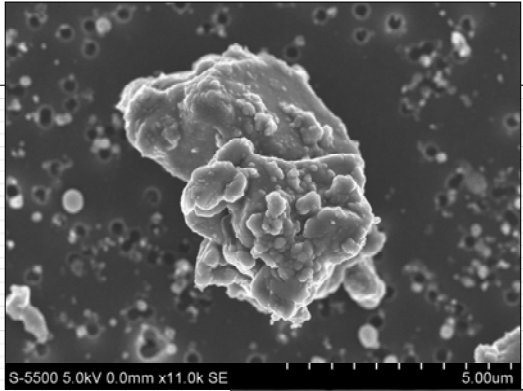
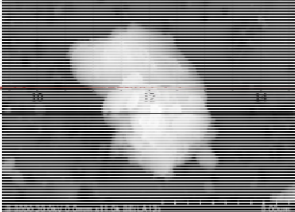
Appendix A – SEM, Secondary Electron Images & Spectra, YPG2005, Gunpad Site 1

<p>Desert Research Institute RJ Lee Group Project No. TEH1004253</p> 	<p>App. A(n) Y47N001, Yuma 2005 Gunpad, Site 1 Copper-bismuth particle with small amount of lead, all coated with potassium sulfate.</p>
<p>Desert Research Institute RJ Lee Group Project No. TEH1004253</p>  <p>Y47N001 Yuma 2005 Site 1 Gun Pad</p>	<p>App. A(o) Y47N001, Yuma 2005 Gunpad, Site 1 Bismuth particle with coating of potassium sulfate</p>

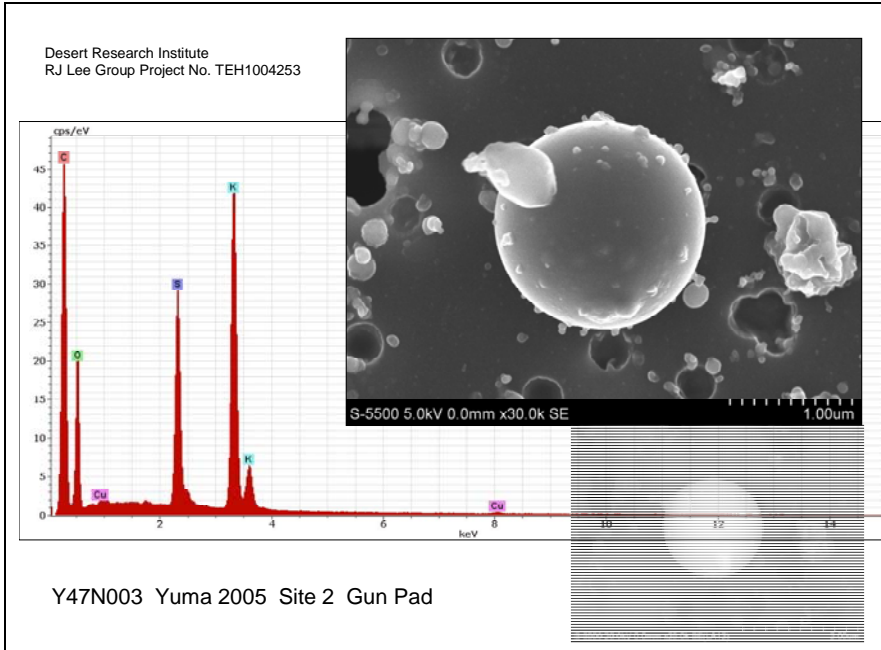
Appendix A – SEM, Secondary Electron Images & Spectra, YPG2005, Gunpad Site 1

<p>Desert Research Institute RJ Lee Group Project No. TEH1004253</p>  <p>Y47N001 Yuma 2005 Site 1 Gun Pad</p>	<p>App. A(p) Y47N001, Yuma 2005 Gunpad, Site 1 Copper particle with coating of potassium sulfate</p> <p>Backscattered Electron Image (BEI) of same particle</p>
<p>Desert Research Institute RJ Lee Group Project No. TEH1004253</p>  <p>Y47N001 Yuma 2005 Site 1 Gun Pad</p>	<p>App. A(q) Y47N001, Yuma 2005 Gunpad, Site 1 Skeletal structure of secondary dolomite, originally inter-granular cement in undisturbed dust</p> <p>Backscattered Electron Image (BEI) of same particle</p>

<p>RJG <i>RJ LeeGroup, Inc.</i> Analysis. Consulting. Development.</p> <p>Y47N003 Yuma 2005 Site 2 Gun Pad</p>  	<p>SEM Images & Spectra Yuma 2005 Gunpad Site 2 Small dark circles on Nuclepore membrane filter approximately 0.4 μm in diameter App. B (a to q) Filter # Y47N003</p>
--	---

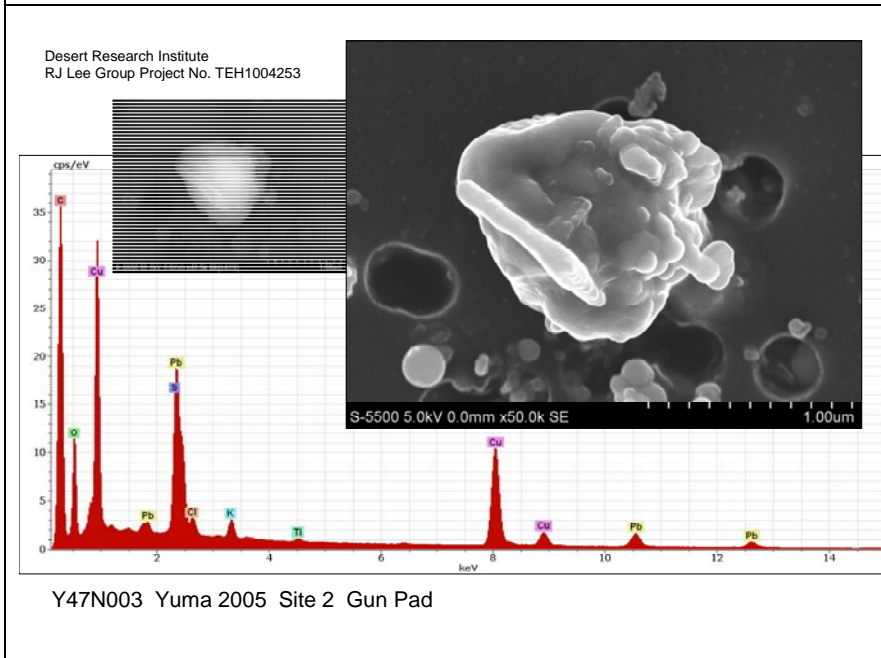
<p>Desert Research Institute RJ Lee Group Project No. TEH1004253</p>    <p>Y47N003 Yuma 2005 Site 2 Gun Pad</p>	<p>App. B(a) Y47N003, Yuma 2005 Gun Pad, Site 2 Thick coating of potassium sulfate on unknown mineral</p> <p>Backscattered Electron Image (BEI) of same particle</p>
--	---

Appendix B – SEM, Secondary Electron Images & Spectra, YPG2005, Gunpad Site
2



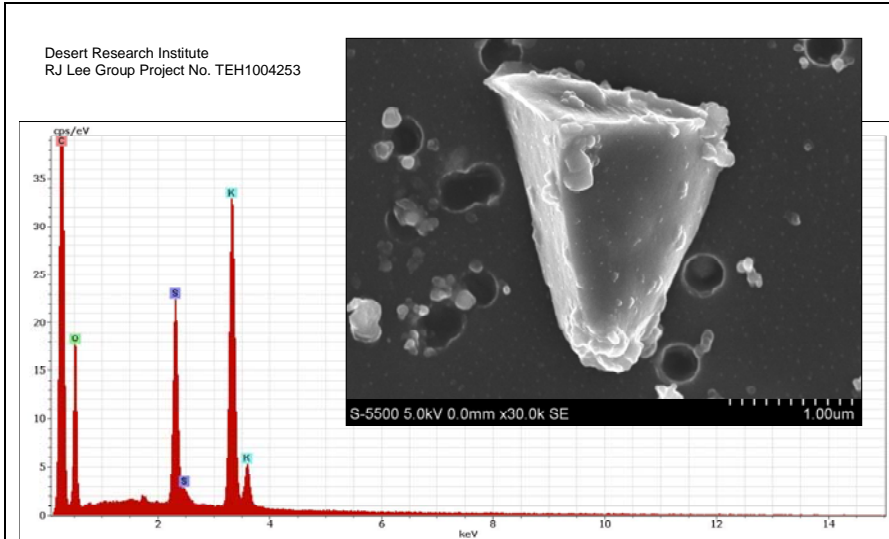
App. B(b)
Y47N003, Yuma 2005
Gunpad, Site 2
Sphere of carbon with
potassium sulfate

Backscattered Electron
Image (BEI) of same particle



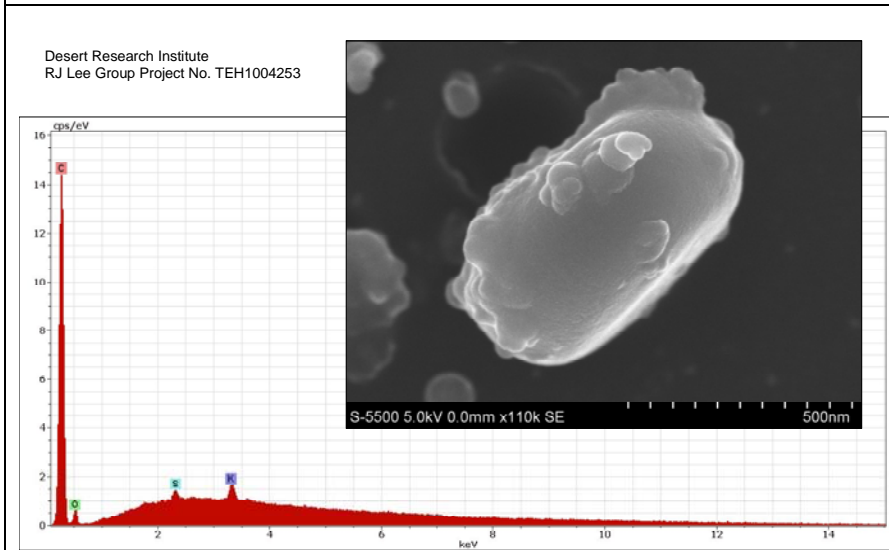
App. B(c)
Y47N003, Yuma 2005
Gunpad, Site 2
Copper-lead particle, with
coating of potassium sulfate
and potassium chloride

Appendix B – SEM, Secondary Electron Images & Spectra, YPG2005, Gunpad Site
2



Y47N003 Yuma 2005 Site 2 Gun Pad

App. B(d)
Y47N003, Yuma05
Gunpad, Site 2
Thick coating of potassium sulfate on unknown tooth-shaped crystal

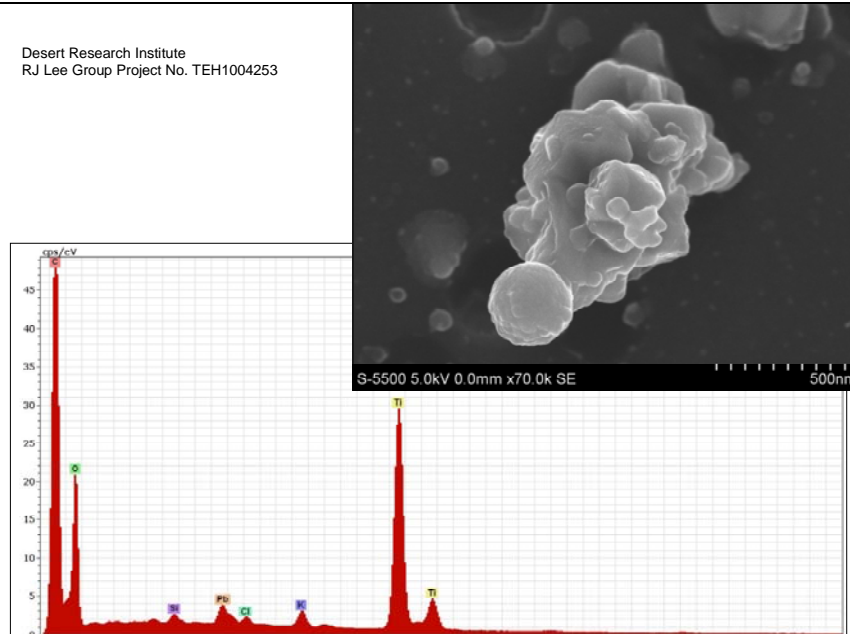
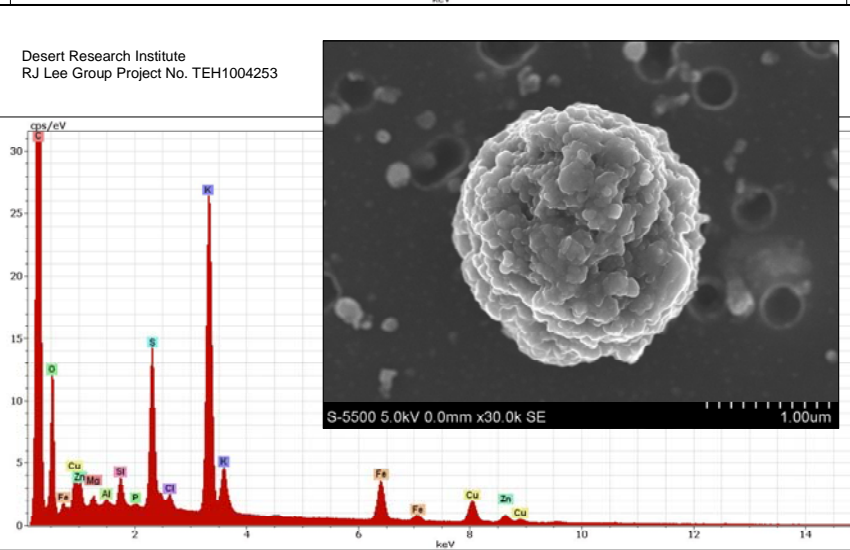


Y47N003 Yuma 2005 Site 2 Gun Pad

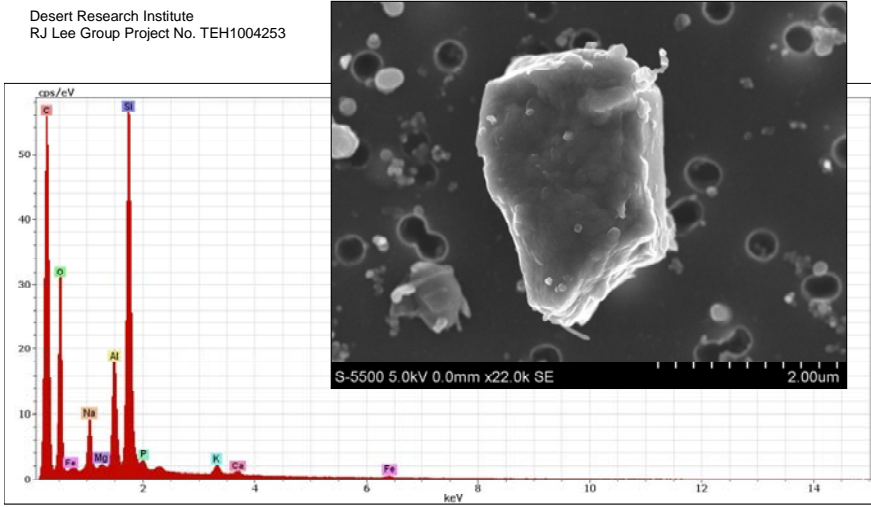
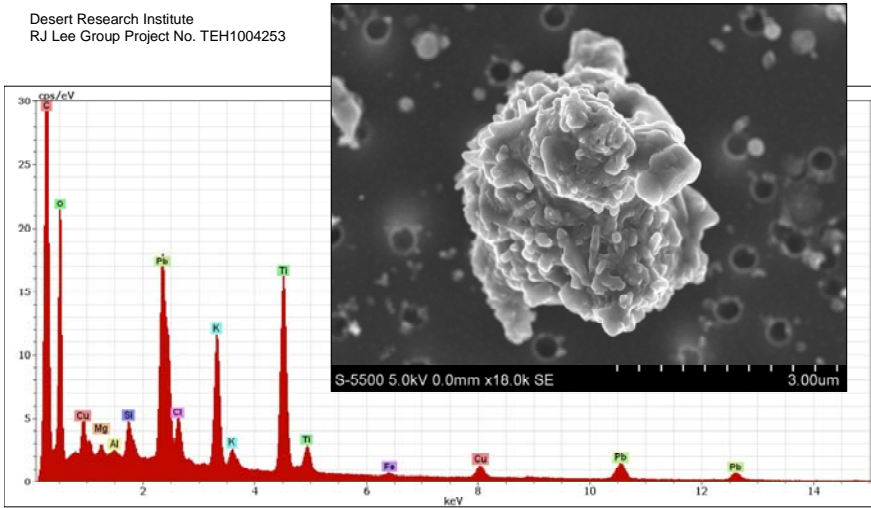
App. B(e)
Y47N003, Yuma 2005
Gunpad, Site 2
Sub-micron carbon particle with small amount of potassium sulfate

Appendix B – SEM, Secondary Electron Images & Spectra, YPG2005, Gunpad Site

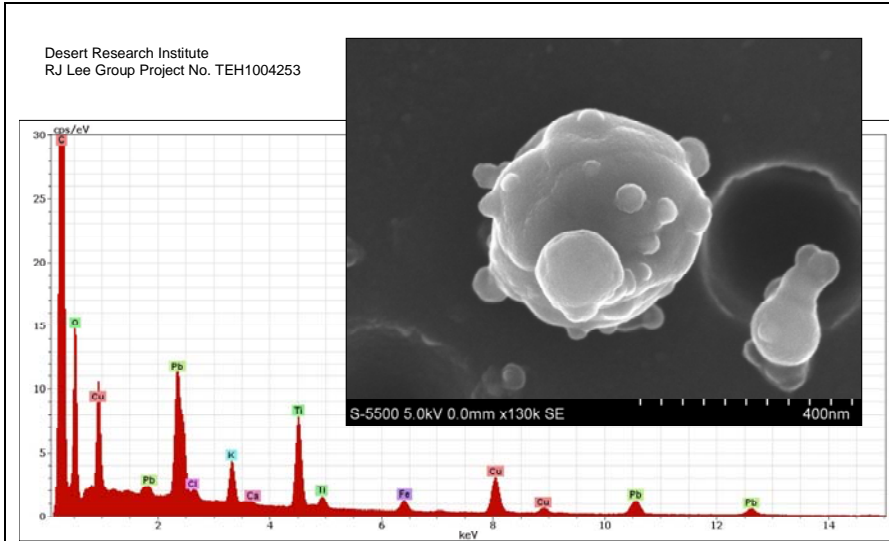
2

<p>Desert Research Institute RJ Lee Group Project No. TEH1004253</p>  <p>S-5500 5.0kV 0.0mm x70.0k SE</p>	<p>App. B(f) Y47N003, Yuma 2005 Gunpad, Site 2 Titanium-carbon particle with small amount of potassium chloride</p>
<p>Desert Research Institute RJ Lee Group Project No. TEH1004253</p>  <p>S-5500 5.0kV 0.0mm x30.0k SE</p> <p>Y47N003 Yuma 2005 Site 2 Gun Pad</p>	<p>App. B(g) Y47N003, Yuma 2005 Gunpad, Site 2 Carbon particle with small amounts of iron, copper, and zinc, and coating of potassium sulfate</p>

Appendix B – SEM, Secondary Electron Images & Spectra, YPG2005, Gunpad Site 2

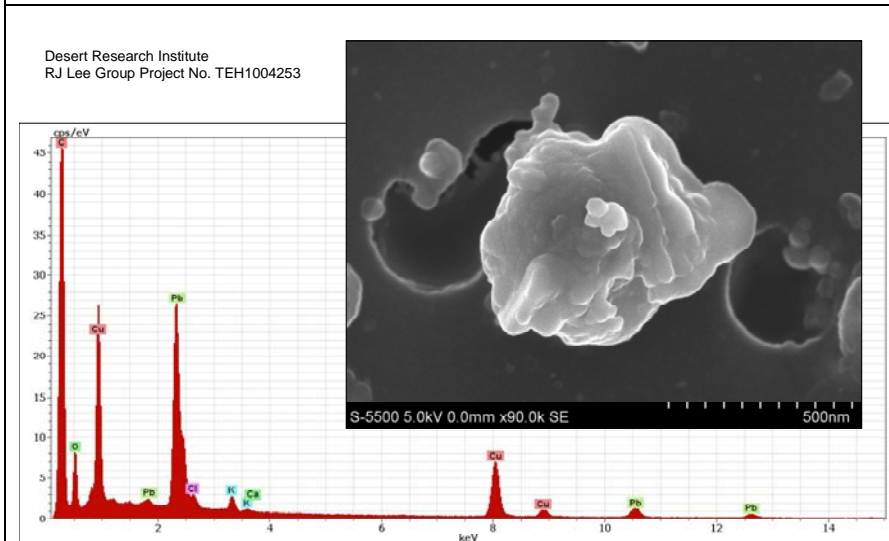
<p>Desert Research Institute RJ Lee Group Project No. TEH1004253</p>  <p>S-5500 5.0kV 0.0mm x22.0k SE 2.00um</p> <p>Y47N003 Yuma 2005 Site 2 Gun Pad</p>	<p>App. B(h) Y47N003, Yuma 2005 Gunpad, Site 2 Plagioclase feldspar crystal with coating of clay minerals, possibly kaolinite and montmorillonite-illite</p>
<p>Desert Research Institute RJ Lee Group Project No. TEH1004253</p>  <p>S-5500 5.0kV 0.0mm x18.0k SE 3.00um</p> <p>Y47N003 Yuma 2005 Site 2 Gun Pad</p>	<p>App. B(i) Y47N003, Yuma 2005 Gunpad, Site 2 Agglomerate of lead, titanium, and copper, with overall encrustations of potassium sulfate and potassium chloride</p>

**Appendix B – SEM, Secondary Electron Images & Spectra, YPG2005, Gunpad Site
2**



Y47N003 Yuma 2005 Site 2 Gun Pad

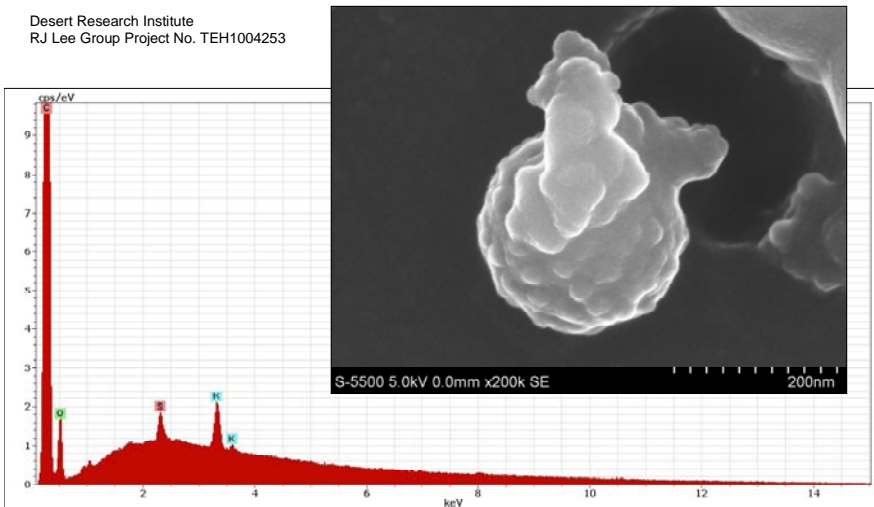
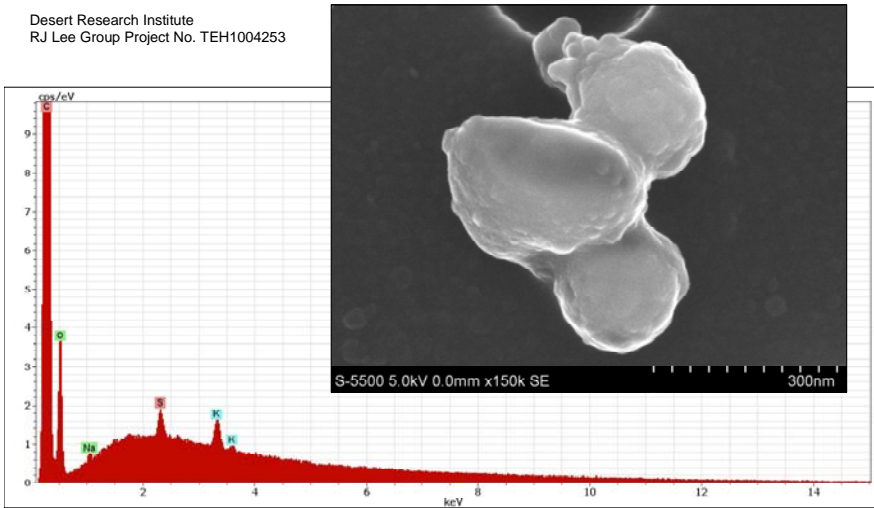
App. B(j)
Y47N003, Yuma 2005
Gunpad, Site 2
Sub-micron particle of lead,
copper, and titanium, with
surface coating of potassium
sulfate and potassium
chloride



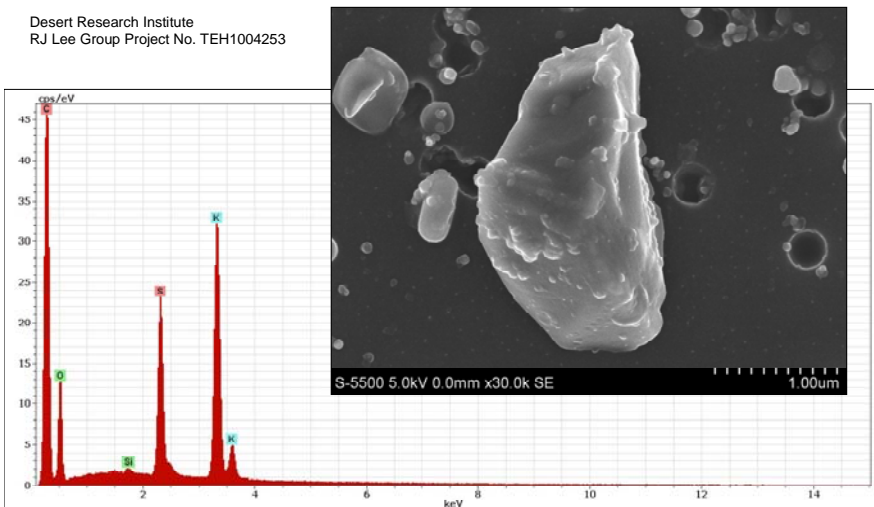
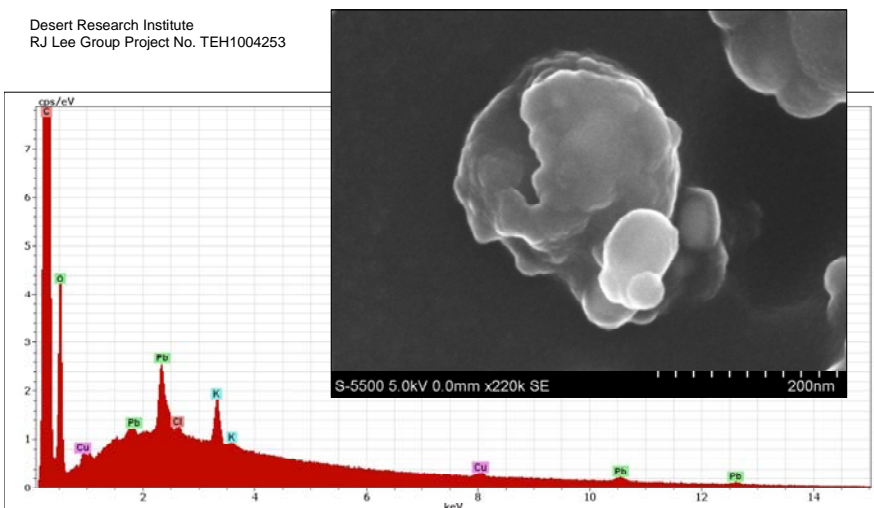
Y47N003 Yuma 2005 Site 2 Gun Pad

App. B(k)
Y47N003, Yuma 2005
Gunpad, Site 2
Copper-lead particle with
small amount of potassium
sulfate and -potassium
chloride

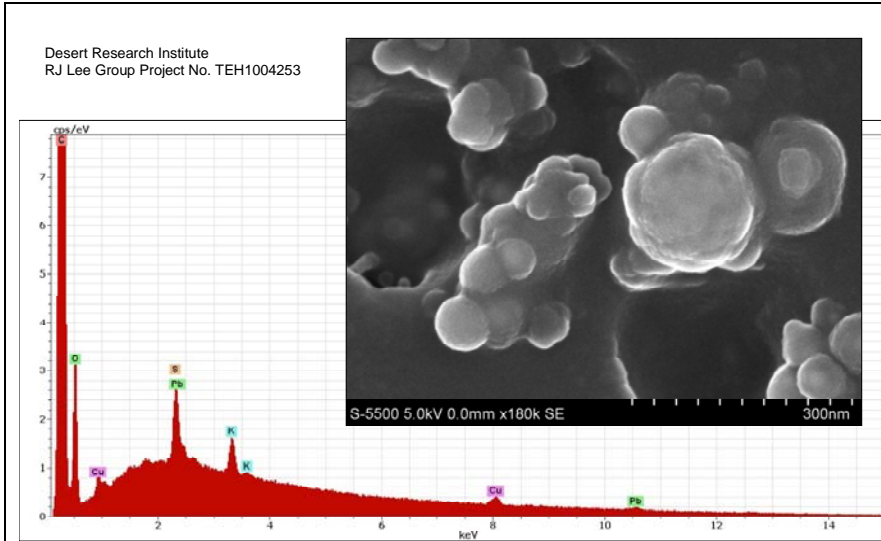
Appendix B – SEM, Secondary Electron Images & Spectra, YPG2005, Gunpad Site
2

<p>Desert Research Institute RJ Lee Group Project No. TEH1004253</p>  <p>The SEM image shows a spherical, multi-lobed carbon particle with a rough, textured surface. The EDS spectrum displays a prominent peak for Carbon (C) at approximately 0.27 keV, with smaller peaks for Oxygen (O) at 0.51 keV, Sulfur (S) at 2.31 keV, Potassium (K) at 3.96 keV, and Calcium (Ca) at 2.99 keV. The x-axis is labeled 'keV' and ranges from 0 to 14. The y-axis is labeled 'cps/eV' and ranges from 0 to 9. The SEM parameters are S-5500 5.0kV 0.0mm x200k SE, and a 200nm scale bar is present.</p> <p>Y47N003 Yuma 2005 Site 2 Gun Pad</p>	<p>App. B(l) Y47N003, Yuma 2005 Gunpad, Site 2 Sub-micron carbon particle with coating of potassium sulfate</p>
<p>Desert Research Institute RJ Lee Group Project No. TEH1004253</p>  <p>The SEM image shows a composite carbon particle with an irregular, multi-lobed shape. The EDS spectrum displays a prominent peak for Carbon (C) at approximately 0.27 keV, with smaller peaks for Oxygen (O) at 0.51 keV, Sulfur (S) at 2.31 keV, Potassium (K) at 3.96 keV, and Calcium (Ca) at 2.99 keV. The x-axis is labeled 'keV' and ranges from 0 to 14. The y-axis is labeled 'cps/eV' and ranges from 0 to 9. The SEM parameters are S-5500 5.0kV 0.0mm x150k SE, and a 300nm scale bar is present.</p> <p>Y47N003 Yuma 2005 Site 2 Gun Pad</p>	<p>App. B(m) Y47N003, Yuma 2005 Gunpad, Site 2 Composite carbon particle of possible biogenic origin, with coating of potassium- and sodium sulfates</p>

**Appendix B – SEM, Secondary Electron Images & Spectra, YPG2005, Gunpad Site
2**

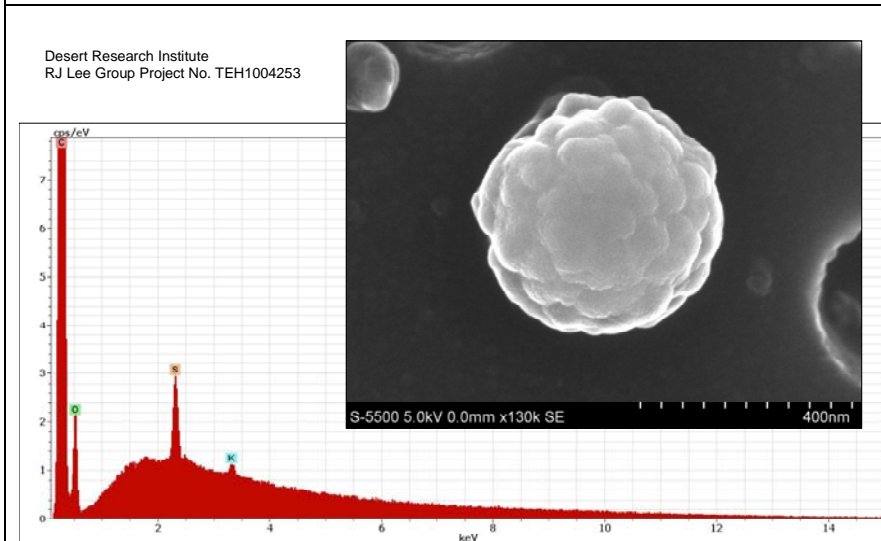
<p>Desert Research Institute RJ Lee Group Project No. TEH1004253</p>  <p>Y47N003 Yuma 2005 Site 2 Gun Pad</p>	<p>App. B(n) Y47N003, Yuma 2005 Gunpad, Site 2 Unidentified crystal with coating of potassium sulfate</p>
<p>Desert Research Institute RJ Lee Group Project No. TEH1004253</p>  <p>Y47N003 Yuma 2005 Site 2 Gun Pad</p>	<p>App. B(o) Y47N003, Yuma 2005 Gunpad, Site 2 Sub-micron carbon particle with lead and copper, as well as potassium sulfate</p>

Appendix B – SEM, Secondary Electron Images & Spectra, YPG2005, Gunpad Site
2



Y47N003 Yuma 2005 Site 2 Gun Pad

App. B(p)
Y47N003, Yuma 2005
Gunpad, Site 2
Sub-micron carbon spheres,
with lead and copper, and
coating of potassium sulfate



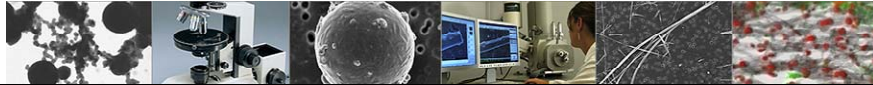
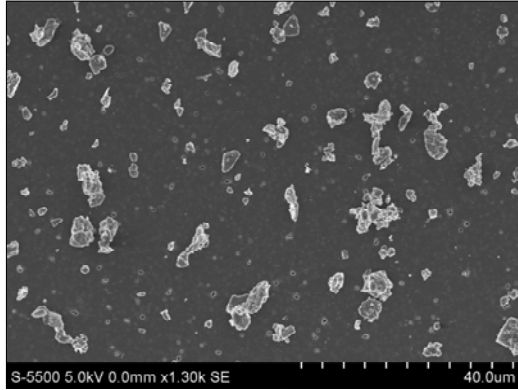
Y47N003 Yuma 2005 Site 2 Gun Pad

App. B(q)
Y47N003, Yuma 2005
Gunpad, Site 2
Sub-micron carbon sphere
with coating of potassium
sulfate

Appendix C – SEM, Secondary Electron Images & Spectra, Yakima 2006, Dirt Road, Site 1



Y47N007 Yakima 2006 Site 1 Dirt Road

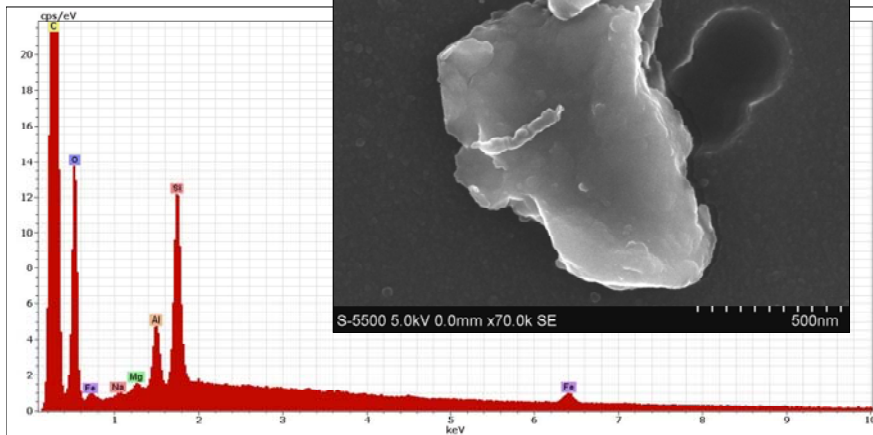


**SEM Images & Spectra
Yakima 2006
Dirt Road, Site 1**

Small circular dots on
Nuclepore membrane filter
approximately 0.4 μm in
diameter

App. C (a to I)
Sample # Y47N007

Desert Research Institute
RJ Lee Group Project No. TEH1004253

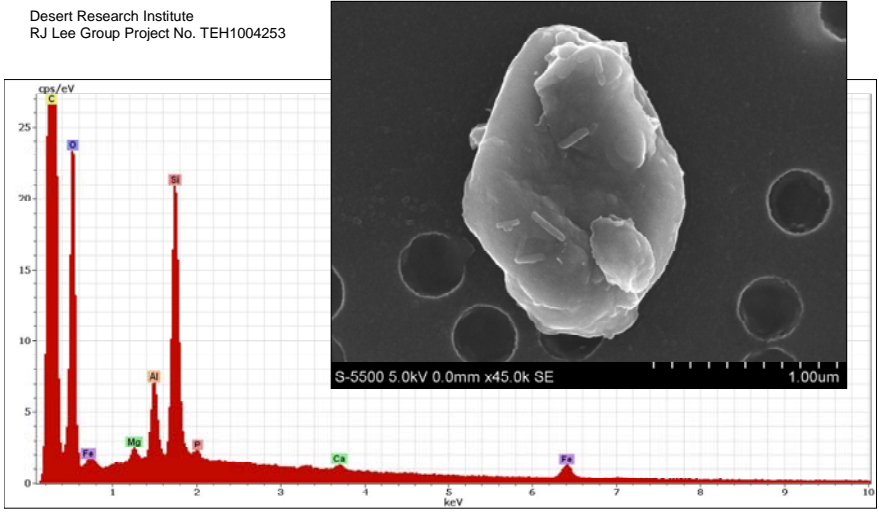
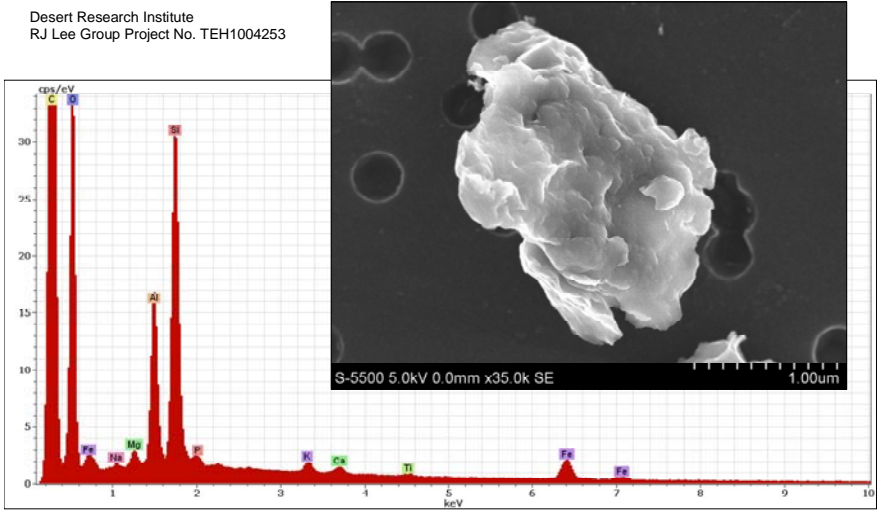


Y47N007 Yakima 2006 Site 1 Dirt Road

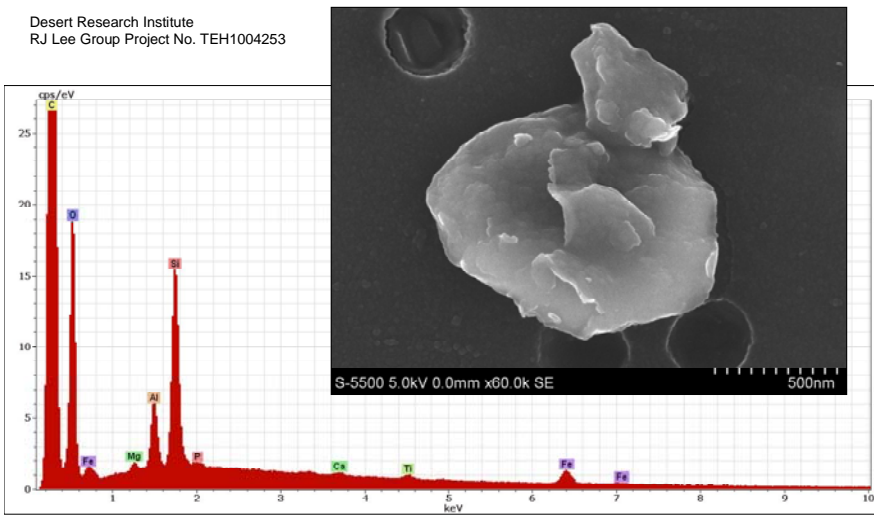
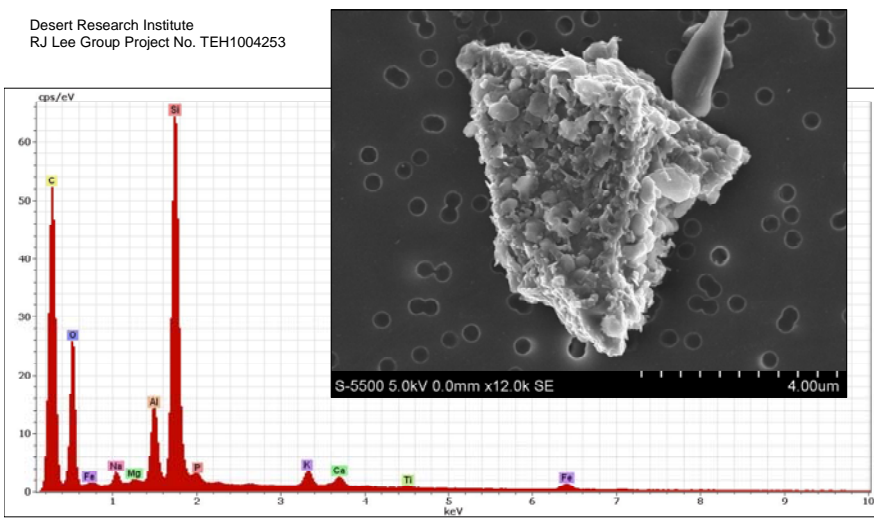
App. C(a)

Y47N007, Yakima 2006
Dirt Road, Site 1
Flake of possibly biotite, with
coating of clay minerals,
possibly montmorillonite

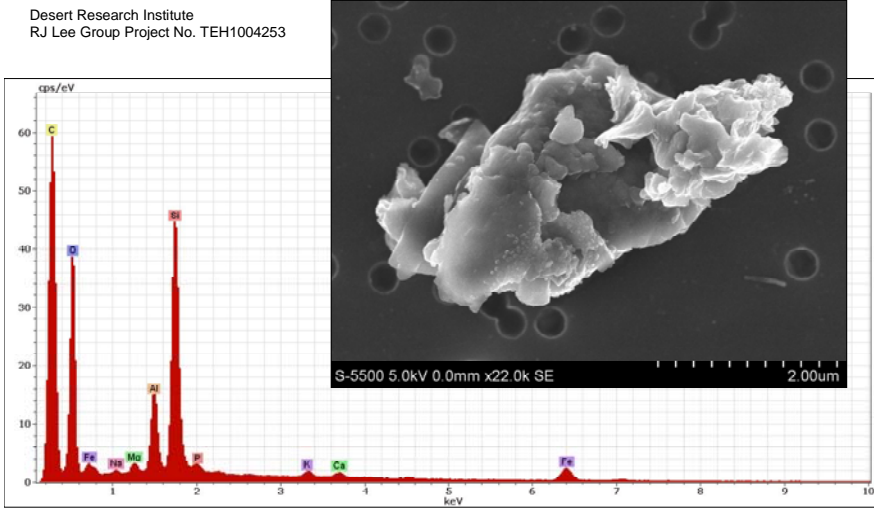
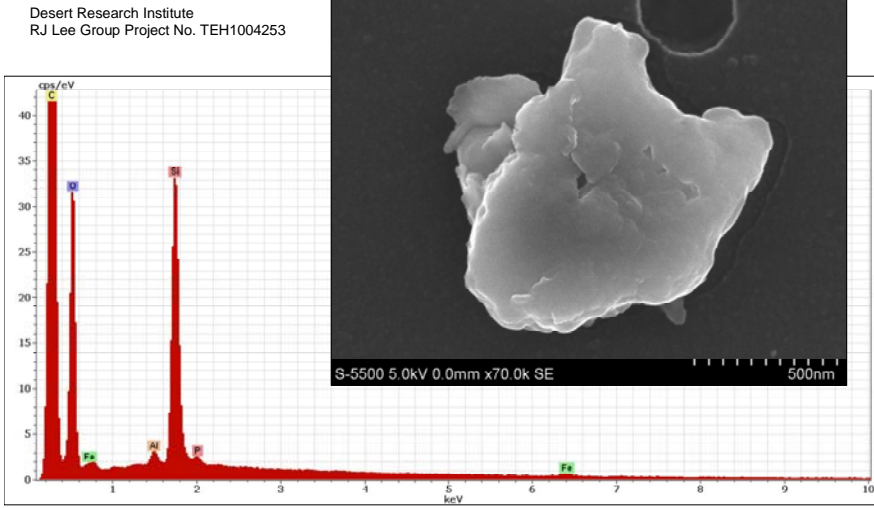
Appendix C – SEM, Secondary Electron Images & Spectra, Yakima 2006, Dirt Road, Site 1

<p>Desert Research Institute RJ Lee Group Project No. TEH1004253</p>  <p>The SEM image shows a large, irregularly shaped flake with a layered, crystalline appearance. The EDS spectrum shows a high concentration of Carbon (C) and Oxygen (O), with significant peaks for Silicon (Si) and Aluminum (Al). Other elements like Magnesium (Mg), Potassium (K), Calcium (Ca), and Iron (Fe) are present in much lower concentrations.</p> <p>Y47N007 Yakima 2006 Site 1 Dirt Road</p>	<p>App. C(b) Y47N007, Yakima 2006 Dirt Road, Site 1 Flake of possibly biotite, with coating of clay minerals, possibly montmorillonite, and needles of the clay mineral palygorskite</p>
<p>Desert Research Institute RJ Lee Group Project No. TEH1004253</p>  <p>The SEM image shows a complex, intergrown structure of clay minerals. The EDS spectrum shows a high concentration of Carbon (C) and Oxygen (O), with significant peaks for Silicon (Si) and Aluminum (Al). Other elements like Magnesium (Mg), Potassium (K), Calcium (Ca), Titanium (Ti), and Iron (Fe) are present in much lower concentrations.</p> <p>Y47N007 Yakima 2006 Site 1 Dirt Road</p>	<p>App. C(c) Y47N007, Yakima 2006 Dirt Road, Site 1 Intergrowth of clay minerals, possibly kaolinite, together with montmorillonite-illite</p>

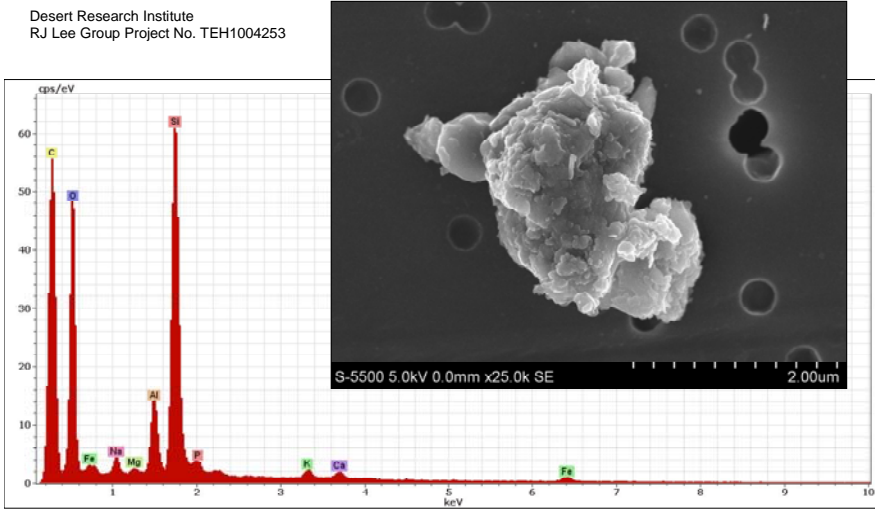
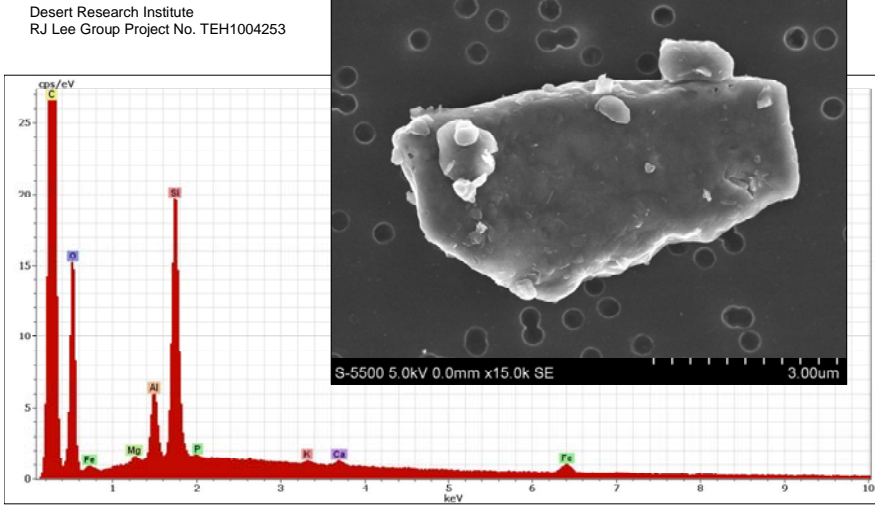
Appendix C – SEM, Secondary Electron Images & Spectra, Yakima 2006, Dirt Road, Site 1

<p>Desert Research Institute RJ Lee Group Project No. TEH1004253</p>  <p>S-5500 5.0kV 0.0mm x60.0k SE</p> <p>Y47N007 Yakima 2006 Site 1 Dirt Road</p>	<p>App. C(d) Y47N007, Yakima 2006 Site 1, Dirt Road Unknown mineral, possibly biotite, with coating of the clay mineral kaolinite and montmorillonite-illite</p>
<p>Desert Research Institute RJ Lee Group Project No. TEH1004253</p>  <p>S-5500 5.0kV 0.0mm x12.0k SE</p> <p>Y47N007 Yakima 2006 Site 1 Dirt Road</p>	<p>App. C(e) Y47N007, Yakima06 Site 1, Dirt Road Tabular crystal of possibly plagioclase feldspar, with coating of bladed clay crystals, possibly kaolinite and montmorillonite-illite</p>

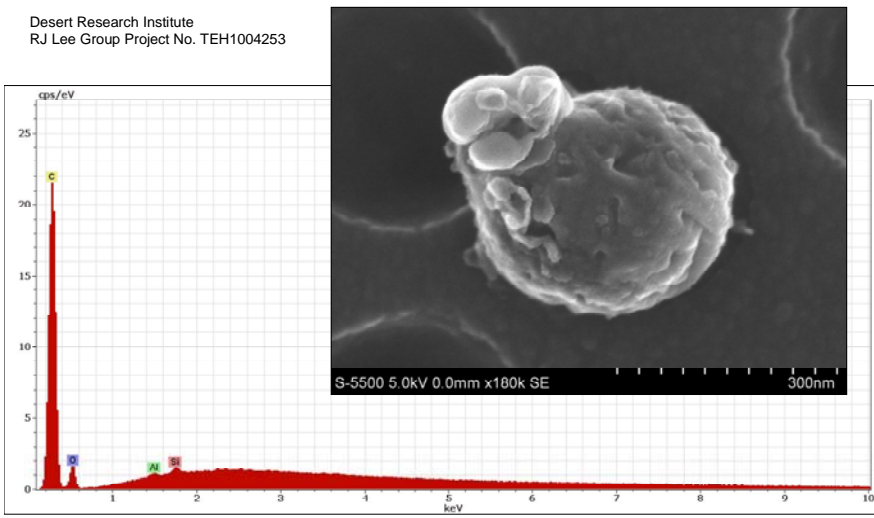
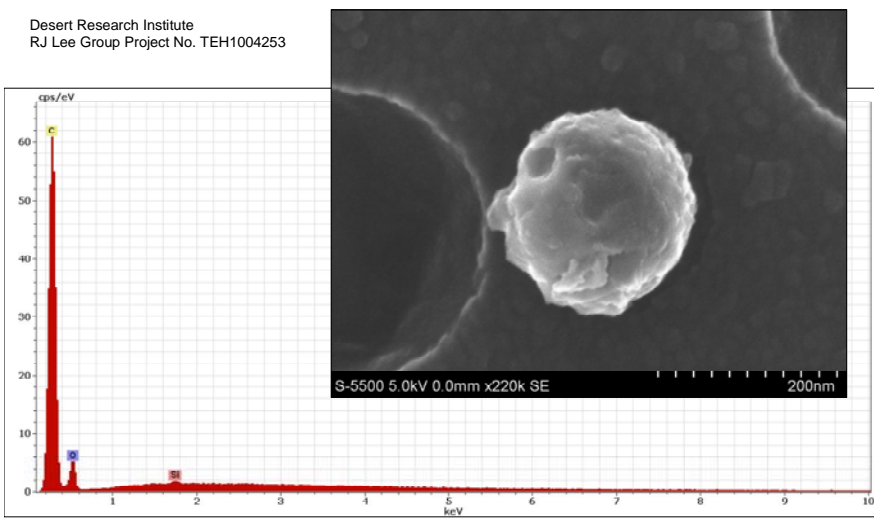
Appendix C – SEM, Secondary Electron Images & Spectra, Yakima 2006, Dirt Road, Site 1

<p>Desert Research Institute RJ Lee Group Project No. TEH1004253</p>  <p>Y47N007 Yakima 2006 Site 1 Dirt Road</p>	<p>App. C(f) Y47N007, Yakima 2006 Dirt Road, Site 1 Biotite?, with coating of clay minerals, possibly montmorillonite-illite</p>
<p>Desert Research Institute RJ Lee Group Project No. TEH1004253</p>  <p>Y47N007 Yakima 2006 Site 1 Dirt Road</p>	<p>App. C(g) Y47N007, Yakima 2006 Dirt Road, Site 1 Quartz with small amount of clay minerals on surface, possibly montmorillonite</p>

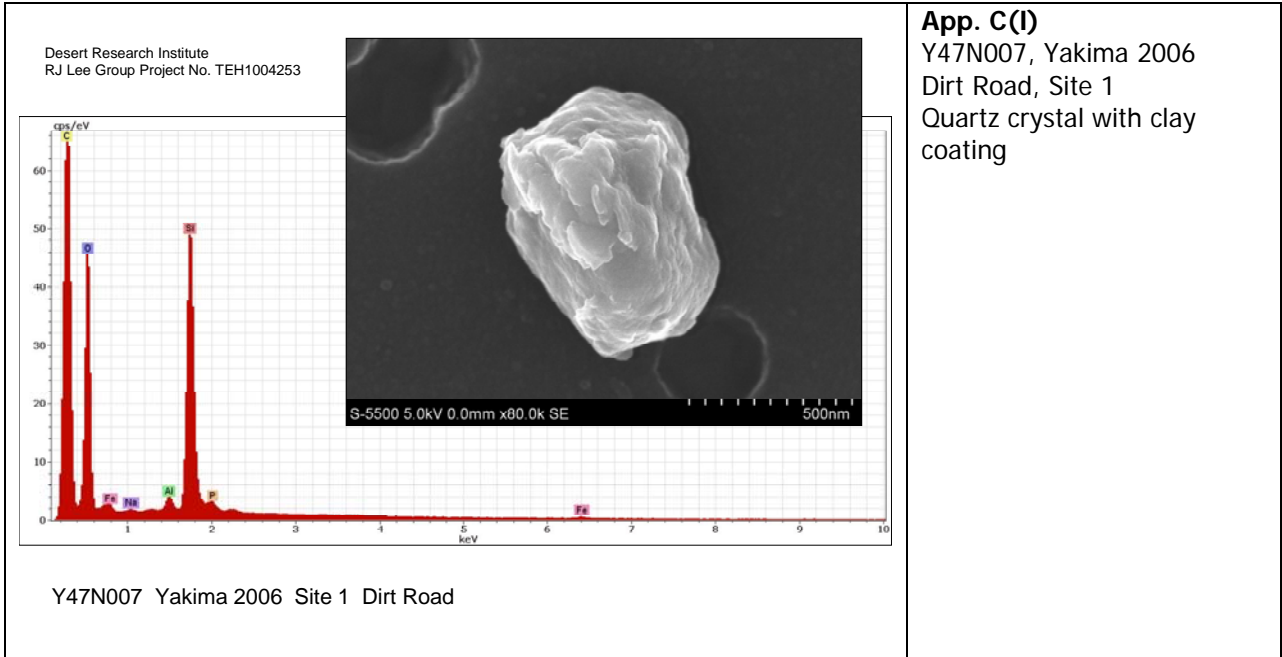
Appendix C – SEM, Secondary Electron Images & Spectra, Yakima 2006, Dirt Road, Site 1

<p>Desert Research Institute RJ Lee Group Project No. TEH1004253</p>  <p>Y47N007 Yakima 2006 Site 1 Dirt Road</p>	<p>App. C(h) Y47N007, Yakima 2006 Dirt Road, Site 1 Plagioclase feldspar? crystal with coating of clay minerals, possibly montmorillonite-illite</p>
<p>Desert Research Institute RJ Lee Group Project No. TEH1004253</p>  <p>Y47N007 Yakima 2006 Site 1 Dirt Road</p>	<p>App. C(i) Y47N007, Yakima 2006 Dirt Road, Site 1 Biotite crystal?, with coating of clay minerals, possibly montmorillonite-illite</p>

Appendix C – SEM, Secondary Electron Images & Spectra, Yakima 2006, Dirt Road, Site 1

<p>Desert Research Institute RJ Lee Group Project No. TEH1004253</p>  <p>The SEM image shows a spherical carbon particle with several smaller, irregular silicate-like particles attached to its surface. The EDS spectrum shows a dominant peak for Carbon (C) at approximately 0.27 keV, with smaller peaks for Oxygen (O) at 0.51 keV, Magnesium (Mg) at 1.30 keV, and Silicon (Si) at 1.74 keV. The x-axis is labeled 'keV' and ranges from 0 to 10. The y-axis is labeled 'cps/eV' and ranges from 0 to 25. The SEM image includes a scale bar of 300nm and technical parameters: S-5500 5.0kV 0.0mm x100k SE.</p> <p>Y47N007 Yakima 2006 Site 1 Dirt Road</p>	<p>App. C(j) Y47N007, Yakima 2006 Dirt Road, Site 1 Sub-micron carbon sphere with silicate (clay?) particles attached</p>
<p>Desert Research Institute RJ Lee Group Project No. TEH1004253</p>  <p>The SEM image shows a single, spherical carbon particle with a textured surface. The EDS spectrum shows a dominant peak for Carbon (C) at approximately 0.27 keV, with smaller peaks for Oxygen (O) at 0.51 keV and Silicon (Si) at 1.74 keV. The x-axis is labeled 'keV' and ranges from 0 to 10. The y-axis is labeled 'cps/eV' and ranges from 0 to 60. The SEM image includes a scale bar of 200nm and technical parameters: S-5500 5.0kV 0.0mm x220k SE.</p> <p>Y47N007 Yakima 2006 Site 1 Dirt Road</p>	<p>App. C(k) Y47N007, Yakima 2006 Dirt Road, Site 1 Sub-micron carbon sphere</p>

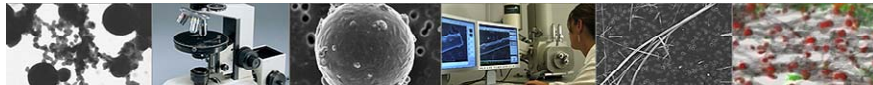
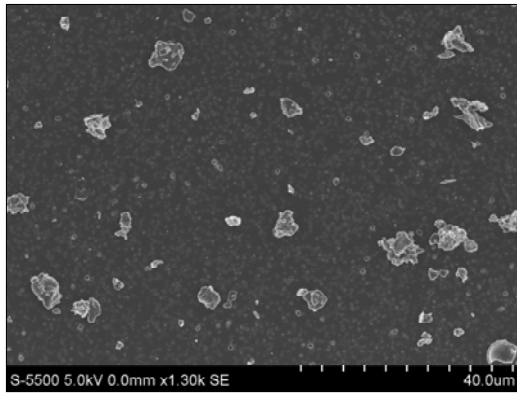
Appendix C – SEM, Secondary Electron Images & Spectra, Yakima 2006, Dirt Road, Site 1



Appendix C – SEM, Secondary Electron Images & Spectra, Yakima 2006, Dirt Road, Site 1

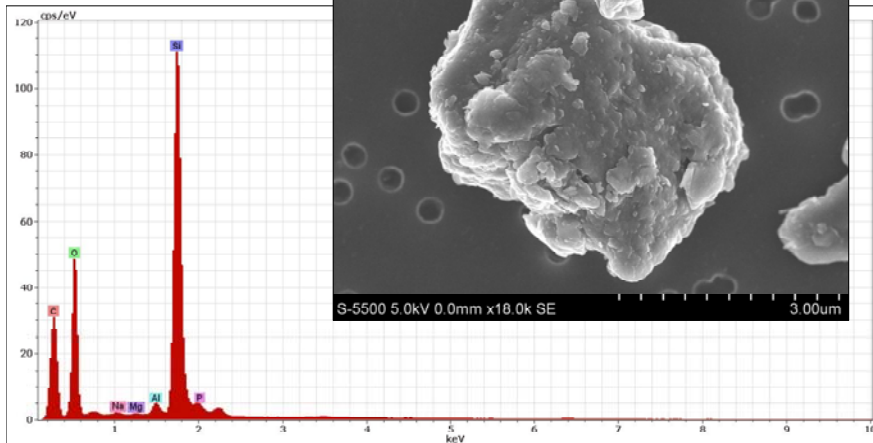


Y47N010 Yakima 2006 Site 1 Dirt Road



App. C(m)
Filter # Y47N010

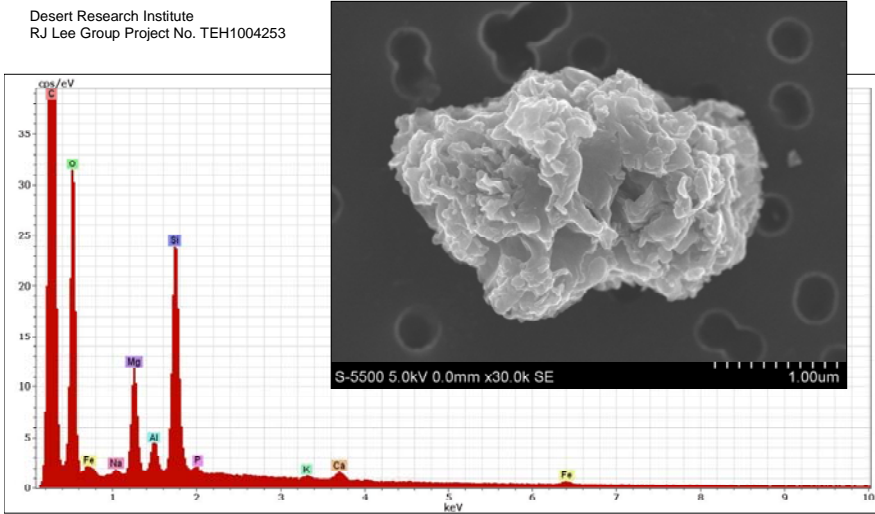
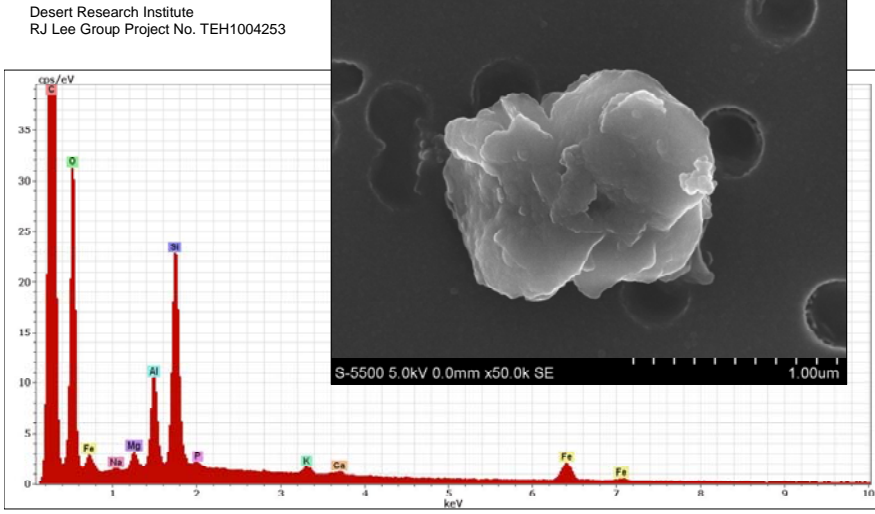
Desert Research Institute
RJ Lee Group Project No. TEH1004253



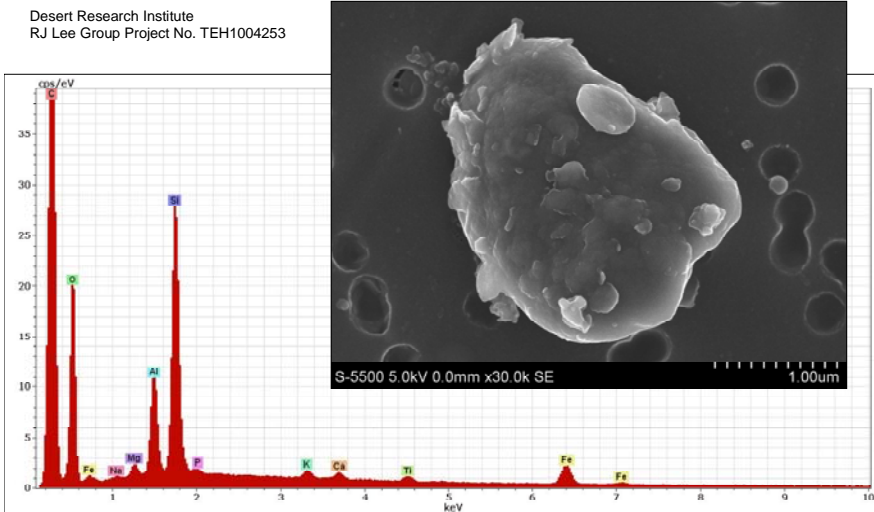
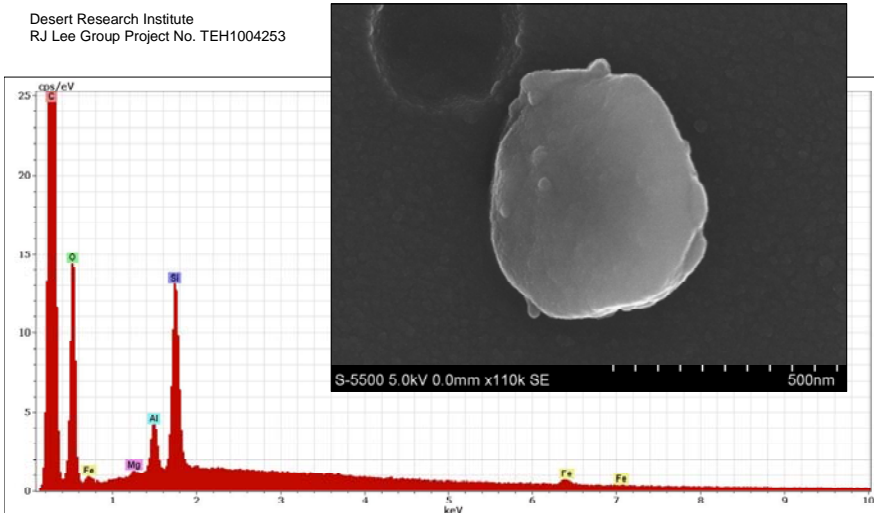
Y47N010 Yakima 2006 Site 1 Dirt Road

App. C(n)
Y47N010, Yakima06
Dirt Road, Site 1
Quartz crystal with clay coating

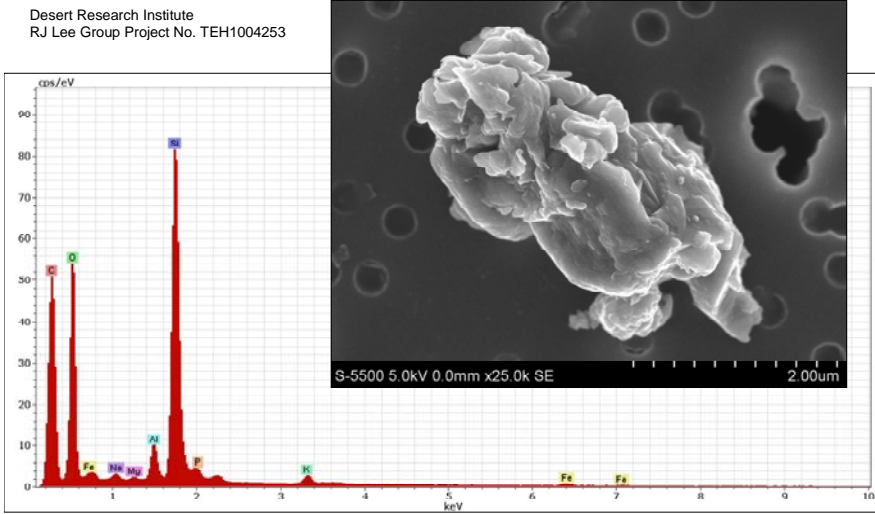
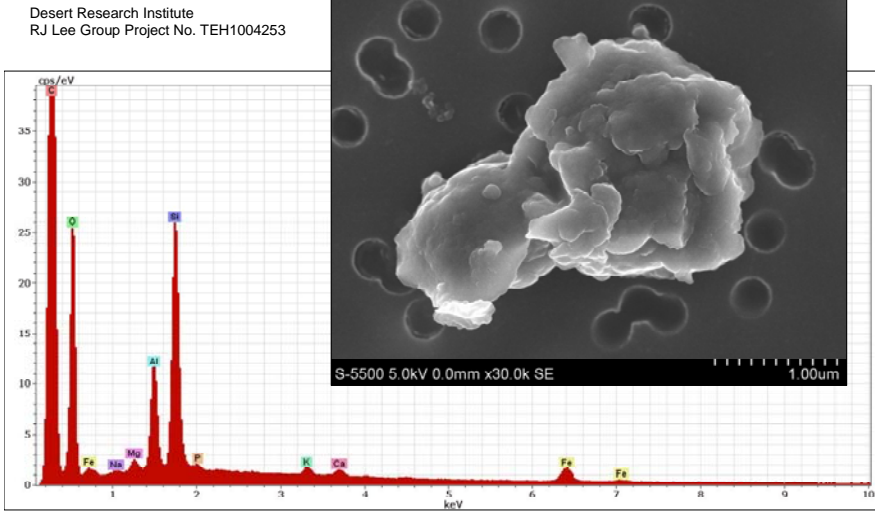
Appendix C – SEM, Secondary Electron Images & Spectra, Yakima 2006, Dirt Road, Site 1

<p>Desert Research Institute R.J. Lee Group Project No. TEH1004253</p>  <p>S-5500 5.0kV 0.0mm x30.0k SE</p> <p>Y47N010 Yakima 2006 Site 1 Dirt Road</p>	<p>App. C(o) Y47N010, Yakima 2006 Dirt Road, Site 1 Intergrowth of clay minerals, possibly montmorillonite- illite, and magnesite?</p>
<p>Desert Research Institute R.J. Lee Group Project No. TEH1004253</p>  <p>S-5500 5.0kV 0.0mm x50.0k SE</p> <p>Y47N010 Yakima 2006 Site 1 Dirt Road</p>	<p>App. C(p) Y47N0010, Yakima06 Dirt Road, Site 1 Biotite with clay mineral coating, possibly montmorillonite-illite</p>

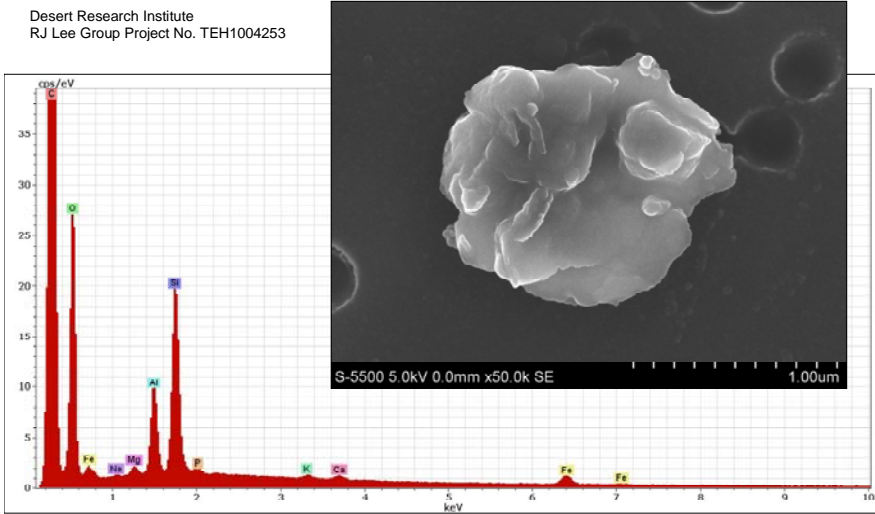
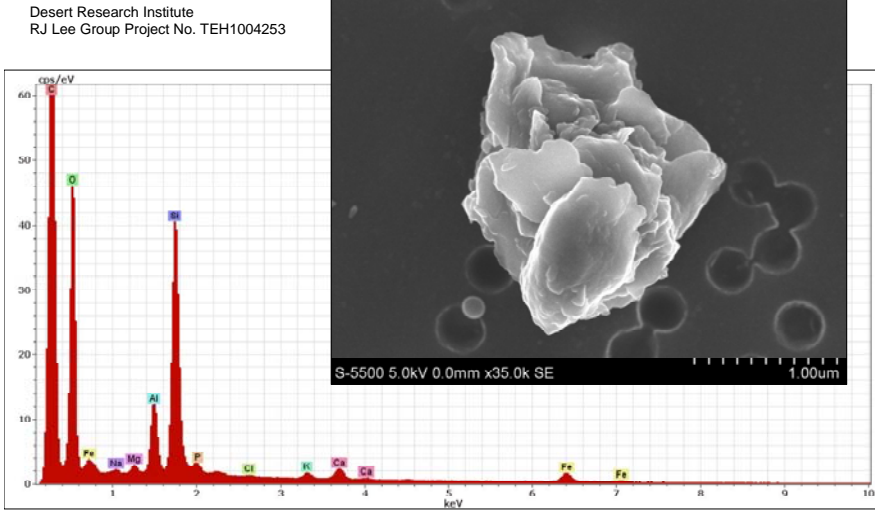
Appendix C – SEM, Secondary Electron Images & Spectra, Yakima 2006, Dirt Road, Site 1

<p>Desert Research Institute R.J. Lee Group Project No. TEH1004253</p>  <p>S-5500 5.0kV 0.0mm x30.0k SE</p> <p>Y47N010 Yakima 2006 Site 1 Dirt Road</p>	<p>App. C(q) Y47N010, Yakima 2006 Dirt Road, Site 1 Biotite with clay mineral coating, possibly montmorillonite-illite</p>
<p>Desert Research Institute R.J. Lee Group Project No. TEH1004253</p>  <p>S-5500 5.0kV 0.0mm x110k SE</p> <p>Y47N010 Yakima 2006 Site 1 Dirt Road</p>	<p>App. C(r) Y47N010, Yakima 2006 Dirt Road, Site 1 Sub-micron flake of carbon and clay, possibly montmorillonite</p>

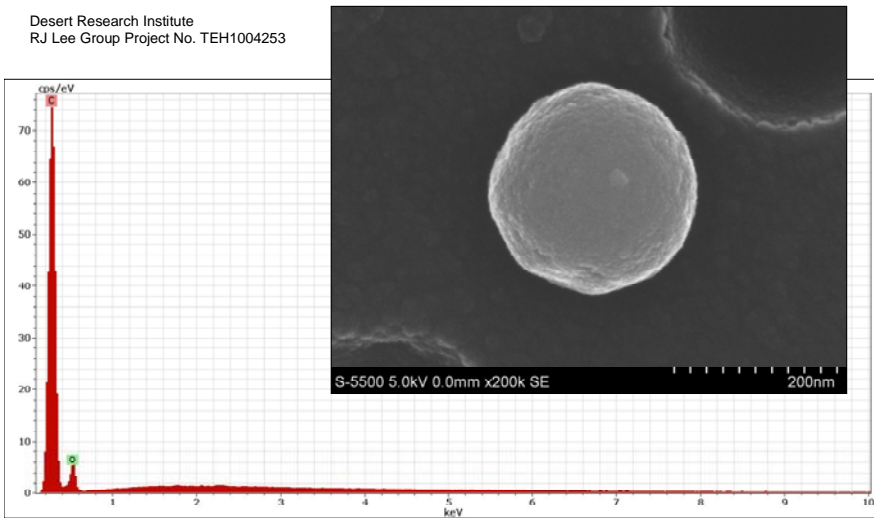
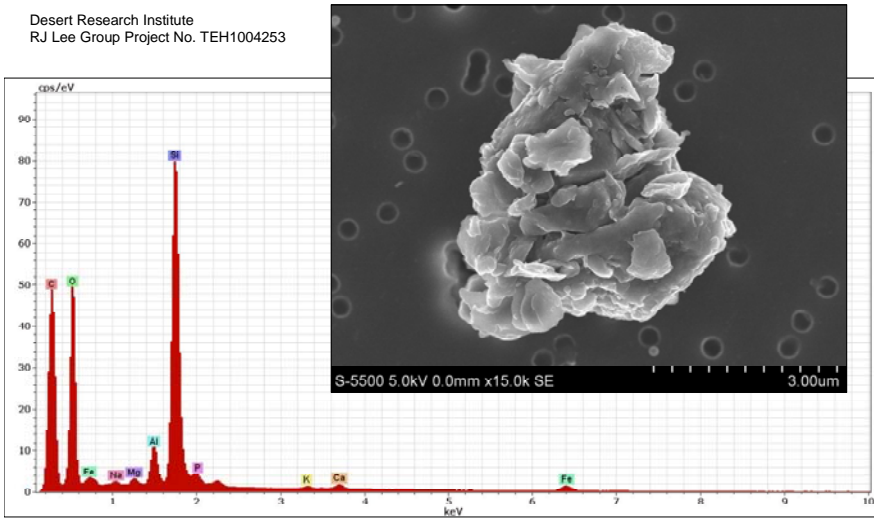
Appendix C – SEM, Secondary Electron Images & Spectra, Yakima 2006, Dirt Road, Site 1

<p>Desert Research Institute R.J. Lee Group Project No. TEH1004253</p>  <p>The SEM image shows a large, irregularly shaped, light-colored crystal with a rough, porous surface texture, surrounded by smaller, smoother particles. The EDS spectrum shows a prominent Si peak at approximately 1.74 keV, with smaller peaks for O, Al, Fe, and K. The x-axis is labeled 'keV' and ranges from 0 to 10. The y-axis is labeled 'cps/eV' and ranges from 0 to 90.</p> <p>Y47N010 Yakima 2006 Site 1 Dirt Road</p>	<p>App. C(s) Y47N010, Yakima 2006 Dirt Road, Site 1 Quartz crystal? with coating of clay minerals, possibly montmorillonite-illite</p>
<p>Desert Research Institute R.J. Lee Group Project No. TEH1004253</p>  <p>The SEM image shows a large, irregularly shaped, light-colored crystal with a rough, porous surface texture, surrounded by smaller, smoother particles. The EDS spectrum shows a prominent Si peak at approximately 1.74 keV, with smaller peaks for O, Al, Fe, and K. The x-axis is labeled 'keV' and ranges from 0 to 10. The y-axis is labeled 'cps/eV' and ranges from 0 to 35.</p> <p>Y47N010 Yakima 2006 Site 1 Dirt Road</p>	<p>App. C(t) Y47N010, Yakima 2006 Dirt Road, Site 1 Biotite, with coating of clay minerals, possibly montmorillonite-illite</p>

Appendix C – SEM, Secondary Electron Images & Spectra, Yakima 2006, Dirt Road, Site 1

<p>Desert Research Institute RJ Lee Group Project No. TEH1004253</p>  <p>Y47N010 Yakima 2006 Site 1 Dirt Road</p>	<p>App. C(u) Y47N010, Yakima 2006 Dirt Road, Site 1 Possible feldspar or biotite with coating of clay minerals</p>
<p>Desert Research Institute RJ Lee Group Project No. TEH1004253</p>  <p>Y47N010 Yakima 2006 Site 1 Dirt Road</p>	<p>App. C(v) Y47N010, Yakima 2006 Dirt Road, Site 1 Flakes of clay minerals, possibly montmorillonite</p>

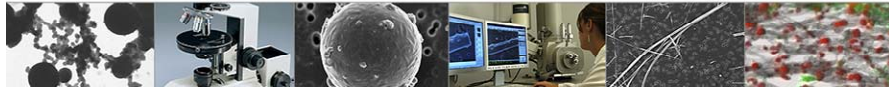
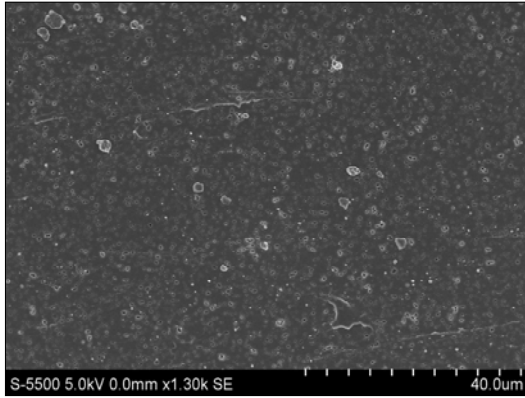
Appendix C – SEM, Secondary Electron Images & Spectra, Yakima 2006, Dirt Road, Site 1

<p>Desert Research Institute RJ Lee Group Project No. TEH1004253</p>  <p>Y47N010 Yakima 2006 Site 1 Dirt Road</p>	<p>App. C(w) Y47N010, Yakima 2006 Dirt Road, Site 1 Sub-micron spheroid of carbon</p>
<p>Desert Research Institute RJ Lee Group Project No. TEH1004253</p>  <p>Y47N010 Yakima 2006 Site 1 Dirt Road</p>	<p>App. C(x) Y47N010, Yakima 2006 Dirt Road, Site 1 Clay mineral cluster, possibly of montmorillonite, coating possibly a feldspar crystal</p>

Appendix D – SEM, Secondary Electron Images & Spectra, YPG2007, Desert Pavement, Site 1



Y47N025 Yuma 2007 Site 1 Desert Pavement



SEM Images & Spectra

Yuma 2007

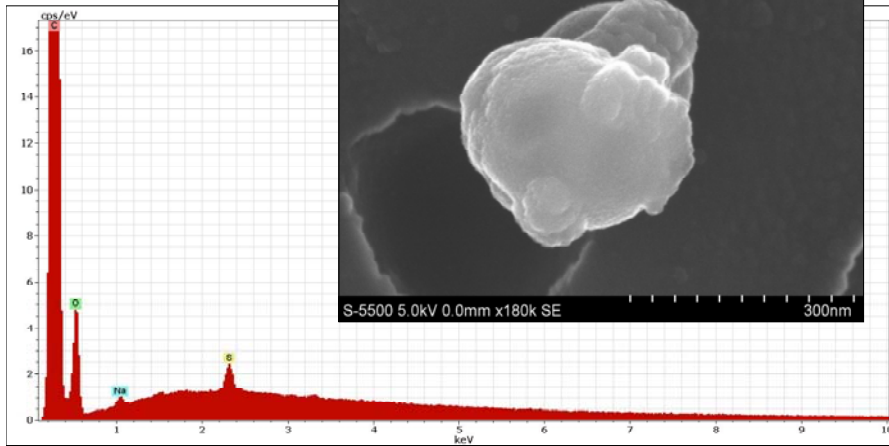
Desert Pavement 1

Small dots on Nucleopore membrane filter approximately 0.4 μm in diameter

App. D (a to I)

Filter # Y47N025

Desert Research Institute
RJ Lee Group Project No. TEH1004253

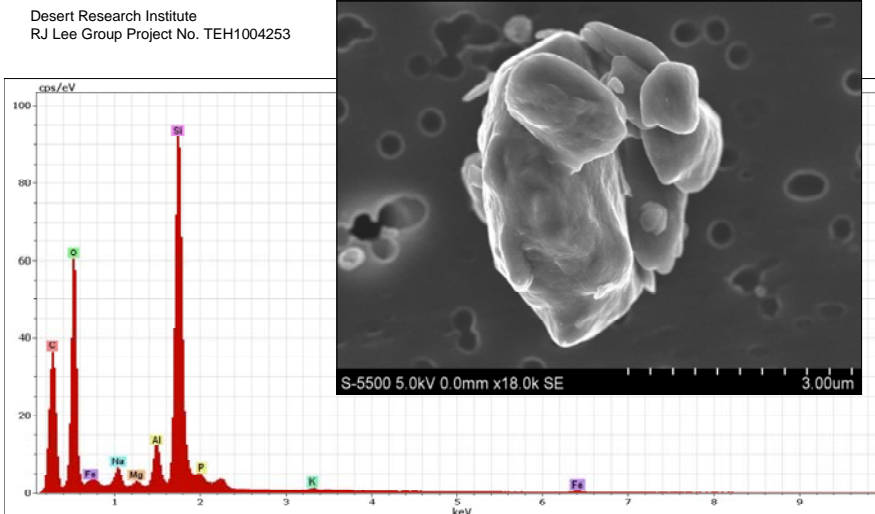
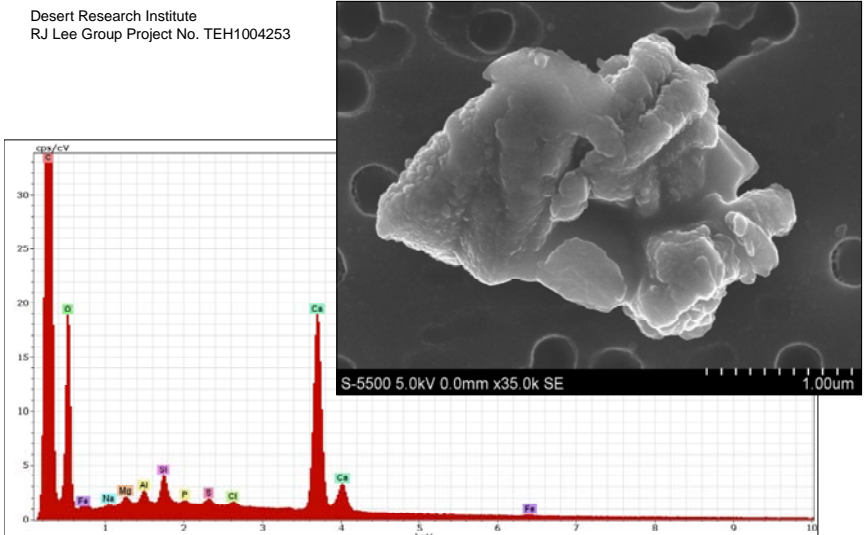


Y47N025 Yuma 2007 Site 1 Desert Pavement

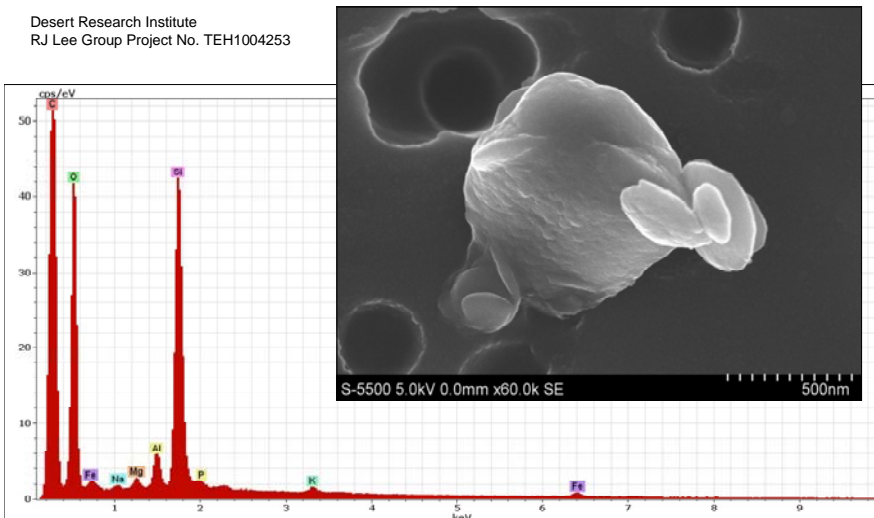
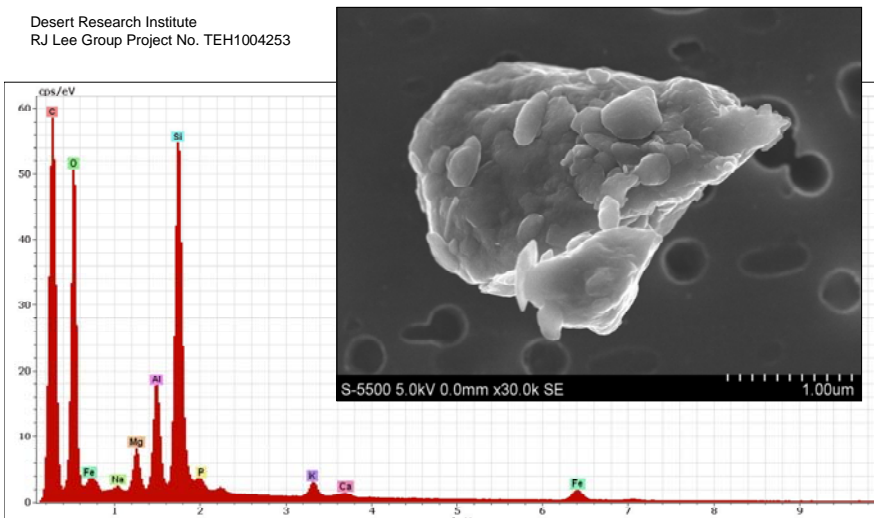
App. D(a)

Y47N025, Yuma 2007
Desert Pavement, Site 1,
Sub-micron carbon spheroid
with sodium sulfate coating

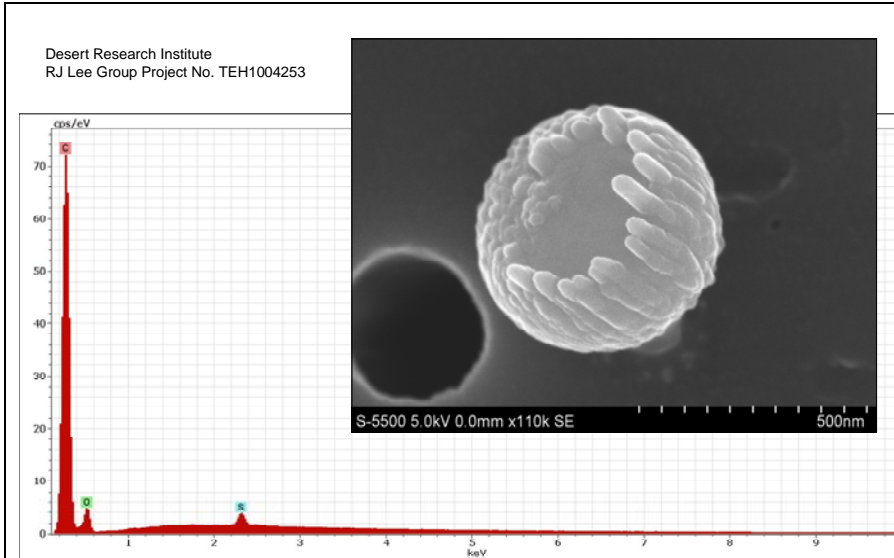
Appendix D – SEM, Secondary Electron Images & Spectra, YPG2007, Desert Pavement, Site 1

<p>Desert Research Institute RJ Lee Group Project No. TEH1004253</p>  <p>S-5500 5.0kV 0.0mm x18.0k SE 3.00um</p>	<p>App. D(b) Y47N025, Yuma 2007 Desert Pavement, Site 1 Irregular quartz particle with clay coating, possibly montmorillonite-illite, and sodium and potassium sulfate</p>
<p>Y47N025 Yuma 2007 Site 1 Desert Pavement</p>	
<p>Desert Research Institute RJ Lee Group Project No. TEH1004253</p>  <p>S-5500 5.0kV 0.0mm x35.0k SE 1.00um</p>	<p>App. D(c) Y47N025, Yuma 2007 Desert Pavement, Site 1 Rhombohedral crystal of calcite with dissolution cavities and surface re-crystallizations</p>
<p>Y47N025 Yuma 2007 Site 1 Desert Pavement</p>	

Appendix D – SEM, Secondary Electron Images & Spectra, YPG2007, Desert Pavement, Site 1

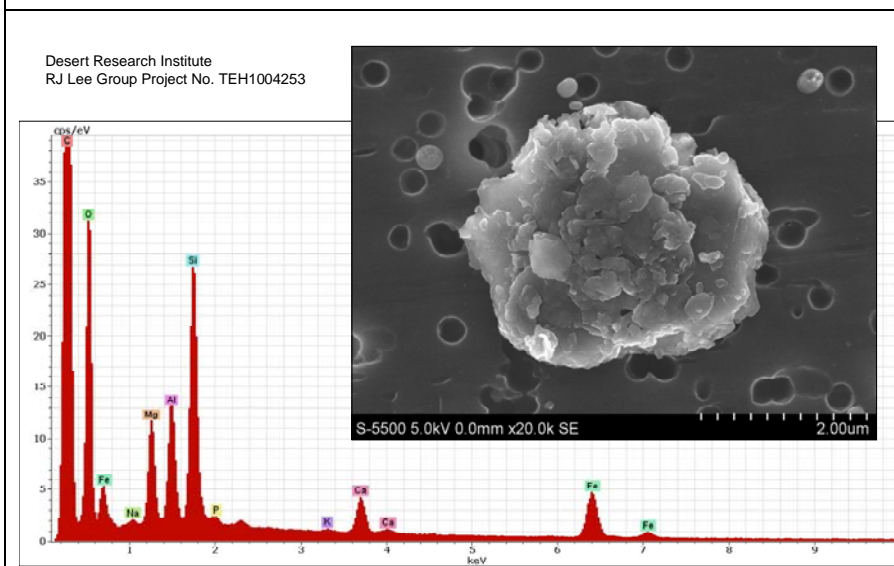
<p>Desert Research Institute RJ Lee Group Project No. TEH1004253</p>  <p>S-5500 5.0kV 0.0mm x60.0k SE</p>	<p>App. D(d) Y47N025, Yuma 2007 Desert Pavement, Site 1 Sub-micron particle of biotite? with surface coating of clay, possibly montmorillonite-illite</p>
<p>Y47N025 Yuma 2007 Site 1 Desert Pavement</p>	
<p>Desert Research Institute RJ Lee Group Project No. TEH1004253</p>  <p>S-5500 5.0kV 0.0mm x30.0k SE</p>	<p>App. D(e) Y47N025, Yuma07 Desert Pavement, Site 1 Biotite? with coating of clay minerals, possibly montmorillonite-illite</p>
<p>Y47N025 Yuma 2007 Site 1 Desert Pavement</p>	

Appendix D – SEM, Secondary Electron Images & Spectra, YPG2007, Desert Pavement, Site 1



App. D(f)
Y47N025, Yuma 2007
Desert Pavement, Site 1
Sub-micron carbon particle
with sulfur, possibly biogenic

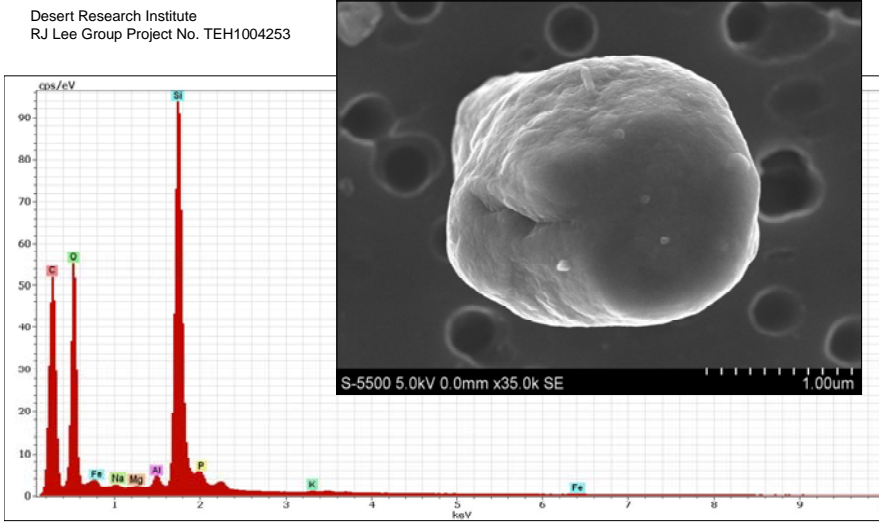
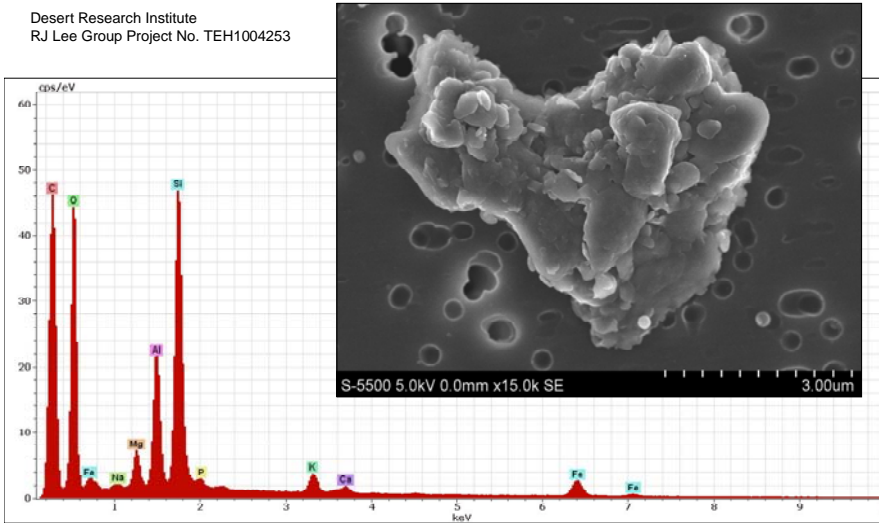
Y47N025 Yuma 2007 Site 1 Desert Pavement



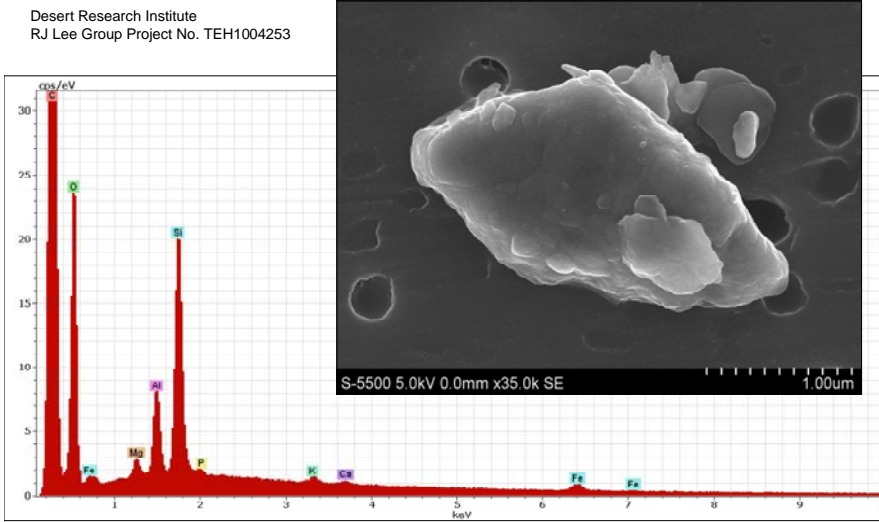
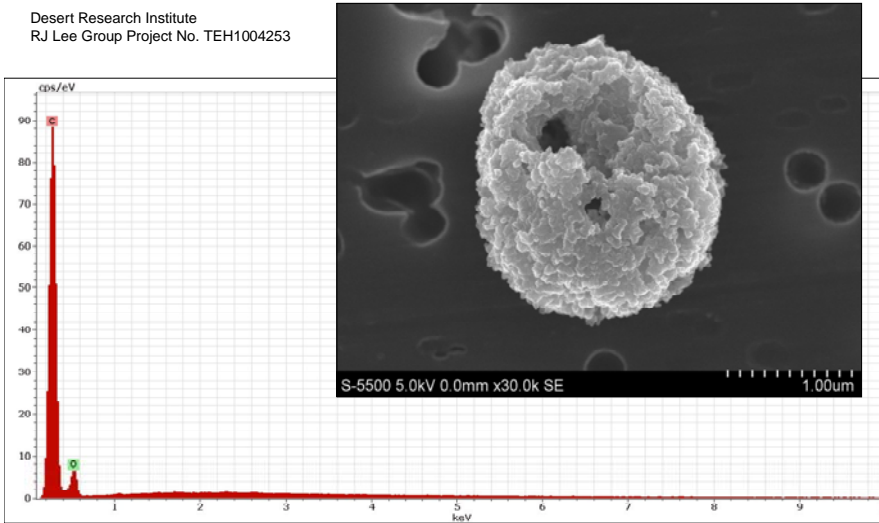
App. D(g)
Y47N025, Yuma 2007
Desert Pavement, Site 1
Plagioclase feldspar? with
coating of clay minerals
montmorillonite-illite, and iron
oxide

Y47N025 Yuma 2007 Site 1 Desert Pavement

Appendix D – SEM, Secondary Electron Images & Spectra, YPG2007, Desert Pavement, Site 1

<p>Desert Research Institute R.J Lee Group Project No. TEH1004253</p>  <p>Y47N025 Yuma 2007 Site 1 Desert Pavement</p>	<p>App. D(h) Y47N025, Yuma07 Desert Pavement, Site 1 Rounded particle of quartz with minor amount of clay minerals</p>
<p>Desert Research Institute R.J Lee Group Project No. TEH1004253</p>  <p>Y47N025 Yuma 2007 Site 1 Desert Pavement</p>	<p>App. D(i) Y47N025, Yuma 2007 Desert Pavement, Site 1 Biotite with coating of clay minerals, possibly montmorillonite-illite</p>

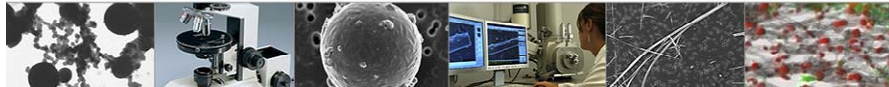
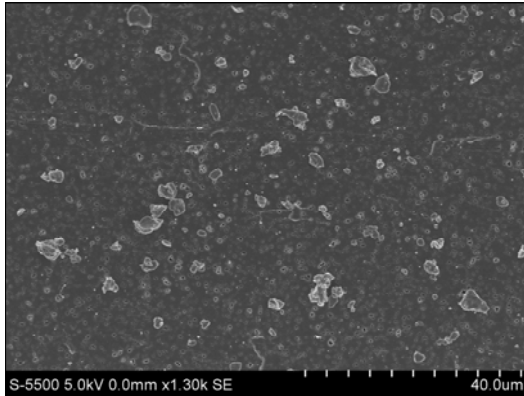
Appendix D – SEM, Secondary Electron Images & Spectra, YPG2007, Desert Pavement, Site 1

<p>Desert Research Institute R.J. Lee Group Project No. TEH1004253</p>  <p>S-5500 5.0kV 0.0mm x35.0k SE 1.00um</p> <p>Y47N025 Yuma 2007 Site 1 Desert Pavement</p>	<p>App. D(k) Y47N025, Yuma 2007 Desert Pavement, Site 1 Biotite with small amount of clay minerals, possibly montmorillonite-illite</p>
<p>Desert Research Institute R.J. Lee Group Project No. TEH1004253</p>  <p>S-5500 5.0kV 0.0mm x30.0k SE 1.00um</p> <p>Y47N025 Yuma 2007 Site 1 Desert Pavement</p>	<p>App. D(l) Y47N025, Yuma 2007 Desert Pavement, Site 1 Spheroid of composited carbon chains, biogenic?</p>

Appendix E – SEM, Secondary Electron Images & Spectra, YPG2007, Disturbed Desert, Site 2



Y47N029 Yuma 2007 Site 2 Disturbed Desert Pavement



**SEM Images & Spectra
Yuma 2007**

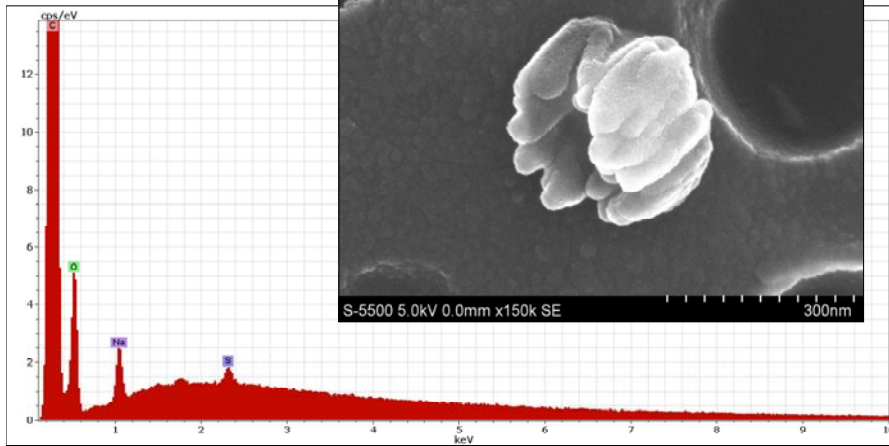
Desert pavement 2

Small dots on Nuclepore membrane filter approximately 0.4 μm in diameter

App. E (a to I)

Filter # Y47N029

Desert Research Institute
RJ Lee Group Project No. TEH1004253



Y47N029 Yuma 2007 Site 2 Disturbed Desert Pavement

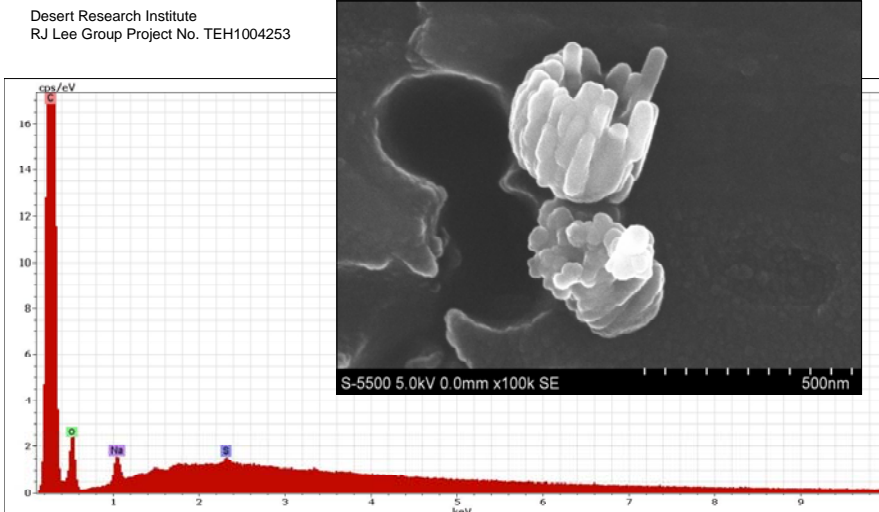
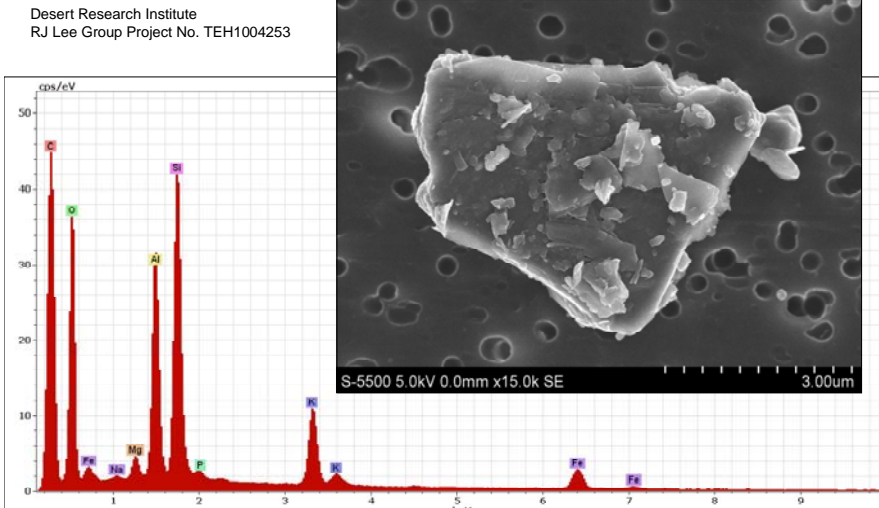
App. E(a)

Y47N029, Yuma 2007

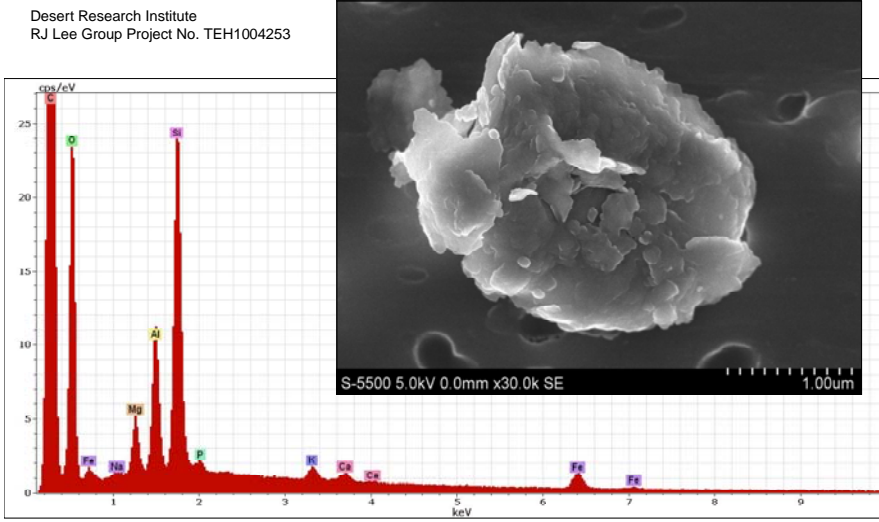
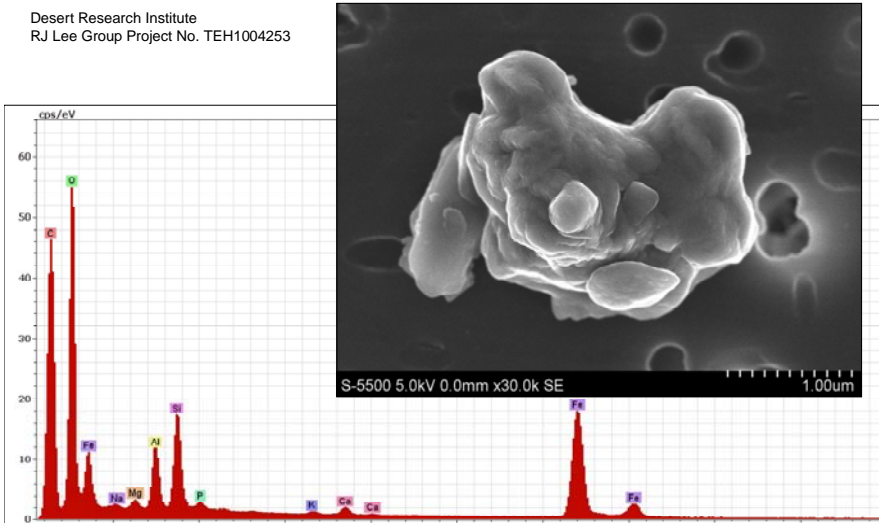
Disturbed desert pavement,
Site 2

Sub-micron carbon particle,
possibly biogenic, with sodium
sulfate,

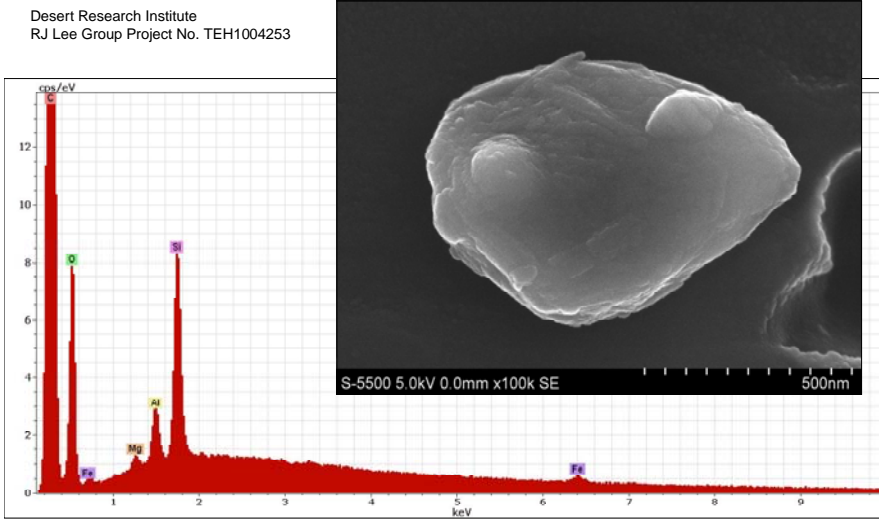
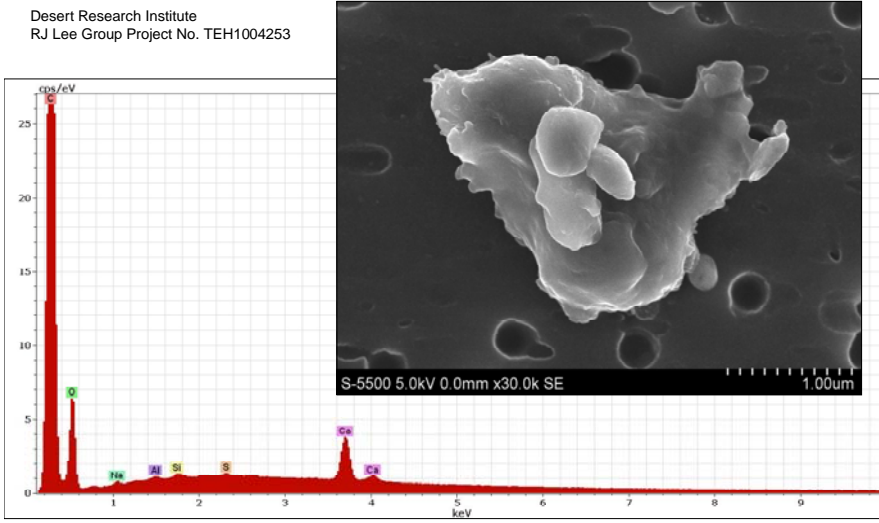
Appendix E – SEM, Secondary Electron Images & Spectra, YPG2007, Disturbed Desert, Site 2

<p>Desert Research Institute R.J. Lee Group Project No. TEH1004253</p>  <p>S-5500 5.0kV 0.0mm x100k SE 500nm</p>	<p>App. E(b) Y47N029, Yuma 2007 Disturbed desert pavement, Site 2 Sub-micron size carbon particles, possibly biogenic, with sodium sulfate,</p>
<p>Y47N029 Yuma 2007 Site 2 Disturbed Desert Pavement</p>	
<p>Desert Research Institute R.J. Lee Group Project No. TEH1004253</p>  <p>S-5500 5.0kV 0.0mm x15.0k SE 3.00um</p>	<p>App. E(c) Y47N029, Yuma 2007 Disturbed desert pavement, Site 2, Biotite mica platelet, with specks of clay minerals, possibly montmorillonite-illite attached</p>
<p>Y47N029 Yuma 2007 Site 2 Disturbed Desert Pavement</p>	

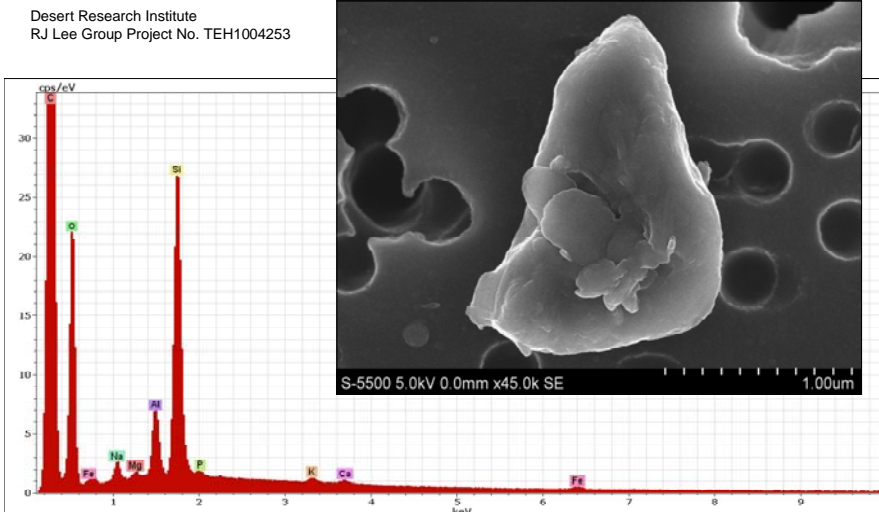
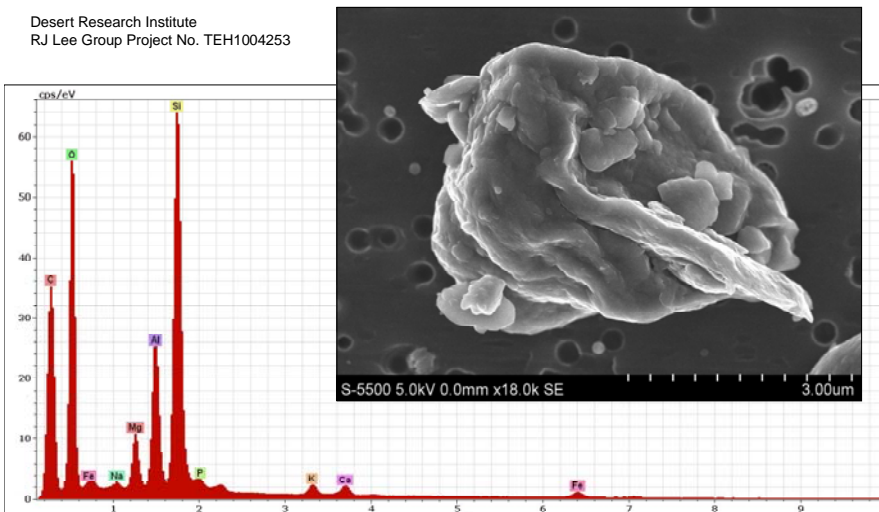
Appendix E – SEM, Secondary Electron Images & Spectra, YPG2007, Disturbed Desert, Site 2

<p>Desert Research Institute R.J. Lee Group Project No. TEH1004253</p>  <p>S-5500 5.0kV 0.0mm x30.0k SE 1.00um</p> <p>Y47N029 Yuma 2007 Site 2 Disturbed Desert Pavement</p>	<p>App. E(d) Y47N029, Yuma 2007 Disturbed desert pavement, Site 2 Biotite, with clay mineral coating, possibly montmorillonite-illite</p>
<p>Desert Research Institute R.J. Lee Group Project No. TEH1004253</p>  <p>S-5500 5.0kV 0.0mm x30.0k SE 1.00um</p> <p>Y47N029 Yuma 2007 Site 2 Disturbed Desert Pavement</p>	<p>App. E(e) Y47N029, Yuma 2007 Disturbed desert pavement, Site 2 Unknown particle with clay mineral coating, possibly montmorillonite-illite, and iron oxide</p>

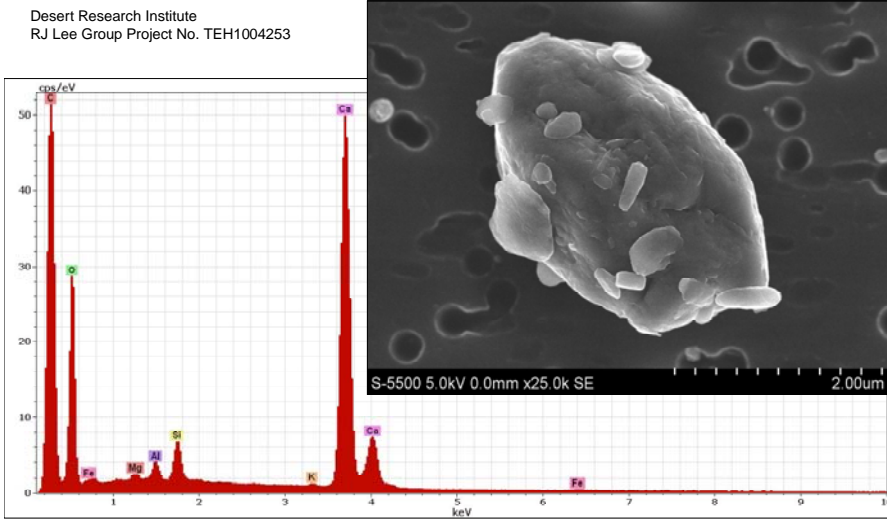
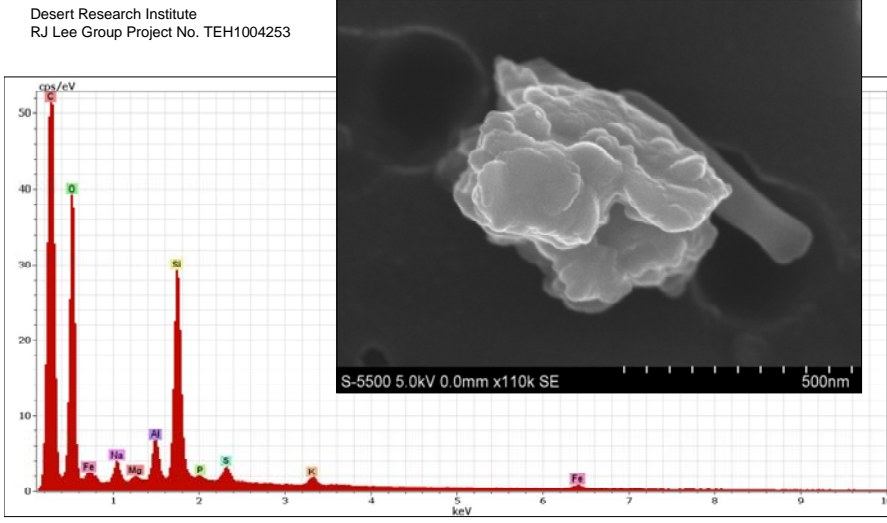
Appendix E – SEM, Secondary Electron Images & Spectra, YPG2007, Disturbed Desert, Site 2

<p>Desert Research Institute R.J Lee Group Project No. TEH1004253</p>  <p>S-5500 5.0kV 0.0mm x100k SE 500nm</p> <p>Y47N029 Yuma 2007 Site 2 Disturbed Desert Pavement</p>	<p>App. E(f) Y47N029, Yuma 2007 Disturbed desert pavement, Site 2 Carbon particle with clay mineral coating, possibly montmorillonite</p>
<p>Desert Research Institute R.J Lee Group Project No. TEH1004253</p>  <p>S-5500 5.0kV 0.0mm x30.0k SE 1.00um</p> <p>Y47N029 Yuma 2007 Site 2 Disturbed Desert Pavement</p>	<p>App. E(g) Y47N029, Yuma 2007 Disturbed desert pavement, Site 2 Calcite and clay minerals</p>

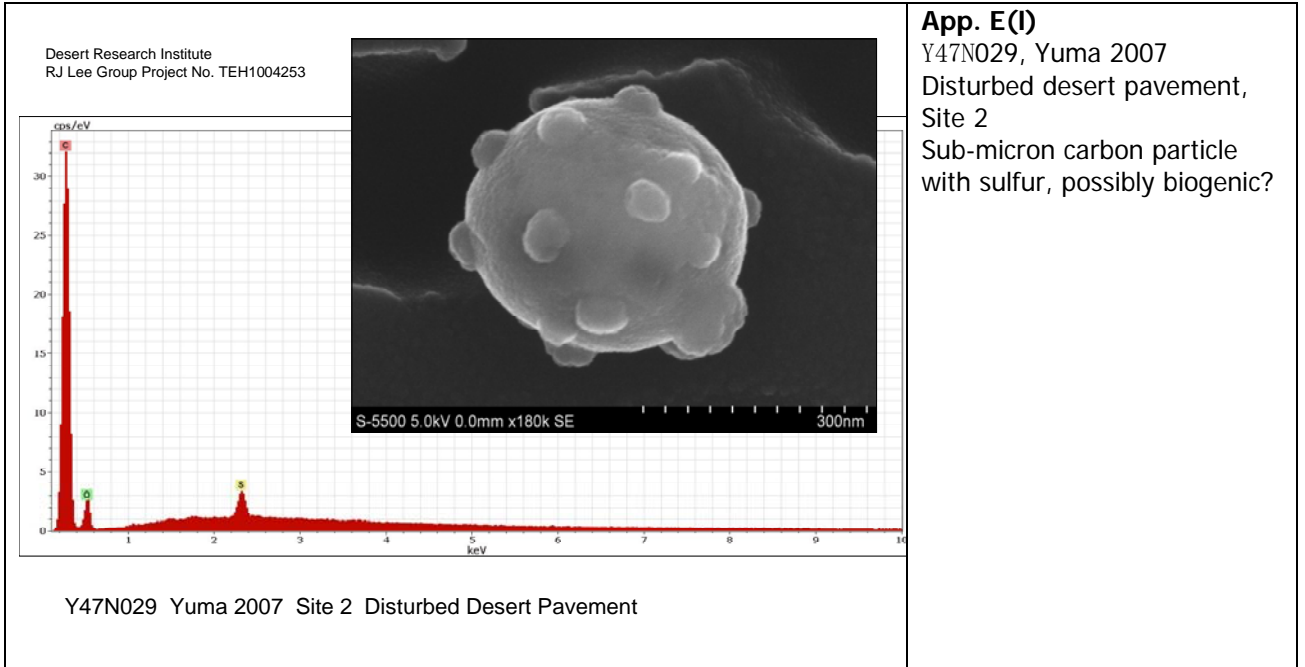
Appendix E – SEM, Secondary Electron Images & Spectra, YPG2007, Disturbed Desert, Site 2

<p>Desert Research Institute RJ Lee Group Project No. TEH1004253</p>  <p>S-5500 5.0kV 0.0mm x45.0k SE 1.00um</p>	<p>App. E(h) Y47N029, Yuma 2007 Disturbed desert pavement, Site 2 Biotite with clay mineral coating, possibly montmorillonite-illite</p>
<p>Y47N029 Yuma 2007 Site 2 Disturbed Desert Pavement</p>	
<p>Desert Research Institute RJ Lee Group Project No. TEH1004253</p>  <p>S-5500 5.0kV 0.0mm x18.0k SE 3.00um</p>	<p>App. E(i) Y47N029, Yuma 2007 Disturbed desert pavement, Site 2 Clay mineral coating, possibly montmorillonite-illite on unknown mineral particle</p>
<p>Y47N029 Yuma 2007 Site 2 Disturbed Desert Pavement</p>	

Appendix E – SEM, Secondary Electron Images & Spectra, YPG2007, Disturbed Desert, Site 2

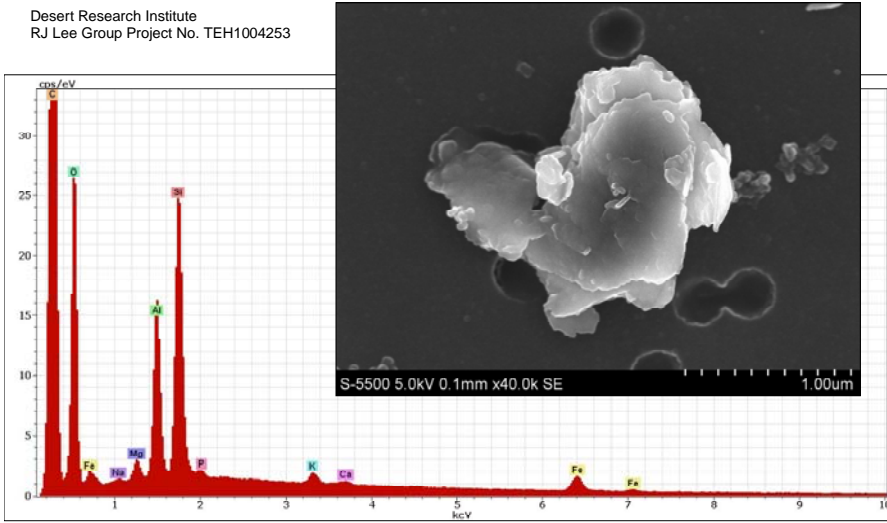
<p>Desert Research Institute R.J Lee Group Project No. TEH1004253</p>  <p>Y47N029 Yuma 2007 Site 2 Disturbed Desert Pavement</p>	<p>App. E(j) Y47N029, Yuma 2007 Disturbed desert pavement, Site 2 Rounded particle of calcite, with clay minerals attached</p>
<p>Desert Research Institute R.J Lee Group Project No. TEH1004253</p>  <p>Y47N029 Yuma 2007 Site 2 Disturbed Desert Pavement</p>	<p>App. E(k) Y47N029, Yuma 2007 Disturbed desert pavement, Site 2, Clay coating of possibly montmorillonite-illite on unknown particle</p>

Appendix E – SEM, Secondary Electron Images & Spectra, YPG2007, Disturbed Desert, Site 2

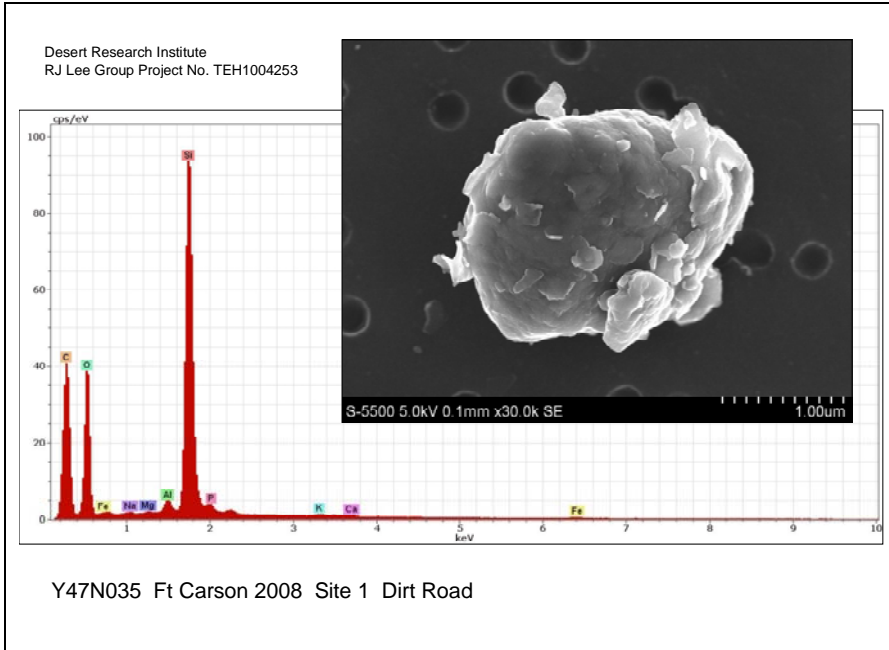


Appendix F – SEM, Secondary Electron Images & Spectra, Ft Carson 2008, Dirt road, Site 1

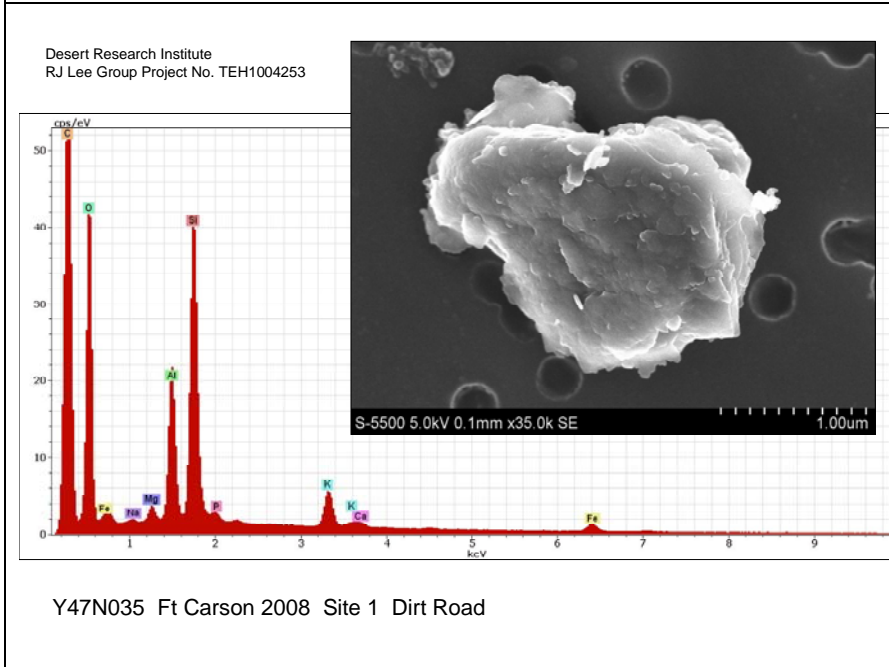
<p>RJG <i>RJ Lee Group, Inc.</i> Analysis. Consulting. Development.</p> <p>Y47N035 Ft Carson 2008 Site 1 Dirt Road</p>  	<p>SEM Images & Spectra Ft Carson 2008 Dirt road 1 Small dots on Nuclepore membrane filter approximately 0.4 μm in diameter App. F (a to o) Filter # Y47N035</p>
--	--

<p>Desert Research Institute RJ Lee Group Project No. TEH1004253</p>  <p>Y47N035 Ft Carson 2008 Site 1 Dirt Road</p>	<p>App. F(a) Y47N035, Ft Carson 2008 Dirt road, Site 1 Biotite flakes, coated with clay minerals, possibly montmorillonite-illite, with needles of palygorskite</p>
--	--

Appendix F – SEM, Secondary Electron Images & Spectra, Ft Carson 2008, Dirt road, Site 1

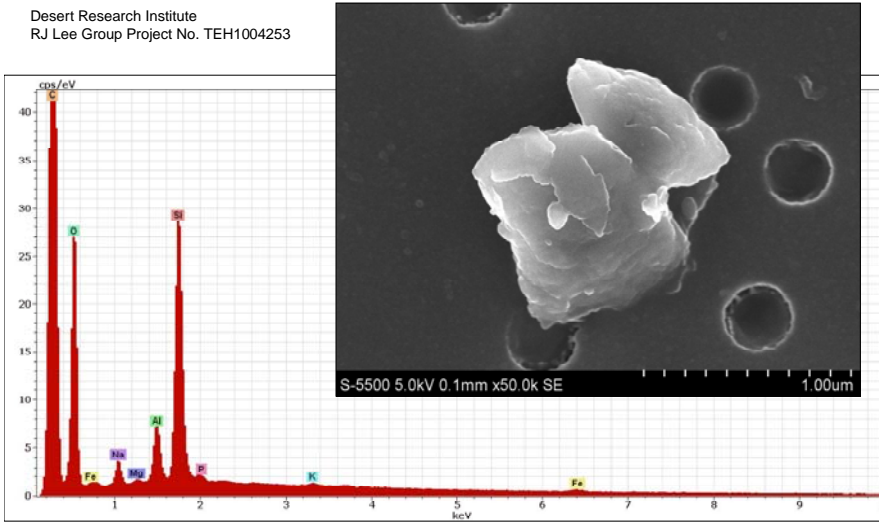
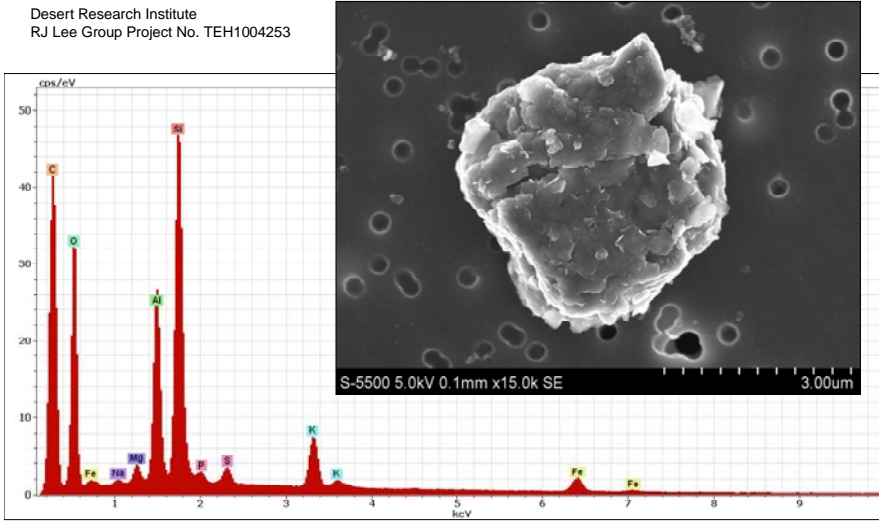


App. F(b)
Y47N035, Ft Carson 2008
Dirt road, Site 1
Rounded quartz grain, partly
coated by clay minerals

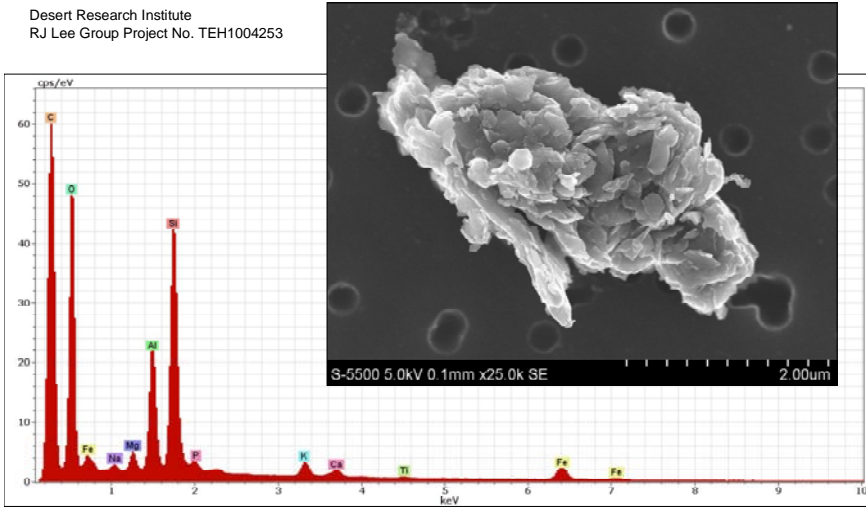
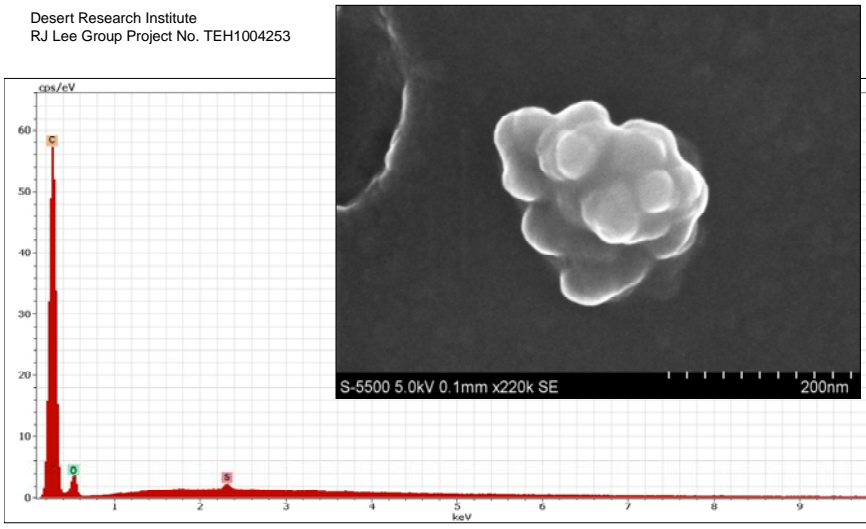


App. F(c)
Y47N035, Ft Carson 2008
Dirt road, Site 1
Biotite?, with small flakes of
clay, possibly
montmorillonite-illite

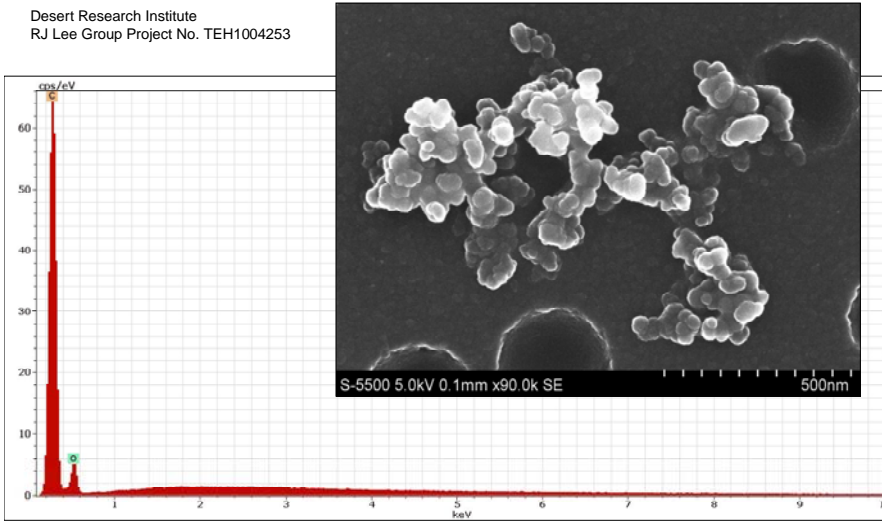
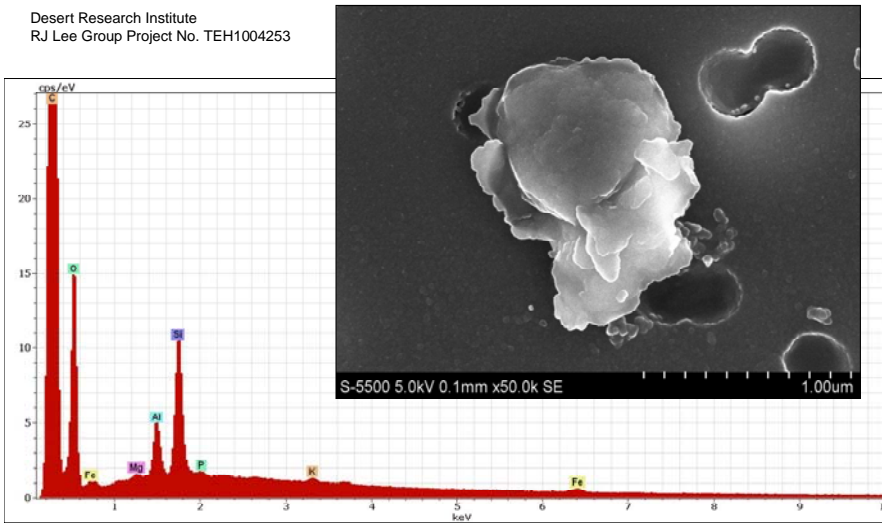
Appendix F – SEM, Secondary Electron Images & Spectra, Ft Carson 2008, Dirt road, Site 1

<p>Desert Research Institute RJ Lee Group Project No. TEH1004253</p>  <p>Y47N035 Ft Carson 2008 Site 1 Dirt Road</p>	<p>App. F(d) Y47N035, Ft Carson 2008 Dirt road, Site 1, Clay coating of montmorillonite-illite on unknown mineral</p>
<p>Desert Research Institute RJ Lee Group Project No. TEH1004253</p>  <p>Y47N035 Ft Carson 2008 Site 1 Dirt Road</p>	<p>App. F(e) Y47N035, Ft Carson 2008 Dirt road, Site 1 Potassium feldspar (microcline?) crystal with fine clay, possibly montmorillonite-illite forming on weathered surface</p>

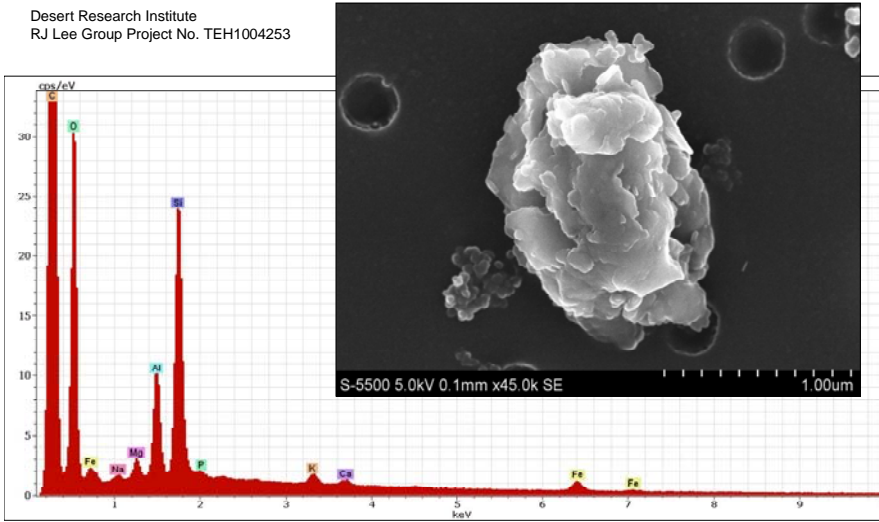
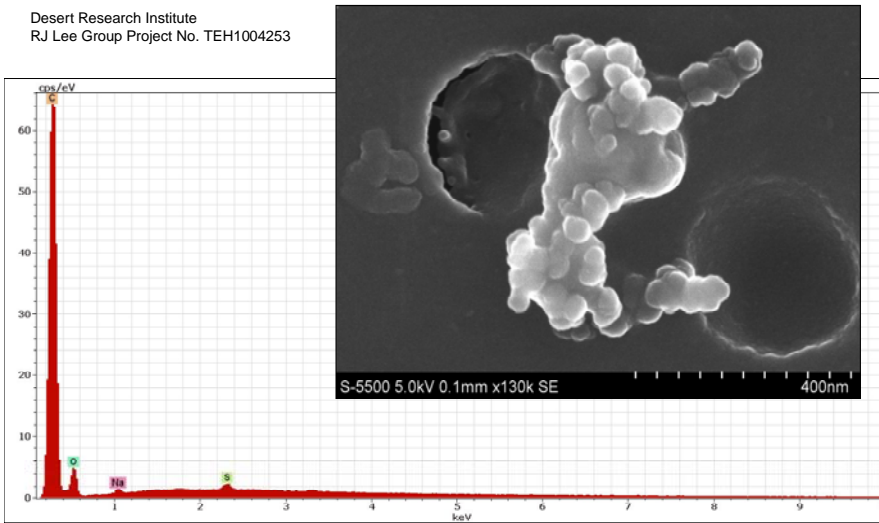
Appendix F – SEM, Secondary Electron Images & Spectra, Ft Carson2008, Dirt road, Site 1

<p>Desert Research Institute RJ Lee Group Project No. TEH1004253</p>  <p>S-5500 5.0kV 0.1mm x25.0k SE 2.00um</p> <p>Y47N035 Ft Carson 2008 Site 1 Dirt Road</p>	<p>App. F(f) Y47N035, Ft Carson 2008 Dirt road, Site 1 Platelets of the clay, possibly montmorillonite-illite</p>
<p>Desert Research Institute RJ Lee Group Project No. TEH1004253</p>  <p>S-5500 5.0kV 0.1mm x220k SE 200nm</p> <p>Y47N035 Ft Carson 2008 Site 1 Dirt Road</p>	<p>App. F(g) Y47N035, Ft Carson 2008 Dirt road, Site 1 Sub-micron particle of carbon, containing sulfur</p>

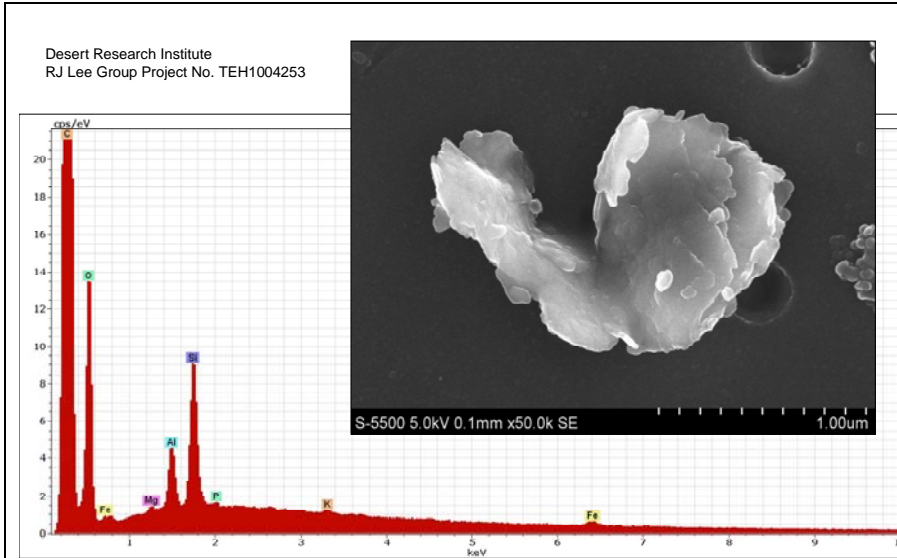
Appendix F – SEM, Secondary Electron Images & Spectra, Ft Carson2008, Dirt road, Site 1

<p>Desert Research Institute RJ Lee Group Project No. TEH1004253</p>  <p>S-5500 5.0kV 0.1mm x90.0k SE 500nm</p> <p>Y47N035 Ft Carson 2008 Site 1 Dirt Road</p>	<p>App. F(h) Y47N035, Ft Carson 2008 Dirt road, Site 1 Carbon chains, possibly from diesel vehicle emissions</p>
<p>Desert Research Institute RJ Lee Group Project No. TEH1004253</p>  <p>S-5500 5.0kV 0.1mm x50.0k SE 1.00um</p> <p>Y47N035 Ft Carson 2008 Site 1 Dirt Road</p>	<p>App. F(i) Y47N035, Ft Carson 2008 Dirt road, Site 1 Clay mineral coating, possibly montmorillonite-illite</p>

Appendix F – SEM, Secondary Electron Images & Spectra, Ft Carson2008, Dirt road, Site 1

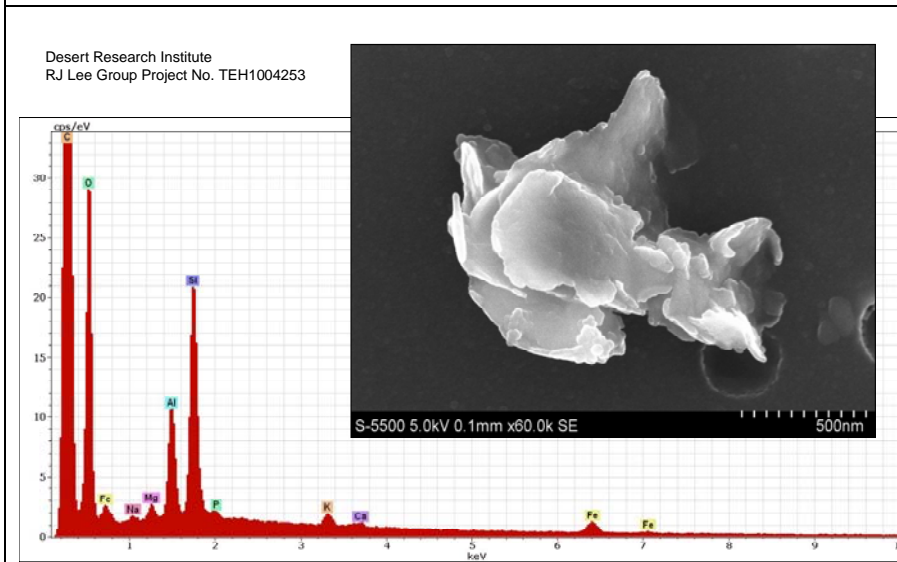
<p>Desert Research Institute RJ Lee Group Project No. TEH1004253</p>  <p>Y47N035 Ft Carson 2008 Site 1 Dirt Road</p>	<p>App. F(j) Y47N035, Ft Carson 2008 Dirt road, Site 1 Clay particles, possibly montmorillonite-illite</p>
<p>Desert Research Institute RJ Lee Group Project No. TEH1004253</p>  <p>Y47N035 Ft Carson 2008 Site 1 Dirt Road</p>	<p>App. F(k) Y47N035, Ft Carson 2008 Dirt road, Site 1 Agglomeration of carbon spheres with minor amounts of sulfur, possibly from diesel vehicle emissions</p>

Appendix F – SEM, Secondary Electron Images & Spectra, Ft Carson 2008, Dirt road, Site 1



Y47N035 Ft Carson 2008 Site 1 Dirt Road

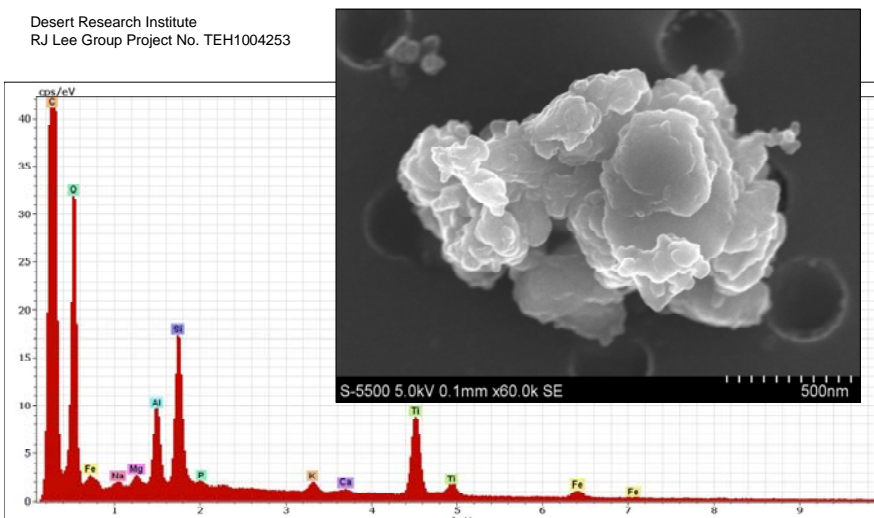
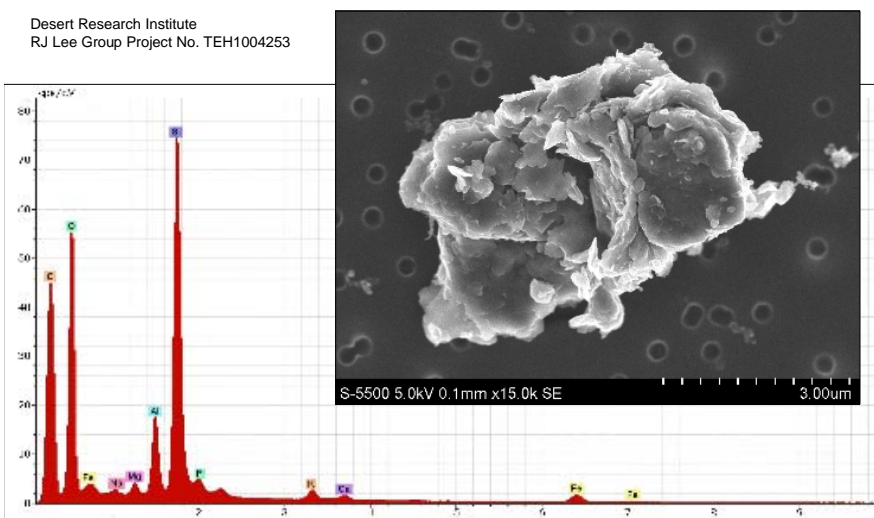
App. F(l)
Y47N035, Ft Carson 2008
Dirt road, Site 1
Biotite?, with coating of clay,
possibly montmorillonite-
illite



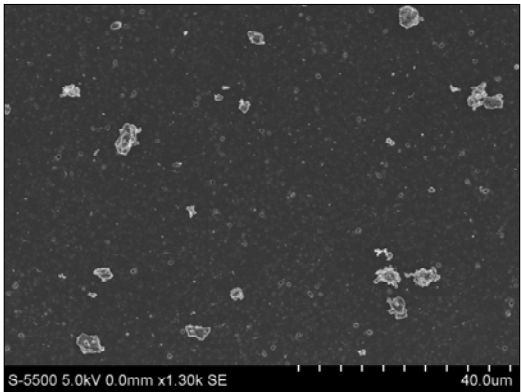
Y47N035 Ft Carson 2008 Site 1 Dirt Road

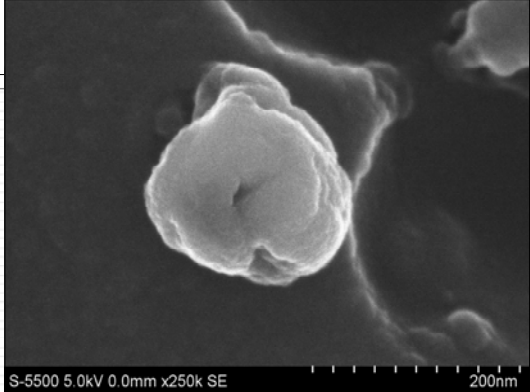
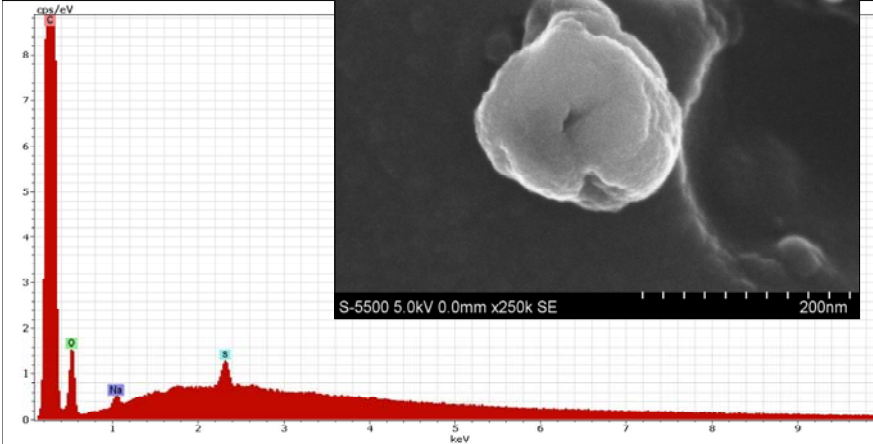
App. F(m)
Y47N035, Ft Carson 2008
Dirt road, Site 1
Biotite?, with coating of clay,
possibly montmorillonite-illite

Appendix F – SEM, Secondary Electron Images & Spectra, Ft Carson2008, Dirt road, Site 1

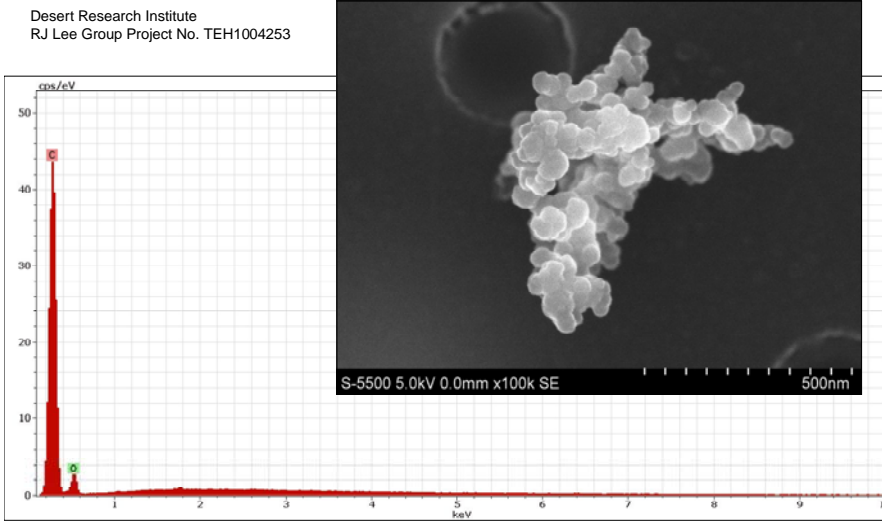
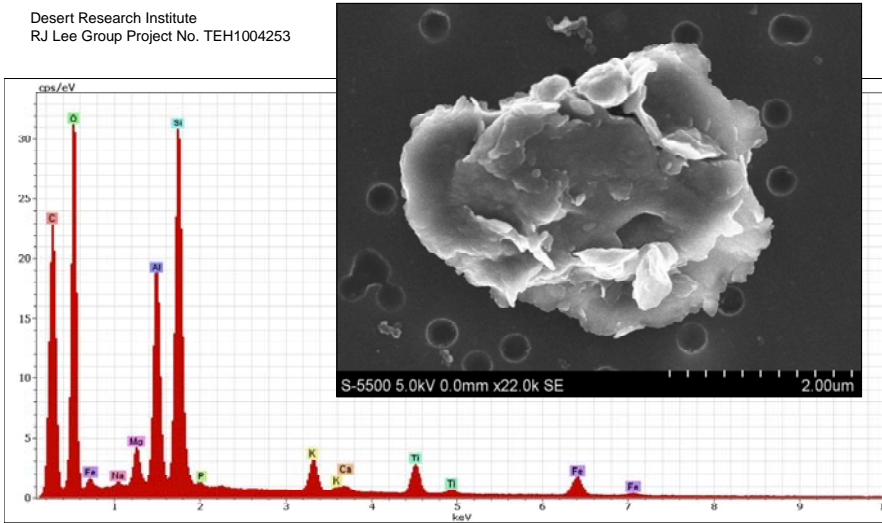
<p>Desert Research Institute RJ Lee Group Project No. TEH1004253</p>  <p>S-5500 5.0kV 0.1mm x60.0k SE</p>	<p>App. F(n) Y47N035, Ft Carson 2008 Dirt road, Site 1 Cluster of clay minerals, possibly montmorillonite- illite, with high titanium content, likely from rutile</p>
<p>Y47N035 Ft Carson 2008 Site 1 Dirt Road</p>	
<p>Desert Research Institute RJ Lee Group Project No. TEH1004253</p>  <p>S-5500 5.0kV 0.1mm x15.0k SE</p>	<p>App. F(o) Y47N035, Ft Carson 2008 Dirt road, Site 1 Composite particle with rounded grains of unknown mineral, and interstitial clay flakes, possibly montmorillonite-illite</p>
<p>Y47N035 Ft Carson 2008 Site 1 Dirt Road</p>	

Appendix G – SEM, Secondary Electron Images & Spectra, Ft Carson 2008, Dirt road, Site 2

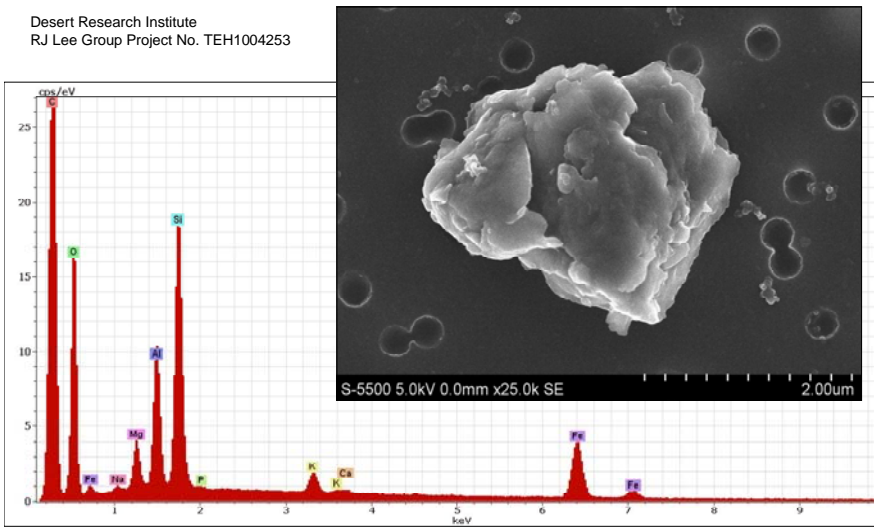
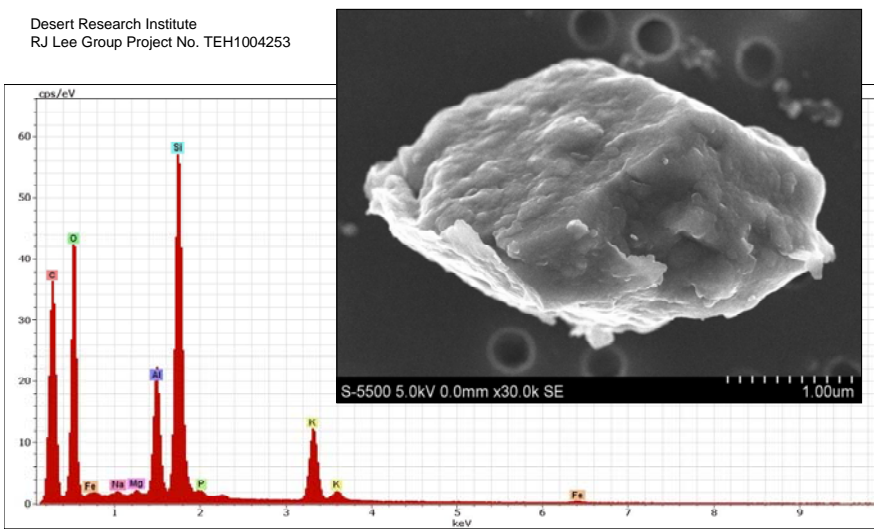
<p>RJLG RJ LeeGroup, Inc. Analysis. Consulting. Development.</p> <p>Y47N041 Ft Carson 2008 Site 2 Dirt Road</p>  	<p>SEM Images & Spectra Ft Carson 2008 Dirt road 2 Small dots on Nuclepore membrane filter approximately 0.4 μm in diameter App. G (a to j) Filter # Y47N041</p>
--	--

<p>Desert Research Institute RJ Lee Group Project No. TEH1004253</p>   <p>Y47N041 Ft Carson 2008 Site 2 Dirt Road</p>	<p>App. G(a) Y47N041, Ft Carson 2008 Dirt road, Site 2 Sub-micron carbon particle containing sodium sulfate</p>
--	--

Appendix G – SEM, Secondary Electron Images & Spectra, Ft Carson2008, Dirt road, Site 2

<p>Desert Research Institute RJ Lee Group Project No. TEH1004253</p>  <p>S-5500 5.0kV 0.0mm x100k SE 500nm</p> <p>Y47N041 Ft Carson 2008 Site 2 Dirt Road</p>	<p>App. G(b) Y47N041, Ft Carson 2008 Dirt road, Site 2 Carbon chain, possibly from diesel vehicle emissions</p>
<p>Desert Research Institute RJ Lee Group Project No. TEH1004253</p>  <p>S-5500 5.0kV 0.0mm x22.0k SE 2.00um</p> <p>Y47N041 Ft Carson 2008 Site 2 Dirt Road</p>	<p>App. G(c) Y47N041, Ft Carson 2008 Dirt road, Site 2 Biotite?, with with clay mineral coating, possibly montmorillonite-illite, with titanium and iron oxides</p>

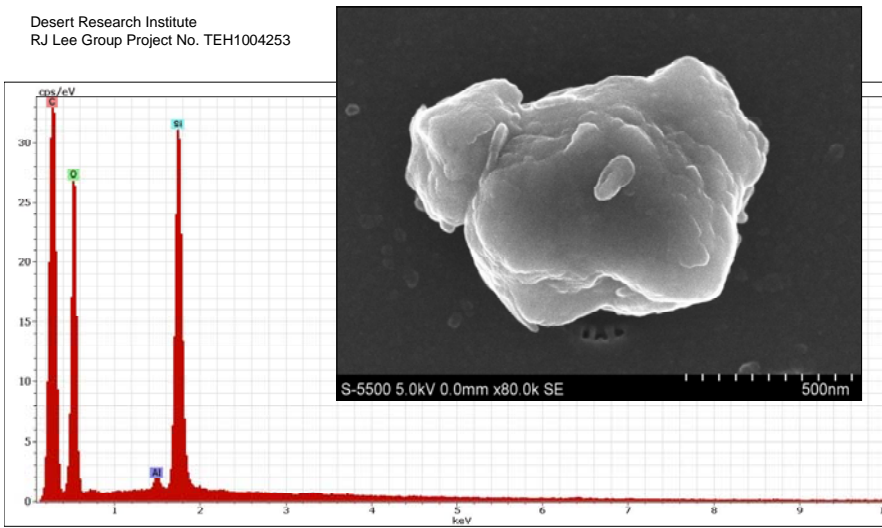
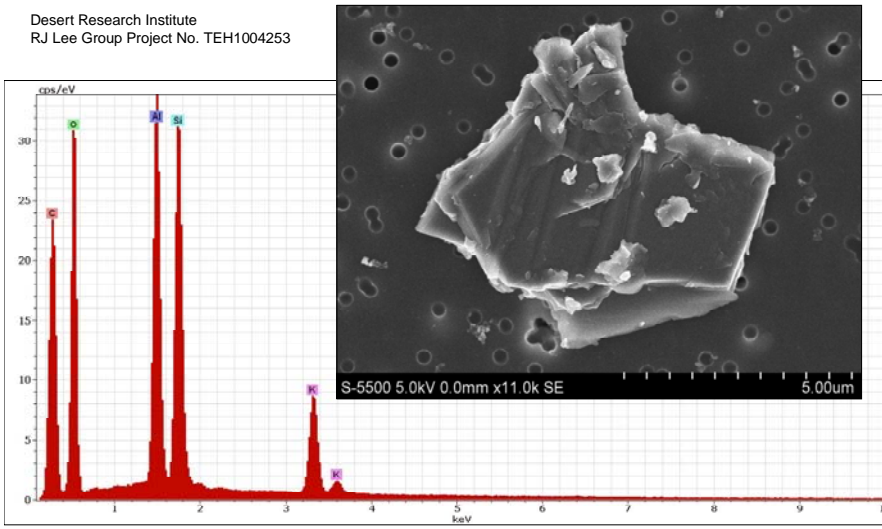
Appendix G – SEM, Secondary Electron Images & Spectra, Ft Carson2008, Dirt road, Site 2

<p>Desert Research Institute RJ Lee Group Project No. TEH1004253</p>  <p>S-5500 5.0kV 0.0mm x25.0k SE 2.00um</p> <p>Y47N041 Ft Carson 2008 Site 2 Dirt Road</p>	<p>App. G(d) Y47N041, Ft Carson 2008 Dirt road, Site 2 Tabular shaped crystal, possibly feldspar with coating of clay minerals, possibly montmorillonite- illite, and hematite</p>
<p>Desert Research Institute RJ Lee Group Project No. TEH1004253</p>  <p>S-5500 5.0kV 0.0mm x30.0k SE 1.00um</p> <p>Y47N041 Ft Carson 2008 Site 2 Dirt Road</p>	<p>App. G(e) Y47N041, Ft Carson 2008 Dirt road, Site 2 Cleavage particle of possibly potassium feldspar with muscovite coating</p>

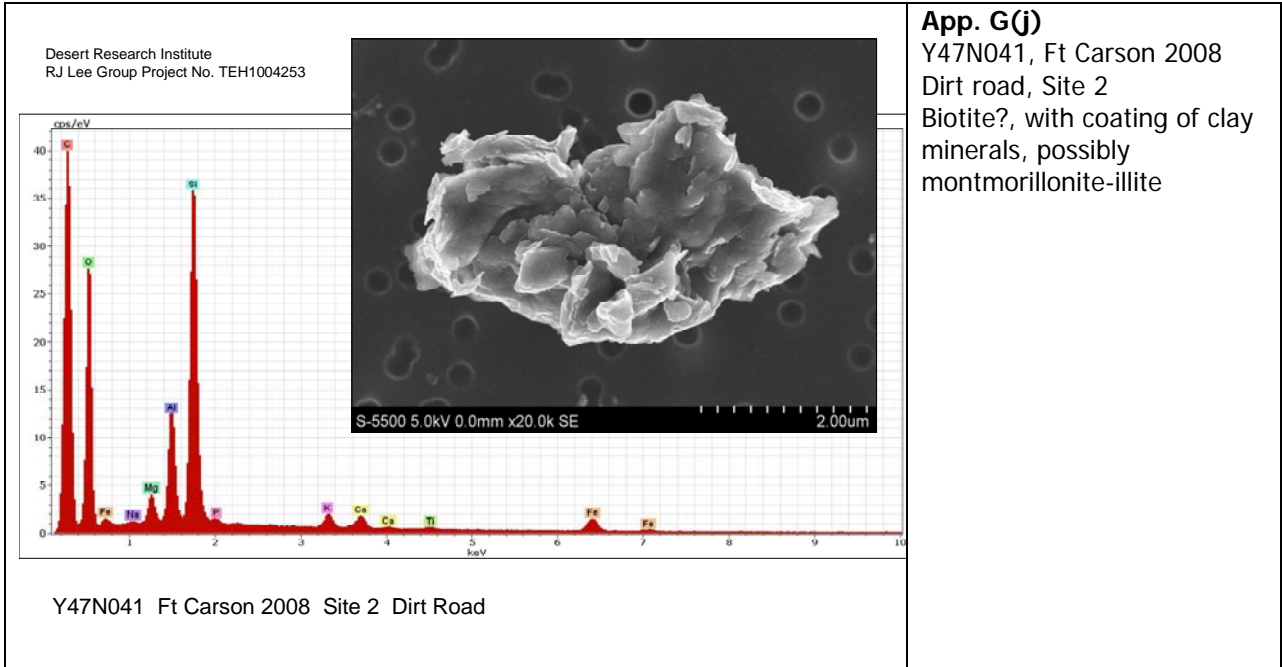
Appendix G – SEM, Secondary Electron Images & Spectra, Ft Carson 2008, Dirt road, Site 2

<p>Desert Research Institute RJ Lee Group Project No. TEH1004253</p> <p>Y47N041 Ft Carson 2008 Site 2 Dirt Road</p>	<p>App. G(f) Y47N041, Ft Carson 2008 Dirt road, Site 2 Quartz particle with minor amount of clay</p>
<p>Desert Research Institute RJ Lee Group Project No. TEH1004253</p> <p>Y47N041 Ft Carson 2008 Site 2 Dirt Road</p>	<p>App. G(g) Y47N041, Ft Carson 2008 Dirt road, Site 2 Biotite?, with coating of clay minerals, possibly montmorillonite-illite, and iron oxides attached</p>

Appendix G – SEM, Secondary Electron Images & Spectra, Ft Carson 2008, Dirt road, Site 2

<p>Desert Research Institute RJ Lee Group Project No. TEH1004253</p>  <p>Y47N041 Ft Carson 2008 Site 2 Dirt Road</p>	<p>App. G(h) Y47N041, Ft Carson 2008 Dirt road, Site 2 Quartz with minor clay minerals</p>
<p>Desert Research Institute RJ Lee Group Project No. TEH1004253</p>  <p>Y47N041 Ft Carson 2008 Site 2 Dirt Road</p>	<p>App. G(i) Y47N041- Ft Carson 2008 Dirt road, Site 2 Potassium feldspar crystal, showing twinning lamellae, with few clay particles attached</p>

Appendix G – SEM, Secondary Electron Images & Spectra, Ft Carson2008, Dirt road, Site 2



Appendix H – Chemical results of 20 PM₁₀ and PM_{2.5} filter samples

H (a) Yuma Proving Ground, gun site filter chemistry, 2005

	1 YUMA		2 YUMA		3 YUMA		4 YUMA		5 YUMA		6 YUMA	
	Gun Site 1		Gun Site 1		Gun Site 2		Gun Site 2		Gun Site 3		Gun Site 3	
	10/20/2005 PM10 YU47T001		10/20/2005 PM2.5 YU47T002		10/27/2005 PM10 YU47T003		10/27/2005 PM2.5 YU47T004		10/28/2005 PM10 YU47T008		10/28/2005 PM2.5 YU47T005	
	Conc. %	Unc. %	Conc. %	Unc. %	Conc. %	Unc. %	Conc. %	Unc. %	Conc. %	Unc. %	Conc. %	Unc. %
Cl ⁻	0.6024 ± 0.0718		1.0629 ± 0.1884		0.3089 ± 0.0433		0.3731 ± 0.0824		1.3429 ± 0.3632		0 ± 0.3447	
NO ₃ ⁻	0.5053 ± 0.0584		2.3641 ± 0.2388		1.3295 ± 0.1017		1.6204 ± 0.1399		6.3465 ± 0.6259		1.1566 ± 0.3582	
SO ₄ ²⁻	5.0414 ± 0.3686		14.072 ± 1.0716		8.4957 ± 0.6165		9.4819 ± 0.6958		9.803 ± 0.8817		11.315 ± 1.0136	
NH ₄ ⁺	0.1986 ± 0.0479		0.7711 ± 0.1704		0.374 ± 0.0432		0.8897 ± 0.101		2.7749 ± 0.4128		3.2836 ± 0.4478	
Na ⁺	0.2694 ± 0.0222		0.5845 ± 0.0501		0.2835 ± 0.0232		0.2415 ± 0.0204		2.1236 ± 0.1947		0.5152 ± 0.0517	
Mg ²⁺	0.1437 ± 0.0106		0.1444 ± 0.0127		0.0961 ± 0.0071		0.061 ± 0.0053		0.3599 ± 0.0328		0.1467 ± 0.0187	
K ⁺	6.8143 ± 0.5526		15.46 ± 1.2918		6.7587 ± 0.5475		6.9 ± 0.5619		0.5745 ± 0.0621		1.2971 ± 0.1238	
Ca ²⁺	2.2541 ± 0.1637		1.8693 ± 0.1608		5.3364 ± 0.3837		1.5157 ± 0.1158		3.0357 ± 0.302		2.2012 ± 0.2523	
OC1	1.463 ± 0.2638		6.2129 ± 1.1237		1.3473 ± 0.242		2.0669 ± 0.3744		12.65 ± 2.332		13.52 ± 2.4982	
OC2	1.8235 ± 0.3033		5.3208 ± 0.902		1.477 ± 0.2441		4.1714 ± 0.6853		5.8632 ± 1.1105		5.3401 ± 1.0434	
OC3	3.2441 ± 0.3818		7.6074 ± 1.0946		2.3725 ± 0.2774		4.7819 ± 0.5896		7.1463 ± 1.8813		7.7959 ± 1.9476	
OC4	1.44 ± 0.2241		3.2752 ± 0.5698		1.6012 ± 0.2366		2.4483 ± 0.3794		5.1107 ± 1.0173		5.8799 ± 1.1168	
OC	7.2315 ± 0.6499		21.19 ± 2.0602		6.6337 ± 0.5627		12.61 ± 1.12		25.66 ± 3.3742		26.655 ± 2.4936	
EC1	0.4423 ± 0.0914		1.8565 ± 0.3678		0.7142 ± 0.1284		0.7876 ± 0.1592		1.3007 ± 0.4377		3.3979 ± 0.7144	
EC2	0.1789 ± 0.1084		1.0288 ± 0.5545		1.0691 ± 0.5305		0.2834 ± 0.174		1.395 ± 0.8338		5.3028 ± 2.6751	
EC3	0 ± 0.0209		0 ± 0.0733		0 ± 0.0151		0 ± 0.0344		0 ± 0.1549		0.0344 ± 0.1656	
EC	1.3602 ± 0.1538		4.111 ± 0.4928		1.9476 ± 0.1969		1.9296 ± 0.2284		7.806 ± 1.009		14.614 ± 1.6599	
TC	8.5917 ± 0.7527		25.302 ± 2.3919		8.5813 ± 0.701		14.539 ± 1.2693		33.466 ± 4.0564		41.27 ± 4.626	
CO ₃ ²⁻	±		±		±		±		±		±	
Na	0.3843 ± 0.083		0.8133 ± 0.2814		0.5361 ± 0.0728		0.8363 ± 0.1464		1.2752 ± 0.5426		0 ± 0.5266	
Mg	0.8023 ± 0.1033		0.6331 ± 0.2905		0.9864 ± 0.0972		0.5021 ± 0.1362		0.5247 ± 0.5552		0.4631 ± 0.584	
Al	2.5014 ± 0.1895		1.5272 ± 0.2274		3.4944 ± 0.2544		2.1134 ± 0.1792		3.7965 ± 0.4995		2.9045 ± 0.4726	
Si	4.8475 ± 0.3546		3.1363 ± 0.2613		8.0722 ± 0.5857		4.4956 ± 0.3344		8.6039 ± 0.7525		6.2586 ± 0.5749	
P	0.0466 ± 0.0059		0.2543 ± 0.0261		0.0827 ± 0.0069		0.1606 ± 0.0142		0.1011 ± 0.0352		0.1398 ± 0.0384	
S	2.3068 ± 0.1656		6.2529 ± 0.4663		3.4149 ± 0.2434		5.6162 ± 0.4033		3.4306 ± 0.2823		4.1049 ± 0.3423	
Cl	0.6549 ± 0.0468		1.0266 ± 0.0774		0.1788 ± 0.013		0.3022 ± 0.0226		0.6724 ± 0.0614		0.0684 ± 0.0278	
K	7.67 ± 0.5441		15.154 ± 1.1173		7.8209 ± 0.554		11.242 ± 0.802		1.7685 ± 0.1444		3.009 ± 0.2492	
Ca	3.0555 ± 0.2171		1.3614 ± 0.1021		4.8442 ± 0.3436		2.0015 ± 0.1433		3.1527 ± 0.2603		2.5127 ± 0.2115	
Ti	1.3459 ± 0.0957		0.6756 ± 0.0508		1.2372 ± 0.0878		0.8548 ± 0.0613		0.2337 ± 0.0259		0.3041 ± 0.0317	
V	0 ± 0.0009		0 ± 0.0033		0 ± 0.0007		0 ± 0.0016		0.008 ± 0.0068		0.0164 ± 0.0071	
Cr	0.0083 ± 0.004		0 ± 0.0142		0.0044 ± 0.0028		0.0029 ± 0.0062		0.0052 ± 0.0275		0 ± 0.0291	
Mn	0.0423 ± 0.0114		0.0239 ± 0.0403		0.078 ± 0.0097		0.0356 ± 0.0182		0.1011 ± 0.0791		0.0656 ± 0.0833	
Fe	1.6991 ± 0.1225		1.0329 ± 0.0987		2.858 ± 0.2036		1.6417 ± 0.1215		2.5552 ± 0.2433		1.8332 ± 0.1995	
Co	0.0022 ± 0.0018		0.0039 ± 0.0067		0.0031 ± 0.0014		0 ± 0.0029		0.0155 ± 0.0132		0 ± 0.0139	
Ni	0.0137 ± 0.003		0.0106 ± 0.0106		0.0067 ± 0.0021		0.0048 ± 0.0048		0.0052 ± 0.0211		0.0221 ± 0.0222	
Cu	7.6057 ± 0.54		6.5506 ± 0.4836		3.1135 ± 0.2207		3.3399 ± 0.2385		0.0518 ± 0.0171		0.6631 ± 0.0581	
Zn	0.1015 ± 0.0079		0.1061 ± 0.014		0.2952 ± 0.0211		0.6257 ± 0.0451		0.0287 ± 0.022		0.1369 ± 0.0262	
As	0 ± 0.0024		0 ± 0.0089		0 ± 0.002		0 ± 0.0045		0 ± 0.0175		0.0246 ± 0.0189	
Se	0 ± 0.0021		0 ± 0.0078		0 ± 0.0015		0 ± 0.0035		0 ± 0.0155		0 ± 0.0164	
Br	0 ± 0.0024		0.1788 ± 0.0163		0.0054 ± 0.0018		0.0107 ± 0.0042		0 ± 0.0175		0 ± 0.0184	
Rb	0 ± 0.0023		0 ± 0.0083		0.0029 ± 0.0017		0 ± 0.0038		0 ± 0.0167		0 ± 0.0176	
Sr	0 ± 0.0054		0 ± 0.0197		0.0369 ± 0.0048		0.0131 ± 0.009		0.0028 ± 0.0386		0.0029 ± 0.0406	
Y	0 ± 0.0035		0 ± 0.0128		0 ± 0.0025		0 ± 0.0059		0 ± 0.0255		0 ± 0.0266	
Zr	0.0657 ± 0.0088		0.1138 ± 0.0284		0.0021 ± 0.0053		0 ± 0.0121		0 ± 0.053		0 ± 0.0557	
Cd	0.0119 ± 0.0092		0 ± 0.033		0.0008 ± 0.0065		0.0178 ± 0.0151		0.1011 ± 0.066		0 ± 0.0684	
Sn	0.0769 ± 0.0119		0.0358 ± 0.0384		0.0226 ± 0.0077		0.0036 ± 0.0171		0 ± 0.0748		0.0574 ± 0.0792	
Sb	0 ± 0.0094		0 ± 0.0344		0 ± 0.0067		0 ± 0.0154		0 ± 0.0681		0 ± 0.0713	
Ba	0.0741 ± 0.0238		0.1325 ± 0.0844		0.0572 ± 0.0171		0 ± 0.0373		0.0884 ± 0.1637		0 ± 0.1721	
Pb	0.3666 ± 0.0274		0.3868 ± 0.0408		1.9992 ± 0.1419		2.1277 ± 0.1527		0 ± 0.0561		0.1918 ± 0.0616	
Bi	4.7463 ± 1		8.3433 ± 1.6		0 ± 0		0 ± 0		0 ± 0		0 ± 0	
U	0.0239 ± 0.0106		0.0555 ± 0.0384		0.0047 ± 0.0075		0 ± 0.0171		0.0466 ± 0.0749		0.066 ± 0.0792	

Appendix H – Chemical results of 20 PM₁₀ and PM_{2.5} filter samples

H (b) Yakima Test Center, unpaved road filter chemistry, 2006

	7 Yakima		8 Yakima		9 Yakima		10 Yakima	
	Unpaved road, personal carrier 8/21/2006 PM10 YU47T007		Unpaved road, personal carrier 8/21/2006 PM2.5 YU47T009		Unpaved road, M1-A1 tank 8/23/2006 PM10 YU47T012		Unpaved road, M1-A1 tank 8/23/2006 PM2.5 YU47T013	
	Conc. %	Unc. %	Conc. %	Unc. %	Conc. %	Unc. %	Conc. %	Unc. %
Cl ⁻	0.0755 ± 0.0142		0.1026 ± 0.0215		0.0139 ± 0.0017		0.0525 ± 0.0079	
NO ₃ ⁻	0.3921 ± 0.0391		0.8913 ± 0.0863		0.0483 ± 0.0047		0.2988 ± 0.0289	
SO ₄ ²⁻	0.2606 ± 0.0248		0.5015 ± 0.0454		0.0308 ± 0.0028		0.1383 ± 0.0131	
NH ₄ ⁺	0.1264 ± 0.0157		0.2567 ± 0.0271		0.0089 ± 0.0014		0.0478 ± 0.0075	
Na ⁺	0.1622 ± 0.0117		0.1985 ± 0.0144		0.0262 ± 0.0019		0.1237 ± 0.0089	
Mg ²⁺	0.2097 ± 0.0149		0.2299 ± 0.0164		0.0445 ± 0.0032		0.1525 ± 0.0108	
K ⁺	0.3556 ± 0.0255		0.367 ± 0.0263		0.0509 ± 0.0036		0.209 ± 0.0149	
Ca ²⁺	1.7056 ± 0.1329		1.7926 ± 0.1399		0.5973 ± 0.0465		1.9067 ± 0.1484	
OC1	0.1025 ± 0.0202		0.2463 ± 0.0446		0.0194 ± 0.0034		0.0482 ± 0.0098	
OC2	0.8099 ± 0.1603		2.0206 ± 0.398		0.1497 ± 0.0295		0.8121 ± 0.1598	
OC3	3.6771 ± 0.4954		6.3978 ± 0.8605		0.658 ± 0.0881		3.7563 ± 0.5028	
OC4	3.0848 ± 0.8238		3.993 ± 1.0666		0.3264 ± 0.0872		2.4321 ± 0.6493	
OC	11.915 ± 1.5145		16.501 ± 2.0986		2.2222 ± 0.282		9.2615 ± 1.1758	
EC1	3.7841 ± 0.81		3.9835 ± 0.8528		1.0206 ± 0.2184		1.9684 ± 0.4213	
EC2	0.7789 ± 0.1488		0.9209 ± 0.1769		0.1472 ± 0.028		0.5705 ± 0.1086	
EC3	0.5747 ± 0.073		0.1092 ± 0.0165		0.0343 ± 0.0044		0.0581 ± 0.008	
EC	0.8968 ± 0.2973		1.1699 ± 0.3883		0.1335 ± 0.0442		0.3841 ± 0.1275	
TC	13.227 ± 1.2388		18.151 ± 1.7021		2.5436 ± 0.2375		10.193 ± 0.9525	
CO ₃ ²⁻	0.4155 ± 0.0509		0.4801 ± 0.0588		0.1879 ± 0.023		0.5471 ± 0.067	
Na	0.0526 ± 0.0664		0 ± 0.0971		0.0255 ± 0.0071		0 ± 0.0329	
Mg	0.4109 ± 0.0364		0.7866 ± 0.0658		0.127 ± 0.0094		0.2929 ± 0.0239	
Al	2.563 ± 0.1827		5.4201 ± 0.3861		0.7959 ± 0.0566		1.6567 ± 0.118	
Si	8.153 ± 0.5796		17.043 ± 1.2116		2.6798 ± 0.1904		5.2793 ± 0.3752	
P	0 ± 0.0032		0 ± 0.0049		0 ± 0.0003		0 ± 0.0016	
S	0.023 ± 0.0019		0.06 ± 0.0045		0.0066 ± 0.0005		0.0098 ± 0.0008	
Cl	0.0096 ± 0.0011		0.0275 ± 0.0023		0.0043 ± 0.0003		0.0073 ± 0.0007	
K	0.8009 ± 0.0567		1.5664 ± 0.1109		0.4199 ± 0.0297		0.6002 ± 0.0425	
Ca	1.1636 ± 0.0824		2.3111 ± 0.1637		0.8821 ± 0.0624		1.201 ± 0.085	
Ti	0.4022 ± 0.0285		0.7384 ± 0.0523		0.271 ± 0.0192		0.3052 ± 0.0216	
V	0.0058 ± 0.0004		0.0095 ± 0.0007		0.0077 ± 0.0005		0.0057 ± 0.0004	
Cr	0.0017 ± 0.0006		0.0032 ± 0.001		0.0012 ± 0.0001		0.0008 ± 0.0003	
Mn	0.0776 ± 0.0057		0.1614 ± 0.0117		0.0659 ± 0.0047		0.0694 ± 0.005	
Fe	4.5077 ± 0.319		9.2413 ± 0.6542		4.0046 ± 0.2833		4.0988 ± 0.29	
Co	0 ± 0.0001		0 ± 0.0002		0 ± 0		0 ± 0.0001	
Ni	0.0003 ± 0.0002		0.0009 ± 0.0003		0.0011 ± 0.0001		0.0017 ± 0.0002	
Cu	0.0038 ± 0.0008		0.0086 ± 0.0013		0.0045 ± 0.0003		0.0047 ± 0.0005	
Zn	0.0102 ± 0.001		0.0257 ± 0.0021		0.0079 ± 0.0006		0.0104 ± 0.0008	
As	0 ± 0.0002		0 ± 0.0004		0.0006 ± 0		0 ± 0.0001	
Se	0 ± 0.0005		0 ± 0.0007		0 ± 0		0 ± 0.0002	
Br	0 ± 0.0007		0.0005 ± 0.001		0.0009 ± 0.0001		0.0012 ± 0.0004	
Rb	0.0041 ± 0.0005		0.0086 ± 0.0009		0.0056 ± 0.0004		0.0045 ± 0.0004	
Sr	0.018 ± 0.0017		0.0334 ± 0.0029		0.0202 ± 0.0014		0.0163 ± 0.0013	
Y	0.0023 ± 0.0006		0.0041 ± 0.001		0.0027 ± 0.0002		0.0017 ± 0.0003	
Zr	0.0238 ± 0.0024		0.0446 ± 0.0041		0.0245 ± 0.0017		0.0209 ± 0.0017	
Cd	0 ± 0.0018		0.0095 ± 0.003		0.0001 ± 0.0002		0 ± 0.001	
Sn	0.0015 ± 0.0022		0.0086 ± 0.0035		0.0001 ± 0.0002		0.0002 ± 0.0012	
Sb	0 ± 0.0036		0 ± 0.0056		0 ± 0.0004		0.0012 ± 0.0019	
Ba	0.0218 ± 0.0019		0.0365 ± 0.0031		0.0214 ± 0.0015		0.0154 ± 0.0012	
Pb	0.0035 ± 0.0015		0.0081 ± 0.0025		0.0017 ± 0.0002		0.0027 ± 0.0008	
Bi	0 ± 0		0 ± 0		0 ± 0		0 ± 0	
U	0.0009 ± 0.0027		0 ± 0.0041		0 ± 0.0003		0 ± 0.0014	

Appendix H – Chemical results of 20 PM₁₀ and PM_{2.5} filter samples

H (c) Yuma Proving Ground, desert pavement filter chemistry, 2007

	11 YPG Site 1		12 YPG Site 1		13 YPG Site 2		14 YPG Site 2	
	Desert pavement, Roadrunner, helicopter 5/21/2007 PM10 YU47T025		Desert pavement, Roadrunner, helicopter 5/21/2007 PM2.5 YU47T026		Desert pavement, disturbed 5/23/2007 PM10 YU47T024		Desert pavement, disturbed 5/25/2007 PM2.5 YU47T028	
	Conc. %	Unc. %	Conc. %	Unc. %	Conc. %	Unc. %	Conc. %	Unc. %
Cl ⁻	0.9202 ± 0.1504		1.1852 ± 0.3856		0.7585 ± 0.1543		0.2895 ± 0.1216	
NO ₃ ⁻	1.5755 ± 0.1703		2.3754 ± 0.4195		1.6891 ± 0.1854		0.8329 ± 0.1337	
SO ₄ ²⁻	3.0192 ± 0.2533		6.7694 ± 0.6808		1.5289 ± 0.1779		1.8738 ± 0.1807	
NH ₄ ⁺	0.8704 ± 0.1457		2.2828 ± 0.4266		0.567 ± 0.1467		0.7984 ± 0.1369	
Na ⁺	0.9988 ± 0.0732		1.399 ± 0.1206		0.8203 ± 0.0605		0.3264 ± 0.0249	
Mg ²⁺	0.323 ± 0.0294		0.4327 ± 0.046		0.2832 ± 0.0261		0.1564 ± 0.0149	
K ⁺	0.1647 ± 0.0201		0.2003 ± 0.0426		0.2107 ± 0.024		0.2266 ± 0.0241	
Ca ²⁺	7.026 ± 0.5221		4.8754 ± 0.4549		8.8252 ± 0.6584		4.4157 ± 0.3304	
OC1	0.8458 ± 0.1996		4.0842 ± 0.8912		0 ± 0.1163		0.6975 ± 0.1716	
OC2	3.5766 ± 0.9703		13.298 ± 3.6231		2.8936 ± 0.7993		3.4887 ± 0.9448	
OC3	3.6663 ± 0.757		15.727 ± 2.5974		3.1722 ± 0.7932		3.985 ± 0.7438	
OC4	0.7567 ± 0.2853		5.7559 ± 1.2178		0.4746 ± 0.2942		1.1134 ± 0.3026	
OC	9.5611 ± 1.5236		41.68 ± 6.1364		6.9852 ± 1.3669		10.043 ± 1.5385	
EC1	0.7151 ± 0.1564		5.1785 ± 0.6806		0.4447 ± 0.1606		0.7581 ± 0.1515	
EC2	0 ± 0.1758		1.0774 ± 0.527		0 ± 0.1934		0 ± 0.1666	
EC3	0 ± 0.0586		0 ± 0.1717		0 ± 0.0645		0.0402 ± 0.0556	
EC	0 ± 0.2233		3.4411 ± 1.2626		0 ± 0.2453		0.0402 ± 0.2114	
TC	11.519 ± 1.6277		46.152 ± 6.1287		9.2899 ± 1.548		11.442 ± 1.5823	
CO ₃ ²⁻	1.9577 ± 1.1114		1.0286 ± 3.1944		2.3047 ± 1.2253		1.3593 ± 1.0433	
Na	0 ± 0.3622		0 ± 1.0253		0.0399 ± 0.4062		0 ± 0.3456	
Mg	0.9578 ± 0.2055		0.8367 ± 0.5417		1.1095 ± 0.2304		1.4993 ± 0.217	
Al	4.0479 ± 0.2983		4.8114 ± 0.4216		4.8287 ± 0.3578		5.6379 ± 0.4125	
Si	10.197 ± 0.7453		9.436 ± 0.8103		12.057 ± 0.8868		13.49 ± 0.9832	
P	0 ± 0.01		0.037 ± 0.0287		0 ± 0.0106		0.0074 ± 0.0096	
S	0.8552 ± 0.0693		2.2121 ± 0.2065		0.4421 ± 0.0457		0.6148 ± 0.0528	
Cl	0.6436 ± 0.0475		0.5842 ± 0.0532		0.4527 ± 0.0344		0.1201 ± 0.011	
K	1.82 ± 0.1323		1.6397 ± 0.1397		2.1491 ± 0.1575		2.2246 ± 0.1613	
Ca	5.981 ± 0.4341		4.2458 ± 0.3592		7.0862 ± 0.5176		4.793 ± 0.3473	
Ti	0.3505 ± 0.0259		0.303 ± 0.0289		0.3769 ± 0.0283		0.3621 ± 0.0266	
V	0.0094 ± 0.0008		0 ± 0.0017		0.0093 ± 0.0008		0.0051 ± 0.0006	
Cr	0.0053 ± 0.0041		0.0118 ± 0.0118		0 ± 0.0047		0.0028 ± 0.004	
Mn	0.0768 ± 0.0107		0.1077 ± 0.0279		0.0917 ± 0.0123		0.0975 ± 0.0109	
Fe	3.6053 ± 0.2621		3.4192 ± 0.291		4.0496 ± 0.2962		4.2797 ± 0.3102	
Co	0 ± 0.0006		0 ± 0.0017		0 ± 0.0007		0 ± 0.0006	
Ni	0.0018 ± 0.0023		0.0017 ± 0.0067		0.0013 ± 0.0027		0.0011 ± 0.0023	
Cu	0.0023 ± 0.0035		0.0219 ± 0.0102		0.0047 ± 0.004		0.0085 ± 0.0034	
Zn	0.0293 ± 0.0044		0.0354 ± 0.0104		0.016 ± 0.0041		0.0215 ± 0.0041	
As	0 ± 0.0006		0 ± 0.0017		0 ± 0.0007		0 ± 0.0006	
Se	0 ± 0.0088		0.0185 ± 0.0253		0.0093 ± 0.01		0 ± 0.0085	
Br	0 ± 0.0064		0 ± 0.0185		0 ± 0.0073		0.0068 ± 0.0062	
Rb	0.0123 ± 0.0047		0 ± 0.0135		0.0106 ± 0.0053		0.0108 ± 0.0046	
Sr	0.0293 ± 0.0089		0.0387 ± 0.0237		0.0372 ± 0.0095		0.021 ± 0.008	
Y	0.0094 ± 0.0065		0.0034 ± 0.0185		0.002 ± 0.0073		0.0057 ± 0.0062	
Zr	0.0123 ± 0.0147		0.0185 ± 0.0421		0.0239 ± 0.0167		0.0147 ± 0.0142	
Cd	0 ± 0.0217		0 ± 0.0623		0.01 ± 0.0246		0.0079 ± 0.021	
Sn	0 ± 0.0164		0 ± 0.0488		0 ± 0.0186		0 ± 0.0159	
Sb	0 ± 0.0311		0 ± 0.0892		0 ± 0.0352		0 ± 0.0295	
Ba	0 ± 0.0023		0 ± 0.0067		0 ± 0.0027		0 ± 0.0023	
Pb	0 ± 0.0111		0 ± 0.032		0 ± 0.012		0 ± 0.0102	
Bi	0 ± 0		0 ± 0		0 ± 0		0 ± 0	
U	0.0147 ± 0.0182		0 ± 0.0505		0.008 ± 0.0199		0 ± 0.017	

Appendix H – Normative mineral abundances for 20 PM₁₀ and PM_{2.5} filter samples

H (d) Ft. Carson, unpaved road filter chemistry, 2008

	15		16		17		18		19		20	
	Ft Carson Site 1		Ft Carson Site 1		Ft Carson Site 2		Ft Carson Site 2		Ft Carson Site 2 south side		Ft Carson Site 2 south side	
	Unpaved road		Unpaved road		Unpaved road		Unpaved road		Unpaved road		Unpaved road	
	9/17/2008 PM10 YU47T035		9/17/2008 PM2.5 YU47T038		9/18/2008 PM10 YU47T039		9/18/2008 PM2.5 YU47T040		9/19/2008 PM10 YU47T041		9/19/2008 PM2.5 YU47T042	
	Conc. %	Unc. %	Conc. %	Unc. %	Conc. %	Unc. %	Conc. %	Unc. %	Conc. %	Unc. %	Conc. %	Unc. %
Cl ⁻	0.0777 ± 0.0272		0.0952 ± 0.1371		0.7072 ± 0.0639		0.656 ± 0.1276		0.7506 ± 0.0683		0.3969 ± 0.0774	
NO ₃ ⁻	0.1336 ± 0.0287		0.4636 ± 0.1425		0.1629 ± 0.0409		0.5677 ± 0.1271		0.2311 ± 0.046		0.3871 ± 0.0781	
SO ₄ ²⁻	0.556 ± 0.0487		1.1694 ± 0.1632		0.2892 ± 0.0442		0.9321 ± 0.1374		0.3517 ± 0.0494		0.5784 ± 0.0837	
NH ₄ ⁺	0.1271 ± 0.0286		0.4579 ± 0.1424		0.139 ± 0.0402		0.4138 ± 0.1227		0.1697 ± 0.0441		0.2344 ± 0.0741	
Na ⁺	0.036 ± 0.0025		0.1288 ± 0.0095		0.0317 ± 0.0023		0.1045 ± 0.0074		0.0436 ± 0.0031		0.0731 ± 0.0052	
Mg ²⁺	0.2665 ± 0.0191		0.2248 ± 0.0166		0.5587 ± 0.04		0.6638 ± 0.0485		0.7144 ± 0.0513		0.4042 ± 0.0292	
K ⁺	0.2091 ± 0.0162		0.2084 ± 0.0165		0.1738 ± 0.0134		0.3149 ± 0.0247		0.3874 ± 0.03		0.1625 ± 0.0128	
Ca ²⁺	1.4225 ± 0.1007		1.5764 ± 0.1149		1.4583 ± 0.1034		2.3571 ± 0.1705		1.5433 ± 0.1096		1.4193 ± 0.1013	
OC1	0 ± 0.0167		0.5326 ± 0.0946		0 ± 0.0243		0.185 ± 0.0755		0.1352 ± 0.0282		0.0975 ± 0.0458	
OC2	0.2852 ± 0.0883		1.7766 ± 0.5392		0.3154 ± 0.1023		1.3042 ± 0.4027		0.6095 ± 0.183		0.8538 ± 0.2612	
OC3	0.5757 ± 0.1678		2.7228 ± 0.8235		0.5307 ± 0.1944		2.2448 ± 0.6915		0.8689 ± 0.2579		1.4355 ± 0.4319	
OC4	0.246 ± 0.1147		1.1234 ± 0.5334		0.177 ± 0.0975		0.7429 ± 0.3713		0.4598 ± 0.2105		0.3944 ± 0.2045	
OC	1.79 ± 0.4259		7.159 ± 1.779		1.64 ± 0.427		5.8433 ± 1.467		3.0316 ± 0.7154		3.5901 ± 0.8982	
EC1	0.595 ± 0.0901		1.4016 ± 0.2368		0.6213 ± 0.0969		1.5415 ± 0.2479		0.9533 ± 0.1443		0.8315 ± 0.1363	
EC2	0.4213 ± 0.1459		1.3827 ± 0.4921		0.4978 ± 0.174		1.3763 ± 0.4841		0.6107 ± 0.2121		0.6243 ± 0.2253	
EC3	0 ± 0.0094		0.0189 ± 0.0484		0 ± 0.0137		0 ± 0.0417		0 ± 0.0148		0 ± 0.0252	
EC	0.3333 ± 0.119		1.7996 ± 0.6407		0.5019 ± 0.1788		1.5514 ± 0.5525		0.6059 ± 0.2142		0.6467 ± 0.2403	
TC	2.3595 ± 0.6316		9.1046 ± 2.5136		2.6134 ± 0.7186		7.7471 ± 2.1401		4.1939 ± 1.1139		4.3448 ± 1.2129	
CO ₃ ²⁻	0.2363 ± 0.1932		0.1461 ± 0.8953		0.4713 ± 0.304		0.3517 ± 0.7798		0.5564 ± 0.3391		0.1081 ± 0.4692	
Na	0.1148 ± 0.0757		0.2019 ± 0.3801		0.3569 ± 0.1161		0 ± 0.3178		0.311 ± 0.1233		0.1852 ± 0.2005	
Mg	0.7179 ± 0.0675		0.8165 ± 0.2161		0.7527 ± 0.0822		0.8636 ± 0.1904		0.801 ± 0.0885		0.8242 ± 0.1262	
Al	4.1856 ± 0.298		4.6307 ± 0.3425		4.0789 ± 0.2911		4.7107 ± 0.3454		4.2256 ± 0.3019		4.257 ± 0.3068	
Si	11.426 ± 0.8127		11.899 ± 0.8741		11.401 ± 0.8122		12.312 ± 0.8965		11.828 ± 0.8435		10.899 ± 0.7824	
P	0.0183 ± 0.0026		0 ± 0.0107		0.0021 ± 0.003		0 ± 0.0092		0.0033 ± 0.0033		0 ± 0.0057	
S	0.2092 ± 0.0163		0.3972 ± 0.0432		0.0746 ± 0.0102		0.2966 ± 0.0347		0.1004 ± 0.0121		0.2133 ± 0.0227	
Cl	0.0634 ± 0.0047		0.0829 ± 0.01		0.5105 ± 0.0363		0.375 ± 0.0283		0.5435 ± 0.0387		0.3213 ± 0.0233	
K	2.0885 ± 0.148		2.0802 ± 0.1518		2.1553 ± 0.1529		2.206 ± 0.1599		2.1935 ± 0.1558		1.9912 ± 0.1423	
Ca	1.7159 ± 0.1216		2.0573 ± 0.1503		1.8098 ± 0.1284		2.367 ± 0.1714		1.8006 ± 0.1278		2.213 ± 0.158	
Ti	0.4371 ± 0.031		0.4341 ± 0.032		0.431 ± 0.0305		0.4307 ± 0.0314		0.4464 ± 0.0317		0.4013 ± 0.0288	
V	0.0205 ± 0.0015		0.0197 ± 0.0013		0.0141 ± 0.001		0.0106 ± 0.0009		0.0129 ± 0.001		0.0089 ± 0.0006	
Cr	0.0057 ± 0.001		0.0033 ± 0.0049		0.0028 ± 0.0014		0.0042 ± 0.0042		0.0033 ± 0.0014		0.0045 ± 0.0024	
Mn	0.0742 ± 0.0057		0.0771 ± 0.0114		0.0582 ± 0.0051		0.072 ± 0.0099		0.0685 ± 0.0057		0.0605 ± 0.0068	
Fe	5.3678 ± 0.3801		5.2264 ± 0.3818		4.3579 ± 0.3092		4.5723 ± 0.3313		4.4776 ± 0.318		4.1892 ± 0.2992	
Co	0 ± 0.0002		0 ± 0.0008		0 ± 0.0002		0 ± 0.0007		0 ± 0.0002		0 ± 0.0004	
Ni	0.0005 ± 0.0005		0.0025 ± 0.0025		0.0005 ± 0.0007		0 ± 0.0021		0.001 ± 0.0007		0.0008 ± 0.0012	
Cu	0.0041 ± 0.0008		0.0082 ± 0.0041		0.0023 ± 0.0012		0.0028 ± 0.0035		0.0029 ± 0.0012		0.0065 ± 0.0021	
Zn	0.0328 ± 0.0025		0.0328 ± 0.0045		0.0174 ± 0.0018		0.0268 ± 0.0038		0.0193 ± 0.0019		0.0329 ± 0.0033	
As	0 ± 0.0002		0 ± 0.0008		0 ± 0.0002		0 ± 0.0007		0 ± 0.0002		0 ± 0.0004	
Se	0 ± 0.0019		0 ± 0.0098		0 ± 0.0028		0 ± 0.0085		0 ± 0.0031		0 ± 0.0053	
Br	0.0024 ± 0.0014		0.0008 ± 0.0066		0.0009 ± 0.0019		0 ± 0.0056		0.0048 ± 0.0022		0 ± 0.0037	
Rb	0.0146 ± 0.0015		0.0041 ± 0.0049		0.0111 ± 0.0017		0.0071 ± 0.0043		0.0145 ± 0.0018		0.0167 ± 0.003	
Sr	0.0212 ± 0.0023		0.0197 ± 0.0091		0.0192 ± 0.0029		0.0226 ± 0.0079		0.0178 ± 0.0032		0.0232 ± 0.005	
Y	0.0037 ± 0.0014		0.0074 ± 0.0066		0.003 ± 0.0019		0.0021 ± 0.0057		0.0052 ± 0.0022		0 ± 0.0037	
Zr	0.0217 ± 0.0035		0.0115 ± 0.0164		0.0271 ± 0.0051		0.0085 ± 0.0141		0.0155 ± 0.0051		0.015 ± 0.0086	
Cd	0.0022 ± 0.0046		0 ± 0.0238		0 ± 0.007		0 ± 0.0205		0.0031 ± 0.0074		0.002 ± 0.0126	
Sn	0 ± 0.0035		0 ± 0.0181		0.0021 ± 0.0051		0 ± 0.0155		0 ± 0.0055		0 ± 0.0097	
Sb	0.0013 ± 0.0067		0 ± 0.0345		0 ± 0.0097		0 ± 0.0297		0 ± 0.0105		0.0004 ± 0.0179	
Ba	0 ± 0.0006		0 ± 0.0025		0 ± 0.0009		0 ± 0.0028		0 ± 0.001		0 ± 0.0016	
Pb	0.0029 ± 0.0024		0.0033 ± 0.0123		0 ± 0.0035		0 ± 0.0106		0.0036 ± 0.0038		0 ± 0.0061	
Bi	0 ± 0		0 ± 0		0 ± 0		0 ± 0		0 ± 0		0 ± 0	
U	0 ± 0.0038		0 ± 0.0197		0 ± 0.0056		0 ± 0.0169		0 ± 0.0059		0.0081 ± 0.0102	

Appendix H – Normative mineral abundances for 20 PM₁₀ and PM_{2.5} filter samples

H (e) Normative mineral abundances calculated from chemical results and X-ray diffraction (XRD) mineral information, for three Yuma gun sites.

SITE	Yuma PG 2005		Yuma PG 2005		Yuma PG 2005	
	Gun Site 1		Gun Site 2		Gun Site 3	
	PM10	PM2.5	PM10	PM2.5	PM10	PM2.5
	YU47T001	YU47T002	YU47T003	YU47T004	YU47T008	YU47T005
OCTRC	11.62	23.50	9.29	19.48	27.54	30.52
ECTRC	2.19	4.56	2.73	2.98	8.38	16.73
Quartz	2.56	4.49	7.54	2.12	4.91	1.76
Orthoclase	4.67	0.13	5.43	5.63	3.12	6.21
Plagioclase	5.90	2.58	6.96	6.56	8.98	6.87
Amphibole	0.00	0.00	0.00	0.00	0.00	0.00
Biotite	7.74	3.42	11.48	6.73	7.39	6.28
Chlorite	0.00	0.00	0.00	0.00	0.00	0.00
Clays	9.31	3.95	9.39	8.57	5.72	3.78
Calcite	11.67	4.04	17.01	4.37	8.02	5.07
Dolomite	1.75	1.21	1.02	0.71	0.62	0.62
Hematite	0.57	0.07	0.70	0.95	0.93	0.12
Pyrolusite	0.11	0.04	0.17	0.09	0.17	0.12
Rutile	3.61	1.25	2.89	2.20	0.42	0.58
Base Metals	20.72	17.11	7.60	9.42	0.09	1.20
Evaporites	16.24	29.92	15.60	24.66	12.49	6.09
(NH ₄) ₂ SO ₄	0.30	0.34	0.63	2.69	9.43	12.35
NH ₄ NO ₃	1.05	3.39	1.56	2.83	1.79	1.71

H (f) Normative mineral abundances calculated from chemical results and X-ray diffraction (XRD) mineral information, for two unpaved road sample sets from Yakima Test Center and two desert pavement sites at Yuma Proving Ground.

SITE	Yakima TC 2006		Yakima TC 2006		Yuma PG 2007		Yuma PG 2007	
	Unpaved road, personnel carrier		Unpaved road, M1-A1 tank		Desert pavement, Roadrunner, Helicopter, Site 1		Desert pavement, disturbed, Helicopter, Site 2	
	PM10	PM2.5	PM10	PM2.5	PM10	PM2.5	PM10	PM2.5
	YU47T007	YU47T009	YU47T012	YU47T013	YU47T025	YU47T026	YU47T024	YU47T028
OCTRC	25.56	19.21	11.44	26.27	13.97	18.14	9.54	14.34
ECTRC	1.92	1.36	0.69	1.09	0.00	0.06	0.00	0.06
Quartz	11.90	19.16	2.41	6.63	14.90	10.82	13.93	15.12
Orthoclase	0.00	0.00	0.00	0.00	0.29	0.31	4.54	5.79
Plagioclase	9.91	11.30	8.94	10.43	5.60	2.98	5.51	5.92
Amphibole	16.32	8.40	23.07	21.54	0.00	0.00	0.00	0.00
Biotite	14.92	17.17	25.91	15.91	10.32	6.85	14.62	18.51
Chlorite	0.23	8.28	6.50	0.61	7.08	7.53	0.70	0.07
Clays	7.92	8.37	2.86	4.95	11.87	15.54	11.71	14.23
Calcite	6.56	1.75	4.76	8.39	22.65	13.96	27.50	17.66
Dolomite	0.62	0.60	0.11	0.12	3.58	4.58	2.94	1.69
Hematite	0.04	0.03	9.61	0.06	0.00	0.20	1.49	0.08
Pyrolusite	0.26	0.30	0.54	0.31	0.18	0.24	0.20	0.22
Rutile	1.44	1.43	2.33	1.44	0.85	0.71	0.86	0.86
Base Metals	0.04	0.06	0.07	0.05	0.05	0.08	0.03	0.04
Evaporites	1.17	1.26	0.57	1.60	4.70	5.61	3.09	0.96
(NH ₄) ₂ SO ₄	0.10	0.00	0.00	0.00	2.20	8.13	0.38	2.91
NH ₄ NO ₃	1.09	1.33	0.20	0.60	2.97	4.28	2.98	1.54

Appendix H – Normative mineral abundances for 20 PM₁₀ and PM_{2.5} filter samples

H(g) Normative mineral abundances calculated from chemical results and X-ray diffraction (XRD) mineral information, for three Ft Carson sampling sites.

SITE	Ft Carson 2008		Ft Carson 2008		Ft Carson 2008	
	Unpaved road, Site 1		Unpaved road, Site 2		Unpaved road, Site 2, South side	
	PM10 YU47T035	PM2.5 YU47T038	PM10 YU47T039	PM2.5 YU47T040	PM10 YU47T041	PM2.5 YU47T042
OCTRC	3.82	12.79	3.57	9.89	6.04	7.51
ECTRC	0.71	3.22	1.09	2.63	1.21	1.35
Quartz	22.00	17.34	24.03	19.77	23.35	20.98
Orthoclase	5.02	4.31	5.97	5.88	5.93	5.95
Plagioclase	13.28	11.86	6.53	6.43	6.49	6.51
Amphibole	0.00	0.00	0.00	0.00	0.00	0.00
Biotite	32.62	28.34	27.33	18.12	23.36	21.88
Chlorite	2.18	0.15	1.47	5.42	3.79	4.38
Clays	10.68	10.66	13.49	12.66	13.03	14.74
Calcite	0.77	2.16	0.77	3.22	0.00	3.48
Dolomite	4.31	3.05	9.21	8.52	10.21	6.41
Hematite	0.15	0.04	0.14	0.10	0.10	0.48
Pyrolusite	0.25	0.22	0.20	0.19	0.22	0.20
Rutile	1.55	1.29	1.56	1.22	1.48	1.40
Base Metals	0.08	0.08	0.05	0.05	0.05	0.08
Evaporites	1.51	1.30	3.40	3.12	3.41	2.65
(NH ₄) ₂ SO ₄	0.69	2.11	0.73	1.54	0.75	0.93
NH ₄ NO ₃	0.37	1.07	0.46	1.24	0.59	1.05

Appendix I – Particle Size Distributions

Yuma PG 2005

Gunsite

Table 1 - Sample 1.

Y47N001

Particle Abundance Distribution by Average Diameter (microns)

Classes	Number%	0.2-0.5	0.5-1.0	1-2	2-5	5-7.5	7.5-10	10-15
Pb-Rich	1.5	34.7	37.8	9.4	18.1	0.0	0.0	0.0
Bi-Rich	34.7	48.7	36.1	11.6	3.5	0.1	0.0	0.0
Cu-Rich	5.2	5.4	32.3	45.8	15.8	0.7	0.0	0.0
Fe-rich	0.0	0.0	0.0	0.0	100.0	0.0	0.0	0.0
Ti-rich	1.2	23.3	35.0	23.3	12.5	1.3	2.2	1.8
Ca-rich	0.1	0.0	0.0	0.0	61.1	38.9	0.0	0.0
Ca/S	0.3	0.0	45.6	0.0	50.9	3.5	0.0	0.0
Ca/Mg	0.0	0.0	0.0	0.0	0.0	0.0	100.0	0.0
Ca-rich	0.1	0.0	0.0	0.0	71.4	23.8	4.8	0.0
Al-Si	2.7	0.0	36.1	20.6	31.9	7.1	3.1	1.2
Si-rich	0.6	0.0	45.7	22.9	21.0	7.9	2.6	0.0
K/S-Rich	23.0	27.4	57.1	14.0	1.4	0.0	0.0	0.0
C-rich	21.7	83.1	15.4	1.3	0.2	0.0	0.0	0.0
Misc.	8.9	43.2	39.3	12.6	4.0	0.7	0.1	0.1
Total	100.0	46.2	36.5	12.1	4.5	0.5	0.1	0.1

Y47N001

Mass Distribution by Average Diameter (microns)

Classes	Mass%	0.2-0.5	0.5-1.0	1-2	2-5	5-7.5	7.5-10	10-15
Pb-Rich	3.1	0.3	2.5	11.7	85.5	0.0	0.0	0.0
Bi-Rich	18.0	1.3	9.0	28.1	49.5	12.0	0.0	0.0
Cu-Rich	11.3	0.1	1.6	22.1	57.0	19.2	0.0	0.0
Fe-rich	0.1	0.0	0.0	0.0	100.0	0.0	0.0	0.0
Ti-rich	16.2	0.0	0.1	0.7	8.8	3.1	25.9	29.4
Ca-rich	1.8	0.0	0.0	0.0	26.3	73.7	0.0	0.0
Ca/S	0.9	0.0	3.0	0.0	38.7	58.3	0.0	0.0
Ca/Mg	0.4	0.0	0.0	0.0	0.0	0.0	100.0	0.0
Ca/Si	1.4	0.0	0.0	0.0	37.6	43.1	19.3	0.0
Al/Si	29.7	0.0	0.2	1.4	17.3	23.1	23.3	34.6
Si-rich	4.1	0.0	0.7	0.7	18.0	44.1	36.5	0.0
K/S	3.9	1.3	16.9	25.0	46.2	10.6	0.0	0.0
C-rich	0.5	25.2	30.5	8.1	36.2	0.0	0.0	0.0
Misc.	8.7	0.4	3.2	8.0	25.3	26.2	10.7	26.1
Totals	100.0	0.5	3.1	10.2	30.9	18.6	14.2	17.3

Appendix I – Particle Size Distributions

I(b) Particle size distribution, per particle abundance, and per particle mass, for Yuma PG gun site sample 2, collected in 2005. CCSEM measurements on PM₁₀ Nuclepore filter samples. The peak value (s) for each particle class is highlighted in yellow.

Yuma PG 2005

Gunsite

Table 1 - Sample 2.

Y47N003

Particle Abundance Distribution by Average Diameter (microns)

Classes	Number%	0.2-0.5	0.5-1.0	1-2	2-5	5-7.5	7.5-10	10-15
Pb-Rich	32.3	35.6	45.2	14.6	4.4	0.2	0.0	0.0
Bi-Rich	0.1	100.0	0.0	0.0	0.0	0.0	0.0	0.0
Cu-Rich	1.8	42.5	30.6	15.3	10.8	0.7	0.0	0.0
Fe-rich	0.1	0.0	0.0	0.0	100.0	0.0	0.0	0.0
Ti-rich	5.6	34.7	46.8	9.9	8.2	0.2	0.2	0.0
Ca-rich	0.8	0.0	0.0	17.8	55.4	18.5	8.4	0.0
Ca/S	0.4	0.0	0.0	78.0	14.7	3.7	0.0	3.7
Ca/Mg	0.0	0.0	0.0	0.0	100.0	0.0	0.0	0.0
Ca-rich	1.4	14.5	49.1	19.7	13.0	1.9	1.9	0.0
Al-Si	8.2	4.2	16.9	35.6	32.8	8.3	1.0	1.1
Si-rich	3.0	7.3	27.7	36.9	24.2	2.6	0.4	0.9
K/S-Rich	31.2	29.9	38.2	20.9	10.2	0.6	0.2	0.0
C-rich	10.7	70.0	26.0	2.6	1.2	0.1	0.0	0.0
Misc.	4.4	34.3	47.3	12.6	5.2	0.3	0.3	0.0
Total	100.0	33.4	37.5	17.6	9.8	1.2	0.3	0.1

Y47N003

Mass Distribution by Average Diameter (microns)

Classes	Mass%	0.2-0.5	0.5-1.0	1-2	2-5	5-7.5	7.5-10	10-15
Pb-Rich	13.0	0.7	7.2	23.3	52.0	16.7	0.0	0.0
Bi-Rich	0.0	100.0	0.0	0.0	0.0	0.0	0.0	0.0
Cu-Rich	1.6	0.3	2.8	4.5	75.8	16.6	0.0	0.0
Fe-rich	0.5	0.0	0.0	0.0	100.0	0.0	0.0	0.0
Ti-rich	3.0	0.5	4.0	7.6	42.9	9.9	35.0	0.0
Ca-rich	9.8	0.0	0.0	0.9	19.8	35.5	43.8	0.0
Ca/S	1.8	0.0	0.0	3.7	11.7	7.7	0.0	76.9
Ca/Mg	0.1	0.0	0.0	0.0	100.0	0.0	0.0	0.0
Ca/Si	2.3	0.0	0.5	2.0	29.5	19.2	48.7	0.0
Al/Si	45.3	0.0	0.1	1.8	20.1	32.6	7.4	26.9
Si-rich	6.4	0.0	0.3	4.1	22.4	26.3	8.0	39.0
K/S	13.9	0.3	2.5	11.3	51.5	19.3	15.2	0.0
C-rich	0.6	4.3	11.4	9.4	49.7	25.1	0.0	0.0
Misc.	1.8	0.6	3.7	13.3	36.1	10.9	35.4	0.0
Totals	100.0	0.2	1.7	6.5	31.3	26.3	13.1	16.1

Appendix I – Particle Size Distributions

I(c) Particle size distribution, per particle abundance, and per particle mass, for Yakima TC dirt road sample, collected in 2006. CCSEM measurements on PM₁₀ Nuclepore filter samples. The peak value (s) for each particle class is highlighted in yellow.

Yakima TC 2006

Dirt Road

Y47N007

Particle Abundance Distribution by Average Diameter (microns)

Classes	Number%	0.2-0.5	0.5-1	1-2	2-5	5-7.5	7.5-10	10-15
Fe-rich	0.2	0.0	84.6	0.0	15.4	0.0	0.0	0.0
Ti-rich	0.3	49.2	43.0	0.0	7.8	0.0	0.0	0.0
Ca-rich	0.0	0.0	0.0	0.0	100.0	0.0	0.0	0.0
Si/Al	91.8	3.3	30.8	40.3	23.0	2.1	0.5	0.0
Si-rich	4.8	10.3	32.1	23.4	29.5	3.7	1.1	0.0
K/S	0.1	0.0	100.0	0.0	0.0	0.0	0.0	0.0
Si/K/S	0.1	0.0	100.0	0.0	0.0	0.0	0.0	0.0
Ca/Si	0.8	0.0	18.6	37.3	44.1	0.0	0.0	0.0
C-rich	0.3	0.0	0.0	91.7	8.3	0.0	0.0	0.0
Misc.	1.5	18.6	9.3	65.3	5.1	1.7	0.0	0.0
Totals	100.0	4.0	30.7	39.6	23.1	2.2	0.5	0.0

Y47N007

Mass Distribution by Average Diameter (microns)

Classes	Mass%	0.2-0.5	0.5-1	1-2	2-5	5-7.5	7.5-10	10-15
Fe-rich	0.1	0.0	15.4	0.0	84.6	0.0	0.0	0.0
Ti-rich	0.1	1.0	1.6	0.0	97.4	0.0	0.0	0.0
Ca-rich	0.1	0.0	0.0	0.0	100.0	0.0	0.0	0.0
Si/Al	92.8	0.0	0.9	8.2	41.9	29.2	17.0	2.7
Si-rich	5.3	0.0	0.7	3.0	41.4	32.2	22.6	0.0
K/S	0.0	0.0	100.0	0.0	0.0	0.0	0.0	0.0
Si/K/S	0.0	0.0	100.0	0.0	0.0	0.0	0.0	0.0
Ca/Si	0.5	0.0	0.3	7.8	91.9	0.0	0.0	0.0
C-rich	0.1	0.0	0.0	41.7	58.3	0.0	0.0	0.0
Misc.	1.0	0.2	1.6	12.2	10.7	75.3	0.0	0.0
Totals	100.0	0.0	0.9	8.0	42.0	29.6	17.0	2.5

Appendix I – Particle Size Distributions

I(d) Particle size distribution, per particle abundance, and per particle mass, for Yakima TC dirt road sample 2, collected in 2006. CCSEM measurements on PM₁₀ Nuclepore filter samples. The peak value (s) for each particle class is highlighted in yellow.

Yakima TC 2006

Dirt Road

Table 1 - Sample 3.

Y47N010

Particle Abundance Distribution by Average Diameter (microns)

Classes	Number%	0.2-0.5	0.5-1.0	1-2	2-5	5-7.5	7.5-10	10-15
Fe-rich	1.0	0.0	11.7	23.5	59.9	0.0	4.9	0.0
Ti-rich	0.2	0.0	70.4	0.0	29.6	0.0	0.0	0.0
Ca-rich	1.2	0.0	18.8	18.8	46.5	11.9	4.0	0.0
Al/Si	71.1	1.8	15.2	38.5	36.1	6.6	1.5	0.2
Si-rich	20.1	3.2	26.1	31.9	33.0	3.7	1.7	0.5
C-rich	5.3	19.5	54.6	21.8	4.0	0.0	0.0	0.0
Misc.	1.1	0.0	31.8	63.7	4.5	0.0	0.0	0.0
Totals	100.0	3.0	19.8	36.1	33.8	5.6	1.5	0.2

Y47N010

Mass Distribution by Average Diameter (microns)

Classes	Mass%	0.2-0.5	0.5-1.0	1-2	2-5	5-7.5	7.5-10	10-15
Fe-rich	1.5	0.0	0.2	2.3	36.9	0.0	60.6	0.0
Ti-rich	0.0	0.0	8.1	0.0	91.9	0.0	0.0	0.0
Ca-rich	1.9	0.0	0.1	1.4	21.1	40.2	37.1	0.0
Al/Si	77.8	0.0	0.2	3.7	31.8	36.4	22.0	5.9
Si-rich	18.4	0.0	0.3	2.3	27.8	23.6	24.4	21.5
C-rich	0.2	0.7	10.5	38.9	49.9	0.0	0.0	0.0
Misc.	0.1	0.0	3.8	68.9	27.2	0.0	0.0	0.0
Totals	100.0	0.0	0.2	3.5	31.0	33.4	23.3	8.5

Appendix I – Particle Size Distributions

I(e) Particle size distribution, per particle abundance, and per particle mass, for Yuma PG undisturbed desert pavement sample, generated by helicopter take-off and landing, collected in 2007. CCSEM measurements on PM₁₀ Nuclepore filter samples. The peak value(s) for each particle class is highlighted in yellow.

Yuma PG 2007

Desert Pavement

Table 1 - Sample 4.

Y47N025

Particle Abundance Distribution by Average Diameter (microns)

Classes	Number%	0.2-0.5	0.5-1.0	1-2	2-5	5-7.5	7.5-10	10-15
Pb-Rich	0.1	0.0	0.0	100.0	0.0	0.0	0.0	0.0
Fe-rich	1.0	0.0	44.6	22.3	33.1	0.0	0.0	0.0
Ti-rich	0.3	0.0	40.2	40.2	0.0	19.5	0.0	0.0
Ca-rich	3.9	0.0	0.0	28.6	61.7	9.7	0.0	0.0
Ca/S	1.2	0.0	9.7	38.7	42.2	9.4	0.0	0.0
Ca/Mg	0.4	0.0	0.0	57.4	42.6	0.0	0.0	0.0
Ca/Si	9.4	0.0	13.2	41.9	42.7	1.7	0.6	0.0
Al/Si	67.2	0.4	10.7	41.9	42.2	4.0	0.8	0.1
Si-rich	13.3	0.8	20.2	48.0	28.0	2.5	0.4	0.0
Na/S	0.1	0.0	100.0	0.0	0.0	0.0	0.0	0.0
C-rich	1.3	0.0	35.1	35.1	29.8	0.0	0.0	0.0
Misc.	1.8	0.0	30.6	36.7	32.8	0.0	0.0	0.0
Totals	100.0	0.4	12.9	41.9	40.5	3.7	0.7	0.1

Y47N025

Mass Distribution by Average Diameter (microns)

Classes	Mass%	0.2-0.5	0.5-1.0	1-2	2-5	5-7.5	7.5-10	10-15
Pb-Rich	0.0	0.0	0.0	100.0	0.0	0.0	0.0	0.0
Fe-rich	0.4	0.0	3.6	6.7	89.7	0.0	0.0	0.0
Ti-rich	0.4	0.0	0.6	7.4	0.0	92.0	0.0	0.0
Ca-rich	5.9	0.0	0.0	2.4	62.5	35.1	0.0	0.0
Ca/S	2.0	0.0	0.0	1.7	29.0	69.3	0.0	0.0
Ca/Mg	0.1	0.0	0.0	15.7	84.3	0.0	0.0	0.0
Ca/Si	7.2	0.0	0.4	6.7	66.4	12.2	14.4	0.0
Al/Si	74.2	0.0	0.2	4.9	49.2	26.8	15.4	3.6
Si-rich	8.5	0.0	0.5	7.7	49.5	30.5	11.7	0.0
Na/S	0.0	0.0	100.0	0.0	0.0	0.0	0.0	0.0
C-rich	0.4	0.0	1.1	7.1	91.8	0.0	0.0	0.0
Misc.	0.9	0.0	1.1	6.8	92.1	0.0	0.0	0.0
Totals	100.0	0.0	0.2	5.1	51.4	27.2	13.4	2.7

Appendix I – Particle Size Distributions

I(f) Particle size distribution, per particle abundance, and per particle mass, for Yuma PG disturbed desert pavement site, generated by helicopter take-off and landing, collected in 2007. CCSEM measurements on PM₁₀ Nuclepore filter samples. The peak value(s) for each particle class is highlighted in yellow.

Yuma PG 2007

Desert Pavement

Table 1 - Sample 5.

Y47N029

Particle Abundance Distribution by Average Diameter (microns)

Classes	Number%	0.2-0.5	0.5-1.0	1-2	2-5	5-7.5	7.5-10	10-15
Fe-rich	0.4	0.0	68.8	0.0	31.2	0.0	0.0	0.0
Ti-rich	0.9	0.0	64.7	16.2	19.1	0.0	0.0	0.0
Ca-rich	2.4	0.0	5.8	17.3	69.6	6.3	1.0	0.0
Ca/S	0.1	0.0	100.0	0.0	0.0	0.0	0.0	0.0
Ca/Si	2.6	0.0	21.3	42.6	30.4	4.8	1.0	0.0
Al/Si	72.6	1.7	22.0	48.2	25.7	2.2	0.2	0.0
Si-rich	14.4	8.4	41.7	33.0	15.4	1.4	0.0	0.0
K/S	0.1	0.0	0.0	100.0	0.0	0.0	0.0	0.0
Na/S	0.4	0.0	100.0	0.0	0.0	0.0	0.0	0.0
C-rich	5.0	39.8	42.2	14.1	3.3	0.5	0.0	0.0
Misc.	0.9	0.0	59.5	14.9	25.7	0.0	0.0	0.0
Totals	100.0	4.5	26.7	42.4	24.1	2.1	0.2	0.0

Y47N029

Mass Distribution by Average Diameter (microns)

Classes	Mass%	0.2-0.5	0.5-1.0	1-2	2-5	5-7.5	7.5-10	10-15
Fe-rich	0.4	0.0	2.7	0.0	97.3	0.0	0.0	0.0
Ti-rich	0.2	0.0	6.6	8.4	85.0	0.0	0.0	0.0
Ca-rich	7.4	0.0	0.2	2.6	60.9	28.9	7.4	0.0
Ca/S	0.0	0.0	100.0	0.0	0.0	0.0	0.0	0.0
Ca/Si	5.3	0.0	0.3	6.4	42.6	31.2	19.5	0.0
Al/Si	78.7	0.0	0.8	12.2	44.4	29.9	9.6	3.1
Si-rich	7.3	0.1	3.0	12.3	44.0	40.6	0.0	0.0
K/S	0.0	0.0	0.0	100.0	0.0	0.0	0.0	0.0
Na/S	0.0	0.0	100.0	0.0	0.0	0.0	0.0	0.0
C-rich	0.2	2.0	15.4	15.0	32.2	35.4	0.0	0.0
Misc.	0.4	0.0	4.1	8.7	87.1	0.0	0.0	0.0
Totals	100.0	0.0	0.9	11.2	45.9	30.4	9.1	2.5

Appendix I – Particle Size Distributions

I(g) Particle size distribution, per particle abundance, and per particle mass, for Ft Carson dirt road sample, collected in 2008. CCSEM measurements on PM₁₀ Nuclepore filter samples. The peak value (s) for each particle class is highlighted in yellow.

Ft Carson 2008

Dirt Road

Table 1 - Sample 6.

Y47N035

Particle Abundance Distribution by Average Diameter (microns)

Classes	Number%	0.2-0.5	0.5-1.0	1-2	2-5	5-7.5	7.5-10	10-15
Pb-Rich	0.1	100.0	0.0	0.0	0.0	0.0	0.0	0.0
Fe-rich	1.4	0.0	26.8	44.7	26.1	0.0	2.5	0.0
Ti-rich	0.8	0.0	47.8	15.9	36.2	0.0	0.0	0.0
Ca-rich	0.8	0.0	0.0	82.0	9.0	9.0	0.0	0.0
Ca/S	0.0	0.0	0.0	0.0	0.0	100.0	0.0	0.0
Ca/Mg	0.5	0.0	24.4	24.4	51.2	0.0	0.0	0.0
Ca/Si	2.4	11.5	43.0	21.5	22.5	1.5	0.0	0.0
Al/Si	68.8	2.3	21.6	38.4	34.6	2.7	0.4	0.0
Si-rich	16.8	7.1	27.0	36.3	26.0	3.2	0.4	0.0
C-rich	6.0	35.9	36.8	21.6	5.1	0.0	0.6	0.0
Misc.	2.3	5.6	50.0	38.9	5.6	0.0	0.0	0.0
Totals	100.0	5.4	24.7	36.8	30.1	2.6	0.4	0.0

Y47N035

Mass Distribution by Average Diameter (microns)

Classes	Mass%	0.2-0.5	0.5-1.0	1-2	2-5	5-7.5	7.5-10	10-15
Pb-Rich	0.0	100.0	0.0	0.0	0.0	0.0	0.0	0.0
Fe-rich	1.7	0.0	0.6	8.9	49.9	0.0	40.6	0.0
Ti-rich	0.3	0.0	4.3	23.1	72.6	0.0	0.0	0.0
Ca-rich	1.7	0.0	0.0	12.0	10.1	78.0	0.0	0.0
Ca/S	0.9	0.0	0.0	0.0	0.0	100.0	0.0	0.0
Ca/Mg	0.6	0.0	1.1	7.7	91.2	0.0	0.0	0.0
Ca/Si	1.7	0.1	1.1	7.5	61.3	30.1	0.0	0.0
Al/Si	77.5	0.0	0.5	6.4	51.9	29.8	11.6	0.0
Si-rich	13.7	0.0	0.7	6.8	42.6	36.0	13.8	0.0
C-rich	1.7	0.3	1.3	5.8	21.8	0.0	70.8	0.0
Misc.	0.3	0.2	13.0	66.2	20.6	0.0	0.0	0.0
Totals	100.0	0.0	0.6	6.7	49.3	30.7	12.7	0.0

Appendix I – Particle Size Distributions

I(h) Particle size distribution, per particle abundance, and per particle mass, for Ft Carson dirt road sample, collected in 2008. CCSEM measurements on PM₁₀ Nuclepore filter samples. The peak value(s) for each particle class is highlighted in yellow.

Ft Carson 2008

Dirt Road

Y47N041

Particle Abundance Distribution by Average Diameter (microns)

Classes	Number%	0.2-0.5	0.5-1.0	1-2	2-5	5-7.5	7.5-10	10-15
Fe-rich	1.8	0.0	29.1	40.8	26.7	3.4	0.0	0.0
Ti-rich	0.2	0.0	0.0	63.4	36.6	0.0	0.0	0.0
Ca-rich	1.2	17.4	0.0	26.2	56.4	0.0	0.0	0.0
Ca/S	0.4	0.0	0.0	100.0	0.0	0.0	0.0	0.0
Ca/Mg	1.7	0.0	18.2	42.5	35.8	3.5	0.0	0.0
Ca/Si	3.0	10.5	24.5	35.1	27.8	0.0	2.0	0.0
Al/Si	70.9	3.4	15.1	30.1	42.6	7.6	1.0	0.3
Si-rich	16.7	7.6	15.5	31.7	39.7	5.0	0.4	0.0
C-rich	2.6	12.7	40.2	24.1	23.0	0.0	0.0	0.0
Misc.	1.5	41.0	27.0	13.5	18.5	0.0	0.0	0.0
Totals	100.0	5.1	16.3	30.8	40.4	6.3	0.8	0.2

Y47N041

Mass Distribution by Average Diameter (microns)

Classes	Mass%	0.2-0.5	0.5-1.0	1-2	2-5	5-7.5	7.5-10	10-15
Fe-rich	1.3	0.0	0.7	4.0	23.9	71.5	0.0	0.0
Ti-rich	0.3	0.0	0.0	1.7	98.3	0.0	0.0	0.0
Ca-rich	0.7	0.1	0.0	5.0	94.9	0.0	0.0	0.0
Ca/S	0.0	0.0	0.0	100.0	0.0	0.0	0.0	0.0
Ca/Mg	2.2	0.0	0.2	3.4	44.2	52.2	0.0	0.0
Ca/Si	2.0	0.0	0.8	6.4	58.6	0.0	34.2	0.0
Al/Si	81.2	0.0	0.2	2.6	39.8	38.1	13.5	5.7
Si-rich	11.9	0.0	0.3	3.4	44.7	41.6	10.0	0.0
C-rich	0.2	0.4	4.7	5.6	89.3	0.0	0.0	0.0
Misc.	0.2	0.4	3.2	9.8	86.6	0.0	0.0	0.0
Totals	100.0	0.0	0.2	2.9	41.4	38.0	12.8	4.7